Hydro-mechanical coupling in a deformable dual-scale fibrous reinforcement : from mesoscale characterization and modeling to liquid resin infusion process simulation

Julie Hemmer

UNIVERSITE BRETAGNE SCIENCES LOIRE POUR L'INGENIEUR

CENTRALE NANTES

THESE DE DOCTORAT DE

L'ÉCOLE CENTRALE DE NANTES
COMUE UNIVERSITE BRETAGNE LOIRE

ECOLE DOCTORALE N° 602
Sciences pour l'Ingénieur
Spécialité : Mécanique des Solides, des Matériaux, des Structures et des Surfaces

Julie HEMMER

Hydro-mechanical coupling in a deformable dual-scale fibrous reinforcement:
from mesoscale characterization and modeling to liquid resin infusion process simulation

Thèse présentée et soutenue à Nantes, le 4 décembre 2018
Unité de recherche : Institut de Recherche en Génie Civil et Mécanique – UMR CNRS 6183

Rapporteurs avant soutenance :

Clemens Dransfeld
Professeur des Universités, Technical University of Delft

Laurent Orgéas
Directeur de recherche CNRS, Laboratoire 3SR – UMR 5521

Composition du Jury :

Clemens Dransfeld
Professeur des Universités, Technical University of Delft

Mylène Lagardère
Maître-Assistant des Ecoles des Mines, IMT Lille-Douai

Didier Lasseux (président du jury)
Directeur de recherche CNRS, Laboratoire I2M – UMR 5295

Laurent Orgéas
Directeur de recherche CNRS, Laboratoire 3SR – UMR 5521

Directeur de thèse
Sébastien Comas-Cardona
Professeur des Universités, Ecole Centrale de Nantes

Co-directeur de thèse
Christophe Binetruy
Professeur des Universités, Ecole Centrale de Nantes

Co-encadrant de thèse
Christian Burtin
Maître de Conférences HDR, Ecole Centrale de Nantes

Acknowledgments

Cette étude a été menée en collaboration entre le laboratoire du GeM de l'Ecole Centrale de Nantes et la plateforme CANOE localisée à Pessac. Je remercie ces deux entités d'avoir permis la réalisation de cette thèse dans les meilleures conditions qui soient.
Mes remerciements vont tout d'abord à mes encadrants industriels, Thibaut Savart, Arthur Babeau et Aline Ferrand, car ils ont su être ouverts à de nombreuses discussions, parfois bien loin du projet initial. J'ai pu apprendre à leurs côtés, et ceux de Mélanie Frechou, des techniques industrielles expérimentales qui ont élargi ma vision du problème scientifique.
J'adresse ma plus profonde reconnaissance à mes deux directeurs de thèse, Sébastien Comas et Christophe Binétruy, ainsi qu'à mon encadrant Christian Burtin. Vous avez su me guider, m'accompagner, m'épauler sans faiblir pendant ces trois ans. Vous m'avez beaucoup appris sur des points de vue technique et scientifique, mais aussi et surtout sur des aspects humains qui me suivront, je le pense, bien longtemps! Honnêtement, j'espère un jour être à la hauteur pour réussir à encadrer des étudiants en thèse, master et autre comme vous l'avez fait. Merci.
Je souhaite remercier les membres du jury, et notamment les rapporteurs, pour leur lecture attentive de ce manuscrit. Les échanges que nous avons eu à la suite de la soutenance m'ont permis de prendre plus de recul vis à vis de ce travail.
Ce travail n'aurait pu être réalisé sans l'aide précieuse de Jean-Michel Lebrun, Gilles Patté et François Bertrand. Je vous remercie pour toutes ces astuces expérimentales que vous avez partagées avec moi.

Je me suis réellement sentie comme chez moi au sein du laboratoire du GeM. Je me rends compte à quel point vous, les chercheurs et apprentis-chercheurs, avez toujours été bienveillants envers moi. Vos conseils scientifiques, pédagogiques et personnels m'ont forgée, et je n'ai pas assez de mots pour vous en remercier. Une liste de noms serait plutôt longue, mais j'ose espérer que les enseignants-chercheurs de l'option Matepro, l'Open-Space-Du-Milieu (l'actuel et l'ancien), les "premiers rangs" en option Matepro ainsi que mes chers Espagnols, Italiens et Belges sauront se reconnaître. Merci.
Il m'est difficile d'exprimer avec des mots simples la ressource sans fin que je puise au sein de ma famille. Maman, Papa, mes soeurs et frères Caroline, Coco, Mick et Gaël, ma tante et mon oncle Huguette et Michel: je vous remercie du fond du coeur.

Contents

Introduction

One of the major challenges in the field of sustainable energies is to increase the length of wind turbine blades. A lightweight design is needed in order to ensure the energy profitability. Therefore, the wind turbine industry has been interested for decades in introducing structural composites parts in their products. In this context, the objective of the company CANOE is to produce composite structural large parts at reduced cost.

Liquid Composite Molding (LCM) processes are now commonly used to manufacture structural composites parts. During these processes, dry fibrous reinforcements are impregnated with a reactive low-viscosity resin. The latter will become, after polymerization, the matrix of organic composite materials. The fibrous reinforcement is usually viewed as a porous continuous material: the fibers, which are the constitutive elements, are separated by open pores. Quasi-unidirectional non-crimp fabric (quasi-UD NCF), usually used for structural applications in the wind turbine industry, are considered as dual-scale porous materials: the size of the pores are characterized by two distinct characteristic lengths (the first one associated to micro-pores inside tows and the second for the meso-pores located between tows). The impregnation of this dual-scale porous material conditions the quality as well as the filling time of final composite parts.
For the manufacturing of large composite parts (as wind turbine blades for instance), the infusion process is competitive on both mechanical and cost aspects. It is a closed mold composite process, where the bottom side of the mold is solid, and the top side is a vacuum bag. Because the vacuum bag is flexible, local compaction state of the porous fabric preform can easily be modified. In the infusion process, first the application of vacuum on the dry and compliant fibrous plies induces a thickness decrease of the fibrous preform. During the filling stage, the stress experienced by the fibrous reinforcement decreases when the fluid flows inside the deformable cavity, as described by Terzaghi's theory. Then, in the saturated area of the part, far behind the flow front, a thickness rise of the fabrics is experimentally observed [2], [3], [4]. The gradient of the resin pressure field generates an unloading on the saturated fibrous plies. The transient macroscopic thickness increase has been extensively studied at the macroscopic scale but the microscopic evolutions of the inter-tow channels (meso-pores) and tows of a given fabric have not been investigated.

New experimental devices are now commonly employed to observe the fiber reorganization inside a tow during the infusion process, near the flow front. Vilà et al. [5] and Larson et al. [6] used X-ray Computed Tomography (XCT) to record a given tow under dry, transient or saturated states; their results show fiber and porosity movements between these states and also highlight an impact on the tow permeability. At the upper scale, very few studies have investigated the tow's movement and swelling inside a fab-

ric: for instance, Francucci et al. [7], [8] showed that, for natural fiber fabrics, the fluid absorption and swelling reduce permeability. However, the impact of the meso-pores distribution, size and location on the global in-plane permeability of fabric is acknowledged [9], [10], [11]. The global fiber volume fraction is a first-order descriptor of the heterogeneous media and cannot capture all the geometric features of the dual-scale fibrous medium that influence the 3D connectivity of flows.

The aim of the first chapter is thus to characterize experimentally the microstructural evolution of the quasi-UD NCF during the infusion process and to quantify its impact on the in-plane permeability, which appears as a relevant macroscopic parameter. New experimental setups will be developed to identify the flow-induced movement and deformation of tows within the fabric.

From an industrial standpoint, it is of great interest to quantify the filling time of composite parts. A simulation-based approach is recognized as a convenient and cost-effective way to predict the filling time in large components. To the authors knowledge, few numerical works [12], [13], [14], [15] are devoted to simulate the dual-scale flow (occurring in a quasi-UD NCF) inside a bidisperse fibrous reinforcement that deforms during its filling (occurring during the infusion process). Moreover, in these numerical studies, authors assume that the fibrous preform is a continuous medium with a varying permeability, and usually Kozeny-Carman [16] and Gebart [17] models are employed to predict the permeability evolution versus the global fiber volume fraction. These models describe macroscopically the permeability evolution but they do not rely on the actual redistribution of inter-tow and intra-tow pores.

Therefore, the aim of the second chapter is to build a numerical tool that simulates the dual-scale flow in a bidisperse deformable porous media. Once implemented, this simulation tool will be used to investigate the influence of the flow-induced microstructural reorganization (occurring during the infusion process) on the filling time.

Finally, the unloading behavior of the fibrous reinforcement is modeled by very few authors [18] and is mostly taken into account in simulation tools by using macroscopic compressive loading models. For instance, Gutowski model [19] is employed by Acheson et al. [12], Robitaille [20] model is used by Correia et al. in their simulation work [21] and a Neo-Hooken hyperelastic material has been selected by Rouhi et al. [15]. Therefore, it is of interest to quantify the mechanical behavior of a single tow and of a single ply during the main stages of the infusion process (dry loading and saturated unloading), in order to improve the existing models commonly implemented in simulation tools.

The aim of the third and last chapter is thus to characterize the 3D mechanical behavior of a single tow and of a single ply subjected to dry loading and saturated unloading stages. A first 3D model will be proposed to reproduce the tow behavior during the dry loading phase.

The main results obtained in this study will be summarized at the end of the manuscript, and perspectives will be proposed and discussed.

CHAPTER I

Experimental investigation of the decompaction phenomenon at macroscopic and mesoscopic scales

1 Introduction

As reviewed in the introduction, fibrous reinforcements manufactured with the infusion process can undergo a decompaction during their filling due to the vacuum bag flexibility. The macroscopic thickness can be 15% higher near the fluid inlet than near the vacuum vent. When dual-scale fabrics are considered, the size and the spatial distribution of intra-tow and inter-tow pores drives the fluid velocity and the global saturation, as a delayed impregnation of tows is occurring. In this context, it is thus of interest to investigate the impact of the decompaction phenomenon at both macroscopic (stack) and mesoscopic (tow) scales. Therefore, new experimental methodologies and setups are implemented to quantify this impact: at meso-scale, a first quantification of the evolution of a same fibrous microstructure under several flow-induced compaction states is proposed.
The main idea of the developed experimental procedure is to record 3D images of a same microstructure at dry state under vacuum (before the infusion) and at saturated state under vacuum (after the infusion). To implement this procedure, a setup is designed to realize in situ downsized infusion inside the X-ray CT device. In this chapter, the objectives are two-folds:

- validate the ability of the downsized setup and the methodology to reproduce the decompaction phenomenon inside the constrained area of the X-ray CT device,
- investigate the influence of the flow-induced decompaction on the tows and inter-tow channels morphological evolution inside the fibrous reinforcement microstructure.

First, the decompaction phenomenon is experimentally investigated at macroscopic scale (refered as *Macro-scale*), using a setup inspired from Yenilmez et al. [3]. The results obtained are used to validate the ability of the downsized setup (named *Macro-meso-scale* setup) to reproduce the decompaction phenomenon. This *Macro-meso-scale* approach gives first trends of the decompaction at mesoscopic scale. A slighlty different downsized setup (named *Meso-scale* setup) is validated at macro-scale and used to propose a deeper investigation of the microstructure displacement (tows displacement) and the

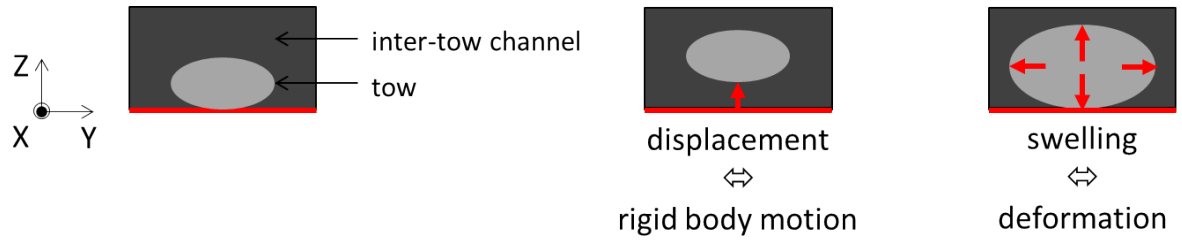

Figure I.1: Illustration of the impact of tow displacement and deformation on the microstructural reorganization

tows deformation due to the flow-induced decompaction. Figure I.1 shows briefly the impact of tow displacement and deformation on the microstructural reorganization. The details about materials, equipment, post-treatment methods as well as obtained results are presented in the following sections. Figure I.2 summarizes the global experimental approach of this chapter.

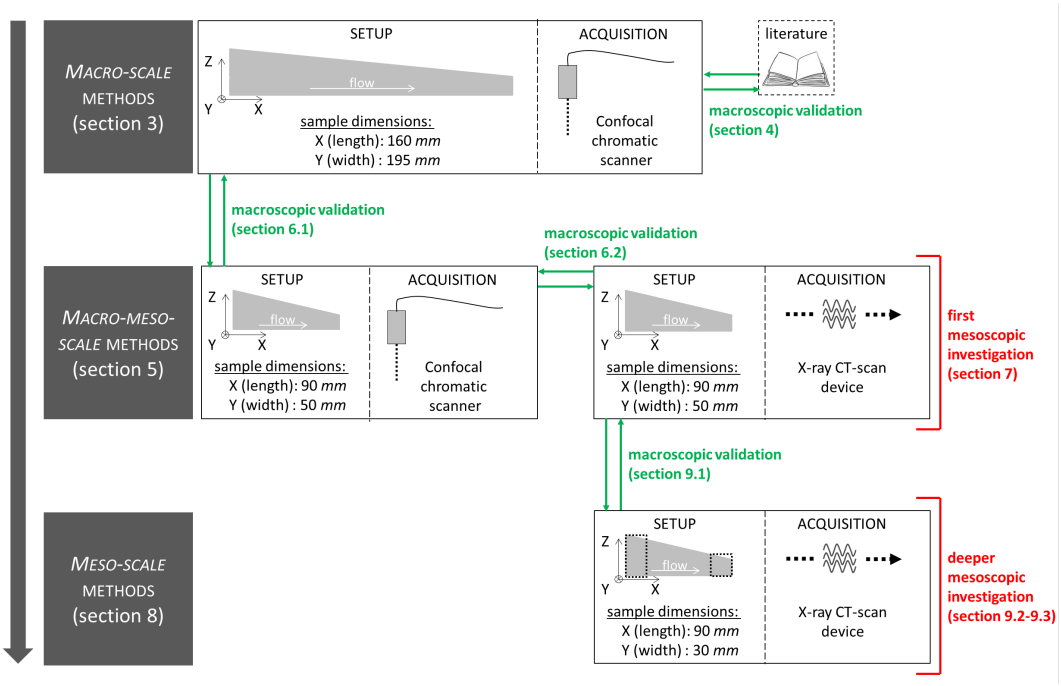

Figure I.2: Graphical summary of the chapter highlighting scales, setups, acquisition systems and presenting the validations and investigations

2 Materials

In this study, a dual-scale porosity fibrous reinforcement that gives rise to measurable decompaction is selected. To investigate the decompaction phenomenon at both macro- and meso-scale, the fabric is impregnated with a model fluid, during the VARTM process. The references of the fabric, the fluid and the consumables are presented hereafter.

2.1 Textile

The quasi-unidirectional non-crimp fabrics (quasi-UD NCF) selected for the study are manufactured from batches of Advantex ® glass roving (Owens Corning). The quasi-UD NCF ply (Figure I.3) of total glass areal weight of 1395 g/m^2 is made of two layers: one layer of UD glass tows (4800 tex) and one weft backing glass layer oriented at $\pm$ 80° (68 tex). Both layers are stitched (warp-knitting) with a very thin polyester thread, symmetrical and spaced of 5 mm, that may constrain locally the tows in the width direction. (Y-direction presented on Figure I.3).

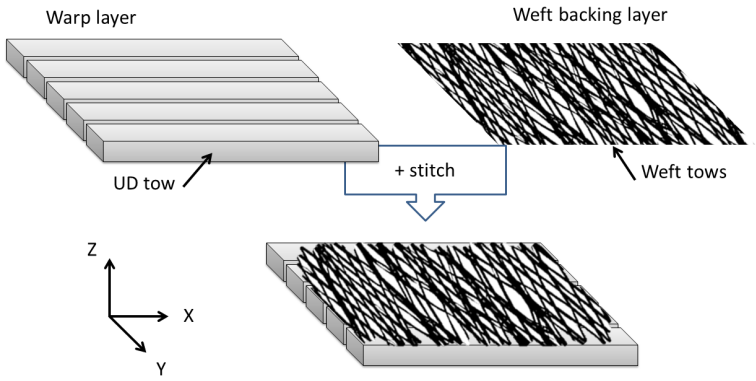

Figure I.3: 3D representation of quasi-UD NCF fabric [22]

2.2 Model fluids

Glycerol is a viscous fluid ($C_3H_8O_2$) with a viscosity of 1.41 $Pa.s$ at 20° C. For this study, Technical Glycerol from VWR is used in dilution with 5% of distilled water to obtain a viscosity of 0.3 $Pa.s$ at 25° C.

2.3 Consumables supplies

To ensure the stability of the developed setups, both rigid and flexible pipes are used. The rigid polyamide pipes *1025P08* of 6 mm inner diameter are provided by Legris and the flexible rubber pipes *GSR* from Saint Gobain have the same inner diameter. To seal the cavity, the bagging film *PA205*, 50 μm thick, and the soft tackytape *LSM7000*, 3 mm thick, are both provided by Diatex. The draining material *OM70* from Diatex drives the fluid from the fluid inlet to the fibrous reinforcement. A non woven breather felt *RC 3000-10 AB 10* made of polyester fibers, commercialized by Cytec, drives the vacuum from the vent to the fibrous reinforcement.

3 Macroscopic scale investigation: setup and methods

In this section, a *Macro-scale* setup inspired from Yenilmez et al. [3] is presented. The principle is to lay down dual-scale fabrics into a cavity closed with a flexible vacuum bag and to measure the vacuum bag displacement between the dry state (before the infusion process) and the saturated state (after the infusion process).

3.1 Experimental principle

A controlled level of vacuum (60 *mbar* abs) is applied in a cavity where plies of quasi-UD NCF are previously laid down (Figure I.4a), the UD fiber direction being along the X-axis. After relaxation of the dry fibrous reinforcement, a first Z-profile of the vacuum bag position along a X-line is recorded (Figure I.4b). A 1D continuous flow of glycerol along the X-axis is then maintained in the cavity, leading to a higher stabilized thickness near the fluid inlet (Figure I.4c) when full saturation is attained. After relaxation of the fully saturated fibrous reinforcement, a second profile acquisition of the vacuum bag position, along the same X-line (e.g. Y is constant between dry and saturated states), is recorded (Figure I.4d).

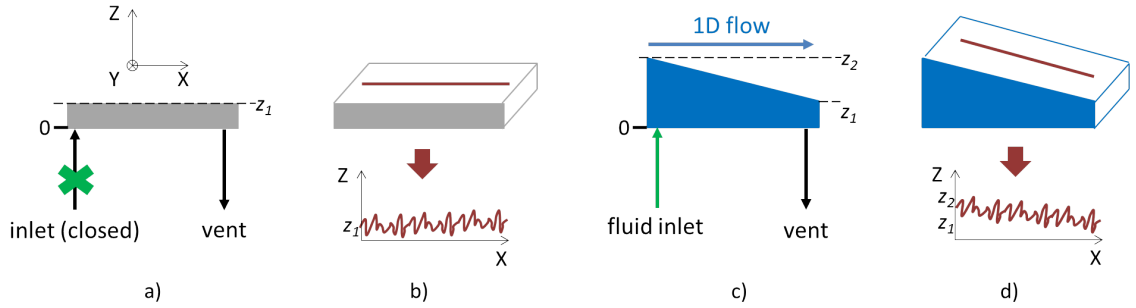

Figure I.4: Experimental steps: a) dry state. b) dry state, acquisition. c) saturated state. d) saturated state, acquisition.

3.2 Proposed setup

To implement this experimental procedure, the *Macro-scale* setup is developed to allow large scale infusion while monitoring the vacuum bag displacement. The setup is composed of an acquisition equipment (a confocal chromatic scanner described in 3.3) and an infusion setup. A schematic view of the setup is shown in Figure I.5 and details about the infusion setup are given hereafter.

3.2.1 Dimensions

To hold the fibrous reinforcement, a PVC plate is designed with respect to the acquisition system constraints and to get an infusion process that best mimics the industrial scale. Table I.1 presents the dimensions of the designed PVC plate and the corresponding dimensions of the quasi-UD NCF.
Pipe lengths and diameters are selected to ensure sufficient flow rate inside the fibrous reinforcement, as recommended by Deleglise et al. [23].

3.2.2 Boundary conditions, edge effects and bagging strategy

If the stack thickness is too high compared to planar dimensions, a high curvature radius locally modifies the thickness (Figure I.6), due to the limited stretch of the vacuum bag. This edge effect might affect the measurement of a representative decompaction phenomenon near the inlet of the considered sample. To limit the edge effects impact near the fluid inlet and the vacuum vent (outlet), a specific bagging strategy is adopted.

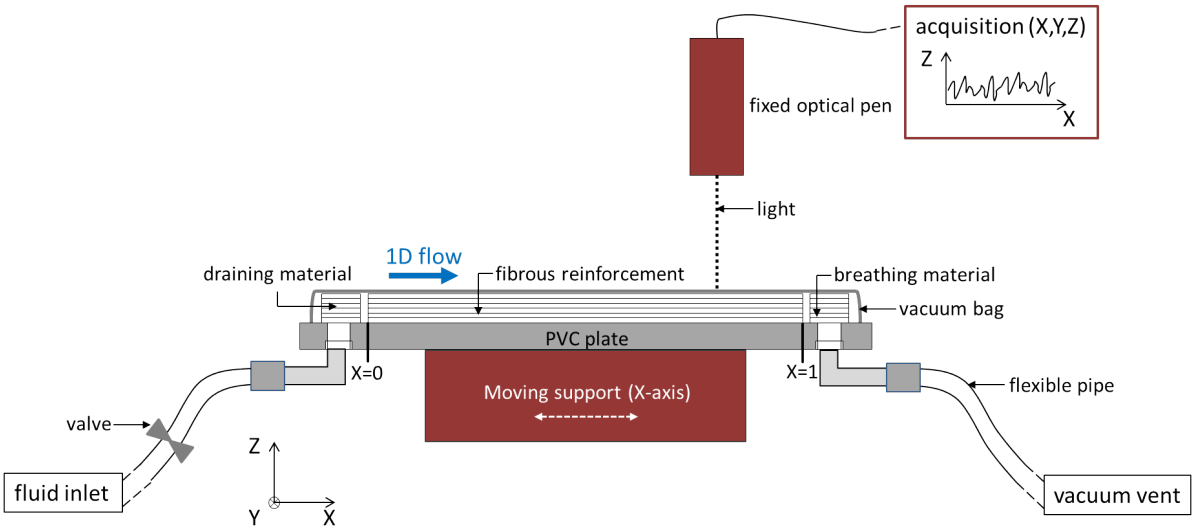

Figure I.5: Schematic view of the *Macro-scale* setup: acquisition equipment (in red) and infusion setup (in grey)

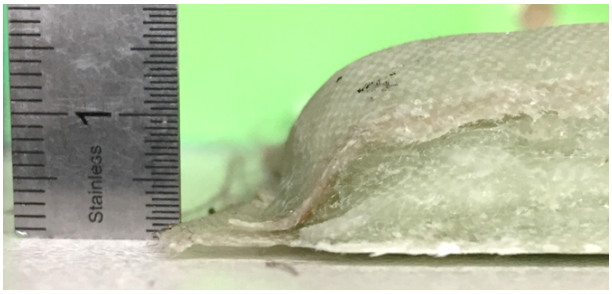

Figure I.6: Illustration of the edge effect for a thick composite part

Near the inlet, several plies of draining material are laid down in contact with the fibrous reinforcement, and several layers of tackytape are used to close the cavity (Figure I.7). The same strategy is adopted near the outlet, where several plies of breathing material are laid down. For instance, for 9 plies of the quasi-UD NCF (section 2.1), 12 plies of draining material, 4 plies of felt breather and 4 layers of tackytape are used.

3.2.3 Stability

During a profile acquisition, the support moves slowly along the X-axis (5 $mm.s^{-1}$). Nonetheless, high stability of the setup must be ensured during the experiment to compare a profile measured along the same X-line at dry state (Figure I.4a) and saturated state (Figure I.4d). Then, flexible pipes are used to avoid spatial constraints, and the PVC plate is taped onto the moving support with a double-sided tape.

3.2.4 Injection equipment

All the infusions conducted during this study have been made using vacuum as driving force. The vacuum pump is a *PC 3001 Vario Pro* from Vacuubrand GmbH allowing an automatic control of the vacuum level thanks to the diaphragm pump motor speed

Table I.1: PVC plate and fabrics dimensions to best mimic an industrial scale infusion process

Axis	PVC plate dimensions (mm)	Fabrics dimensions (mm)	Comments
X-axis (length)	220	165	The length is sufficient to obtain a representative fluid flow.
Y-axis (width)	220	190	The width is sufficient to limit edge effects.
Z-axis (thickness)	10	9 max. (9 plies)	The PVC plate thickness is sufficient to avoid bending effect due to the pressure difference between the upper side (vacuum) and lower side (atmospheric pressure).

adjustment. The minimum vacuum value is 1.5 *mbar* (abs) and the maximal air flow rate is 2 $m^3.h^{-1}$.

3.3 Measurement and acquisition equipment

A chromatic confocal scanner (*CCS Prima*, STIL company), illustrated in Figure I.8 monitors the vacuum bag position along a X-line in the XY-plane for each compaction state. The confocal chromatography principle and the acquisition parameters selected in this study are detailed hereafter.

3.3.1 Confocal chromatography principle

A classical confocal scanner provides a sharp image for its unique focal plane and thus requires a vertical sweep to obtain the image of an object of variable thickness. Alternatively, the chromatic confocal scanner provides this image without any vertical sweep (during an acquisition, the optical pen has a stationary Z-position, previously defined by the operator). It is based on the control of chromatic aberration: as refractive index of lenses depends on wavelength, a white light source will result in several focal planes associated with each wavelength. The collected light is then analyzed: for each wavelength, a spectral analysis provides an intensity maximum, which is correlated to the Z-coordinate of the intersection point between the scanned object and the focal plane associated to the considered wavelength. Therefore, after a scan of the object surface, the altitudes are known. More details are presented in [24].

3.3.2 Acquisition parameters

Several optical pens for the confocal chromatic scanner are provided by STIL. The selected one for this study (*CL4 CCS-Prima*), with 7 μm lateral resolution, presents a

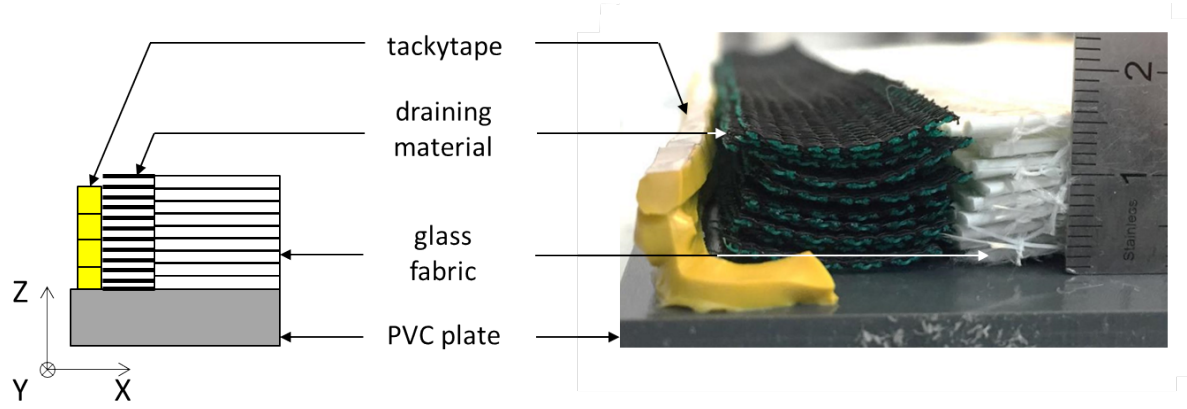

Figure I.7: Bagging strategy adopted near the fluid inlet to limit edge effects

good compromise between a wide range of thickness acquisition (4000 μm) and a sufficient thickness accuracy (0.2 μm). While the support is moving in the X-direction at 5 $mm.s^{-1}$, the optical pen records an intensity (and then an altitude) with a constant step of 5 μm. The acquisition software (Surface Map) also allows profiles acquisition over time.
The acquisition of one Z-profile along the X-axis (e.g. Y constant) is considered representative of the overall decompaction (see section 4.2): the Y-displacement of the support is then not of interest in this experimental protocol.

3.4 Experimental protocol

The experimental protocol follows the steps presented in Figure I.9.

3.5 Macroscopic post-treatment

The raw data recorded by the Software Surface Map are *.csv* files where the altitude $h(X)$ is a vector of length N_X ($X \in [1, N_X]$). For each X-position, the relative decompaction is defined by:

$$\varepsilon_{macro}(X) = \frac{Z_{saturated}(X) - Z_{dry}(X)}{Z_{dry}(X)} \tag{I.1}$$

where X is the normalized position (e.g $X = x/L$ where x stands for the position in mm and L stands for the fabric length in mm), $Z_{saturated}$ and Z_{dry} respectively stands for the altitude at the normalized position X during the saturated state and during the dry state. The post-treatment is automated with Matlab, and an example of raw data is illustrated in Figure I.10.

4 Macroscopic scale investigation: validation

In this section, results about the stack thickness variation between the dry and the saturated states (called macroscopic decompaction), obtained with the *Macro-scale* setup and methodology previously presented, are analyzed. In a first part, the *Macro-scale* methodology using the confocal chromatic scanner is compared to literature works. Then, the

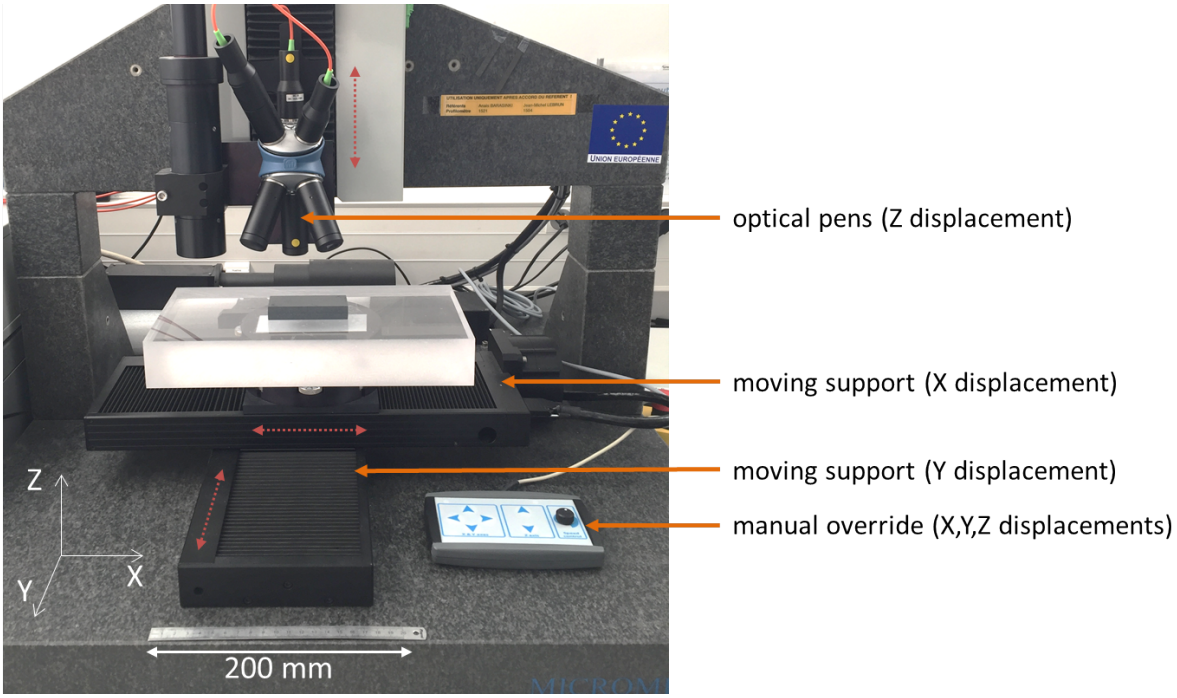

Figure I.8: *CCS Prima* chromatic confocal scanner and its principal components

use of a Z-profile located at a single Y-position to deduce the overall fabric decompaction is justified.

4.1 Literature validation: general trends

The fluid pressure gradient during the infusion process induces a thickness gradient when the part is filled up. Experimental studies are mainly focused on transient state, and present the thickness evolution of a localized spatial point over time. Tackitt et al [2] work with several LVDT sensors to monitor the stack thickness evolution with the X-position (fluid flow direction) during the transient state. The macroscopic decompaction is found to be non-linear with X-position during the transient state for a felt fabric (Figure I.11a) and for a woven glass fabric (Figure I.11b). Nonetheless, when a part is demolded, its thickness gradient with X-position can be considered as linear (Figure I.11c).
In this study, the visualization of the results are presented as the decompaction evolution (e.g the thickness rise between the dry and the fully-saturated state) along the X-position (e.g. the flow front direction). At the end of the transient state the decompaction is non-linear with the X-position (Figure I.12a). Nonetheless, 20 minutes after the end of the transient state (as presented in Figure I.9), while fluid flow and vacuum are still maintained, the macroscopic decompaction tends to linearize with the X-position (Figure I.12b). Moreover, a step of decompaction (around 1.5 %) is observed near the vacuum vent: it could be justified by a delayed decompaction of the breather felt, not monitored here. Van Oosterom et al. [25] report that such boundary conditions can impact drastically the thickness evolution.
These observations at the macroscopic scale match the ones by Tackitt et al. However, attention should be payed to the outlet felt breather behavior.

Step	Description	Duration
Setup preparation	The fabrics, breather felt and draining material are placed on the PVC plate. The mold is closed hermetically with tackytape and vacuum bag, following the bagging strategy presented before.	around 1 h
Setup positioning	The infusion setup is taped on the moving support of the chromatic confocal scanner.	around 1 min
Vacuum stabilization	The vacuum is stabilized inside the fluid trap and the pipes at 60 mbar (abs).	around 2 min
Thickness measurement	The optical pen is manually focused on the PVC plate, at a defined X position near the middle of the sample, to record its altitude (e.g. intensity).	around 1 min
Dry state under vacuum (static) – preset	1) The vacuum level is set inside the cavity. 2) 1 minute after the vacuum level has settled, the optical pen is manually focused on several tows (the same X position as in *Thickness measurement* step) to record their altitudes (the same intensity as PVC plate during the *Thickness measurement* step). It estimates the average thickness of the stack with an error estimated around 1%. 3) A Y-position is selected, in the middle of the stack. This Y-position will remain the same during the overall experiment.	1 h for every tests
Dry state under vacuum (static) – acquisition	1) 6 Z-profiles along the X-axis acquisitions are automatically recorded each 10 min, beginning 1 min after the vacuum level has settled. 2) After 1 h of fibrous reinforcement stabilization (e.g. 1 h after the vacuum level has settled), the last acquisition of a Z-profile along the X-axis is launched. Each acquisition lasts 1 min.	
Infusion state under vacuum (transient)	At the end of the last acquisition, the fluid inlet is opened. The fluid is then infusing the fibrous reinforcement.	depends on the tests
Saturated state under vacuum (quasi-static)	When the flow front arrives at a defined position of the outlet pipe, the fibrous reinforcement is considered saturated. The inlet valve is kept open.	
Saturated state under vacuum (quasi-static)	Saturated Z-profiles are automatically acquired along the X-axis every 10 min 3 Z-profiles are recorded. One acquisition duration is around 1 min.	30 min for every tests
Cleaning	The infusion setup is removed from the moving support of the chromatic confocal scanner. The mold is opened and the cavity so as the pipes are cleaned and dried.	around 10 min

Figure I.9: Detailed description of the experimental protocol steps during a *Macro-scale* test

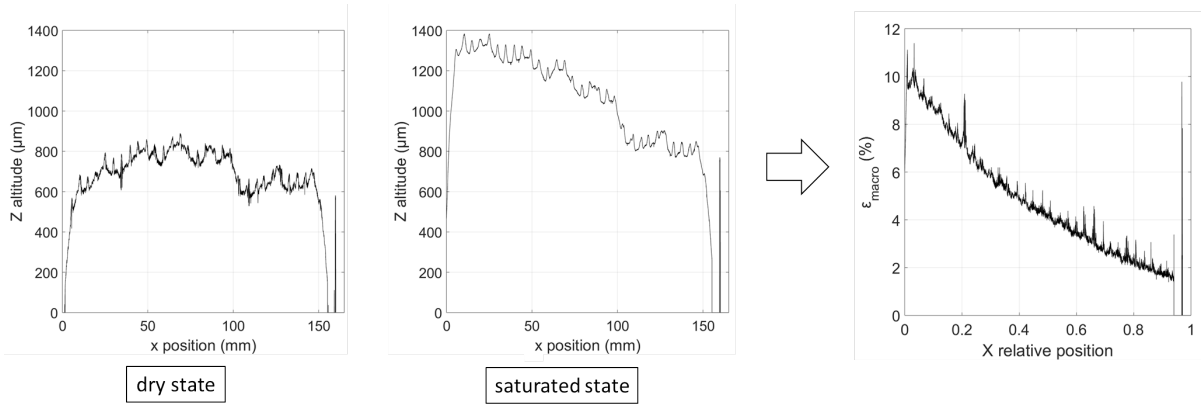

Figure I.10: Illustration of the post-treatment for the *Macro-scale* setup test

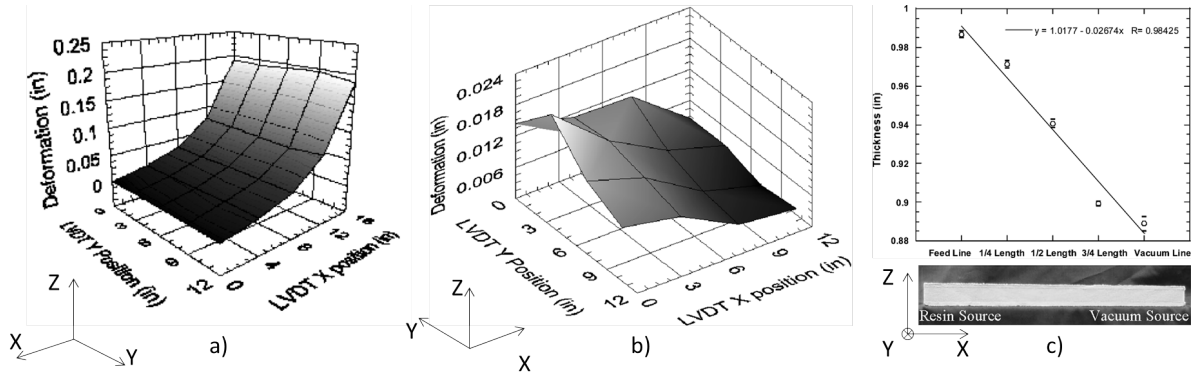

Figure I.11: Results from Tackitt [2] study: a) Felt fabric, end of the transient state. b) Woven fabric, end of the transient state. c) Final part thickness gradient.

These results validate the ability of the *Macro-scale* setup and methodology to reproduce and capture the decompaction phenomenon for the materials of the study.

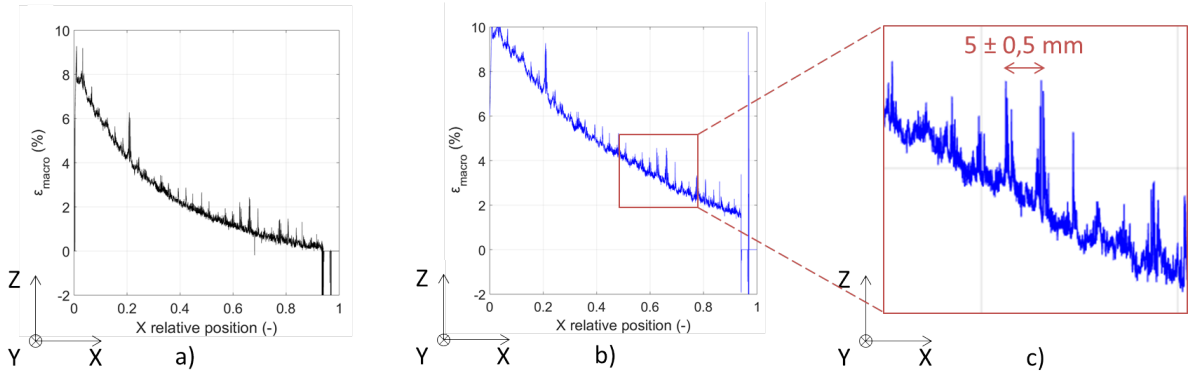

Figure I.12: Results from this study: a) quasi-UD fabric, end of the transient state. b) quasi-UD fabric, end of the transient state + 20 minutes. c) Finest visualisation of the decompaction.

Moreover, the quasi-continuity of the confocal chromatic scanner acquisition (one Z-point each 5 μm) allow a finest visualization of the macroscopic decompaction. Locally, a higher periodic decompaction is highlighted each 5 mm (Figure I.12c), which corresponds to the distance between two stitches of the quasi-UD fabric. Two interpretations are possible at this scale. Each decompaction peak may correspond to a X-position between two stitches; tows are then not constrained locally and the tows swelling is observed. Otherwise, each decompaction peak mays correspond to a stitch position and then, the swelling of the PET stitch thread is observed. These interpretations should be enhanced with the *Meso-scale* approach and results (section 9).

4.2 Y-position during the acquisition

Depending on the fabric architecture and on the fluid flow, the thickness gradient can be considered homogeneous in the width direction (Y-axis on Figure I.11a) or not (Y-axis on Figure I.11b). A verification is made with the *Macro-scale* setup and the quasi-UD fabric: 3 Z-profiles are recorded at 3 Y-positions ($Y-4.5mm$, Y, $Y+4.5mm$), and macroscopic decompaction levels are compared (Figure I.13). In that case, the thickness gradient is considered as homogeneous along the Y-axis: a unique Z-profile is then representative of the overall fabric decompaction.

A unique Z-profile acquisition is considered sufficient to represent the overall macroscopic fabric decompaction.

4.3 Conclusion on macroscopic scale investigation

The developed *Macro-scale* approach has been validated with literature results: the proposed methods and setup reproduce the macroscopic decompaction phenomenon and

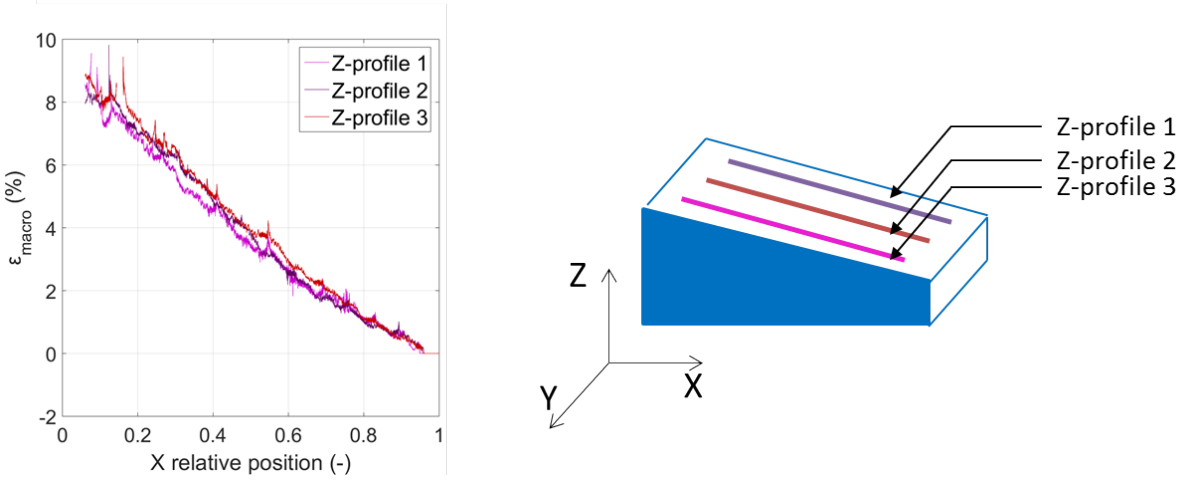

Figure I.13: Thickness gradient visualization of 3 Z-profiles recorded on the same stack of quasi-UD fabric.

the vacuum bag displacement is monitored. Nonetheless, with this approach, no mesoscopic information can be observed. Thus, novel setup and methods developed at a *Macro-meso-scale* will be detailed in the next section.

5 Macro-mesoscopic scale investigation: setup and methods

In this section, a new *Macro-meso-scale* approach is described. Dual-scale fabrics are laid down into a cavity closed with a flexible vacuum bag, and an X-ray CT-scan device is used to monitor a same microstructure under several decompaction state (at dry state prior to the infusion and at saturated state after the infusion). It should allow both the quantification of the vacuum bag displacement (at macroscopic scale) and a first visualization of the associated microstructural evolution between the two states (at mesoscopic scale). The experimental principle, setup and associated post-treatment are detailed hereafter.

5.1 Experimental principle

A controlled level of vacuum (60 *mbar* abs) is applied in a cavity where plies of quasi-UD NCF are previously laid down (Figure I.14a), fiber direction being along the X-axis. After relaxation of the dry fibrous reinforcement, two 3D images are recorded with a X-ray Computed Tomography device (X-ray CT-scan): the first one near the fluid inlet (in red in Figure I.14b) and the second one near the vacuum vent (in orange in Figure I.14b). The microstructure A obtained near the inlet at dry state is illustrated in Figure I.14b. A 1D continuous flow of glycerol along the X-axis is then maintained in the cavity, leading to a higher stabilized thickness near the fluid inlet (Figure I.14c) when full saturation is reached. After relaxation of the fully saturated fibrous reinforcement, two 3D images are recorded at the same locations as in the dry state. The same microstructure A obtained at the same location at saturated state is illustrated in Figure I.14d.

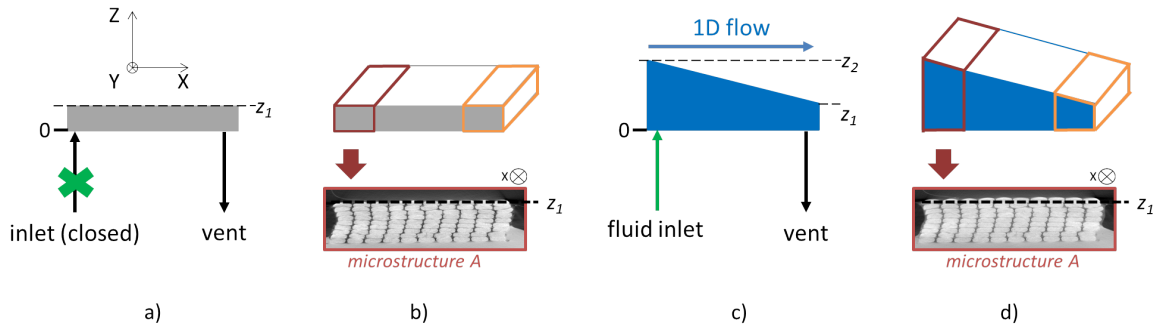

Figure I.14: Experimental steps: a) dry state. b) dry state, CT-scan acquisition. c) saturated state. d) saturated state, CT-scan acquisition.

5.2 Proposed setup

To implement this experimental procedure, the *Macro-meso-scale* setup is developed to carry out downsized scale in situ infusion inside the X-ray CT-scan constrained area. This setup is composed of the acquisition equipment (X-ray CT-scan described in 5.3) and a downsized infusion setup. A schematic view of the setup is given in Figure I.15. The X-ray CT-scan environment and acquisition imposes several constraints:

- the resolution of the recorded images depends on the distance between the X-ray source and detector and on the attenuation coefficient of the infusion setup (see details in section 5.3.1). It then imposes high constraints on the setup dimensions and on the used components (details are given in section 5.2.1).
- the X-ray source and detector remain stationary, but the overall infusion setup spins around X-axis during an acquisition. A really high stability of the infusion setup is essential to record sharp 3D images (details are given in section 5.2.3).
- the inlet and outlet fittings, containing Nickel, induces streak artefacts on the final images [26]. Then, fittings are positioned so as to remain out of the region of interest (ROI).

5.2.1 Dimensions

To hold the fibrous reinforcement, a PVC plate (whose attenuation coefficient is low enough for an in situ CT-scan test) is designed with respect to the acquisition system constraints (Figure I.16). The dimensions of the designed PVC plate and the corresponding dimensions of the quasi-UD NCF are shown in Table I.2.
Pipe lengths and diameters are selected to ensure sufficient flow rate inside the fibrous reinforcement, as recommanded by Deleglise et al.[23].

5.2.2 Boundary conditions, edge effects and bagging strategy

As presented in section 3.2.2, several plies of draining material, felt breather and tacky-tape are laid down to limit the edge effects near the fluid inlet and the vacuum vents. Due to the limited width of the PVC plate, edge effects can still occur along the X-axis. Vacuum bag folds are realized (Figure I.17a) to allow a free displacement of the vacuum

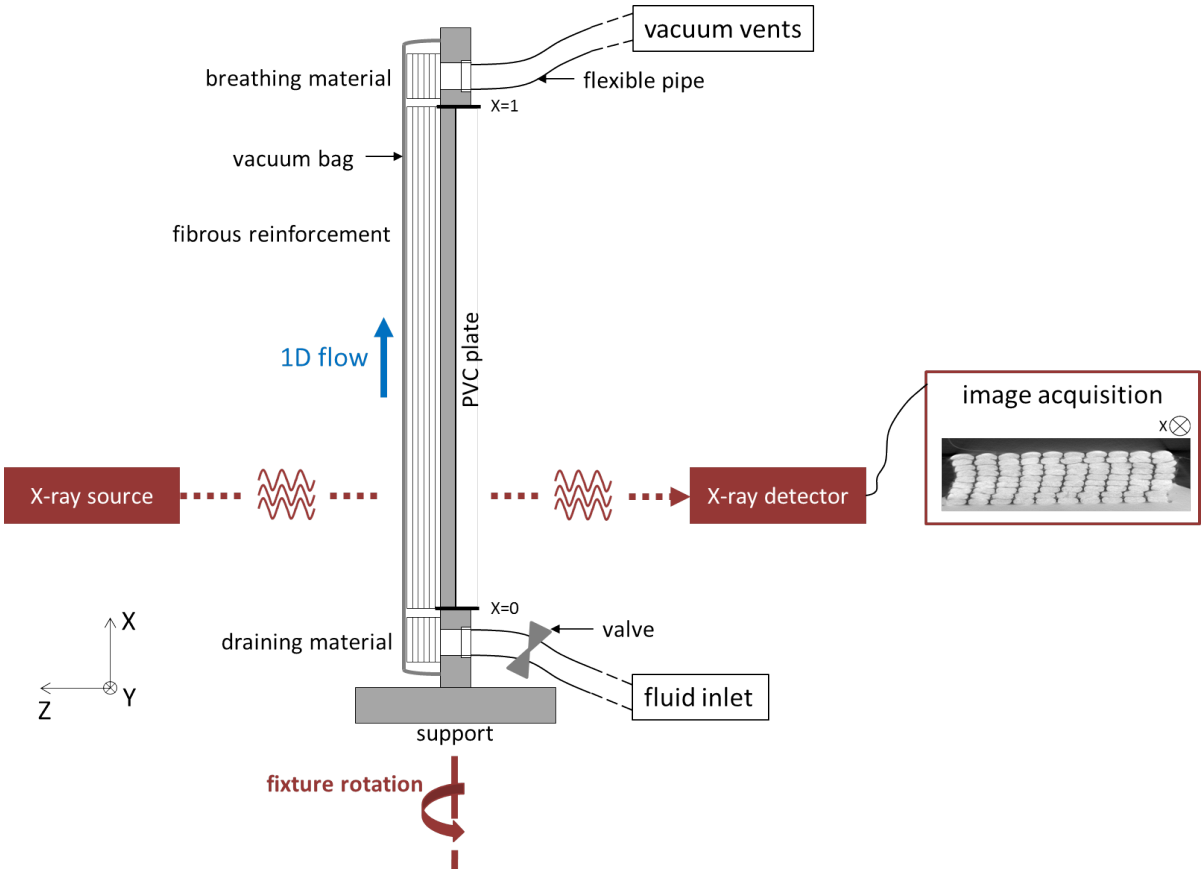

Figure I.15: Schematic view of the *Macro-meso-scale setup*: acquisition equipment effects (in red) and infusion setup (in grey)

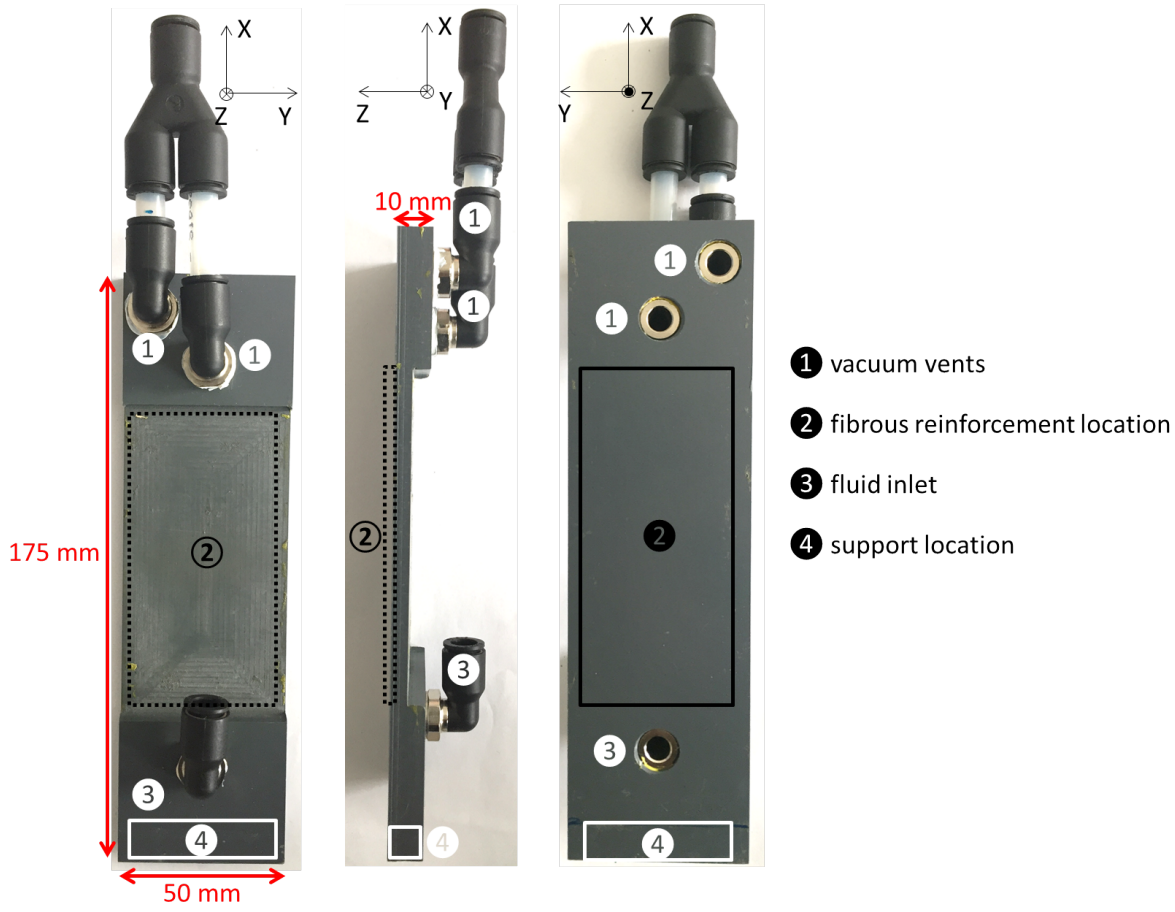

Figure I.16: PVC plate with its dimensions and main fittings

Table I.2: PVC plate and fabrics dimensions for the downsized *Macro-meso-scale* setup

Axis	PVC plate dimensions (mm)	Fabrics dimensions (mm)	Comments
X-axis (length)	175	90	This length is sufficient to obtain a representative fluid flow, but is also limited in order to ensure stability (the weight of the fittings system at the top can affect the setup stability while spinning).
Y-axis (width)	50	35	This width is limited due to the distance between the X-ray source and detector (details about the limitation of edge effect are provided hereafter).
Z-axis (thickness)	10 at inlet and outlet fittings, 5 at fabrics location	9 max. (9 plies)	The PVC plate thickness is limited at fabrics location to reduce the attenuation coefficient and then to enhance the contrast of the obtained images.

bag during both the compaction and the decompaction steps. This technique is well detailed by the company Easy Composites Ltd [27].
The sealing of the setup, which will be positioned inside an X-ray CT-scan, must be reinforced because of the folds. It is ensured with a double vacuum circuit, illustrated in Figure I.17b.

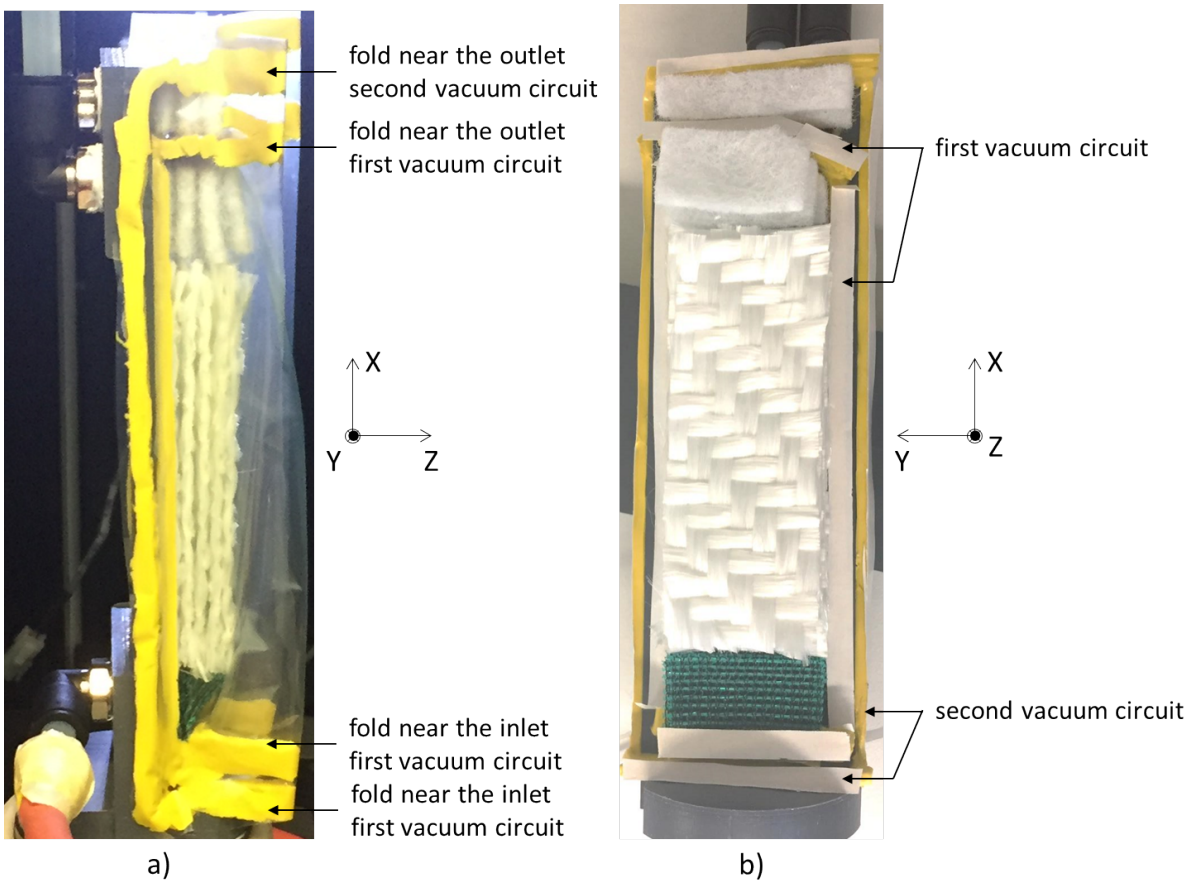

Figure I.17: Picture of the bagging strategy: a) visualization of folds, closed cavity. b) visualization of the double vacuum circuit, open cavity.

5.2.3 Stability

The overall infusion setup spins around the X-axis very slowly (around 0.01 ° $/s$) during an acquisition. Nonetheless, a really small movement of the setup (few μm) blurs the reconstructed 3D image. To ensure a high stability, flexible pipes are used and carefully positioned before an acquisition to avoid twist. Moreover, a PVC support is taped onto the infusion setup. This PVC support is then placed on the X-ray CT-scan turntable, and plastercine is used to join them and to avoid vibrations.

5.2.4 Injection equipment

The vacuum pump from Vacuubrand presented in section 3.2.4 is also used for this experimental setup.

5.3 Measurement and acquisition equipment

An X-ray CT-scan device (*Micro-XCT400*) with the objective *Macro70* from the company Xradia records the 3D images. The X-ray CT principle and the acquisition parameters selected in this study are detailed herefafter.

5.3.1 X-ray Computed Tomography principle

X-ray Computed Tomography (CT) is a non-destructive technique providing a quantitative visualization of features within bulky objects. An X-ray beam, provided by the source, is sent on a sample placed on a turntable; N_R radiographs corresponding to N_R angular positions of the sample are collected on a CCD detector. A commercial reconstruction software, mainly based on a weighted backprojection, takes as inputs the N_R radiographs and computes the 3D distribution of the linear X-ray attenuation coefficient μ within the sample. This attenuation coefficient is directly linked to the photon energy provided by the source, the density and the atomic number of the investigated material. Then, when considering an in situ experiment, the user of X-ray CT techniques should be aware about materials used to design the setup. More details are presented in [28].

5.3.2 Acquisition parameters

The chosen acquisition parameters relies on the expertise and know-how of the operator. The parameters presented in this section are exactly the same for each acquisition to ease the post-treatment.
2323 images are recorded prior to the 3D reconstruction, from -110° to 110° (around the Z-axis), and each image is exposed to X-ray during 10 s. The X-ray source is placed 90 mm away from the sample, and the distance between the sample and the detector is 36.7 mm. In this configuration and for these parameters, the 3D image obtained has a region of interest (ROI) of $40 \times 40 \times 40$ mm^3 and the resolution is 23.8 μm. To follow the experimental principle, two ROI are selected: the first one near the fluid inlet (inlet ROI), beginning at $X = 0$ (draining materials are visible on the first slices), and the second one near the vacuum vents (outlet ROI), ending at $X = 1$ (breather felts are visible on the last slices).

5.4 Experimental protocol

The experimental protocol follows the steps presented in Figure I.18. At the end of the entire experiment, four 3D images are recorded: during the dry state at inlet and outlet ROIs and, for the same two ROIs, during the saturated state.

5.5 Macroscopic post-treatment

The post-treatment presented in this section is based on image processing. First, the image processing tools used and the particularity of 3D images are detailed. Then, a methodology to determine the stack thickness and decompaction is proposed at macroscale.

Step	Description	Duration
Setup preparation	The fabrics, breather felt and draining material are placed on the PVC plate. The mold is closed hermetically with tackytape and vacuum bag, following the bagging strategy presented before.	around 2 h
Setup positioning	The infusion setup is taped on its PVC support. The PVC support is placed on the X-ray CT-scan turntable.	around 1 min
Vacuum stabilization	The vacuum is stabilized inside the fluid trap and the pipes at 60 mbar (abs).	around 2 min
Dry state under vacuum (static) – preset	1) The vacuum level is set inside the cavity. 2) The X-ray source and detector positions are chosen to obtain the best resolution and contrast in the acquired images. Then, positions are set. 3) A particular care is given to position the flexible pipes, and stability is checked twice by spinning the turntable while doors of the CT-scan are kept open (X-ray off). 4) The X and Y positions of the infusion setup inside the CT-scan are determined to obtain the desired field of view (inlet ROI, outlet ROI). These values are stationary during the acquisition and are the same for the dry and the saturated states.	1 h for every tests
Dry state under vacuum (static) – acquisition	1) After 1 h of fibrous reinforcement stabilization, the acquisition is launched at the inlet position. The acquisition lasts 8 h. 2) At the end of the inlet acquisition, the X-ray CT-scan turntable is positioned to get the outlet ROI. 3) The outlet acquisition is launch at the outlet position. It also lasts 8 h.	8 h for the inlet ROI + 8 h for the outlet ROI
Infusion state under vacuum (transient)	At the end of the outlet acquisition, the fluid inlet is opened. The fluid is then infusing the fibrous reinforcement.	around 10 min
Saturated state under vacuum (quasi-static)	When the flow front arrives at a defined position of the outlet pipe, the fibrous reinforcement is considered saturated. The inlet valve is kept open.	
Saturated state under vacuum (quasi-static) – acquisition	1) After 1 h of fibrous reinforcement stabilization, the acquisition is launched at the inlet position. The acquisition lasts 8 h. 2) At the end of the inlet acquisition, the X-ray CT-scan turntable is positioned to get the outlet ROI. 3) The outlet acquisition is launched at the outlet position. It also lasts 8 h.	1 h stabilization 8 h for the inlet ROI + 8 h for the outlet ROI
Cleaning	The infusion setup is removed from the turntable of the X-ray CT-scan. The mold is opened and the cavity so as the pipes are cleaned and dried.	around 20 min

Figure I.18: Detailed description of the experimental protocol steps during a *Macro-meso-scale* test

5.5.1 Generalities: 3D images and post-processing tools

When reconstructed, the 3D image is a matrix, named hereafter $Im(i,j,k)$, where $i \in [1,m]$, $j \in [1,n]$, and $k \in [1,N]$. A slice k is then an $(m \times n)$ image in the YZ-plane, and the 3D image is composed of N slices. Each value of the matrix, between 0 and 255, is a voxel gray-level value.
Each k value corresponds to an X-location (a slice) in the fibrous reinforcement. Illustration of a 3D image, linked with the setup, is proposed in Figure I.19.

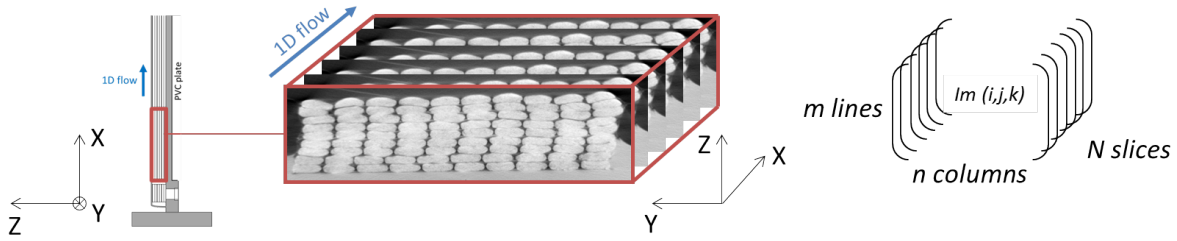

Figure I.19: Link between the setup and the 3D image recorded (inlet ROI)

The softwares ImageJ and Matlab are used to post-process these images. In order to automate the analysis, the plug-in MIJ [29] controls ImageJ features with Matlab. The plug-in FeatureJ [30], added to ImageJ is also used to detect edges of object in an image.

5.5.2 Macro-scale determination of decompaction percentage

For each 3D image acquired, the following analysis is performed.
Crop. First, the 3D image is manually cropped using ImageJ. This operation defines the same reference (at the left-bottom edge) for a slice at dry state or saturated state. The error of this step is estimated less than 1.8% of the stack (error of 5 pixels over a stack of max. 300 pixels). The post-processing steps realized hereafter are identical for all the 3D images and are automated. The results are then presented for the 3D image recorded at the inlet ROI during the dry state.
Slice selection. For a 3D image (around 2000 slices, in the YZ-plane), only 6 slices are selected to be post-treated: the first 200 and last 200 slices are not studied because of the blurring induced by the 3D reconstruction. Then, a slice is selected each 300 slices (e.g. each 7.1 mm) to limit the amount of the post-treated data.
Vacuum bag detection. For the 6 slices, an edge detection algorithm based on the computation of the gray-scale gradient in the image is achieved by the plug-in FeatureJ (Figure I.20b). To select the significant edges, a value of threshold is imposed (Figure I.20c). This value of threshold is identical for all the slices, in both dry and saturated states. At some location, the vacuum bag folds are detected. A minimum size of connected black voxel is imposed to remove this out-of-interest black pixels. Then, a structural disk element is choosen to perform morphological closing (Figure I.20d). It is applied to close the gap between the detected upper tows.
Thickness stack measurement. A gray level histogram is automatically plotted along a line on a considered slice (Figure I.21). While browsing from the top to the bottom along the line, the first black voxel (gray level=255) corresponds to the vacuum bag. Then, for each line, the thickness of the stack is measured (modulo a number of voxel corresponding to the PVC plate, manually measured during the **Crop** step). A gray level

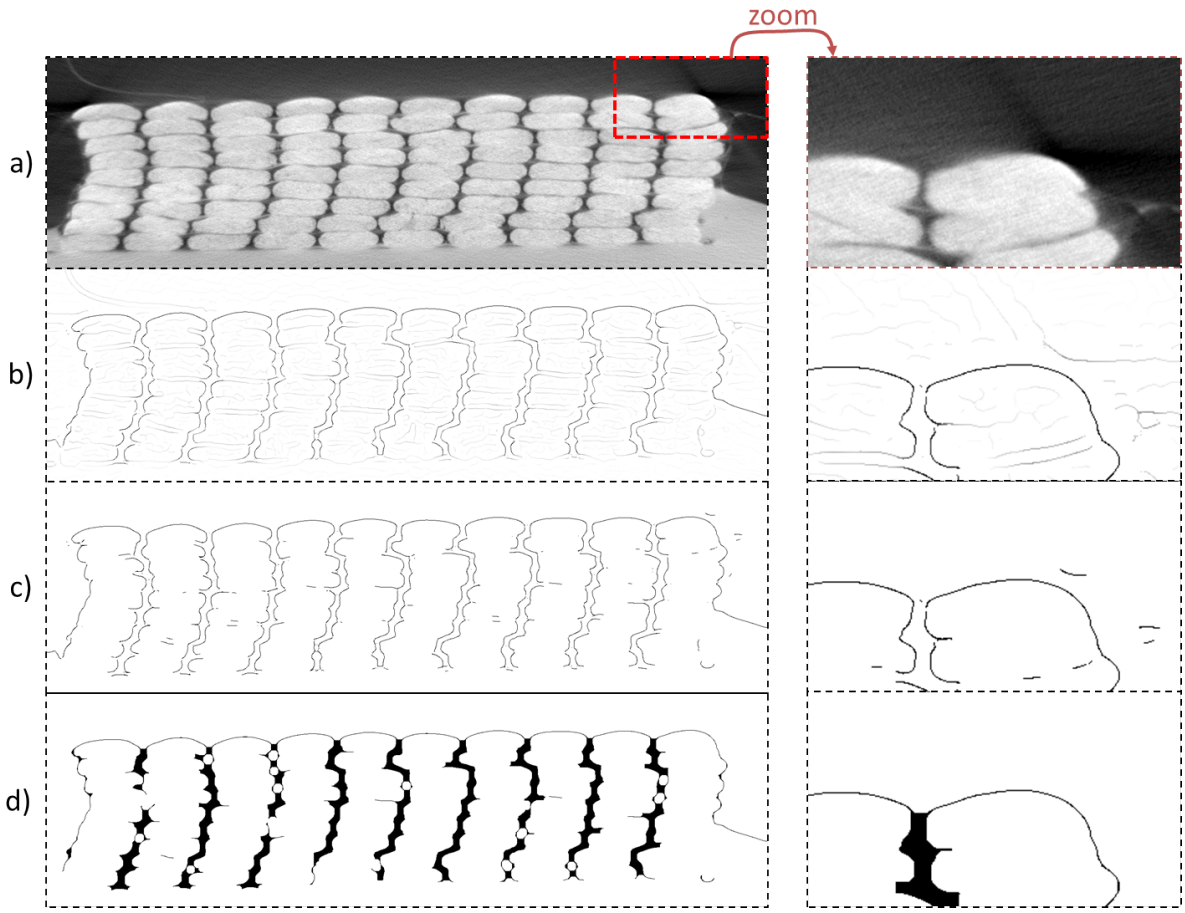

Figure I.20: Illustration of the post-processing on a slice selected near the fluid inlet (X=0.09). a) Raw image after the cropping step. b) Application of the FeatureJ plugin. c) Selection of the significant edges. d) Remove of the isolated black pixels and horizontal closing of the gap between upper tows.

histrogram is plotted every 10 pixels for a slice (along the Y-axis, the corresponding line is named hereafter Y-line).

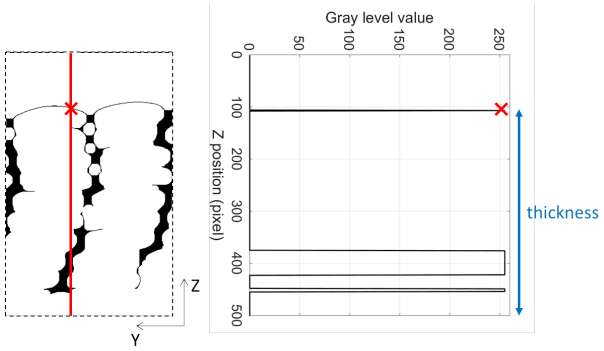

Figure I.21: Illustration of the Y-line allowing the thickness stack measurement at a defined Y position

Percentage of decompaction. The percentage of decompaction for a defined slice at a X-location is:

$$\varepsilon_{CT}(X,Y) = \frac{Z_{saturated}(X,Y) - Z_{dry}(X,Y)}{Z_{dry}(X,Y)} \tag{I.2}$$

where $Z_{saturated}$ and Z_{dry} respectively stands for the thickness of the stack estimated at the position X, along the Y-line, during the saturated and dry states.
Then, an average percentage of decompaction of the stack (Eq. I.3), and its corresponding standard deviation (Eq. I.4) can be defined as: :

$$\overline{\varepsilon}_{CT}(X) = \frac{\sum_j \varepsilon_{CT}(X,j)}{n} \tag{I.3}$$

$$\sigma_{\varepsilon_{CT}}(X) = \sqrt{\frac{\sum_j (\varepsilon_{CT}(X,j) - \overline{\varepsilon}_{CT}(X))^2}{n}} \tag{I.4}$$

where X is a fixed X-location (e.g. corresponding to a slice in the YZ-plane), and $j \in [1,n]$ as defined in the section 5.5.1.

All the post-treatment steps are summarized in Figure I.22.

6 Macro-mesoscopic scale investigation: validation

In the previous section, novel setup and methods to monitor a same microstructure under several compaction states have been presented. In this section, the first aim is to validate the ability of the downsized *Macro-meso-scale* setup to reproduce the macroscopic decompaction. Then, this downsized setup is used to validate the ability of the experimental protocol (using an X-ray CT-scan device) to capture the vacuum bag displacement, and the ability of the developed image post-treatment to compute the macroscopic decompaction.

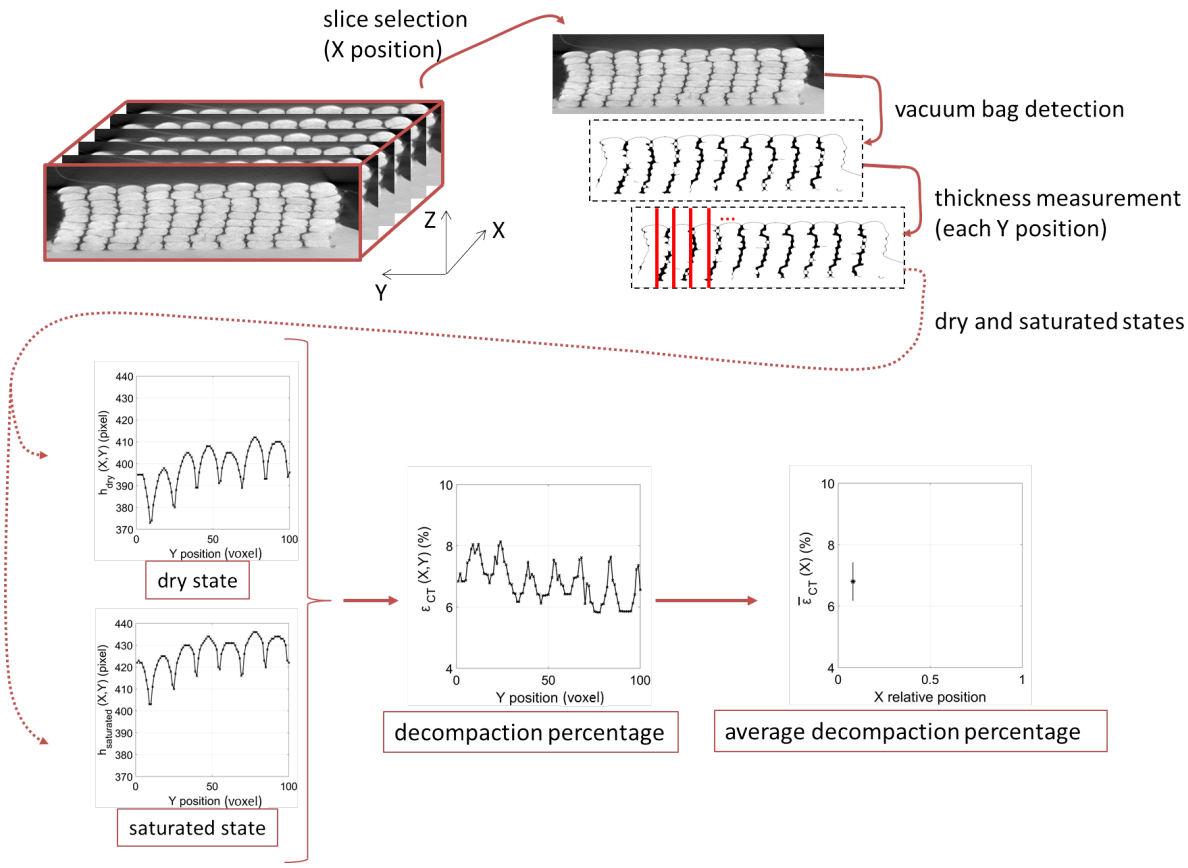

Figure I.22: Summary of the presented steps to obtain the average decompaction percentage: from the slice selection to its measurement.

6.1 Validation of the *Macro-meso-scale* setup with the confocal chromatic scanner

In this section, the experimental protocol detailed in Figure I.9 and validated in the section 4.1 is followed and applied to the *Macro-meso-scale* setup. First, the macroscopic decompaction trends using the *Macro-meso-scale* setup are compared to the one obtained with the *Macro-scale* setup. Then, the relaxation time of the fabrics in both dry and saturated states is investigated to prepare the *Macro-meso-scale* methods (using CT-scan acquisitions) validation. Finally, the tests repeatability is studied.

6.1.1 General trends

The main difference between the *Macro-scale* setup and the *Macro-meso-scale* setup is the dimensions of the fabric laid down. For the *Macro-scale* case, the flow length in the quasi-UD fabric is 165 mm, and the fabric width is 190 mm (Table I.1); for the *Macro-meso-scale* case, the flow length is 90 mm and the width is 35 mm (Table I.2). For the *Macro-meso-scale* setup, a special bagging strategy, described in the section 5.2.2 is adopted to limit the edge effects.
Figure I.23 presents the macroscopic decompaction trends for both setups during the stabilized saturated state (saturated + 20 min). When representing the real flow length (Figure I.23a), the *Macro-scale* gradient shows more non-linearity than the *Macro-meso-scale* one. The limited length in the second case leads to reduce the bending of the tows in the fiber direction (X-axis); it then tends to linearize the macroscopic decompaction gradient profile. When the flow length is adimensionalized, the thickness gradient evolution is comparable using both setups: the maximum decompaction near the fluid inlet is around 9% and the minimum decompaction near the vacuum vent is around 1.5%.

These matching experimental trends validate the ability of the downsized *Macro-meso-scale* setup to reproduce the decompaction phenonenon: the bagging strategy is efficient to limit the edge effects.

6.1.2 Fabric stabilization

Before the impregnation, 6 Z-profiles are recorded during 1 h in order to quantify the dry fabric stabilization. After the impregnation, 4 Z-profiles are recorded during 40 min in order to quantify the saturated fabric stabilization. These relaxation times of the fabrics are crucial to design the *Macro-meso scale* experimental protocol (with the CT-scan device): to obtain sharp 3D images, even small relaxation movements should be limited. To improve the quantification of the fabric stabilization, a spatial *X-mean* of the macroscopic decompaction (at saturated state) is defined as:

$$\widetilde{\varepsilon}_{macro,saturated} = \frac{\sum_{X} \varepsilon_{macro}(X)}{N_X} \tag{I.5}$$

where X is the X-position, $X \in [1, N_X]$ as defined in the section 3.5 and $\varepsilon_{macro}(X)$ is defined in Eq. I.1.
To evaluate the dry fabric stabilization, a similar definition of a spatial *X-mean* is given by:

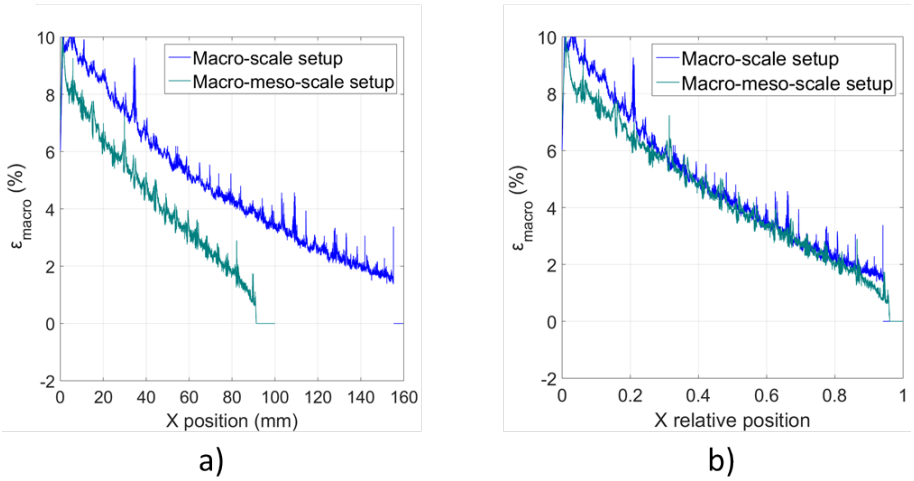

Figure I.23: Comparison of the decompaction gradient obtained with the *Macro-* and the *Macro-meso scale* setups: a) representation with the real flow length. b) adimensionalization of the flow length.

$$\widetilde{\varepsilon}_{macro,dry} = \frac{\sum_{X} \varepsilon_{macro,dry}(X)}{N_X} \tag{I.6}$$

where X, and N_X are defined hereinbefore, and $\varepsilon_{macro,dry}(X)$ is defined as:

$$\varepsilon_{macro,dry}(X) = \frac{Z_{dry,0}(X) - Z_{dry,t}(X)}{Z_{dry,t}(X)} \tag{I.7}$$

where $Z_{dry,0}$ and $Z_{dry,t}$ stands for the vacuum bag altitude at the position X, respectively at the beginning of the dry state (t=0) and during the dry state (t).
During the dry state, the fabric thickness evolution with X-position is chaotic and leads to an average of about -1 % (Figure I.24a). The thickness of the fabric decreases with time and the maximum dry compaction stabilizes after 1 h around -1.3 % (Figure I.24b). During the saturated state, the thickness gradient tends to linearize with X-position (Figure I.24c) and is stabilized 40 min after the impregnation.

The quasi-UD fabric is stabilized after 1 h under vacuum at dry state and is also stabilized after 1 h under vacuum during the saturated state, while the fluid flow is maintained.

6.1.3 Repeatability

Three repetitions are conducted with the *Macro-meso-scale* setup. For these tests, the dry state stabilization with time and the stabilized saturated state (saturated + 20 min) thickness gradient are investigated. The dry state stabilization level differs from a stack to another (Figure I.25a): it could be explained by the possible nesting between plies, that completely depends on the way plies are laid down from a test to another. Even if the dry state stabilization differs, the overall decompaction trends of the three tests are very comparable (Figure I.25b).

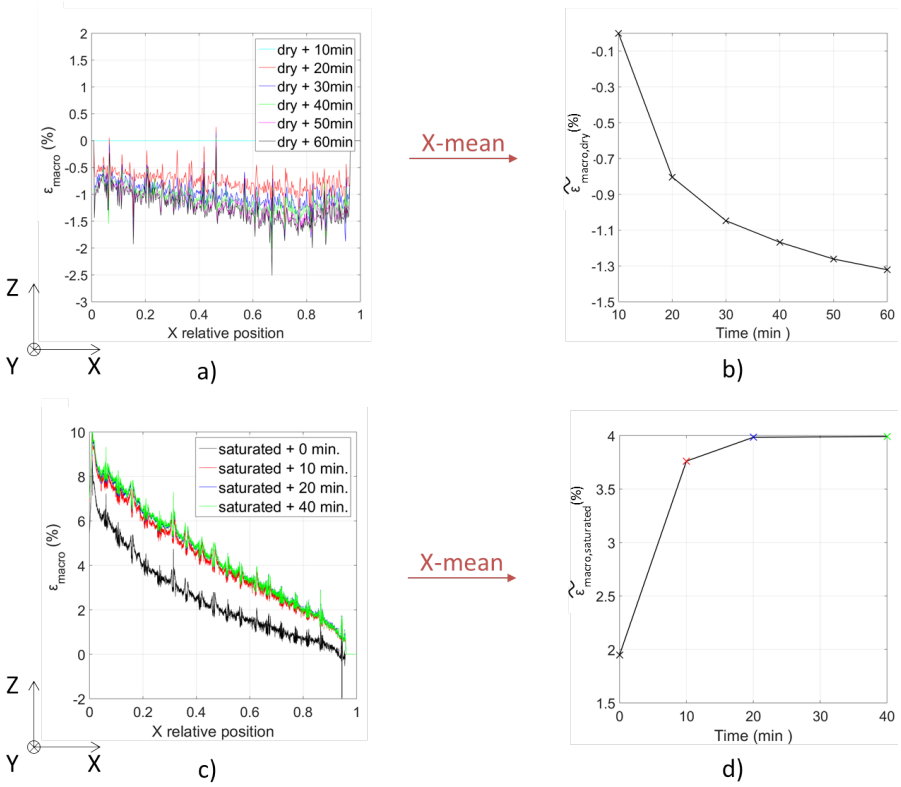

Figure I.24: Relaxation at dry state, with the *Macro-meso-scale setup*: a) Evolution with X-position. b) Evolution with time. Relaxation at saturated state, with the *Macro-meso-scale setup*: c) Evolution with X-position. d) Evolution with time.

As presented in the section 5.4, the ROIs are recorded at the end of the dry state (e.g. 1 h after the vacuum level being settled) and at the end of the saturated state (e.g. 1 h after the fully-impregnation of fabrics). With the previous results, it means that from a stack to another, the decompaction gradient computed with the *Macro-meso-scale* setup and methodology should be similar.

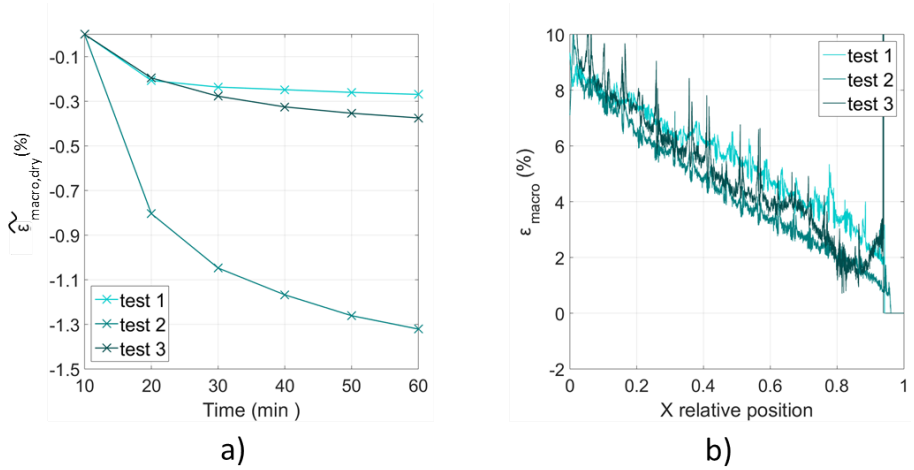

Figure I.25: Repeatability of the *Macro-meso-scale* tests conducted with the chromatic confocal scanner: a) dry state stabilization with time. b) thickness gradient at stabilized saturated state.

6.2 Validation of the *Macro-meso-scale* methodology (X-ray CT-scan device)

In the previous section, the macroscopic decompaction phenomenon has been reproduced with the *Macro-meso-scale* down-sided setup and measured using the chromatic confocal scanner. Besides, the stabilization of the fabrics has been quantified. The objective of this section is to study the ability of the *Macro-meso-scale* methodology using an X-ray CT-scan device to monitor the macroscopic decompaction. First, the sharpness of the 3D images obtained, which is directly linked to the setup stability and the fabric stabilization, is investigated. Then, the macroscopic decompaction is computed using the post-treatment summarized in Figure I.22 and compared to the one obtained with the *Macro-scale* approach.

6.2.1 Stability

The sharpness of the 3D images obtained is directly linked to:

- the limited movement of the fabric stack during the acquisition (8 h),
- the stability of the global setup during the acquisition (turntable spining).

Figure I.26 illustrates two extracted slices (YZ-plane) from two acquisitions of the same microstructure. The only changing parameter between these two acquisitions is the vacuum level inside the cavity. In the first case (Figures I.26a, b, c), the vacuum level is 60 *mbar* (abs) and in the second case (Figures I.26d, e, f), the vacuum level is near the

atmospheric pressure 850 *mbar* (abs), which then allow a stack movement. In the first case, the tows near the vacuum bag are clearly distinguishable (Figure I.26b) and the gray level profile shows a good signal to noise ratio (Figure I.26c). In the second case, the tows near the vacuum bag are blurred (Figure I.26e) and the signal to noise ratio is poor (Figure I.26f). The proposed experimental setup, even if the acquisition duration is long, is stable enough to ensure the obtention of sharp images.

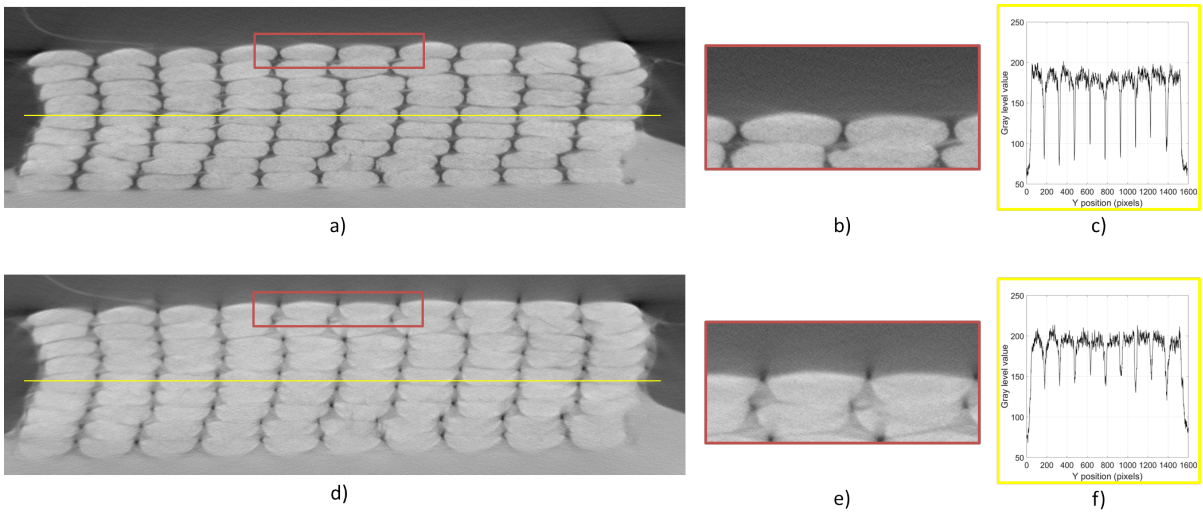

Figure I.26: A sharp raw image (a) extracted near the fluid inlet with a zoomed view (b) and a gray level profile in yellow (c). A blurred raw image (d) extracted at the same X-location with a zoomed view (e) and a gray level profile in yellow (f).

Moreover, the setup is stable between the dry and the saturated state. For 2 slices extracted near the fluid inlet, at the same X-location, during the dry (Figure I.27a) and saturated (Figure I.27c) states, the detected defaults of the tows (see zoomed views in Figures I.27b and d) seem identical.

6.2.2 General trends

Following the post-treatment protocol summarized in Figure I.22, one slice (YZ-plane) is extracted each 100 slices (e.g. each 7.1 *mm*): 6 slices are extracted in the inlet ROI and 5 slices extracted in the outlet ROI for both dry and saturated states. It allows the computation of the average macroscopic decompaction (Eq. I.3) and the standard deviation (Eq. I.4) along the X-position (fluid flow direction). Figure I.28 shows a comparison between:

- the decompaction gradients obtained with the *Macro-scale* and the *Macro-meso-scale* setups using a chromatic confocal scanner acquisition (Figure I.28a)
- the decompaction gradient obtained with the *Macro-meso-scale* setup, the CT-scan acquisition and the developed post-treatment (Figure I.28b).

The trends obtained are really similar: the maximum macroscopic decompaction, near the fluid inlet, is around 9% and the minimum near the vacuum vent is around 1% with all the methodologies used. Thus, performing the infusion vertically, with a downsized setup and for long acquisition duration inside the X-ray CT-scan device does not impact

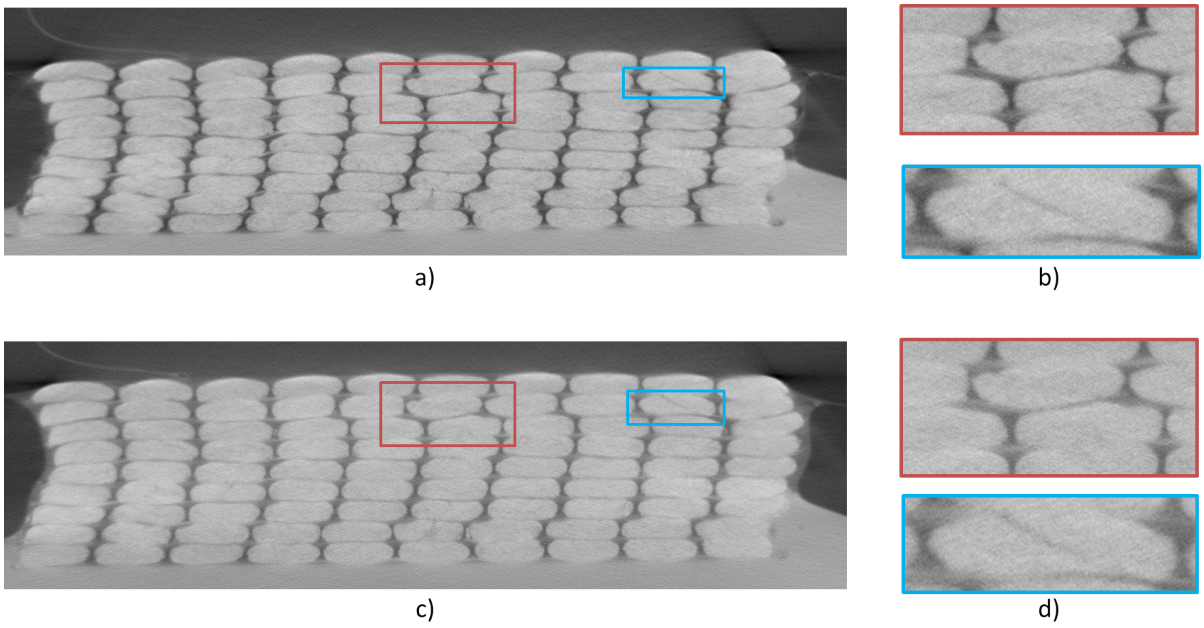

Figure I.27: Extracted slice near the inlet fluid during the dry state (a) and its corresponding zoomed view (b). Extracted slice at the same location during the saturated state (c) and its corresponding zoomed view (d).

the maximal macroscopic decompaction measured. Moreoever, for the two experimental protocols (*Macro-scale* or *Macro-meso-scale*), the decompaction gradient is linear with the X-position. It should be noticed that the standard deviations obtained are partly due to the computation of the decompaction on the overall width of the stack. The same trend is illustrated in Figure I.13, where the 3 Z-profiles are similar but not identical.

The specific bagging strategy is efficient to limit the edge effects: the decompaction phenomenon occurring during the infusion process is reproduced at a downsized scale. Moreover, the X-ray CT-scan device, despite its long acquisition duration and the infusion verticality, is able to measure the decompaction phenomenon: the experimental methodology and the vacuum bag detection algorithm are then efficient to quantify it.

6.3 Conclusion on macro-mesoscopic investigation

The *Macro-meso-scale* setup has been validated by using the chromatic confocal scanner to measure the vacuum bag displacement. This downsized setup, with a bagging strategy limiting the edge effects, reproduces the macroscopic decompaction happening at larger scale. Besides, the developed experimental protocol to monitor a same microstructure at dry and saturated states (with an X-ray CT-scan) is efficient to detect the vacuum bag displacement.
3D images of a same microstructure at dry and saturated states might provide a first mesoscopic investigation of the decompaction phenomenon: post-treatment methods and results will be detailed in the next section.

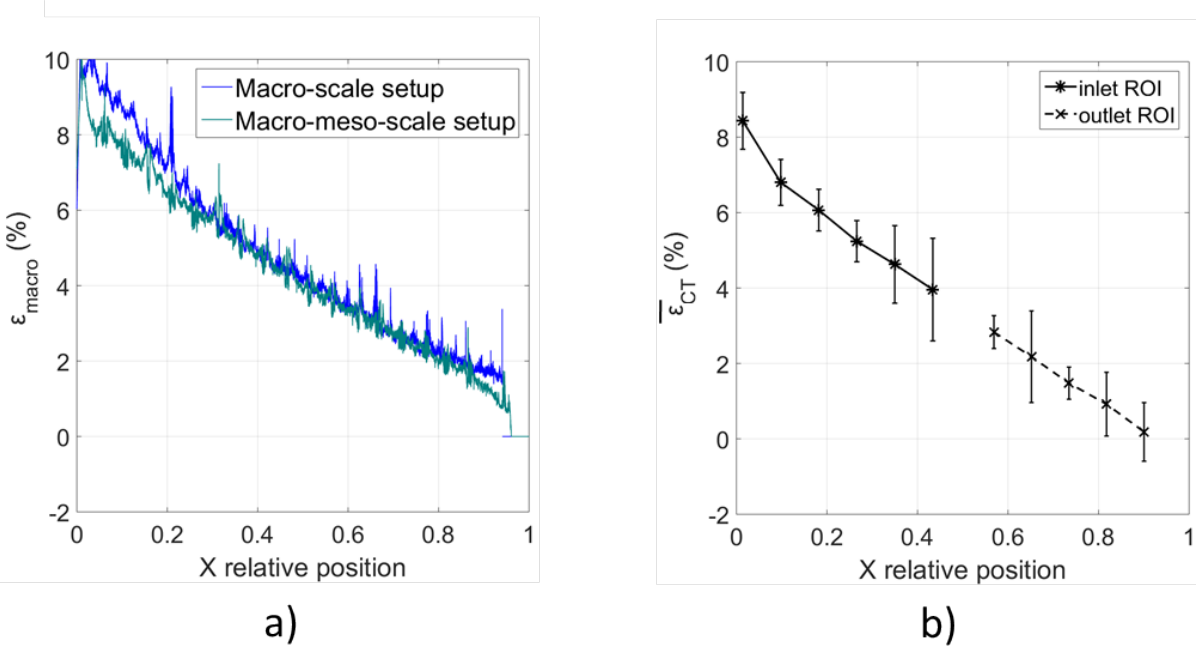

Figure I.28: Macroscopic decompaction gradient: a) using the *Macro-scale* methodology (confocal chromatic scanner). b) using the *Macro-meso-scale* methodology (CT-scan) and the *Macro-meso-scale* setup.

7 First mesoscopic scale investigation: methods and results

In this section, methods and results about a first investigation of the fibrous microstructure evolution due to the flow-induced decompaction are detailed. First, different mesoscopic post-treatments, based on image matching and image processing, are presented. Then, the associated results, mainly concerning microstructure displacement and tow deformation, will be discussed.

7.1 Mesoscopic scale post-treatment

In this section, a visualization of the microstructure evolution between the dry and the saturated states is proposed and an algorithm of image matching is presented to compute the microstructure displacement. Then, a methodology to determine tows boundaries and then tows area evolution between the dry and the saturated state is detailed. Finally, a method based on 3D-thresholding is proposed to quantify the inter-tow channels volume evolution. In the overall manuscript, the terms *channels* as well as *inter-tow channels* will designate the same entity which are the gaps located in between the tows.

7.1.1 Microstructure displacement: visualization and image matching

The image obtained with the *Macro-scale* post-processing (Figure I.20c) gives an overview of partial tow boundaries. Then, at a defined X-position, the superposition of the post-processed slices at dry and saturated state gives a first visualization of the microstructure evolution due to the decompaction phenomenon (Figure I.29).

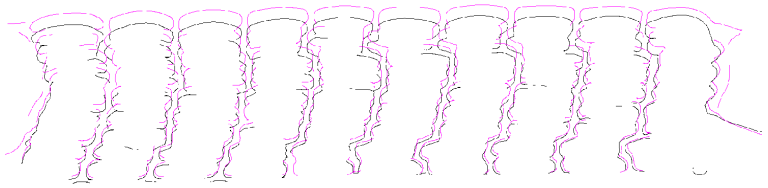

Figure I.29: Visualization of the microstructure displacement near the fluid inlet (X=0.09): in black, the microstructure at dry state; in pink, the same microstructure at saturated state.

Besides, Thirion et al. [31] proposes an algorithm to match two images and highlights its efficiency when an object in the reference image (R) is overlapping the same object in the image to be registered (D). Figure I.29 shows that, at a defined X-location, each tow in the dry state (R) is overlapping each tow in the saturated state (D). This algorithm, implemented in Matlab (*imregdemons* function), is then used to compute the displacement of each voxel between the dry and the saturated states. The outputs provide a displacement field and a new version (D') of the image (D), deformed according to the displacement field (an example is given in Figure I.30).

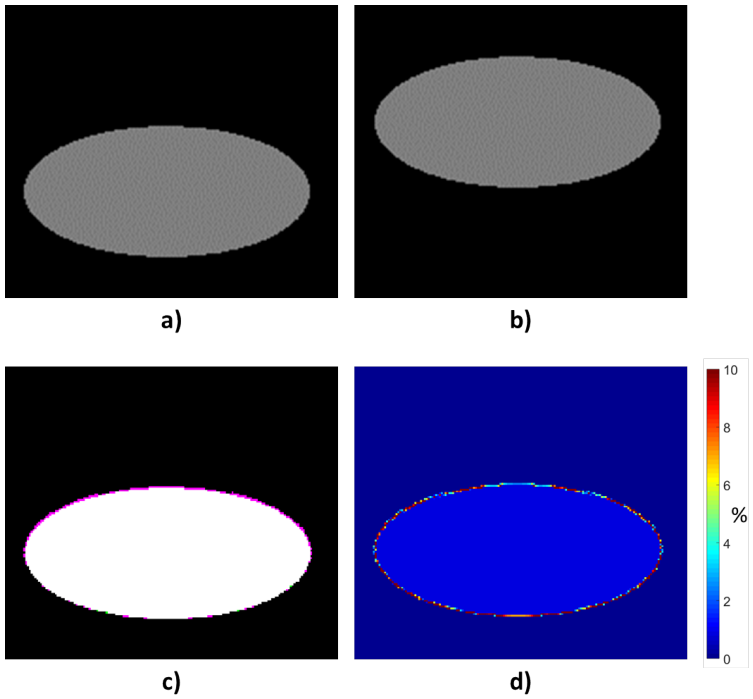

Figure I.30: Algorithm demons applied to a simplified image. a) Reference image (R). b) Deformed image (D). c) New version of the deformed image (D') superposed to the reference image (R). The intersection between (R) and (D') is white. d) Computed error between (R) and (D').

To test the algorithm efficiency, an error $e(v)$ between the initial image (R) and the obtained image with the algorithm (D') can be defined at each voxel v by:

$$e(v) = \frac{|D'(v) - R(v)|}{255} \tag{I.8}$$

Figure I.31 illustrates the error computed for each voxel when applying the Thirion algorithm for a slice located near the inlet in the dry (R) and saturated (D) states. The error is mainly close to zero, except locally near the tows boundaries. Thirion algorithm applied to these experimentally recorded images can then provide a global information about the microstructure displacement.

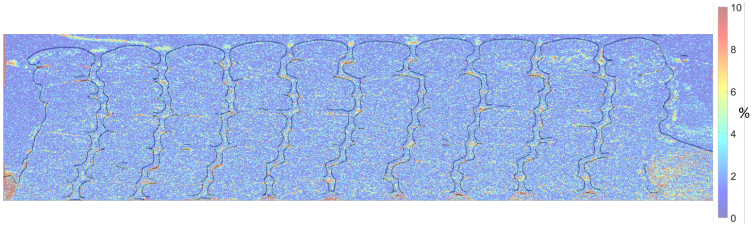

Figure I.31: Error computed between the dry state (R) and the deformed saturated state (D) near the inlet (X=0.08). To enhance the interpretation, the partial detected tows boundaries are also reported.

7.1.2 Tow detection

The 3D images are reconstructed as presented in section 5.5.1: when a slice (YZ-plane) is considered, an edge detection algorithm is not sufficient to find the horizontal tows boundaries (see for instance the edge detection illustrated in Figure I.20c). This is mainly due to the weft backing glass layer of the fabrics (Figure I.32a), whose out-of-interest weft tows gray-levels are near the warp tows gray-levels. Because the weft tows orientation is $\pm$ 80°, the horizontal channel in between two warp tows is easy to identify when moving toward the X direction of a 3D image: an horizontal channel not detectable at a defined position X is visible at X+δX (Figures I.32b, c and d). A distance of $\delta x = 2.4\ mm$ (e.g. 100 slices) seems enough to detect a maximum of tows boundaries while not affecting the initial tows position and geometry: Figure I.32f highlights the pixels modified by the concatenation algorithm detailed hereafter.

Image concatenation. A concatenation algorithm is then developed to get rid of the weft tows. A concatened image, illustrated on Figure I.32e, is defined as:

$$GLc_k(v) = \min_{k-50 \to k+50} GL_k(v) \tag{I.9}$$

where GLc_k is the gray-level concatened image around the centered slice k ($k-50$ to k+50), v is the considered voxel, GL_k is the gray-level slice k. Applying an edge detection to these concatened images enhance drastically the detection of tows boundaries: this point is detailed hereafter.

The following steps, designed to detect tow boundaries, are presented for two 100-slices-concatened images extracted at the same centered X-position in the inlet ROI at dry (Figure I.33a) and saturated states.

Edge detection. The Matlab fonction *edge* with Canny filter is used to compute the gray-level gradient in the considered images. To keep the significant edges, a unique

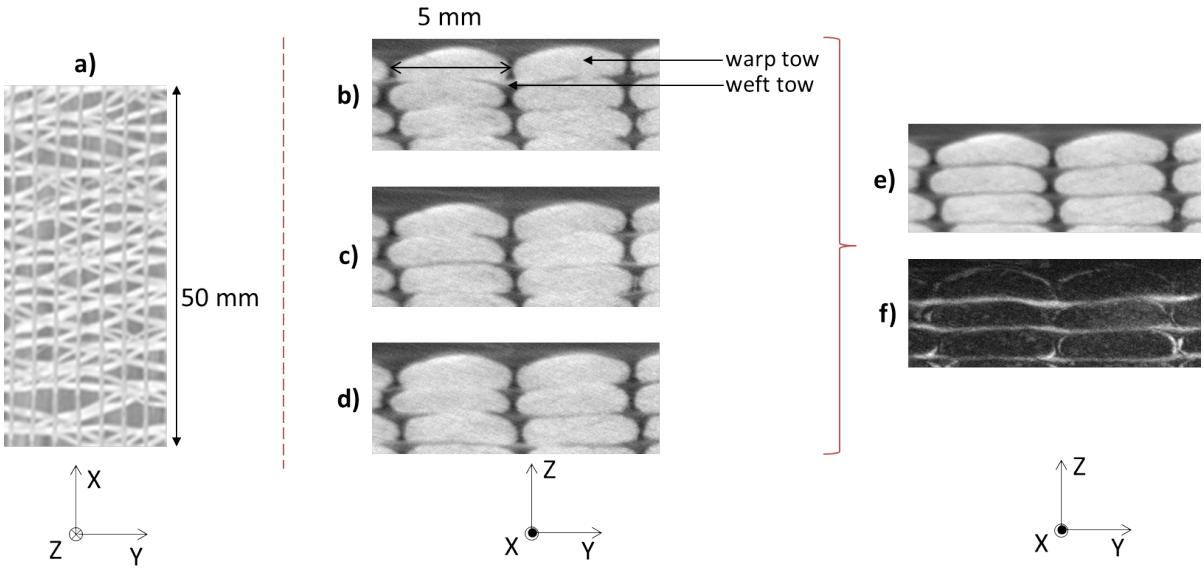

Figure I.32: Illustration of image concatenation effect: a) Weft backing glass layer. b) Raw slice #500, inlet ROI, dry state. c) Raw slice #450, inlet ROI, dry state. d) Raw slice #550, inlet ROI, dry state. e) Concatenation of slices #450 to #550. f) Soustraction between a mean slice from #450 to #550 and the concatened slice.

value of threshold is imposed for the concatened images at dry and saturated states (Figure I.33b).

Close boundaries. A structural line element of 5 pixels is used to perform morphological closing. This line is rotated from -10° to +10° (0° being the horizontal direction) to close a maximum of tow boundaries (Figure I.33c). Then, closed tows are filled and a minimum size of white connected pixels is imposed to clean the image (Figure I.33d).

Remove burrs and connected tows. Some tows are still connected, mainly due to the closing boundaries action. To remove this burr, each white voxel that is not located inside a 4 white pixels square is turned to black. Finally, tows still connected are removed by setting a minimum object area (Figure I.33e).

Application to a 150-slices-concatened image. A new concatened image is produced with 150 slices (instead of 100 slices presented in Figure I.32). This image is sharpen and the four previous steps are applied. The new detected tows are then added to the one detected in the 100-slices-concatened image (Figure I.33f).

Centroid association. At dry state, the coordinates of each tow centroid are computed. Then, with the help of the Thirion algorithm presented in section 7.1.1, the global field displacement between the dry and the saturated states is used to associate automatically the previous computed tow centroid to the corresponding saturated tow. Some tows can remain unassociated (e.g. a saturated tow without its corresponding dry or the reverse) and are automatically removed.

Figure I.34 illustrates the limits of the developed post-treatment. At the global view, tows boundaries detected by the algorithm fit well with the tows in the raw image. Nonetheless, in the zoomed views, tow detection seems unaccurate: this limitation is due to the resolution of the raw images, which is not sufficient to detect properly the tows boundaries.

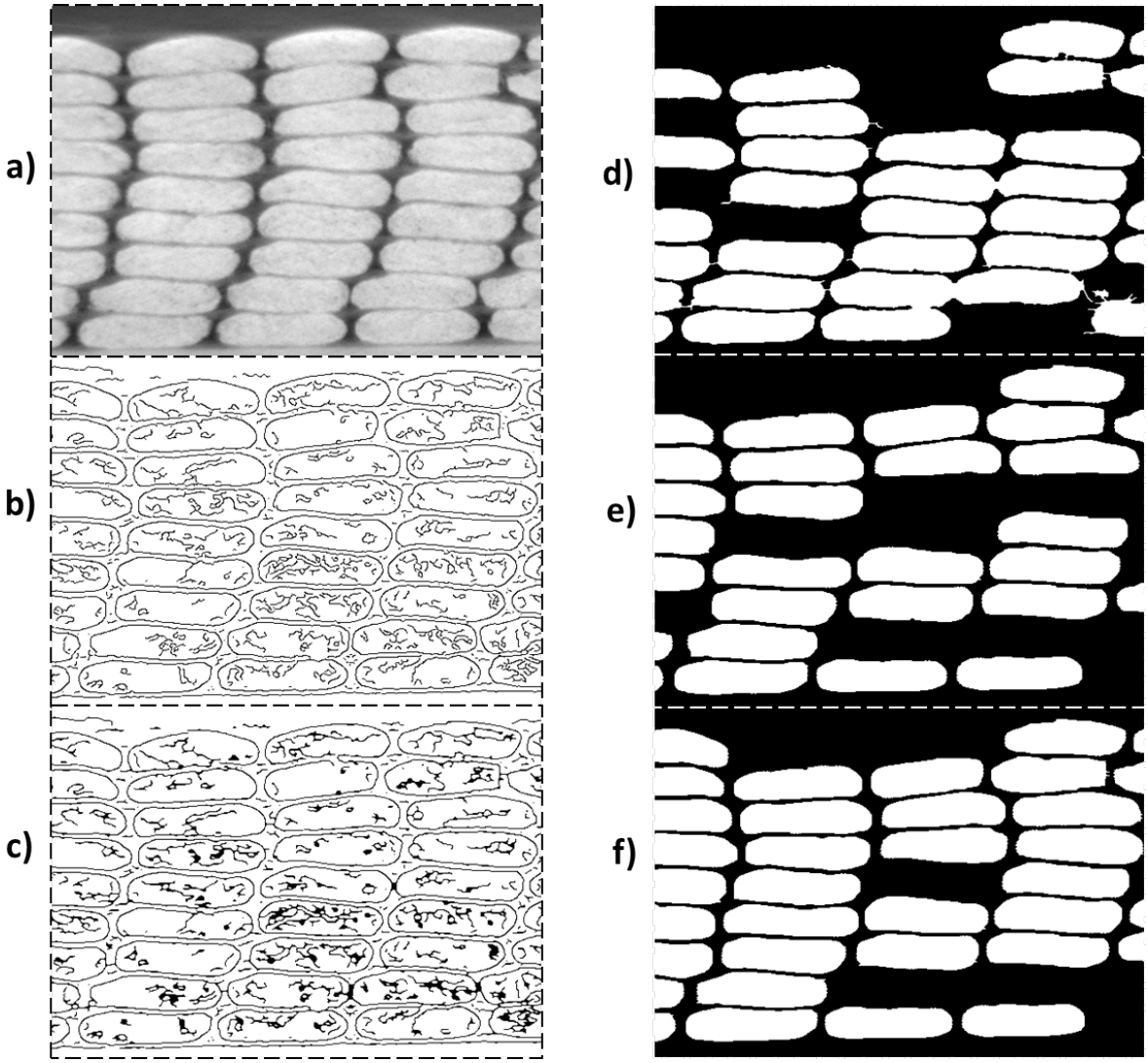

Figure I.33: Illustration of the post-processing for a concatened slice centered near the fluid inlet (X=0.01, e.g. x=0.9 mm). a) Concatened slice (raw). b) Application of Canny edge detection and threshold. c) Closing the boundaries. d) Filling of the tows and cleaning. e) Erosion of the burrs. f) Addition of the tows detected on the corresponding 150-slices-concatened image.

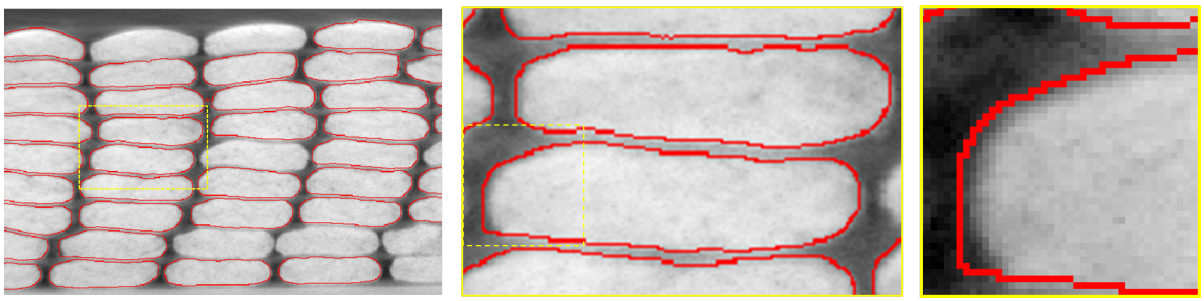

Figure I.34: Superposition of a 100-slices-concatened image and the corresponding detected tow boundaries. Several zoomed views are presented to enhance the analysis.

A first quantitative approach is still proposed to compare the tows area between the dry and the saturated states. First, the percentage of decompaction for each tow is defined using tow area:

$$\alpha_{CTmeso}(X, tow) = \frac{A_{saturated}(X, tow) - A_{dry}(X, tow)}{A_{dry}(X, tow)} \tag{I.10}$$

where $A_{saturated}$ and A_{dry} respectively stands for the area of a single *tow* computed at the position X during the saturated and the dry states.
Then, an average percentage of decompaction of all the detected tows (Eq. I.11), and its corresponding standard deviation (Eq. I.12) can be defined as: :

$$\overline{\alpha}_{CTmeso}(X) = \frac{\sum_{l=1}^{N_{tow}} \alpha_{CTmeso}(X, l)}{N_{tow}} \tag{I.11}$$

$$\sigma_{\alpha_{CTmeso}}(X) = \sqrt{\frac{\sum_{l=1}^{N_{tow}} (\alpha_{CTmeso}(X, l)) - \overline{\alpha}_{CTmeso}(X))^2}{N_{tow}}} \tag{I.12}$$

where X is a fixed X-location (e.g. corresponding to a slice in the YZ-plane), l is the considered *tow* and N_{tow} is the total number of detected tows at X-position.

7.1.3 Inter-tow channels detection

A substack of 100 slices (a slice is in the YZ-plane) is selected inside the inlet ROI to present the following post-processing. For each slice, at dry state, a region (R) is manually selected. The Thirion algorithm is then used to find the equivalent region at the saturated state (D) by collecting the displacement field around the boundaries of the image (R). The histograms of the cropped substacks obtained at dry state and at saturated state are matched prior to thresholding. A unique value of threshold (between 0 and 255), for both dry and saturated states, is then manually defined to detect the inter-tow channels (Figure I.35). The percentage of channels in a cropped substack is finally defined as the volume of white voxel over the entire volume of the cropped substack. The impact of the selected threshold value on the analysis is detailed in the mesoscopic results section (section 7.2.3).

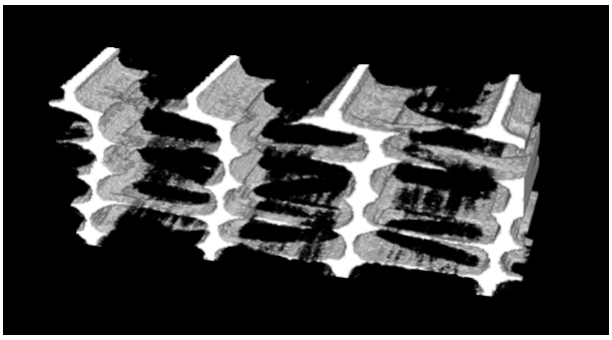

Figure I.35: Detection of inter-tow channels (in white) in a substack extracted near the inlet (around X=0.08)

7.2 Mesoscopic scale results

In the previous subsection, first tools to investigate the decompaction at the mesoscopic scale have been presented. In this subsection, the results obtained with these tools are detailed and analyzed. First, the displacement of the overall microstructure between the dry and the saturated state is provided near the fluid inlet location (X=0.1) and near the vacuum vent location (X=0.8). Then, a tow decompaction, based on the tows area evolution between the dry and the saturated states, is computed along the X-axis (fluid flow direction) and compared to the macroscopic decompaction, based on the vacuum bag displacement. Finally, the inter-tow channels volume evolution between the dry and the saturated states is analyzed.

7.2.1 Microstructure displacement

The Thirion algorithm is applied to two slices (YZ-plane) located near the fluid inlet at X=0.1: the first slice has been recorded during the dry state (named (ID) as inlet dry) and the second one, a the same location, during the saturated state (named (IS) as inlet saturated). (ID) is considered as the reference image (R), and (IS) is the image that will be deformed to match the reference one (D to D').
Figure I.36 illustrates the displacement field obtained and the corresponding algorithm error (defined in Eq. I.8). The maximal vertical displacement is -30 pixels near the vacuum bag (z=50 pixels in Figure I.36a). At this specific X-location, the computed dry average thickness is 405 pixels; it then corresponds to 7.4% of decompaction, which is in good agreement with the macroscopic scale trends (6.8 $\pm$ 0.6 % at X=0.1, as illustrated in Figure I.28b). Nonetheless, the minimum vertical displacement is around 0 voxel, near the PVC plate (z=400 pixels). A gradient of decompaction is then quantified (Figure I.36a) and highlighted (Figure I.36c) in the stack thickness direction.
Besides, the horizontal microstructure displacement can be considered mainly close to 0 voxel.

The fibrous reinforcement microstructure undergoes an heterogeneous displacement between the dry and the saturated states near the fluid inlet: a negligible horizontal displacement (Y-axis) is observed but a gradient of vertical displacement (Z-axis) is highlighted. Tows located near the vacuum bag undergo the highest vertical displacement while the ones located near the PVC plate undergo a negligible vertical displacement.

The same analysis is applied to for two slices located near the vacuum vent (X=0.8). Again, the reference image is the one corresponding to the dry state and the image to be matched corresponds to the saturated state. At this location, the macroscopic decompaction is 0.9 $\pm$ 0.8 % (Figure I.28b). Both the vertical (Z-axis) and horizontal (Y-axis) can be considered near 0 voxel.

Near the vacuum vent location, both the vertical and horizontal fibrous reinforcement microstructure displacements between the dry and the saturated states are negligible.

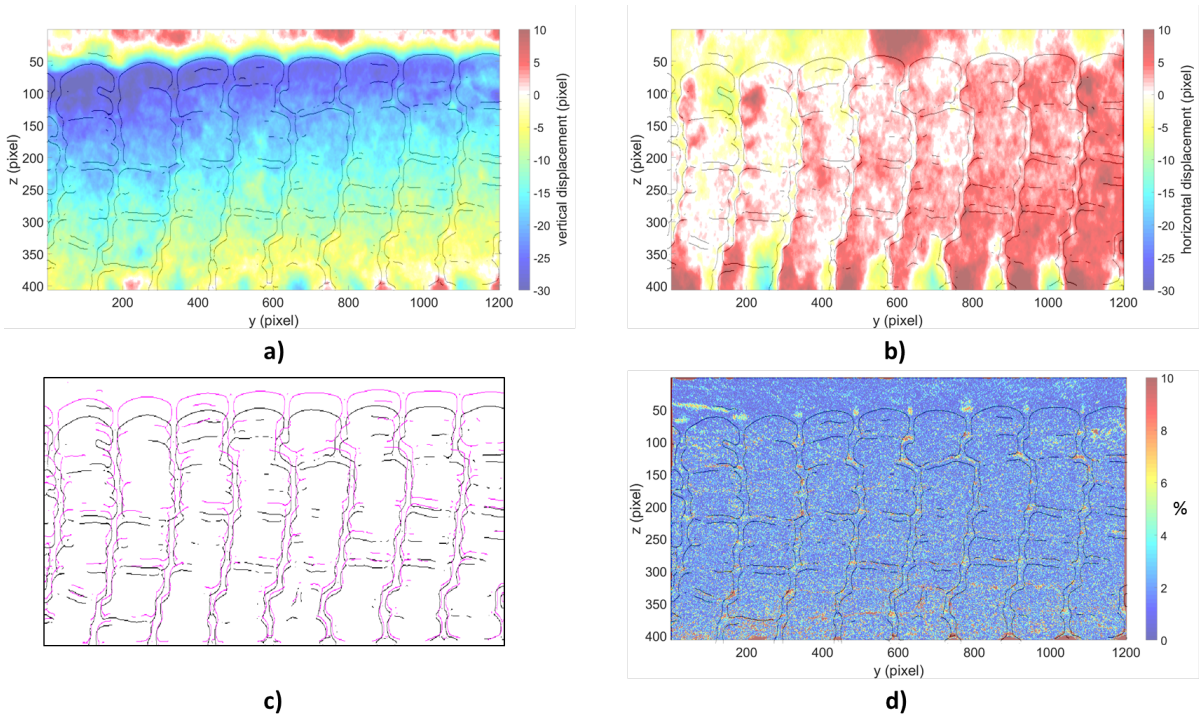

Figure I.36: Displacement fields between the dry and the saturated states at an X-position near the fluid inlet (X=0.1): a) Vertical microstructure displacement (Z-axis) in voxel. b) Horizontal microstructure displacement (Y-axis) in voxel. c) Visualization of the microstructure evolution (in black: dry state, in pink: saturated state. d) Error of the Thirion algorithm for the considered images.

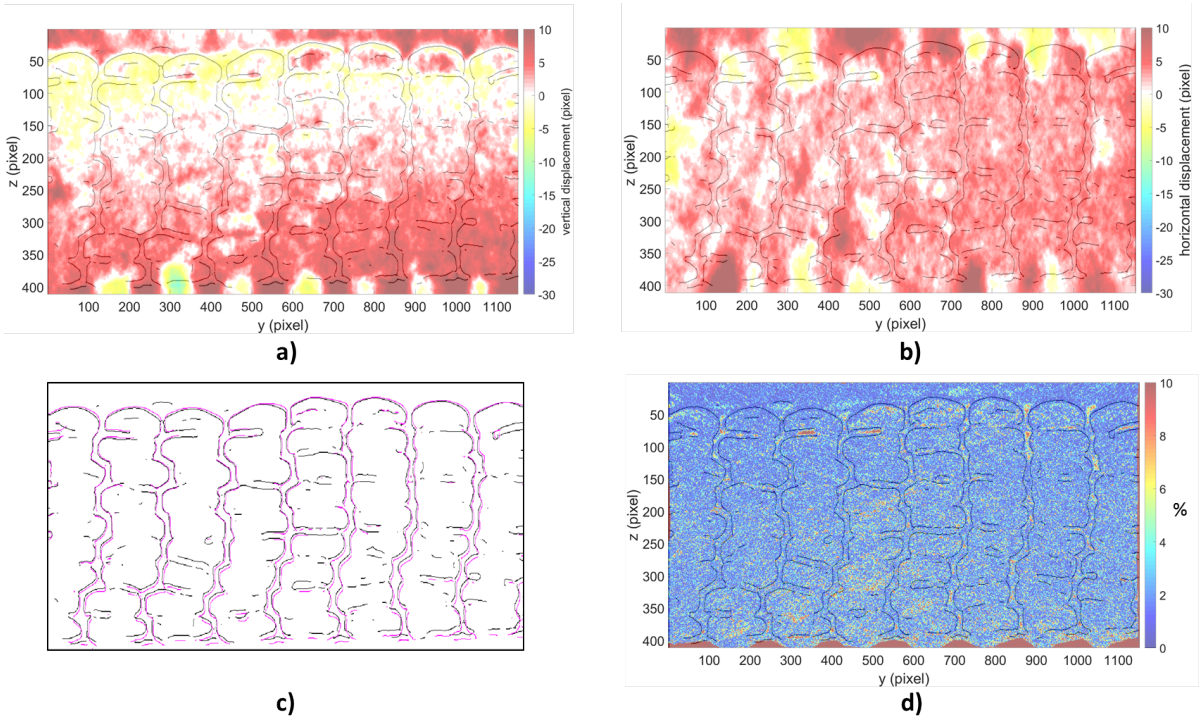

Figure I.37: Displacement fields between the dry and the saturated states at an X-position near the vacuum vent (X=0.8): a) Vertical microstructure displacement (Z-axis) in voxel. b) Horizontal microstructure displacement (Y-axis) in voxel. c) Visualization of the microstructure evolution (in black: dry state, in pink: saturated state. d) Error of the Thirion algorithm for the considered images.

7.2.2 Evolution of tows area

The proposed quantification of tows area evolution between the dry and the saturated states revealed some limitations due to the resolution of the recorded images (Figure I.34). A global trend of tows area evolution is still observed (Figure I.38b): a gradient of tows area with the X-position is highlighted. Near the fluid inlet (X=0.1), the macroscopic vertical decompaction is 6.8 ± 0.6 % (Figure I.38a), while the tows area decompaction is 6.9 ± 2.5 %. Near the vacuum vent (X=0.9), the macroscopic vertical decompaction is 0.2 ± 0.8 % and the corresponding tows area decompaction is 1.1 ± 1.9 % .
High standard values are computed for the evolution of tows area due to the limited resolution of the images. Besides, comparing a vertical decompaction (macroscopic scale) to an area decompaction (mesoscopic scale) cannot provide further information about an overall microstructure reoganization due to the decompaction. In order to overcome this issue, adapted *Meso-scale* setup and methods are designed (described in section 8) to provide a deeper mesoscopic scale analysis (detailed in section 9).

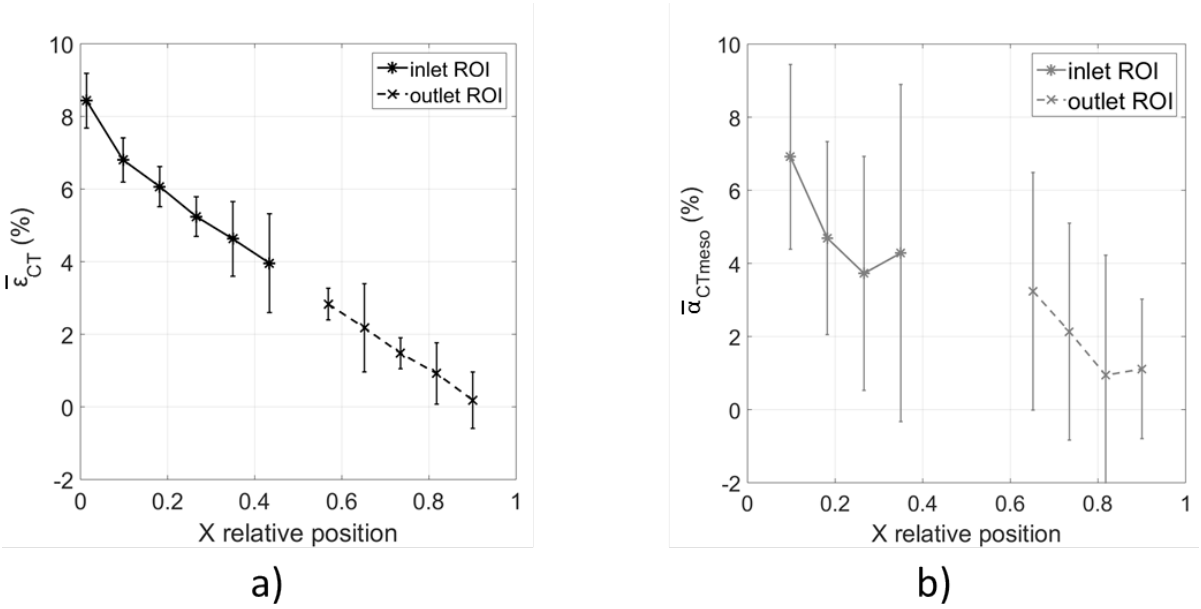

Figure I.38: Comparison between the macroscopic decompaction (vertical vacuum bag displacement) and the mesoscopic decompaction (tow area evolution): a) macroscopic decompaction. b) mesoscopic decompaction.

A first mesoscopic analysis is provided: a gradient of tows area decompaction with the X-position (fluid flow direction) is highlighted. As this analysis is limited due to the images resolution, a deeper mesoscopic investigation is presented in sections 8 and 9.

7.2.3 Evolution of inter-tow channels volume

The proposed 3D-thresholding approach to compute the volume of inter-tow channels is applied to several substacks at two specific locations:

- a substack composed of 100 slices centered around an X-position near the fluid inlet (X=0.1) recorded during the dry state; the same substack (centered at X=0.1) recorded during the saturated state,
- a substack composed of 100 slices centered around an X-position near the vacuum vent (X=0.8) recorded during the dry state; the same substack (centered at X=0.8) recorded during the saturated state.

Qualitative approach. A visualization of the thresholded substacks is given in Figure I.39: in this case, the threshold value is manually imposed at 155 to obtain an optimal visualization. Near the fluid inlet, slight differences can be observed: for instance, when comparing the inter-tow channels in the right-hand columns, the horizontal ones seem reducing between the dry (Figure I.39a) and the saturated (Figure I.39b) states. A similar trend can be observed near the vacuum vent (Figure I.39c and d).

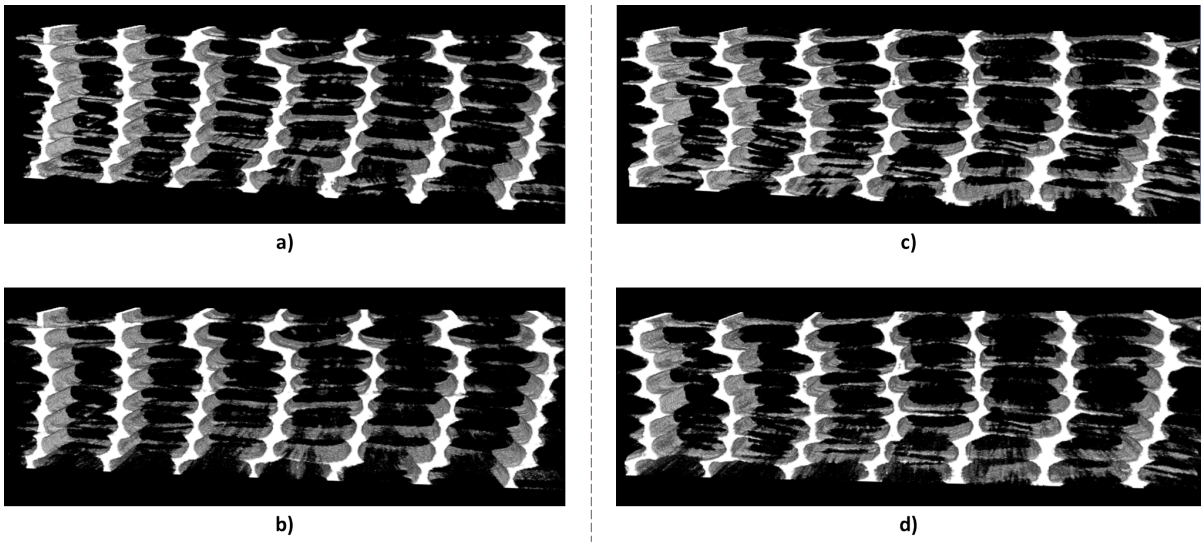

Figure I.39: 3D visualization of the inter-tow channels (threshold=155): a) inlet ROI (centered around X=0.1), dry state. b) inlet ROI (centered around X=0.1), saturated state. c) outlet ROI (centered around X=0.8), dry state. d) outlet ROI (centered around X=0.8), saturated state.

Quantitative approach. The corresponding percentage of inter-tow channels is computed in the four cases (X=0.1 at dry and saturated states, X=0.8 at dry and saturated states) and the threshold is setted at 3 several values to estimate its influence on the analysis. Results are summarized in Table I.4 and a visualization of the threshold impact on the obtained microstructure is given in Figure I.40. For a given threshold value and for both locations, the volume of inter-tow channels (in % with respect to the entire volume of the substack) is not evolving between the dry and the saturated state. Nonetheless, for a given location and state, the threshold value is impacting drastically the percentage of detected inter-tow channels.

These results are in good agreement with the conclusion drawn in the previous subsection: a global trend might be highlighted (channels volume seem not impacted by the flow-induced decompaction) but a deeper analysis is needed to consolidate this first investigation.

Table I.3: Cross table giving the volume of inter-tow channels (in % with respect to the entire substack volume) at inlet and outlet locations for dry and saturated states. Impact of the threshold value.

	X centered around 0.1, dry state	X centered around 0.1, saturated state	X centered around 0.8, dry state	X centered around 0.8, saturated state
threshold=155	16.45 %	16.47 %	16.65 %	16.67 %
threshold=160	14.64 %	14.98 %	15.79 %	15.97 %
threshold=165	19.09 %	18.45 %	17.83 %	17.49 %

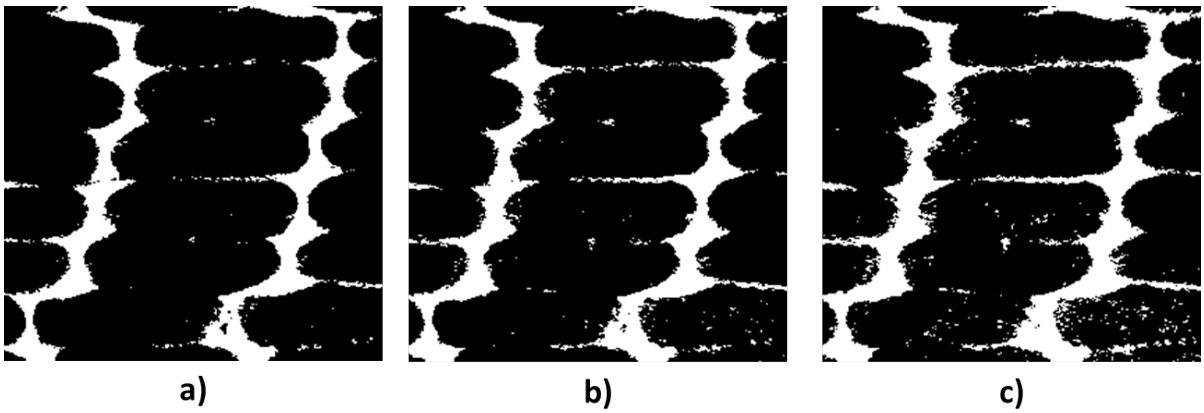

Figure I.40: Visualization of the threshold impact on inter-tow channels detection (illustration for the dry state at inlet location: X-position=0.01). a) threshold=150. b) threshold=155. c) threshold=160.

7.3 Conclusion on first mesoscopic scale investigation

The 3D images of a same fibrous microstructure at dry and saturated states provide a first mesoscopic investigation of the decompaction phenomenon. First, it has been highlighted that the microstructure displacement, occuring near the fluid inlet, is quite linear within the stack thickness: tows located near the vacuum bag undergo the highest vertical displacement while the ones located near the mold (PVC plate) remain static. Besides, a first quantification of both tows and channels deformation is provided: tows area are evolving linearly with the X-position (X being the fluid flow direction) due to the decompaction phenomenon, while channels volume seem to remain unchanged. These tows and channels deformation need a further investigation: results obtained are limited by the image resolution. Then, a new *Meso-scale* setup, that could provide higher image resolution while reproducing the decompaction phenomenon, has been designed and is described in the following section.

8 Deeper mesoscopic scale investigation: setup and methods

In this section, a *Meso-scale setup* is described. The approach is identical to the one presented in section 5: dual-scale fabrics are laid down into a cavity closed with a flexible vacuum bag, and the vacuum bag displacement between the dry and the saturated states, due to the decompaction phenomenon, is monitored with an X-ray CT-scan device. First tools and algorithms to visualize the decompaction phenomenon at the mesoscopic scale has been presented in section 7.1. A better resolution is needed to quanfity the microstructure evolution between the dry and the saturated state. The improved setup (*Meso-scale* setup) and the post-treatment developed to allow a deeper quantification of tows displacements and deformations at mesoscopic scale are detailed in this section.

8.1 Experimental principle

The experimental principle is identical to the one described in section 5.1.

8.2 Proposed setup

The *Meso-scale setup* is almost identical to the *Macro-meso-scale setup*. The only difference lies in its dimensions, that allow novel position of the X-ray source and detector to enhance the final 3D images resolution.

8.2.1 Dimensions

The PVC plate holding the fibrous reinforcement, shown in Figure I.41, is designed to respect new constraints of the acquisition system (Table I.4).

8.2.2 Boundary conditions, edge effects and bagging strategy

The bagging strategy and boundary conditions presented in section 5.2.2 are adopted to limit the edge effects in this *Meso-scale setup*.

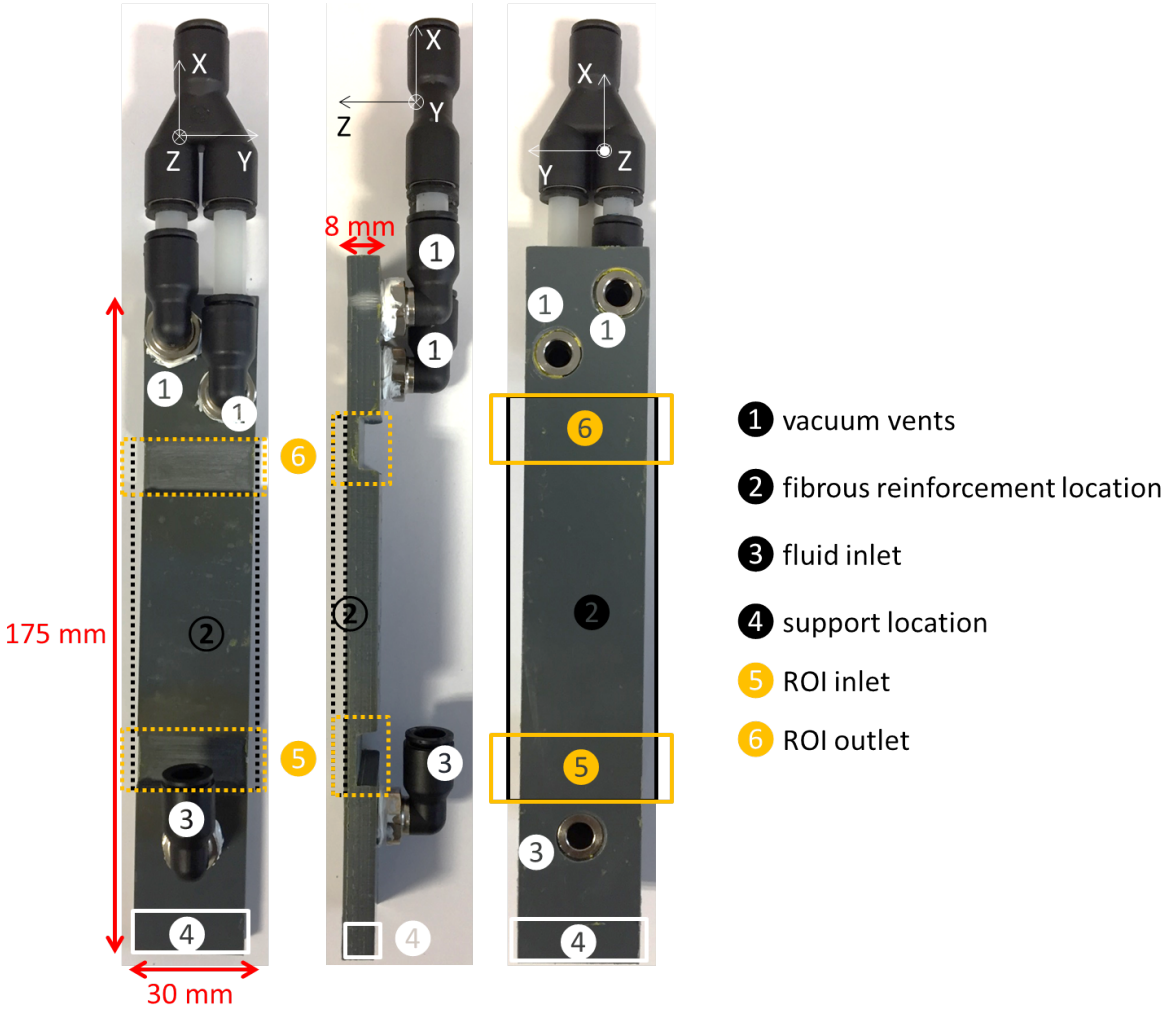

Figure I.41: PVC plate with fittings designed for the *Meso-scale setup*

Table I.4: PVC plate and fabrics dimensions for the downsized *Meso-scale* setup

Axis	PVC plate dimensions (mm)	Fabrics dimensions (mm)	Comments
X-axis (length)	175	90	The length is sufficient to obtain a representative fluid flow, but is also limited in order to ensure stability (the weight of the fittings system at the top can affect the setup stability while spinning).
Y-axis (width)	30	20	The width is limited due to the distance between the X-ray source and detector.
Z-axis (thickness)	8 at inlet and outlet fittings, 3 at the inlet and outlet ROIs	5 max. (5 plies)	reduced PVC plate thickness at inlet and outlet ROIs locations to reduce the attenuation coefficient and then to enhance the contrast of the obtained images.

8.2.3 Stability

A PVC support is taped onto the infusion setup and then placed on the X-ray CT-scan turntable. As presented in section 5.2.3, pipes are carefully positioned prior to the acquisition.

8.2.4 Injection equipment

The vacuum pump from Vacuubrand presented in section 3.2.4 is also used for this experimental protocol.

8.3 Measurement and acquisition equipment

The CT-scan presented in section 5.3 is used to record the 3D images. The same operator as in section 5.3.2 proposed the following parameters to obtain the best resolution and contrast allowed with the *Meso-scale* setup.
1947 images are recorded prior to the 3D reconstruction, from -98° to 98° (around the X-axis), and each image is exposed to X-ray during 20 s. The X-ray source is placed 65 mm away from the sample, and the distance between the sample and the detector is 23 mm. In this configuration and for these parameters, the 3D image obtained has a region of interest (ROI) of $19 \times 19 \times 19$ mm^3 and the resolution is 10.6 μm. To follow the experimental principle, two ROI are selected: the first one is near the fluid inlet (inlet ROI), beginning at $X = 0$ (draining materials are visible on the first slices), and the

second one is near the vacuum vents (outlet ROI), ending at $X = 1$ (breather felts are visible on the last slices).

8.4 Experimental protocol

To record 3D images of the inlet and outlet ROIs during the dry and the saturated states, the experimental protocol presented in Figure I.18 is adopted. The only difference lays in the duration of one CT-scan acquisition: due to the new acquisition parameters, the duration is 12 h instead of 8 h.

8.5 Post-treatment

The post-treatment presented in this section is based on image processing at mesoscopic scale. First, the algorithm of concatenation presented in the section 7.1.2, which ease the tows boundaries detection, is applied to the recorded images. Then, a methodology to determine tows areas in both dry and saturated states and then tows decompaction is proposed.

8.5.1 Image concatenation

The image concatenation presented in the section 7.1.2 is applied to the 3D images recorded according to the *Meso-scale* methodology. A distance of $\delta X = 1mm$ (e.g. 100 slices) is enough to detect a maximum of tows boundaries while not affecting the initial tows position and geometry: Figure I.42 highlights the impact of the concatenation on the boundaries tow detection.

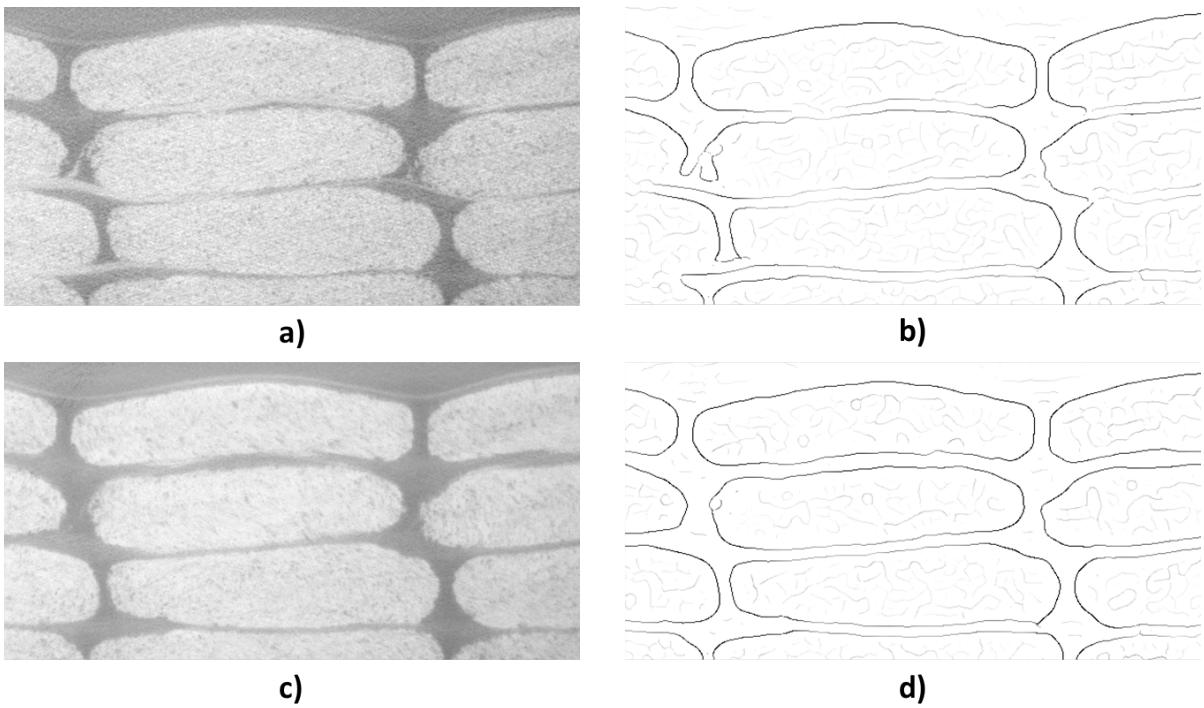

Figure I.42: Illustration of image concatenation effect: a)Raw slice #300. b) FeatureJ edge detection on the raw slice. c) Concatenation of slices #250 to #350. d) FeatureJ edge detection on the concatened slice.

8.5.2 Determination of tows areas

All the following steps are presented for two concatened images extracted at the same centered X position in the inlet ROI at dry (Figure I.43a) and saturated states.
Edge detection. The plug-in FeatureJ (see "Vacuum bag detection" in the section 5.5.2) is again used to compute the gray-level gradient in the considered images (Figure I.43b). To keep the significant edges, a unique value of threshold is imposed for all the concatened images at dry and saturated states (Figure I.43c) and a minimum size of connected black voxel is imposed (Figure I.43d).
Boundaries closing. A structural line element of 5 pixels is used to perform morphological closing. This line is rotated from -45° to +45° (0° being the horizontal direction) to close a maximum of tow boundaries (Figure I.43e).
Area computation. The detected tows are then filled with white pixels and a minimum size of white connected pixels is also imposed to clean the image (Figure I.43f). Then, the area of each detected tow is computed with the help of the Matlab *regionprops* function.

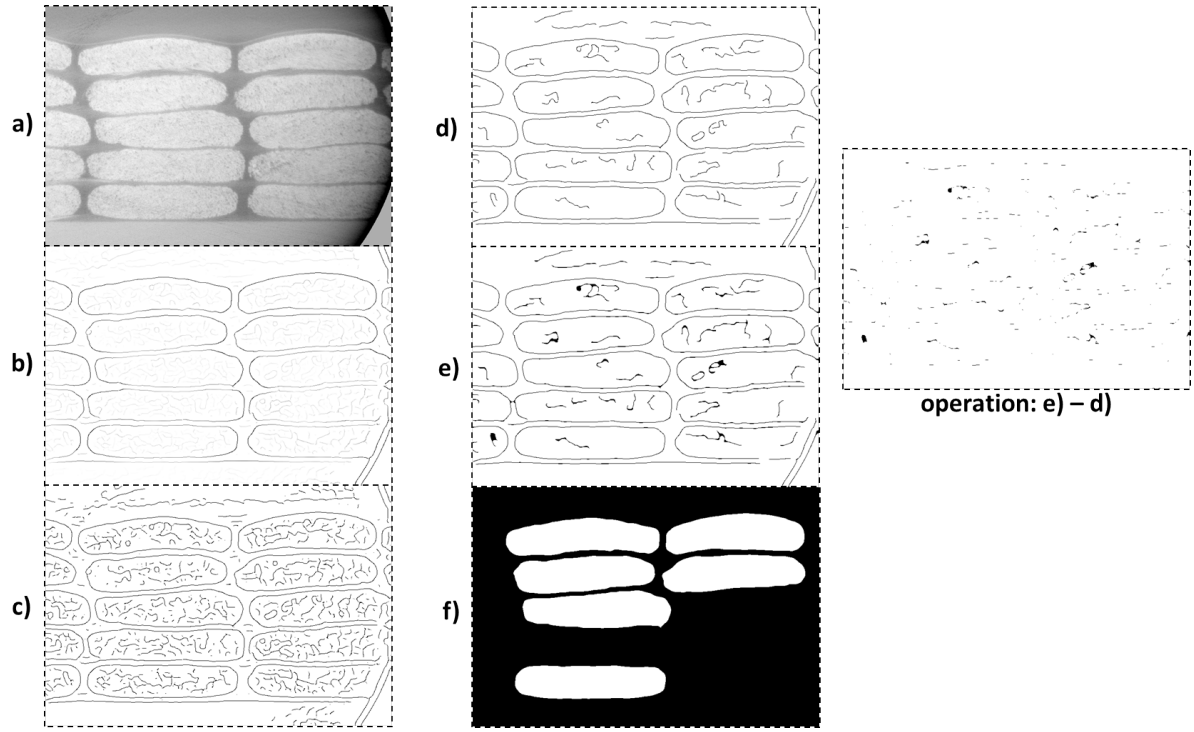

Figure I.43: Illustration of the post-processing for a concatened slice centered near the fluid inlet (x=3mm). a) Concatened slice (raw). b) Application of FeatureJ. c) Selection of the significant edges by thresholding. d) Application of a minimum connected black pixels. e) Boundaries closing (an operation is presented to enhance the visibility "e)-d)"). f) Filled tows.

8.5.3 Determination of tows decompaction

Centroid association. At dry state, the coordinates of each tow centroid are computed. Then, with the help of the Thirion algorithm presented in section 7.1.1, the global field displacement between the dry and the saturated states is used to associate automatically the previous computed tow centroid to the corresponding saturated tow.

Suppression of non associated tows. The algorithm developed hereinbefore is not able to detect all the tows of the considered stack. Then, some tows remain unassociated (e.g. a saturated tow without its corresponding dry or the reverse) and are automatically removed.

Decompaction computation. Each tow area is computed and each dry tow is associated to its corresponding saturated tow. Then, the relative decompation of a tow is defined as:

$$\alpha_{CTmeso}(X, tow) = \frac{A_{saturated}(X, tow) - A_{dry}(X, tow)}{A_{dry}(X, tow)} \tag{I.13}$$

where $A_{saturated}$ and A_{dry} respectively stands for the area of the tow computed at the position X during the saturated state and during the dry state.

A superposition of the tow at dry state and at saturated state provides also a visualization of tow deformation due to flow-induced decompaction. Figure I.44 illustrates the tows boundaries obtained at a defined X-position for dry and saturated states and the corresponding visualisation of tow deformation.

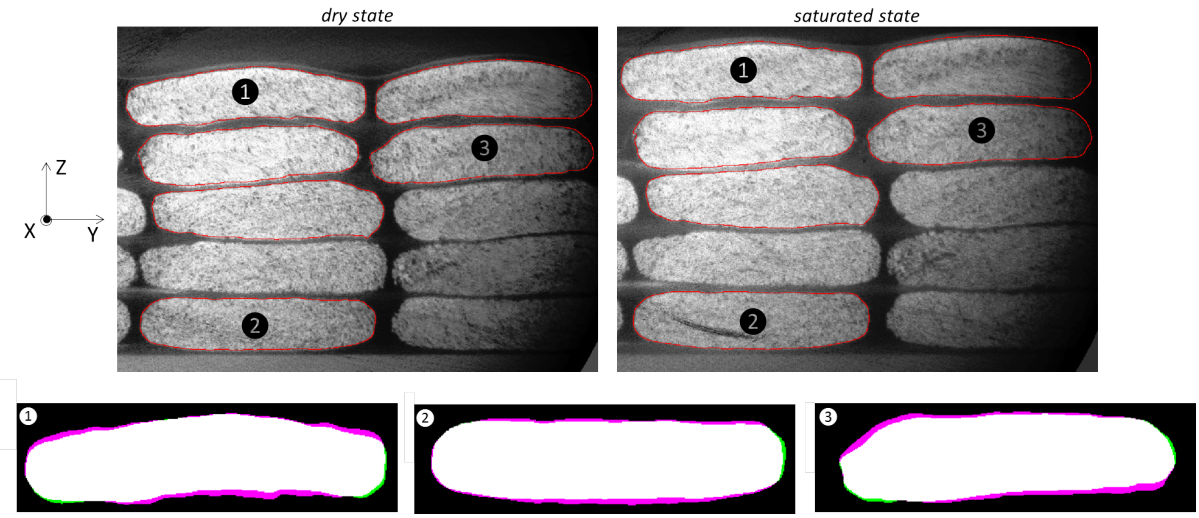

Figure I.44: Raw images and their corresponding tows boundaries (in red) at dry and saturated states. For each tow, superposition of the dry and the saturated tow (in white: intersection; in green: dry tow; in pink: saturated tow).

9 Deeper mesoscopic scale investigation: results

A novel downsized setup, called *Meso-scale* setup, has been described in the previous section: it allows the acquisition of 3D images with enhanced resolution (10 $\mu m/voxel$). A validation of the *Meso-scale* setup is presented at the macroscopic scale in this section. Then, a deep mesoscopic analysis is provided by post-processing the recorded images and findings on microstructural reorganization due to the decompaction phenomenon are proposed. Finally, the influence of this microstructural reoganization within a stack of quasi-UD NCF is evaluated at macroscopic scale throught permeability computation in the flow direction.

9.1 Validation of the *Meso-scale* setup and methodology

The two main differences between the *Macro-meso-scale* and the *Meso-scale* approaches lay in the setup width dimensions (respectively 50 *mm* and 30 *mm*) and in the CT-scan acquisition duration (respectively 8 h and 12 h). As in section 6.2, the objective is to quickly validate the *Meso-scale* setup and methodology. First, the sharpness of the 3D images obtained, directly linked to the setup stability, is investigated. Then, the localized macroscopic decompaction is computed and compared to the one obtained with the *Macro-scale* and the *Macro-meso-scale* approaches.

9.1.1 Stability

The sharpness of the images obtained with the *Meso-scale* setup and methodology is illustrated in Figure I.45. On both dry and saturated states, the signal to noise ratios are comparable (Figures I.45c and f) and the singularities observed are similar (Figures I.45b and e). It then validates that the microstructure movements during an acquisition (12 h) are limited and that the overall setup stays stable during the dry and the saturated acquisitions.

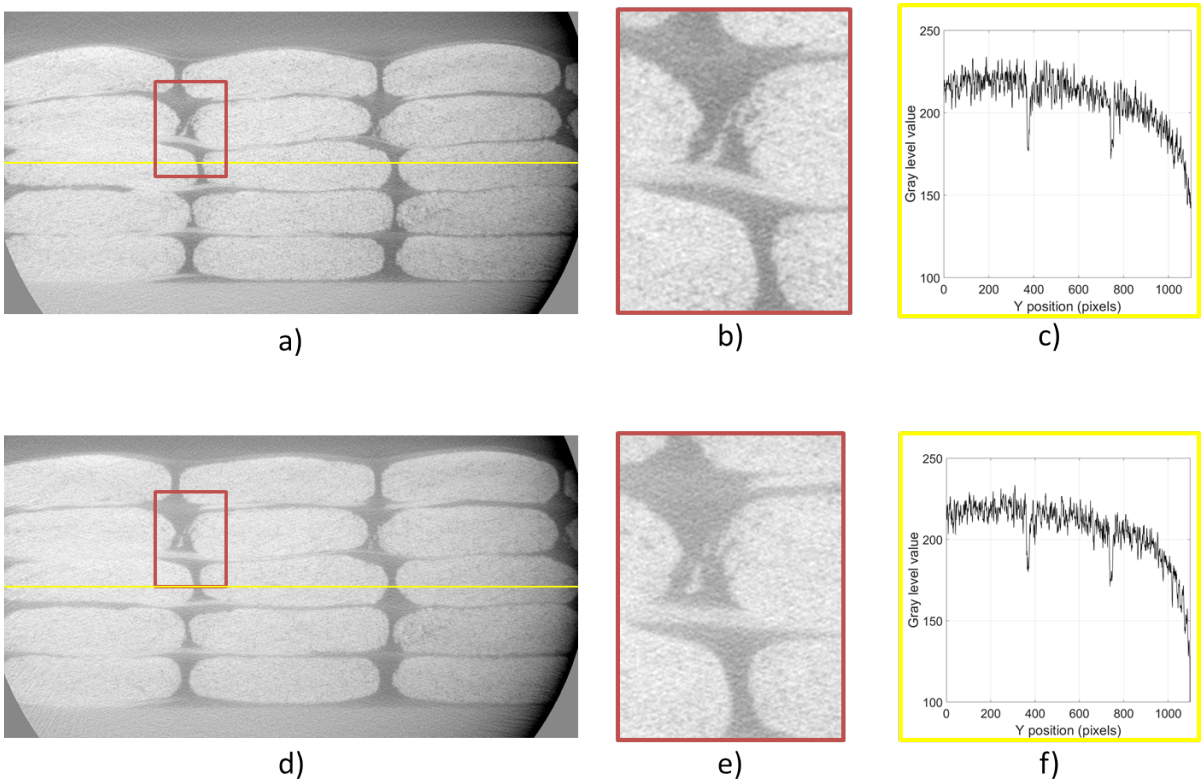

Figure I.45: Slice extracted near the fluid inlet at dry state: a) raw initial image. b) zoomed view on a singularity. c) extracted gray level profile from yellow line. Slice extracted at the same X-location at saturated state: d) raw initial image. e) zoomed view on a singularity. f) extracted gray level profile from yellow line.

9.1.2 General trends

Following the post-treatment protocol summarized in Figure I.22, one slice is extracted each 100 slices (e.g. each 1 mm) in the inlet and outlet ROIs, for both dry and saturated states. It allows the computation of the average macroscopic decompaction (and its corresponding standard deviation, as presented in equation I.4) along the X-position (fluid flow direction). In the *Meso-scale* configuration, the ROIs obtained are smaller than in the *Macro-meso-scale* configuration (respectively 19×19×19 mm^3 and 40×40×40 mm^3): the macroscopic gradient is then obtained in localized X-positions (near the fluid inlet and near the vacuum vent outlet).
Figure I.46 compares:

- the macroscopic decompaction gradient obtained with the *Macro-scale* and the *Macro-meso-scale* setups using a chromatic confocal scanner acquisition (Figure I.46a),
- the macroscopic decompaction gradient obtained with the *Macro-meso-scale* setup, the CT-scan acquisition and the developed post-treatment (Figure I.46b),
- the localized macroscopic decompaction gradient obtained with the *Meso-scale* setup and methodology (Figure I.46c).

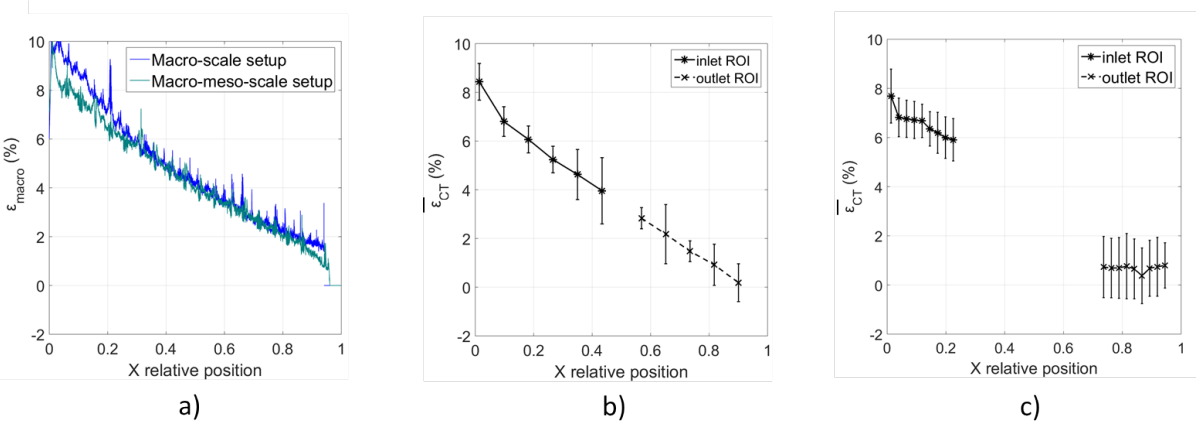

Figure I.46: Macroscopic decompaction evaluation: a) using the *Macro-scale* methodology (confocal chromatic scanner). b) using the *Macro-meso-scale* methodology (CT-scan) and the *Macro-meso-scale* setup. c) using the *Meso-scale* methodology (CT-scan) and the *Meso-scale* setup.

The trends obtained are similar: the maximum macroscopic decompaction, near the fluid inlet, is around 8-9 % and the minimum near the vacuum vent is around 1% in all the techniques used. Again, with the *Meso-scale* approach, the gradient is expected to be linear with the X-axis (Figure I.46c). It should be noticed that the decompaction trend extracted from the outlet ROI is more chaotic: due to the really little movement between the dry and the saturated states (between 5 and 10 pixels), the computation of the decompaction percentage, based on image processing, is less accurate.

These results validate the ability of the *Meso-scale* methodology and setup to reproduce the macroscopic decompaction of a fabric inside the CT-scan device constrained area.

9.2 Microstructural reorganization due to the decompaction phenomenon

In this section, tow displacements and deformations are analyzed. First, as presented in section 7.2.1, the displacement of the overall microstructure between the dry and the saturated states is provided near the fluid inlet location (X=0.04) and near the vacuum vent location (X=0.76). Then, tows deformation due to the flow-induced decompaction is studied on average and for singular tows. Finally, conclusions on microstructural reorganization for the considered quasi-UD NCF are provided.

9.2.1 Microstructure displacement

The Thirion algorithm, presented in the section 7.1.1, is applied to two slices (YZ-plane) located near the fluid inlet (X=0.04). The first slice has been recorded during the dry state, and is considered as the reference image (R); the second one has been recorded during the saturated state and is considered as the image that will be deformed to match the reference (D to D').
Figure I.47 shows the displacement field obtained and the corresponding algorithm error (defined in Eq. I.8). The maximal vertical displacement, near the vacuum bag (z=80 pixels) is -35 pixels, which corresponds to a decompaction of 7% (the average stack thickness at X=0.04 is 500 pixels). This is in good agreement with the macroscopic scale trends (6.8 $\pm$0.8 % at X=0.04, as illustrated in Figure I.46c). As observed in section 7.2.1, tows located near the PVC plate (z=500 pixels) undergo no vertical displacement: a gradient of decompaction is then quantified (Figure I.47a) and higlighted (Figure I.47c) in the stack thickness direction.
A homogenenous horizontal displacement around -5 pixels is observed: it could be explained by the error made while choosing manually the reference between the dry and the saturated ROIs (see "Crop" in the section 5.5.2).

The same analysis is applied near the vacuum vent (X=0.76). The maximal vertical displacement (Figure I.48a) near the vacuum bag (z=50 pixels) is around -7 pixels, which corresponds to a decompaction of 1.4% (the average stack thickness at X=0.76 is 485 pixels). This is in good agreement with the macroscopic scale trends (1.4 $\pm$0.9 % at X=0.76, as illustrated in Figure I.46c). As observed in the section 7.2.1, tows located near the PVC plate (z=500 pixels) undergo no vertical displacement: a gradient of decompaction is quantified (Figure I.48a) and higlighted (Figure I.48c) in the stack thickness direction, as previously highlighted at X=0.04.
Again, an homogenenous horizontal displacement around -5 pixels is observed: it could be due to the error made while choosing manually the reference between the dry and the saturated ROIs (see "Crop" in the section 5.5.2).

As already highlighted in section 7.2.1, the fibrous reinforcement microstructure undergoes a gradient of vertical displacement between the dry and the saturated states. For each X-position (near the fluid inlet or near the vacuum vent), tows located near the vacuum bag undergo the maximal vertical displacement which is in good agreement with the vertical vacuum bag displacement measured with confocal chromatic scanner or CT-scan device. Tows located near the PVC plate undergo a negligible vertical displacement.

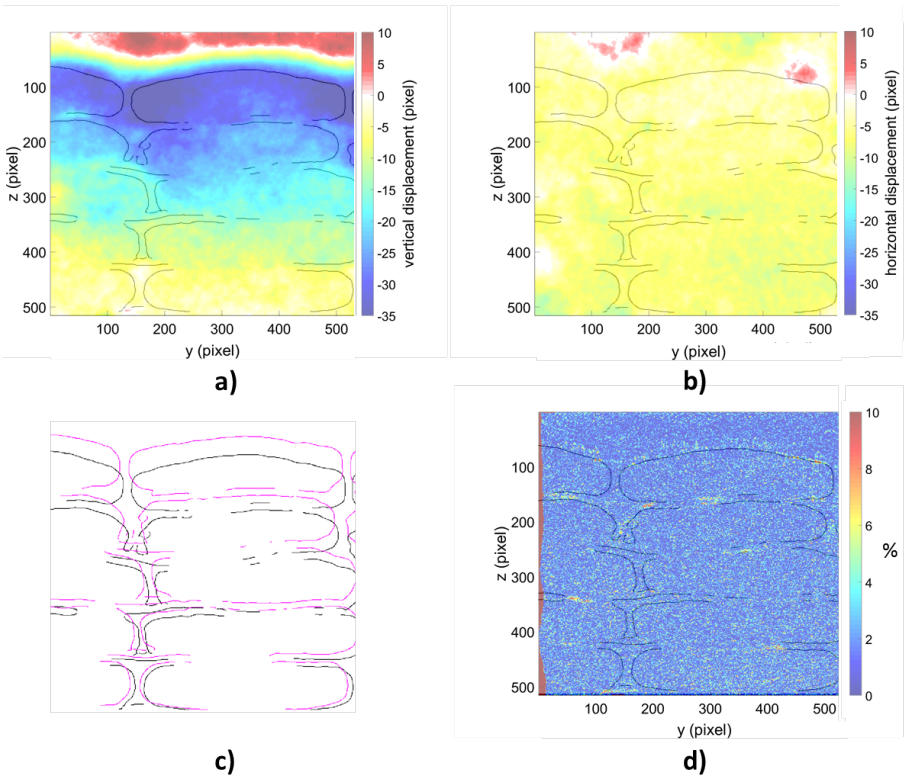

Figure I.47: Displacement fields between the dry and the saturated states at an X-position near the fluid inlet (X=0.04): a) Vertical microstructure displacement (Z-axis) in voxel. b) Horizontal microstructure displacement (Y-axis) in voxel. c) Visualization of the microstructure evolution (in black: dry state, in pink: saturated state. d) Error of the Thirion algorithm for the considered images.

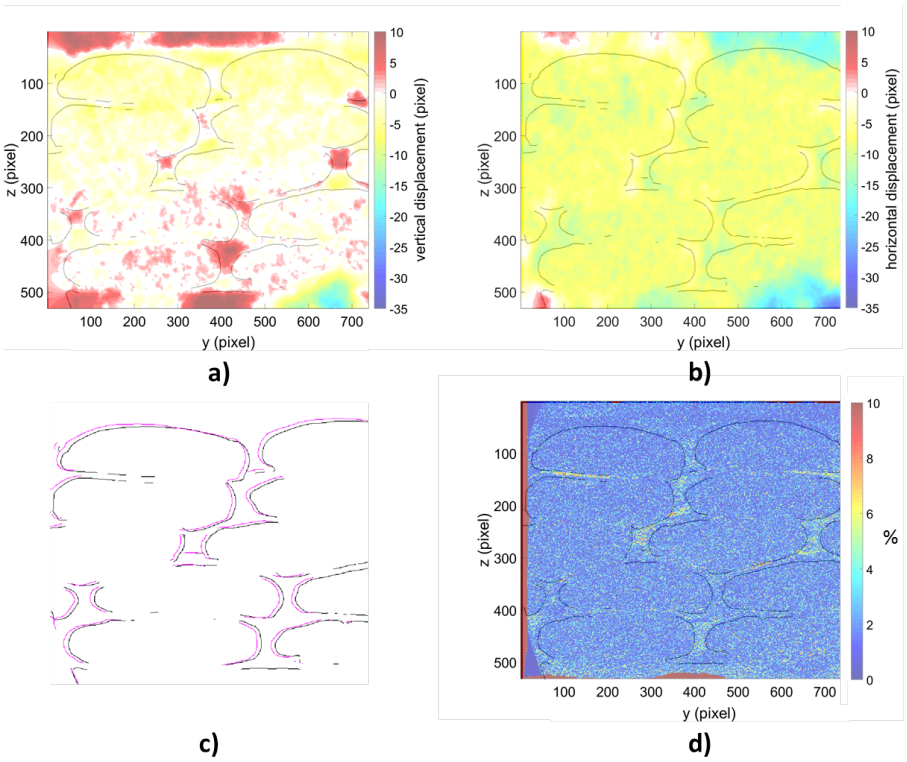

Figure I.48: Displacement fields between the dry and the saturated states at an X-position near the vacuum vent (X=0.76): a) Vertical microstructure displacement (Z-axis) in voxel. b) Horizontal microstructure displacement (Y-axis) in voxel. c) Visualization of the microstructure evolution (in black: dry state, in pink: saturated state. d) Error of the Thirion algorithm for the considered images.

9.2.2 Evolution of tows: area and deformation

The tows detection algorithm presented in the section 7.1.2 allows to perform two analyses. First, the average decompaction of all detected tows is compared to the one obtained with the *Macro-meso* scale approach. Then, a deeper investigation of particular tows decompaction between the dry and the saturated states is provided near the fluid inlet (X=0.04) and near the vacuum vent (X=0.76). For these analyses, a deeper investigation is proposed near the vacuum vent, where three 3D images of the same microstructure were recorded: the first one at dry state, under 60 *mbar* (abs), the second one at saturated state, under 60 *mbar* (abs), and the third one at saturated state, under 600 *mbar* (abs).

Analysis of all detected tows. Figure I.49 represents the vertical vacuum bag displacement (in black) superposed to the tows area decompaction (in grey) along the X-axis (flow direction). This analysis is performed with the *Macro-meso-scale* approach (as presented in the section 7.2.2: 11 slices are analyzed, and 50 tows per slice are, on average, detected) and the *Meso-scale* one (18 slices are analyzed and 4 tows per slice are, on average, detected). The standard deviation computed for the tows area evolution ($\sigma_{\alpha_{CTmeso}}$ as defined in Eq. I.12) is reduced with the *Meso-scale* approach: the improved tows area computation, due to a better edge detection of tows, is explained by the enhanced resolution of the recorded images. The tows area evolution and the vacuum bag displacement evolution between the dry and the saturated states have similar trends along the fluid flow (X-axis), with similar standard deviation: during the decompaction phenomenon tows swells while vacuum bag displaces. It should be noticed that, at macroscopic scale, the vacuum bag displacement corresponds to the entire stack deformation.

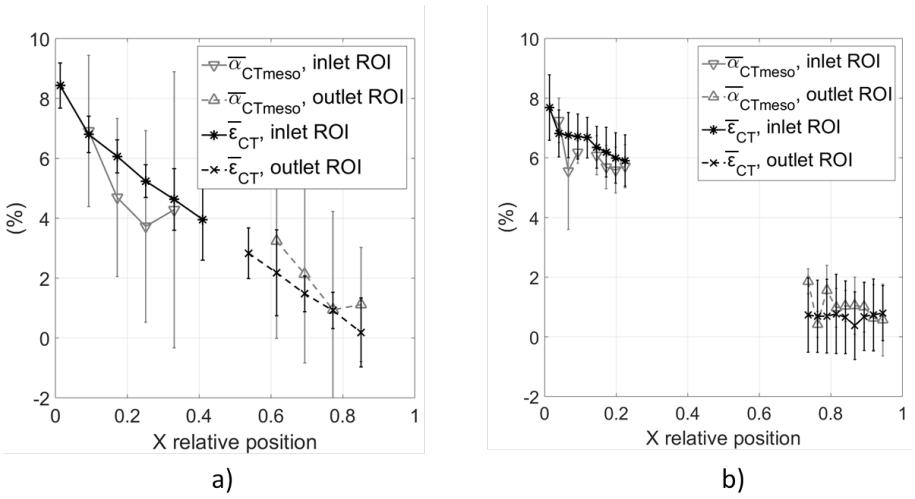

Figure I.49: Computation of the macroscopic decompaction (vertical vacuum bag displacement $\overline{\varepsilon}_{CT}$) and the mesoscopic decompaction (tows area evolution $\overline{\alpha}_{CTmeso}$): a) results obtained with the *Macro-meso-scale* approach. b) results obtained with the *Meso-scale* approach.

Near the outlet, due to the fluid pressure release, the stack thickness rise is higher at 600 *mbar* than at 60 *mbar* (Figure I.50a). The same trend is observed for the tow area rise (Figure I.50b). It then confirms that a thickness rise of the stack at macroscopic scale is correlated with a swelling of tows at the mesoscopic scale.

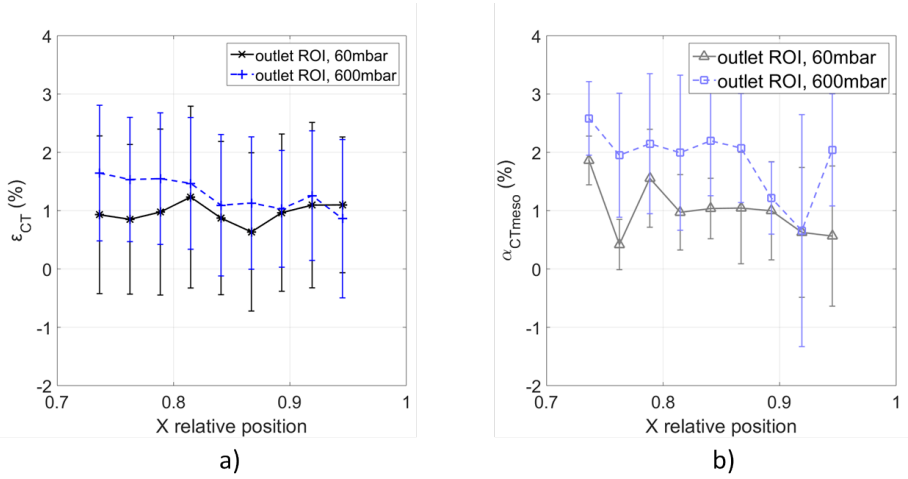

Figure I.50: Computation of the macroscopic decompaction (vertical vacuum bag displacement $\overline{\varepsilon}_{CT}$, a) and the mesoscopic decompaction (tows area evolution $\overline{\alpha}_{CTmeso}$, b) for the outlet ROI, at 60 and 600 $mbar$.

Analysis of each particular tow. A quantitative approach to evaluate the decompaction of each tow is detailed at two selected X-locations: near the fluid inlet (X=0.04, presented in Figure I.51) and near the vacuum vent (X=0.76, presented in Figure I.52). The centroids of dry tow and its corresponding saturated tow are superposed to enhance the visibility of each tow decompaction. Besides, the initial dry tow is represented in green, the final saturated tow is in pink, and the intersection between the dry and the saturated tow is in white (Figure I.51c and Figure I.52e).
First, the tows area evolution (α_{CTmeso} in %) does not depend on the tow location inside the stack near the fluid inlet (Figure I.51c): tows near the vacuum bag and tows near the PVC plate decompact equally. Near the vacuum vent (Figure I.52c), tows located near the vacuum bag undergo higher decompaction than the other tows. Both tows might be less constrained by the stitch threads at this specific location. In fact, there is a gap (probably due to the presence of the stitch yarn) between the vacuum bag and the tows at the inlet location (Figure I.51a) whereas no gap (probably due to the absence of the stitch yarn) is visible at the outlet location (Figure I.52a). It should be noticed that, even if both tows have a higher decompaction level, no gradient of tow deformation within the stack thickness is observed: then, tows area evolution is not depending on the tow location inside the stack.
When comparing the evolution of tows at the saturated state between 60 and 600 $mbar$, same trends are highlighted (Figures I.52c and e) while the stack thickness rises ($\overline{\varepsilon}_{CT}(0.76) = 0.8 \pm 1.3\%$ at 60 $mbar$ and $\overline{\varepsilon}_{CT}(0.76) = 1.5 \pm 1.1\%$ at 600 $mbar$), tows area increases in most cases. Each tow seems to evolve individually: for instance, a first one evolves from 0.4 to 0.9% while another one evolves from 0.4 to 1.5%. Again, no link between the tow position and the to evolution is found.
Finally, the proposed visualization shows that the tow deformation occurs in the thickness direction (Z-axis); lateral tow deformation (Y-axis) is negligible. It could be explained by the stitch tread (not visible in the recorded CT-scan images), whose limiting the spreading of tows during the compressive loading.

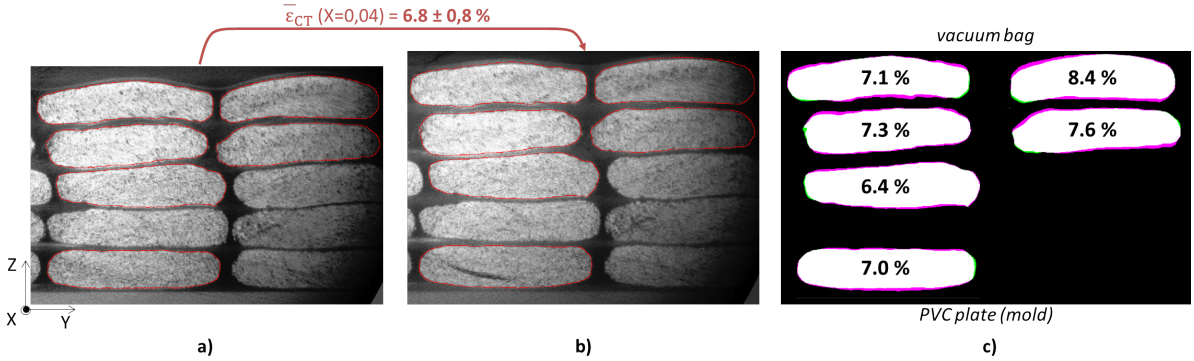

Figure I.51: Illustration and quantification of tow deformation near the inlet (X=0.04): a) Raw data with detected tow boundaries at dry state. b) Raw data with detected tow boundaries at saturated state. c) Tow decompaction with the corresponding area evolution α_{CTmeso}.

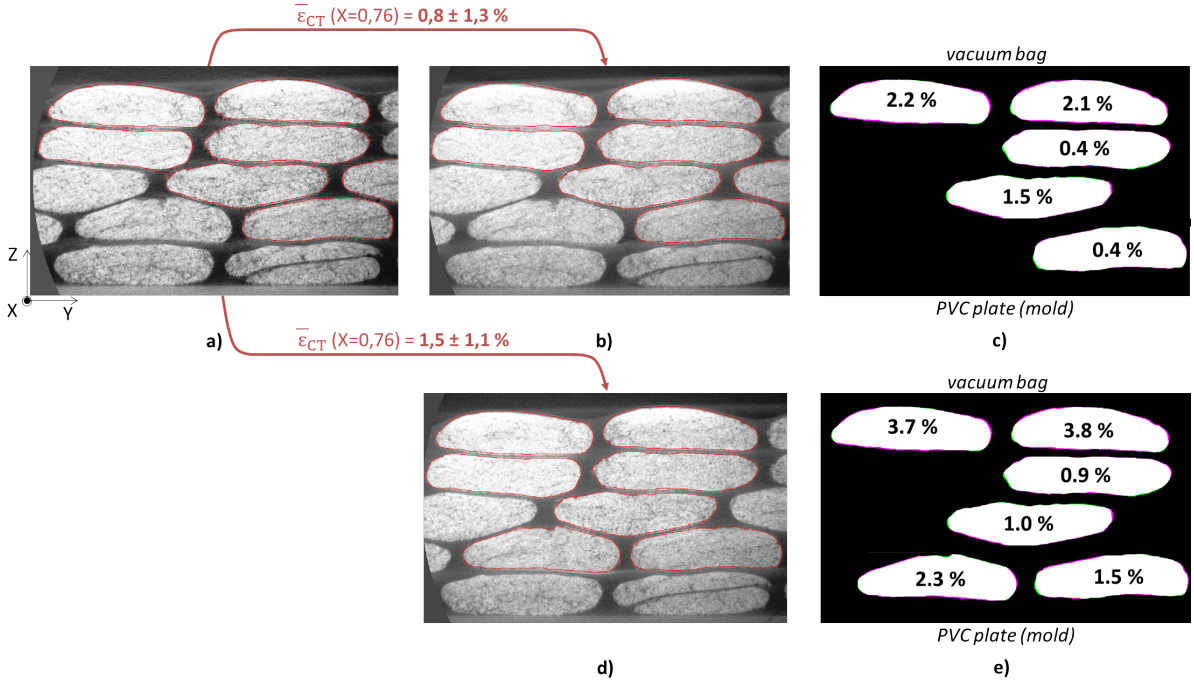

Figure I.52: Measurement of tow deformation near the inlet (X=0.76): a) Raw data with detected tow boundaries at dry state. b) Raw data with detected tow boundaries at saturated state (60 $mbar$). c) Tow decompaction with the corresponding area evolution α_{CTmeso} (60 $mbar$). d) Raw data with detected tow boundaries at saturated state (600 $mbar$). e) Tow decompaction with the corresponding area evolution α_{CTmeso} (600 $mbar$).

The decompaction phenomenon induces a vertical displacement of the vacuum bag and tow swelling. The relative macroscopic decompaction (displacement of the vacuum bag, corresponding to the global stack deformation) is close to the relative mesoscopic decompaction (tows deformation). Only vertical deformation of tows is observed: the lateral deformation is negligible for these tows within the quasi-UD NCF.

9.2.3 Conclusion on microstructural reorganization

A gradient of vertical displacement along the stack thickness direction is highlighted. The maximal displacement, occuring for tows located near the vacuum bag, is similar to the vacuum bag displacement monitored at macroscopic scale with the chromatic confocal scanner or CT-scan device. The minimal displacement is observed for the tows located near the mold.
For a given X-position, each tow in the stack deforms individually: no link was found between the tow position and the tow deformation. Besides, on average, the relative mesoscopic decompaction (e.g. the area deformation of all detected tows) is similar to the relative macroscopic decompaction (e.g. the stack deformation). Finally, the tows deformation occurs in the thickness direction: no widening is observed.
Combining the microstructure displacement (vertical gradient) and the measured tows deformation (homogeneous) allows one to deduce the channels deformation. For instance, a vertical vacuum bag displacement of 7% between the dry and the saturated states is directly linked to a tow swelling of 7% (on average) in the vertical direction: channels are then also deforming in the vertical direction, with a value of 7%, between the dry and the saturated states. This channel evolution will also have an impact on permeability.

9.3 Consequences on the in-plane permeability

Previous experiments revealed that the decompaction phenomenon induces a microstructural reorganization of the fabric between the dry and the saturated states. As reported by Caglar et al. [10] and Salvatori et al. [9], a detailed knowledge of the fabric microstructural morphology is essential because it impacts intra-tow and inter-tow permeabilities and then, for instance, fibrous preform filling time. In this section, the aim is to evaluate the impact of the microstructural reorganization on the in-plane permeability along the fluid flow direction (X-axis). A simplified computational method based on geometrical considerations is first detailed. Then, three microstructural reorganizations with a same macroscopic decompaction level are developed to quantify the impact on permeability evolution.

9.3.1 Simplified computational method

For the quasi-UD NCF of the study, Martin [32] modeled the fabric unit cell and tow cross-section by rectangles (Figure I.53a). Based on geometrical considerations, a simplified in-plane permeability along the X-axis can be estimated from the 3 components of the unit cell: the tow, the horizontal inter-tow channel and the vertical inter-tow channel (illustrated in Figure I.53b, with the corresponding dimensions reported in Table I.5). First, the tow permeability (K_{tow}) is computed, with the model proposed by Gebart et al. [17] (hexagonal fiber arrangement):

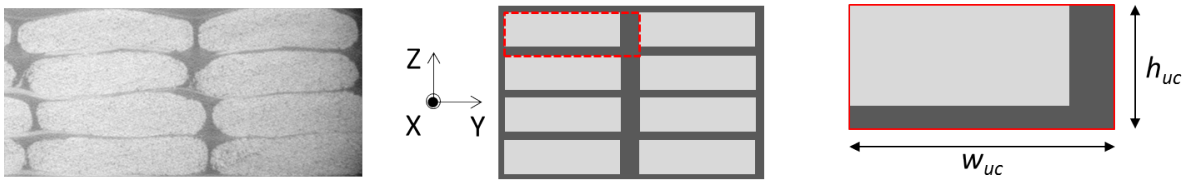

a)

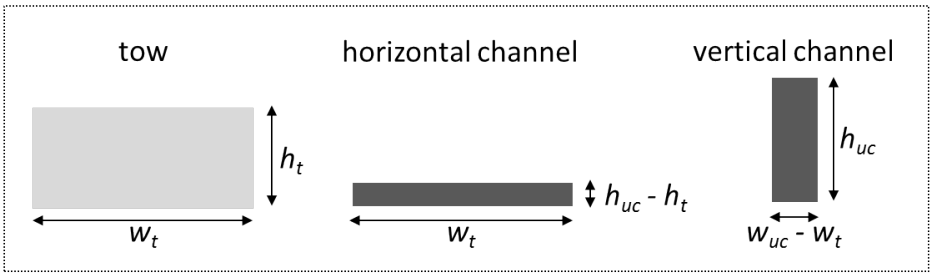

b)

Figure I.53: Quasi-UD NCF stack representation (a) and components of its unit cell (b)

$$K_{tow} = \frac{8r_f^2}{c}\frac{(1-fvf)^3}{fvf^2} \tag{I.14}$$

where $c = 53$, $r_f = 8.5\ \mu m$ and $fvf = \frac{L_w}{w_t h_t}$ with L_w the lineal weight of the fabric ($L_w = 4800\ tex$ for the fabric of the study). The permeability of inter-tow channels (K_{vert} for vertical channel, K_{horiz} for horizontal channel) is computed using the model for Poiseuille flow in a rectilinear duct of rectangular cross-section [33]:

$$K_c = \frac{b^2}{3}\left(1 - \frac{192b}{a\pi^5}\sum_{i=0}^{\infty}\frac{1}{(2i+1)^5}tanh\left(\frac{(2i+1)\pi a}{2b}\right)\right) \tag{I.15}$$

where K_c is the permeability of the considered rectangle duct of semi-minor edge b and semi-major edge a ($b < a$).
Finally, the permeability of all the inter-tow channels inside the unit cell ($K_{channels}$) and the permeability of the stack (K_{stack}) are computed, considering that the flow in the unit cell components are in parallel (stratified flow):

$$K_{channels} = \frac{K_{horiz}(h_{uc}-h_t)w_t + K_{vert}h_{uc}(w_{uc}-w_t)}{(h_{uc}-h_t)w_t + h_{uc}(w_{uc}-w_t)} \tag{I.16}$$

$$K_{stack} = \frac{K_{channels}(h_{uc}w_{uc} - h_t w_t) + K_{tow}h_t w_t}{h_{uc}w_{uc}} \tag{I.17}$$

where h_{uc}, w_{uc}, h_t and w_t are respectively the dimensions of the unit cell and of the tow, whose values are given in Table I.5 and illustrated in Figure I.53b. Create an array of parallel inter-tow channels (e.g.: there is no fluid exchange between the 3 unit cell components) may imply some errors in absolute permeability predictions. Nonetheless, these fluid exchange contributions will be equal in the three studied cases: then, relative comparison between permeability estimations can be considered as representative.

The porosity content inside a unit cell of the stack ($\phi_{stack} = 1 - \frac{fvf h_t w_t}{h_{uc} w_{uc}}$) is divided between the porosity content inside a tow ($\phi_{tow} = 1 - fvf$) and the amount of channels ($\phi_{channels} = 1 - \frac{h_{uc} w_{uc} - h_t w_t}{h_{uc} w_{uc}}$).

Unit cell dimensions		
thickness (Z-axis) (mm)	h_{uc}	1
width (Y-axis) (mm)	w_{uc}	3.5
Tow parameters		
thickness (Z-axis) (mm)	h_t	0.9
width (Y-axis) (mm)	w_t	3.27
fiber volume fraction (%)	fvf	57
glass fiber radius (μm)	r_f	8.5

Table I.5: Microstructural parameters of the studied quasi-UD NCF

9.3.2 Validity

Before the infusion at the compressed dry state, all the considered microstructures have the same fibrous and tow distribution, called the *reference case* (Table I.6). Then, after the infusion process at saturated state, three microstructural reorganizations are analyzed (Table I.6):

- *case 1*, measured with XCT: stack thickness and tow thickness increase equally; no variation of tow width,
- *case 2*, quasi-UD NCF where tows are highly constrained by the stitch yarn: only the stack thickness increase; no variation of tow width and thickness,
- *case 3*, quasi-UD NCF where tows are slightly constrained by the stitch yarn: stack thickness and tow thickness increase equally; tow width slightly decrease due to spring back in the Y-direction.

	ref.	**case 1**	**case 2**	**case 3**
	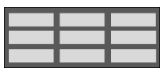			
$h_{uc}(mm)$	1	1.1	1.1	1.1
$w_{uc}(mm)$	3.5	3.5	3.5	3.5
$h_t(mm)$	0.9	0.9×1.1	0.9	0.9×1.1
$w_t(mm)$	3.27	3.27	3.27	3.27×(-1.05)

Table I.6: Geometrical parameters to compute the in-plane permeability: for the reference case, values are taken from [32]. For the other cases, values are chosen for a maximal thickness rise ($\overline{\varepsilon} = 10\%$, then $h_{uc} = 1.1mm$)

Order of magnitude. The stack permeability is first computed for the *reference case*: $K_{stack} = 3.3 \cdot 10^{-10} m^2$ for a fiber volume content of 48% ($\phi_{stack} = 0.52$). It is in good agreement with the one experimentally measured ($2 \cdot 10^{-10} m^2$, for the fabric named A in [22]): despite its simplicity, the proposed method to compute the in-plane permeability

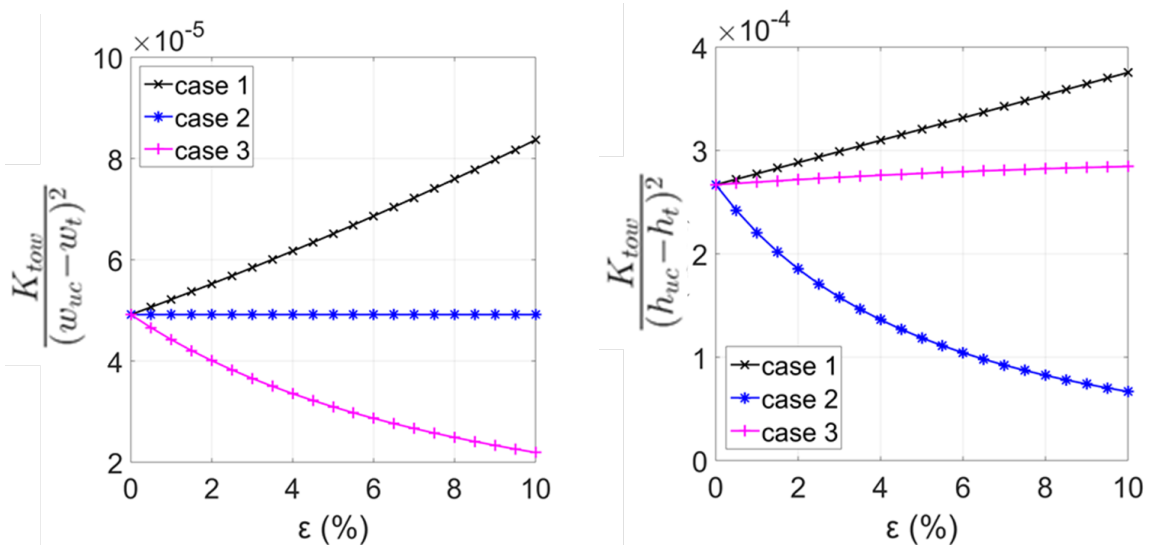

(a) (b)

Figure I.54: Scale separation during the decompaction phenomenon: (a) for inter-tow vertical channels dimensions. (b) for inter-tow horizontal channels dimensions.

is enough representative to investigate the impact of the microstructural reorganization. Similar conclusion was drawn in [34], where a permeability network was developed to address non-crimp fabrics.

Stratified flow hypothesis. A strong scale separation is kept while the microstructure is evolving: $\frac{K_{tow}}{(h_{uc}-h_t)^2} < 10^{-3}$ and $\frac{K_{tow}}{(w_{uc}-w_t)^2} < 10^{-3}$ (Figure I.54), as prescribed in [11]. Flow inside inter-tow channels and flow inside tows can be considered independent: it then validates the assumption of unit cell components parallelism (Eq. I.16 and Eq. I.17).

Geometrical assumptions. The recent work conducted by Endruweit et al. [35] present the impact of the tow cross-sectional shape on the estimation of the quasi-UD in-plane permeability. The main hypothesis they formulated is that the axial tow permeability K_{tow} is negligible compared to the equivalent inter-tow channels permeability $K_{channels}$. Figure I.55 illustrates the evolution of the ratio $\frac{K_{permeable}}{K_{impermeable}}$, where $K_{permeable}$ is equal to K_{stack} (defined in Eq. I.17) and $K_{impermeable}$ corresponds to K_{stack} where tows are impermeable (K_{tow}=0). Thus, the assumptions of axial tow permeability negligibilily is applicable for the cases studied in this section.
Figure I.56 has been extracted from [35] for rectangular to elliptical tows cross-sectional shape, and for a channel porosity $\phi_{channels}$ equal to 0.3. In this study, the simplifications are made the same way for all the 3 cases studied (tows remains rectangular). Therefore, the shift of around $5 \cdot 10^{-10} m^2$ generated (highlighted in Figure I.56 between n=0.25 and 0.75) remains for *cases 1* and *2*. In *case 3*, the channels width increase slightly (5%, then w_{uc} increases from 3.5 to 3.675 mm), thus the shift can be considered identical ($5 \cdot 10^{-10} m^2$ between n=0.25 and 0.75). Therefore, the error made by considering rectangular tow cross-sectional shape remains small and equal for all the cases studied.

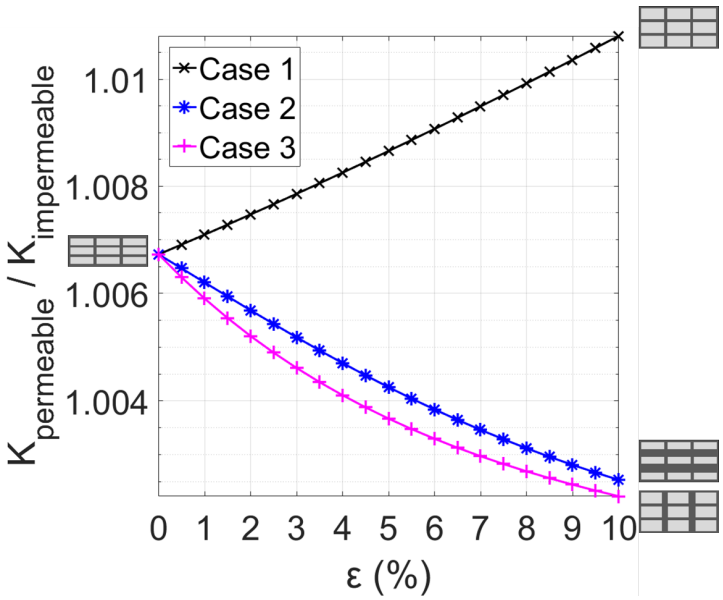

Figure I.55: Ratio $\frac{K_{permeable}}{K_{impermeable}}$ evolution with stack thickness rise for the 3 proposed microstructural reorganizations

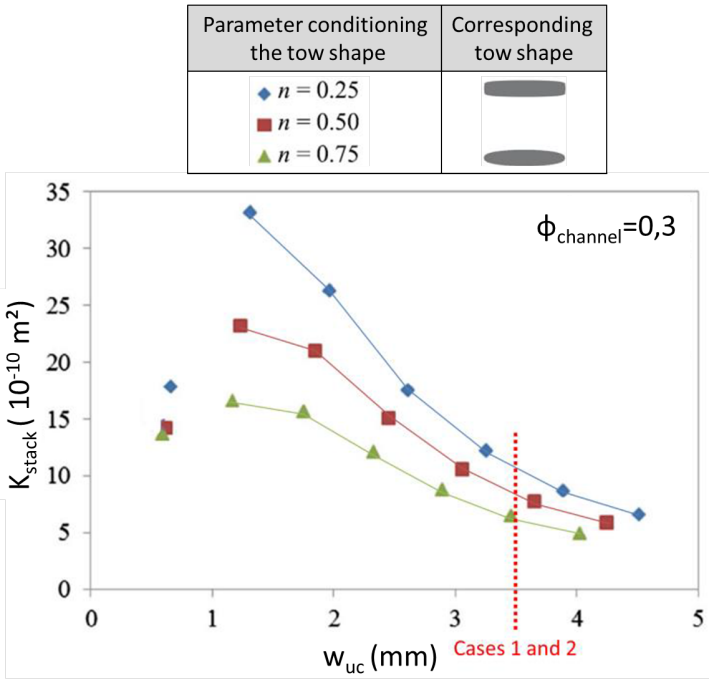

Figure I.56: Evolution of the in-plane permeability for several tow cross-sectional shapes, at a given channel content ($\phi_{channels}$=0.3) [35]

9.3.3 Results

For a same porosity content evolution inside the stack with the thickness rise (ε in Figure I.57a), the pores distribution differs in tows and channels (Figures I.57b and I.57c): as expected, in *case 1*, $\phi_{channels}$ is constant because tows are swelling as stack thickness is increasing, while in *case 2*, as tows are constrained, $\phi_{channels}$ evolution is significant. *Case 3* presents, in term of porosity contents, trends between *case 1* and *case 2*. These porosity contents evolution have impact on the stack permeability evolution with the thickness rise (Figure I.57d): channels content evolution impacts the permeability as its lowest evolution is observed for *case 1*. Nonetheless, it shows that a combination between $\phi_{channels}$ and ϕ_{tow} increase (*case 3*) results in higher permeability than when only the inter-tow channels size increases, even higher (*case 2*).

These results indicate that the fibrous microstructural reorganization occurring during the infusion process has a significant impact on the resulting macroscopic in-plane permeability.

10 Conclusion

Due to the vacuum bag flexibility, the fibrous reinforcement manufactured with the infusion process undergo a decompaction phenomenon : during the filling, the stack thickness rises up to 15% near the fluid inlet. When dual-scale fabrics are considered, the size and the spatial distribution of pores drive significantly the saturation. It would be thus of great interest to quantify the tows displacement and deformation that might occur.

Therefore, new experimental setups and methodologies have been developed to monitor a given fibrous microstructure at dry state, prior to the infusion, and at saturated state, during the filling. A downsized vertical infusion of a quasi-UD NCF stack has been conducted inside a XCT device, where the acquisition duration of one 3D image can reach 12 hours. Despite this long duration and spatial constraints, the decompaction phenomenon measured with the XCT device at macroscopic scale fits well with the one measured at larger scale, when a representative horizontal infusion process is considered.

The 3D images of the same microstructure under several compaction states have been thus analyzed at mesoscopic scale. Image post-processing methods have been developed and adapted to allow the quantification of both tow displacement and deformation. The results show that for the considered quasi-UD NCF, when the stack thickness rises by X% in the Z-direction, all the tows swell by X% in the Z-direction. A gradient of tows displacement is revealed in the Z-direction whereas no gradient is observed concerning the tows deformation. Both intra-tow and inter-tow pores size and spatial distribution are thus impacted by the decompaction phenomenon.

Finally, an evaluation of the impact of this microstructural reorganization on the in-plane permeability have been proposed. With simple geometrical considerations, the in-plane permeability of quasi-UD NCF stacks have been computed for a same macroscopic decompaction and different pores spatial distributions. The results show that the macroscopic fiber volume fraction is not the appropriate descriptor to estimate the in-plane

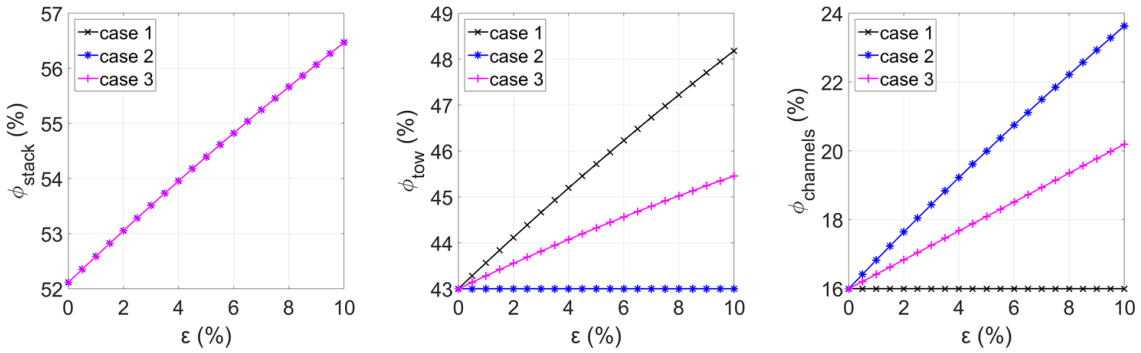

(a) (b) (c)

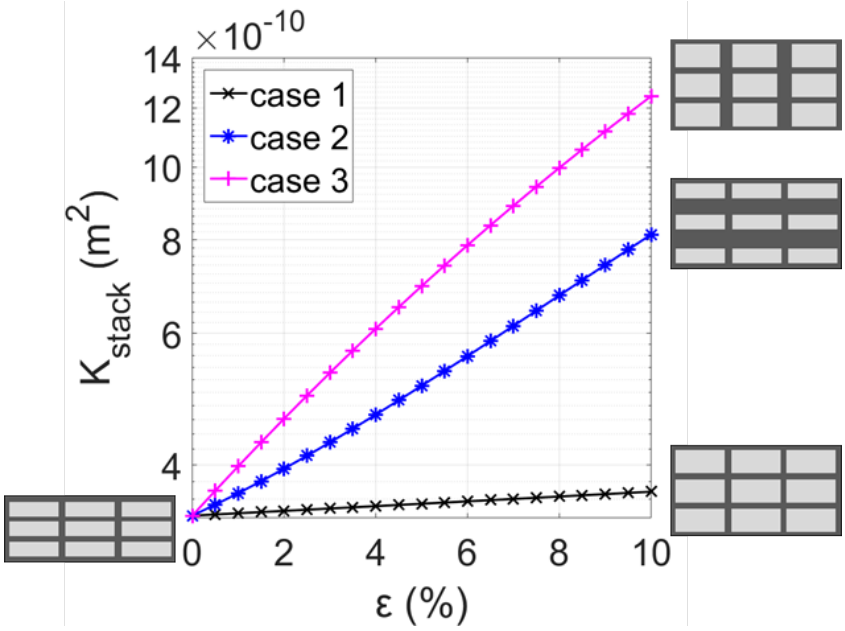

(d)

Figure I.57: Porosity contents evolution with stack thickness rise (a-c) for the 3 proposed microstructural reorganizations (Table I.6) and resulting in-plane permeability changes (d)

permeability when the infusion of dual-scale fabrics is considered. In fact, depending on the microstructural fibrous reorganization scenario, the permeability evolution of the stack is impacted by a factor 3.

CHAPTER II

Numerical simulation of the infusion process: dual-scale flow in a bidisperse deformable porous media

1 Introduction

The experimental investigations conducted in the previous chapter highlighted the actual dual-scale nature of the decompaction phenomenon: while the stack thickness increases, the tows swell and displace. This microstructural reorganization impacts the global in-plane permeability of the fabric during its filling. A unique first-order descriptor known as the macroscopic fiber volume fraction may not be sufficient to describe dual-scale flows. In this context, new numerical methods are implemented to investigate the influence of a dual-scale decompaction on a dual-scale filling of a composite part.
The simulation tool developed by Imbert et al. [36] for the Resin Transfer Molding (RTM) process is able to predict finely the 2D flow front position during the dual-scale filling of a composite part. This tool will be upgraded to take into account the dual-scale decompaction occuring during the infusion process. In this chapter, the objectives are to:

- build a numerical tool that simulates dual-scale flow in a bidisperse deformable porous media,
- investigate the influence of the microstructural reorganization due to the flow-induced dual-scale decompaction during composite manufacturing.

The second point will be studied from a composite manufacturer and a textile designer standpoint. To achieve these aims, a literature review about the theoretical equations and numerical methods commonly used to simulate flow inside a porous material is first conducted. The simulation tool developed by Imbert et al. [36] is then detailed and the main hypothesis made to include a dual-scale decompaction in this tool are presented. After numerical validations of the upgraded simulation tool, results concerning the influence of the dual-scale decompaction on the filling time and the saturation are analyzed for a 2D plane part.

2 Literature overview: theoretical equations and numerical methods

A fibrous reinforcement impregnated by a viscous polymer to manufacture composites is viewed as a porous material: the fibers are the constitutive elements and are separated by open pores. Depending on the reinforcement architecture, the size of these pores can be described by one characteristic length (single-scale porous material) or two characteristic lengths (dual-scale porous material). A dual-scale fibrous reinforcement with its two characteristic lengths is illustrated in Figure II.1. The impregnation behavior of dual-scale porous material is widely reported in the literature ([37], [38], [39]): when viscous effects are dominant, the inter-tow channels are first filled and a delayed impregnation of intra-pores inside tows is observed.

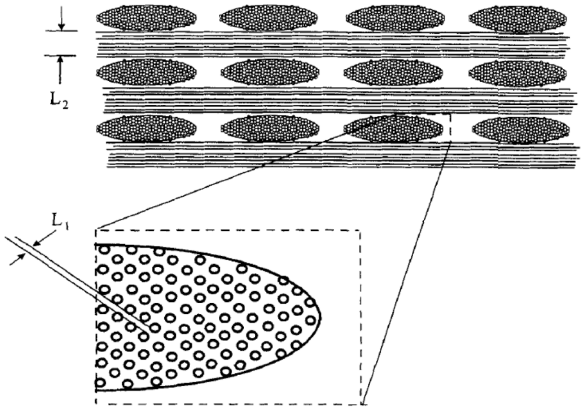

Figure II.1: Dual-scale architecture of a bi-directional fibrous reinforcement, with two characteristic lengths [37]

Moreover, depending on the manufacturing process, this fibrous reinforcement may undergo deformations. For instance, during the RTM process, the fibrous reinforcement is laid down between the lower and the upper molds, that are both rigid. If the pressure gradients are low enough (no fiber preform washing [40]), the fibrous reinforcement can be considered as non-deformable. Nonetheless, during the infusion process, the upper mold is a flexible vacuum bag: as observed experimentally in the previous chapter, the vacuum bag allows a transverse deformation of the global stack.

In this section, theoretical background and numerical methods to compute the flow inside a porous material are presented. Starting from a single-scale flow inside a non-deformable porous material, the working hypothesis are gradually modified to investigate the dual-scale flow inside a bidisperse deformable porous material.

2.1 Single-scale flow in a non-deformable porous material

2.1.1 Theoretical equations

Mass balance. The governing equation of fluid flow inside a non-deformable single-scale porous material is the mass balance equation:

$$\frac{\partial \rho}{\partial t} + \nabla \cdot (\rho \mathbf{v}) = 0 \tag{II.1}$$

A degassing state is commonly applied to the fluid prior the infusion process, in order to remove the entrapped air bubbles. The fluid can be then considered incompressible and the mass balance becomes:

$$\nabla \cdot \mathbf{v} = 0 \tag{II.2}$$

Darcy's law. Many authors from different fields (soils, rocks, filters) investigated the flow of a Newtonian fluid in a porous material. The Darcy's law [41], empirically determined from 1D observations of the flow rate of water throught a column of sand, is the most widely used equation to describe this phenomenon:

$$Q = \frac{K \Delta P}{\mu A \Delta z} \tag{II.3}$$

where Q is the volumic flow rate, K the permeability of the porous medium, ΔP the presure difference between the outlet and the inlet of the domain, μ the dynamic viscosity of the fluid, A the total cross-section of the porous material and Δz the length of the flow domain.
This equation describes the unidirectional flow of a Newtonian fluid in a single-scale porous material. It can be also generalized from the volume averaging of Navier-Stokes equation under the following conditions [42]: (i) the fluid is incompressible, (ii) inertial effects in the flow are negligible (small Reynolds numbers), (iii) the volumic forces and the forces at the domain interfaces are small compared to the other forces, (iv) there is no slip-condition on the pore walls. Under these assumptions, the 3D form of the Darcy's equation comes from the Navier-Stokes one:

$$\mathbf{v} = -\frac{\mathbf{K}}{\mu} \cdot \nabla P \tag{II.4}$$

where $\mathbf{v}$ is the Darcy's velocity ($\mathbf{v} = \phi \mathbf{v}_{pores}$ with ϕ the porosity of the medium and $\mathbf{v}_{pores}$ the true, or interstitial, pore flow velocity) and $\mathbf{K}$ is the permeability tensor of the porous material.

2.1.2 Numerical methods

To compute the filling of a composite part made of a single-scale porous material, the Finite Element Method/Control Volume (FEM/CV [43]) with fixed mesh is the most used technique among the others (finite difference method [44], boundary element method [45] or FEM with level set [46]). The pressure field is computed over the mesh in the saturated domain using the mass balance equation (Eq. II.2) and Darcy's law (Eq. II.4). The fluid volume distribution is computed using the volume of fluid technique in the CV associated to each node (see Figure II.2) or to each element.
It should be noticed that the wide majority of commercial software for Liquid Composite Molding process simulation is based on FEM/CV techniques (LIMS [48], or PAM-RTM [49]).

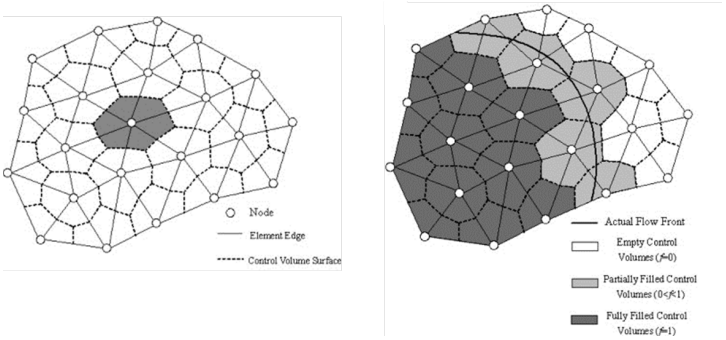

Figure II.2: Principle of the Control Volume method: CV are associated to each node of the mesh [47]

2.2 Dual-scale flow in a non-deformable porous material

2.2.1 Theoretical equations

As reviewed by Michaud [50], two main strategies are used to model the unsaturated flow occuring during the impregnation of a dual-scale porous material. The first one, directly derived from soil science, consists in solving the set of traditional multiphase flow equations for porous media; the second one reproduces the delayed impregnation of tows by introducing a sink term in the mass balance equation.

Multiphase flow equation. In this approach, several parameters are characterized as a function of the saturation S. Among the others, the permeability is calculated as a function of the saturation:

$$\mathbf{K} = k_r \mathbf{K_s} \tag{II.5}$$

where $\mathbf{K}$ is the permeability tensor of the overall fabric, $\mathbf{K_s}$ is the geometric permeability tensor of the fully saturated preform, and k_r, the relative permeability, is a dimensionless scalar function of the saturation. Several relative permeability laws are proposed in literature ([51], [52]) but the saturation is also impacted by the local pressure distribution ($S(P)$ where P stands for the pressure of the fluid).

Sink term approach. In this approach, the pores between the fibers (intra-tow pores) and the pores between the tows (inter-tow channels) are considered separetely as single-scale porous media where the Darcy's law is satisfied. In the saturated region, tows are fully saturated and thus the flow occurs only in the inter-tow channels; in the unsaturated region, flow occurs both in the inter-tow channels and from the inter-tow channels to the intra-tow pores.
In the unsaturated region, the mass balance equation is not satisfied in the inter-tow channels because a certain amount of fluid is removed to fill the intra-tow pores. This amount of fluid is represented by a sink term q in the mass balance governing equation in the inter-tow channels:

$$\nabla \cdot \mathbf{v} = q \tag{II.6}$$

This sink term can be evaluated using measurements or estimations of the local tow permeability (named K_{tow} in the previous chapter (section 9.3). The intra-tow pores

domain is considered as a single-scale porosity media where the mass balance (Eq. II.2) governs its saturation.

2.2.2 Numerical methods

As reported by Patiño-Arcila et al. [53], the FEM/CV method have been by far the most employed in the filling simulations at macroscopic scale of dual-scale porous material, when considering the sink term approach described hereinbefore. Two representative numerical methods are detailed hereafter.

Tow as a 1D element. Simacek et al. [54] model the sink term q by appending extra 1D elements ("slaves" representing the tows) to control volumes ("master" representing the inter-tow channels), as illustrated in Figure II.3. The fill factor is then divided in two parts: the fill factor inside the "master" control volumes, representing the saturation of the inter-tow channels, and the fill factor inside the 1D "slaves" elements, representing the saturation of the intra-tow pores. The fluid transfer between inter-tow channels and tows depends both on the geometry of the tow (rectangular in [54]) and on the flow direction assumption (transverse flow in [54]).

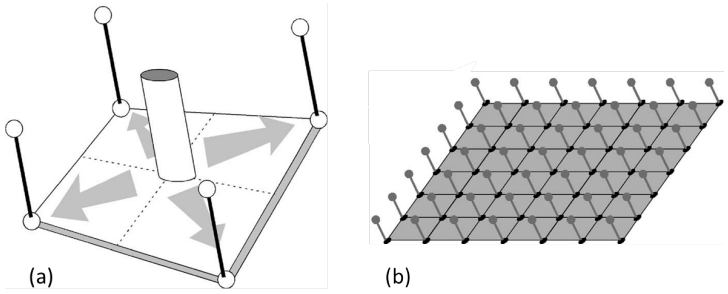

Figure II.3: 1D "slave" element attached to all the nodes of a "master" element [54]: (a) a quad element. (b) a global view.

Microscopic tow discretization. Imbert et al. [36] compute the saturation of tows and inter-tow channels by discretizing both the macroscopic scale (inter-tow channels) and the microscopic scale (tows). Based on purely geometrical considerations (tow size, inter-tow channel size, fiber orientation), an equivalent microstructure is associated to each macroscopic element. This microstructure, finer than the one proposed by [54], is discretized and again, the flow direction is assumed transverse to compute the microscopic filling (Figure II.4).

2.3 Single-scale flow in a deformable porous material

2.3.1 Theoretical equations

Fluid infiltration in consolidating (i.e. deformable) porous material was studied first by authors from the soil field (Biot in 1941 [55], Preziosi et al. in 1996 [56], to cite a few). These hydrological theory have been adapted to composites manufacturing mainly by Gutowski et al. [57], [19].

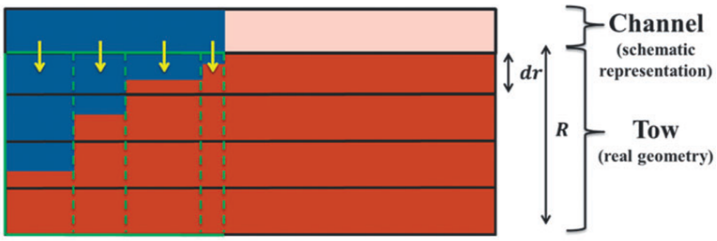

Figure II.4: Representation of the microscopic tow discretization with an assumed transverse flow [36]

Darcy's law. The deformability of a single-scale porous media does not affect the assumptions validity to use the Darcy's law (Eq. II.3).

Mass balance. The theory of a single-scale flow in a deformable porous material is based on the mass balance of the fluid and the solid (i.e. the fibrous reinforcement considered as a continuum medium) phases [58]:

$$\nabla \cdot \mathbf{v} = \frac{1}{fvf}\left(\frac{\partial fvf}{\partial t} + \mathbf{u_s} \cdot \nabla(fvf)\right) \tag{II.7}$$

where $\mathbf{v}$ is the Darcy velocity defined previously, fvf is the fiber volume fraction, t is the time and u_s is the solid velocity. For a 1D flow, Correia et al. [21] proposed a unification of the published equations for the vacuum infusion:

$$\frac{\partial h}{\partial t} = -\frac{\partial(\mathbf{v}h)}{\partial x} \tag{II.8}$$

where h stands for the thickness of the considered stack, $\mathbf{v}$ for the Darcy velocity, and x for the fluid flow direction.

Stress equilibrium. In most of the composites manufacturing studies, authors have been using the Terzaghi's law to describe the link between the interstitial fluid pressure P, the total stress tensor $\sigma_{\mathbf{tot}}$ applied to the domain "fluid + solid" and the stress tensor only applied to the solid phase σ (i.e. the fibrous reinforcement):

$$\sigma_{\mathbf{tot}} = \sigma + P\mathbf{I} \tag{II.9}$$

where $\mathbf{I}$ stands for the second order unit tensor.
Terzaghi's law is a simplification of the Biot theory, where the deformation of the constituents due to their own compressibility is taken into account:

$$\sigma_{tot} = \sigma + P\mathbf{B} \tag{II.10}$$

where $\mathbf{B}$ stands for the second order Biot tensor. The components of this tensor have been studied, predicted and measured by Tran et al. [59].

2.3.2 Numerical methods

When considering a 1D in-plane flow, analytical formulations combining the previous presented equations with permeability and compaction models can be solved using sev-

eral numerical methods: finite difference [21], finite element [60], or mathematically (Goodman's integral method in [61]).
For 2D simulations, the FEM/CV method is the most widely used to compute the filling of a single-scale deformable porous material. Correia et al. [62] use the software LIMS, originally developed to simulate the RTM process (single-scale flow in a non-deformable porous material): at each time-step, the thickness, the porosity and the local permeability are updated, following usual models that are function of the fluid pressure (Robitaille [63] for compaction, Kozeny-Carman [64] for permeability). The results provided fit well with the 1D analytical solution, but the mass balance modification due to the evolution of the part thickness is not mentioned. Dang-Huu [65] used the same approach by coupling LIMS and Matlab, and evaluate the impact of the part thickness (or volume) evolution on the mass balance.

Adding an upper draining material [66], or a pure fluid layer ([67]) in the infusion process complicates the formulation as a Stokes flow is considered in the draining material or pure fluid layer and a Darcy flow in the fibrous reinforcement. Coupling these two flows (with a Beaver-Shaffman-Joseph condition for instance) adds numerical considerations (Arbitrary-Lagrangian-Eulerian method) that are beyond the scope of this study.

2.4 Dual-scale flow in a deformable porous material

To the authors knowledge, few papers are devoted to the dual-scale flow inside a deformable fibrous reinforcement [12], [13], [14]. The theoretical equations and numerical methods employed for these works are detailed hereafter. A small aside is also proposed to cite the recent work from Rouhi et al. [15], [68]: their approach is mainly based on poromechanics of the coupled dual-scale flow deformation.

2.4.1 Theoretical equations

Several strategies are reported while combining the equations presented in sections 2.2 and 2.3. Acheson et al. [12] write the mass balance equation on a non-rigid Control Volume and add a sink term to take into account the dual-scale flow. Darcy's law is used to model the flow inside tows and then links the macroscopic sink term to the tow saturation. Wolfrath et al. [13] express the general stress equilibruum depending on the saturation, and with a similar approach, the Darcy's law is written for non-saturated infiltration depending on the saturation. The mass balance is written by distinguishing the fluid and the solid phases. In this multiphase flow approach, the permeability and the pressure depend both on the saturation. Concerning the compressiblity of the fibrous reinforcement, the variation of the fiber volume fraction is only treated in the numerical part of the work. Bayldon et al. [14] use a mass balance formulation equivalent to the one described by Correia et al. [21] (Eq. II.8) and represent the dual-scale saturation by considering separately the resin flowing within the tows and the resin flowing within the inter-tow channels.
In all this studies, the overall stack is considered deformable, but the geometry and thus the permeability of the tows are kept constant.

2.4.2 Numerical methods

Acheson et al. [12] solved their proposed analytical solution using a 1D finite element model, where the flow front is considered as a moving boundary. The pressure and the saturation are calculated at each node; the fiber volume fraction and the permeability, assigned to each element, are updated at each time step. Wolfrath et al. [13] used a finite element code initially developed for soil mechanics (GEFDYN) to solve the non-linear differential equation obtained analytically. To take into account the flow inside the bundles, the compressibility of the fluid is modified at each time step to compensate the mass loss induced. Bayldon et al. [14] use a control volume method where the time step calculation is governed by the flow front velocity, which depends both on the global and on the tow saturation.

2.4.3 Poromechanical approach

The development proposed by Rouhi et al. [15] differs from the ones presented previously. Concerning the dual-scale flow, the governing equations are presented with a porous media approach, where two phases considered: a compressible solid phase (the porous medium, made of incompressible fibers and compressible voids) and an incompressible fluid phase (the fluid). The mass balance obtained formulation corresponds to the one presented before (Eq. II.7). However, other governing equations, based on balance of energy and entropy inequality, seem necessary to add the mechanical response of the compressible fibrous reinforcement. This thermodynamical approach has been also employed by Coussy to propose several mechanical behavior laws of porous materials [69] and by Cheng et al. [70] to propose a rate-independent model for fiber reinforcements.
Rouhi et al. mention the use of a distinct permeability tensor for tows and for inter-tow channels and unified them into a permeability tensor of the overall stack. However, the potential variation of the tow permeability tensor is not mentioned in their different publications.

2.5 Conclusion about the literature review

In this literature review, theoretical background and numerical methods dealing with flow in porous material have been investigated. Few work has been done to couple the interaction between a dual-scale flow and a bidisperse deformable porous media. To the author knowledge, there is no published model or numerical study able to deal with a deformation of the porous media occuring at both macroscopic and mesoscopic scale. The studies presented in section 2.4 keep the geometry and the permeability of the tows constant in the analytical formulation or in the process simulation.
The two numerical methods presented in section 2.2 could be adapted to couple a 2D dual-scale flow with a dual-scale deformation: in both cases, the modification of the tows geometry and permeability seems possible, but a particular attention should be paid to the mass balance, as highlighted by Dang-Huu [65].

3 Developed numerical methods

Novel numerical methods are implemented to simulate the dual-scale flow inside a porous fabric undergoing a dual-scale decompaction phenomenon during its filling, . This work is mainly based on the simulation tool developed by Imbert et al. [36] which is first detailed

in this section. The strategy to implement dual-scale decompaction inside this existing tool is then presented and assumptions are discussed. Finally, numerical validations based on mesh convergence and fluid mass balance are analyzed.

3.1 General concept of the existing simulation tool

The variables, equations and numerical algorithm detailed in this section have been extracted from the work realized by Mathieu Imbert in his PhD thesis [71], dealing with the dual-scale flow inside a non-deformable porous media. To track the fluid flow at the two scales, tows and inter-tow channels are treated separately. The variables and parameters are first detailed for each scale (inter-tow channel scale, with subscript c and tows scale, with subscript t). Then, the numerical explicit method developed by Imbert to compute the fluid volume distribution between the inter-tow channels and tows is detailed and schematic views are proposed to illustrate the numerical algorithm step by step.

3.1.1 Macroscopic scale: flow in the inter-tow channels

The overall domain to be filled is considered as a dual-scale porous media but inter-tow channels and tows are treated separately. Macroscopic triangular control volume, which are the elements themselves, are dedicated to the inter-tow channels flow. This flow is considered as single-scale far from the flow front, where tows are fully saturated, and as dual-scale in the unsaturated region.

Pressure and velocity. The pressure field in channels P_c is defined using the finite element method:

$$P_c = \sum_i \epsilon_{no} P_{no} \tag{II.11}$$

where P_{no} is the pressure value at each macroscopic node and ϵ_{no} are the linear shape functions associated to each node no of the model. To compute the pressure field in the unsaturated region, the Darcy's law is combined with the mass balance equation, modified with a sink term (see Eq. II.7):

$$\nabla \cdot (\frac{-\mathbf{K_c}}{\mu} \nabla P_c) = q \tag{II.12}$$

where $\mathbf{K_c}$ is the in-plane permeability tensor of the inter-tow channels (i.e. corresponding to the permeability of the stack when tows are fully saturated as defined in section 9.3 in the previous chapter), μ is the viscosity of the fluid and q is the relative absorption of the fluid in the tows. The numerical technique developed by Imbert to estimate the value of q is detailed in section 3.1.3. It shoud be noticed that in the saturated region located far from the flow front, $q = 0$ because tows are fully saturated.

Fluid fraction. The fluid fraction I_c indicates the ratio between the volume of fluid present in the inter-tow channels of an element e ($VOF_c(e)$) to the overall volume of inter-tows channels inside this element ($V_c(e) = \phi_c V(e)$ where ϕ_c is the volume fraction of channels inside an element of volume $V(e)$). Numerically, a surface exchange exists between two consecutive elements to compute the fluid flow. I_c represents also the ratio between the saturated exchange surface between two inter-tow channels to the overall

surface exchange. The fluid fraction evolution is governed by the advection equation, modified with the sink term q:

$$\frac{\partial I_c}{\partial t} + \mathbf{v_c} \cdot \nabla I_c = q \tag{II.13}$$

where $\mathbf{v_c}$ is the Darcy's fluid velocity in the inter-tow channels. Again, in the fully-saturated region, $q = 0$.

3.1.2 Microscopic scale: flow in the tows

Tows are considered as single-scale porous media. A discretization of tows is proposed by Imbert to use a classical FEM/CV approach to compute the pressure and the filling of the microscopic elements.

Microscopic tow discretization. The tow filling is assumed to occur exclusively transversely. The ratio $\frac{K_c}{K_t}$ has been reported to be in the range of 50 to 2000: for viscous pressure driven flows, inter-tow channels are filled much faster than tows. The tows being impregnated are then considered surrounded with fluid over their periphery. Tow filling can be thus reduced to a 1D filling problem where the inlet pressure (P_c) is imposed on the surface of the tow. In the case of rectangular cross-section of tows, the flow problem is solved in the half-thickness domain of the tow (1D Cartesian formulation). Moreover, a minimal size is required to assume that the flow occurs in an homogeneous medium (and then use Darcy's law): Imbert chooses a criterion where the half-thickness of the tow cannot be discretized in elements smaller than 10 times the radius of glass fiber. More details concerning the microscopic meshing and its advantages could be found in [36].

Parameters and variables. As tows are single-scale porous media, the combination of Darcy's law and mass balance equation allows the tow pressure field computation:

$$\nabla \cdot (\frac{-\mathbf{K_t}}{\mu} \nabla P_t) = 0 \tag{II.14}$$

where $\mathbf{K_t}$ stands for the permeability tensor inside the considered tow and P_t the pressure field to be estimated inside the considered tow. Moreover, the fluid fraction evolution inside a tow I_t is governed by the advection equation:

$$\frac{\partial I_t}{\partial t} + \mathbf{v_t} \cdot \nabla I_t = 0 \tag{II.15}$$

where $\mathbf{v_t}$ is the Darcy's fluid velocity in the tows.

3.1.3 Macroscopic-microscopic scale: link between the inter-tow channel and the tow flows

As presented previously, a macroscopic mesh made of triangular elements is dedicated to the flow in the inter-tow channels, while a microscopic discretization is dedicated to compute the flow into the tows. Geometrical assumptions made by Imbert allow to adapt the fibrous microstructure associated to each macroscopic element.

Associated fibrous microstructure. Purely geometrical parameters are considered: tow geometry (rectangular cross-section, with its corresponding dimensions), inter-tow

gaps size in the weft and warp direction and tow orientation in the warp and weft directions. Using the size and the shape of each macroscopic triangular element, the number of tows in both directions (n_1 and n_2) as well as the average length of tows (L_1 andL_2) are defined and illustrated in Figure II.5. Knowing exactly the amount of tow inside a macroscopic element and the tow porosity ϕ_t, it is possible to calculate the repartition of volume between inter-tow channels and tows inside each macroscopic element.

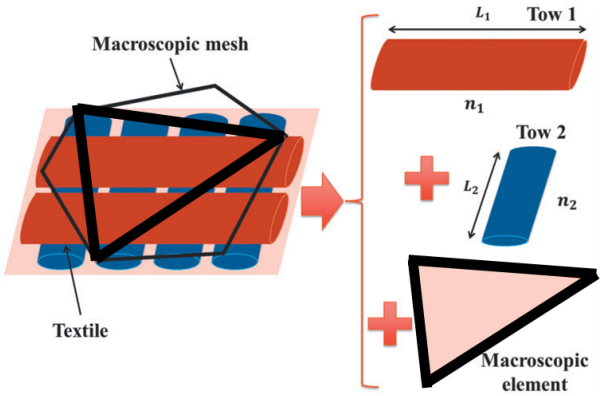

Figure II.5: Principle of the microstructure determination associated to a macroscopic element [36]

This representation leads to the definition of the boundary condition for tow filling: in each macroscopic element, the ratio between the impregnated tow surface S_{imp} and the overall tow surface S_{tot} is assumed equal to the fluid fraction in inter-tow channels I_c (Figure II.6). This assumption is discussed in [36].

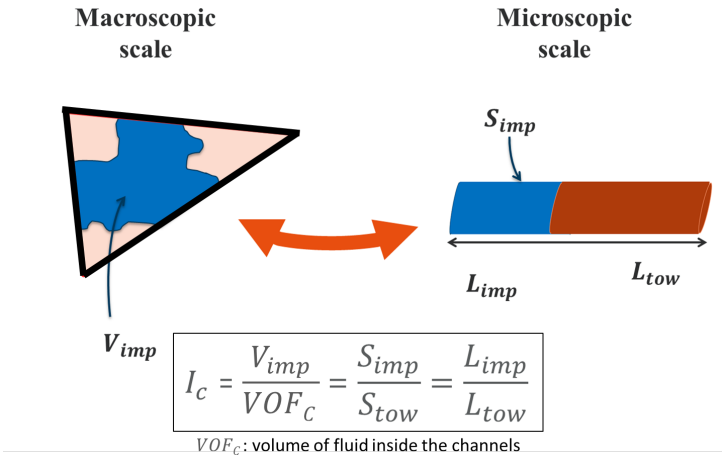

Figure II.6: Equivalence between the macroscopic fluid fraction I_c and the tow geometrical parameters [71]

First filling solution. From the pressure field and fluid velocity in each macroscopic element, the amount of fluid V_{in} coming into a considered element during a time step can be computed (details of these steps are given in the next section). This volume has to be splited between the inter-tow channels and the tows to satisfy both Darcy's law

and mass balance for this volume repartition. First, the 1D filling problem at tow scale leads to the computation during one time step of the fluid pressure P_t and velocity $\mathbf{v_t}$ and thus to the volume of fluid absorbed by tows in both directions (VOF_{t1} and VOF_{t2}). Then, the macroscopic volume of fluid coming into the element V_{in} is splited to satisfy mass balance:

$$V_{in} = VOF_{t2}\frac{S_{imp1}}{S_{tot1}} \cdot n_1 + VOF_{t2}\frac{S_{imp2}}{S_{tot2}} \cdot n_2 + VOF_c \tag{II.16}$$

where VOF_c stands for the volume of fluid remaining in the inter-tow channel of the considered macroscopic element.

Second filling solution. Imbert wrote significant conclusions about the influence of the length of the unsaturated region on the filling time [36]: if the length of the unsaturated region is smaller than 1/5 of the length of the part, sink effects are negligible. In this case, the time required to fully saturate the part is very close to the single-scale time. Then, the microscopic tow filling can be simplified: in a macroscopic element, the saturation of tows is assumed equal to the saturation of the inter-tow channels ($I_c = I_t$) and the sink term is equal to 0 ($q = 0$). Nonetheless, the geometrical assumptions presented hereinbefore are retained to deal with the repartition of voids in the dual-scale porous material.

In the following subsection, the algorithm is presented for the first microscopic filling solution: the dual-scale decompaction phenomenon has to be first implemented with this complex microscopic filling in order to compute the length of the unsaturated region.

3.1.4 General algorithm and flow chart

The main parameters presented previously at each scale are summarized in Table II.1 to ease the interpretation of the general algorithm. Notations concerning the tow and inter-tow channel dimensions have been introduced in the previous chapter (Table I.6 and Figure I.53 in section 9.3).

Macroscopic scale	
Inter-tow channel/overall volume ratio	ϕ_c
Inter-tow channel permeability	$\mathbf{K_c}$
Microscopic scale	
Intra-tow porosity	ϕ_t
Tow permeability	$\mathbf{K_t}$
Link between the two scales	
Tow width	w_t
Tow thickness	h_t
Inter-tow channel width	$w_c = w_{uc} - w_t$
Inter-tow channel thickness	$h_c = h_{uc} - h_t$

Table II.1: Main parameters for the dual-scale flow simulation

For the sake of clarity, the numerical algorithm is illustrated step by step following a 2D-simulation of a simplified 1D flow. The inlet pressure of fluid P_{inj} and the pressure at the flow front P_{out} are the boundary conditions of this problem. The simulation of the injected fluid reactivity (degree of cure, temperature and viscosity evolutions) is

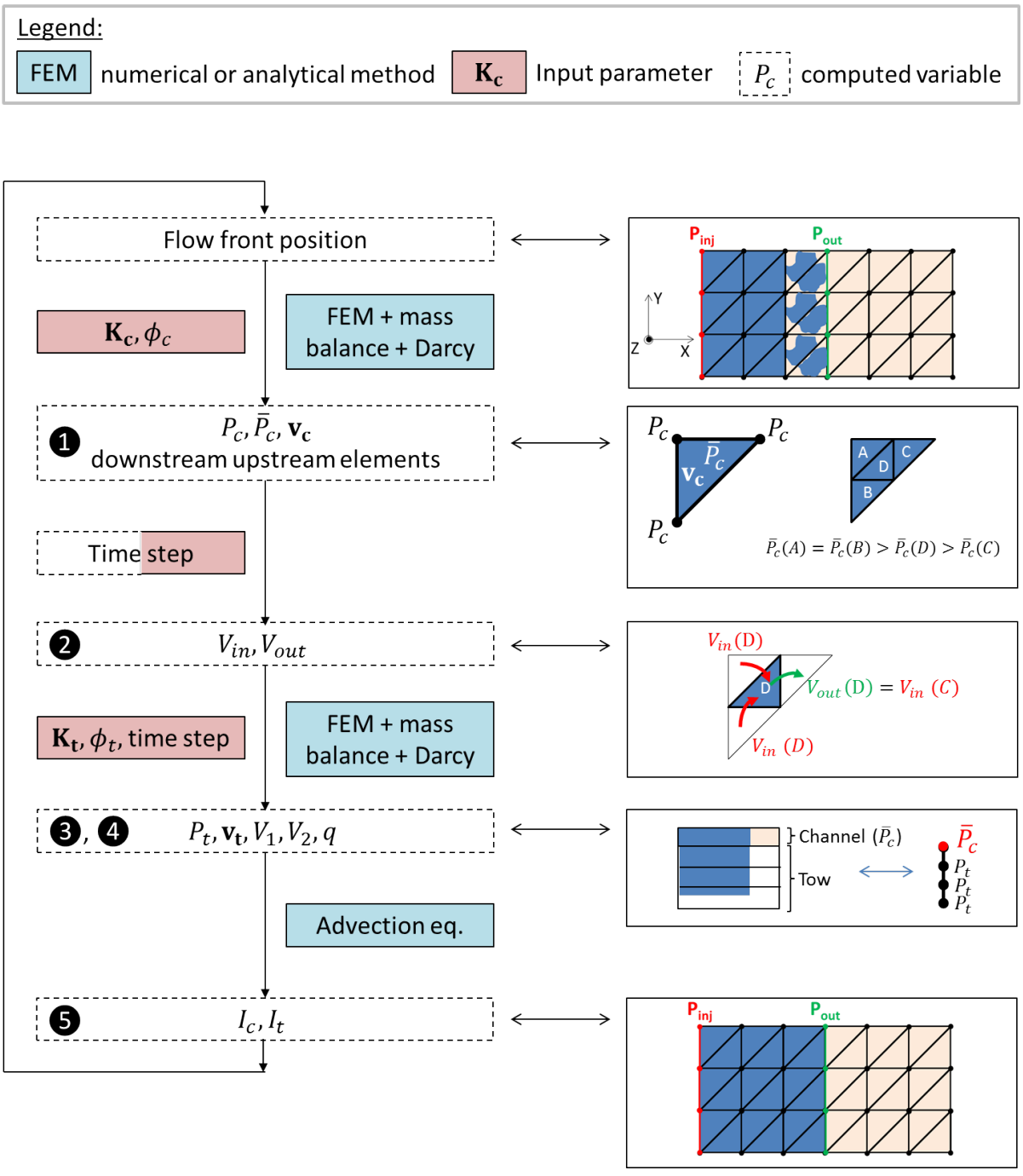

Figure II.7: Flow chart of the algorithm developed by Imbert with step by step illustrations

beyond the scope of this study: the viscosity of the fluid μ is then a constant parameter. The numerical algorithm can be subdivided in five steps (illustrated in Figure II.7):

❶ Macroscopic pressure field, velocity and element numerotation: with a FEM/CV method, the macroscopic pressure field is computed in the impregnated area using a variational formulation of Eq. II.12. Knowing the pressure P_c for each node allows to determine the list of upstream and downstream elements (i.e. in which direction the fluid flows for each surface exchange). The velocity $\mathbf{v_c}$ is computed in each macroscopic element with the Darcy's law.
❷ Amount of fluid flowing: from the fluid velocity and the list of upstream and downstream elements, the amount of fluid flowing in V_{in} and out of each element is computed during a time step.
❸ Microscopic 1D-filling: Using the transverse discretization and the average pressure inside the considered macroscopic element $\overline{P_c}$ surrounding the tow, the pressure field P_t is analytically computed. Again, the Darcy's law is used to compute the fluid velocity $\mathbf{v_t}$. The amount of fluid absorbed by the tow during a time step is then calculated. The impregnated surface S_{imp} illustrated in Figure II.6 is determined with Eq. II.16 and by assuming that:

$$\frac{S_{imp}}{S_{tow}} = \frac{V_{imp}}{VOF_c} = I_c \tag{II.17}$$

❹ Sink term: The amount of fluid absorbed being just computed, the new sink term q is saved to be updated in the mass balance for the next macroscopic pressure field computation time step in the unsaturated region. No convergence loop is required since the scheme is explicit.
❺ Fluid fractions: Eq. II.17 allows the computation of the fluid fraction in inter-tow channels I_c. I_t is computed using the weak form of Eq. II.15.

A time step evolution depending on the fluid velocity allows to speed up the computation. Thus, Imbert imposes two conditions to define the time step: (i) no overfilling of macroscopic element may occur, (ii) no more than one microscopic element may be filled in the transverse direction of the tows.

In the simulation tool developed by Imbert, the link between the macroscopic scale (inter-tow channels) and the microscopic scale (tows) is based on purely geometrical considerations (Table II.1). Mass balance and Darcy's law are used at both scales to compute pressure fields and fluid velocities. Then, introducing the dual-scale decompaction by modifying the geometrical parameters linking both scales and associated permeabilities at each time step seem achievable. A particular care should be given to the mass balance at each scale: the volume of each macroscopic element will evolve due to the decompaction.

3.2 Integration of dual-scale decompaction inside the existing simulation tool

The first chapter of this manuscript highlighted a decompaction phenomenon occuring at both macroscopic and microscopic scales between the dry and the saturated states. Moreover, the literature review presented hereinbefore underlined the novelty of introducing dual-scale decompaction in a dual-scale flow simulation. Upgrading the algorithm

developed by Imbert is the way proposed to reach this objective. In this section, the parameters of the existing simulation tool that are impacted by this dual-scale decompaction are first listed. Then, a simplified model of dual-scale decompaction is proposed and the associated assumptions are discussed. A methodology to ensure mass balance is presented and the general algorithm of the upgraded simulation tool is detailed and illustrated with a flow chart.

3.2.1 Parameters impacted by the dual-scale decompaction

Macroscopic geometry. The decompaction phenomenon induces a macroscopic rise of the stack thickness. To deal with the link between the macroscopic element and the microstructure, Imbert introduced a parameter for the thickness of a ply, directly linked to the thickness of all the macroscopic elements ($h(e)$). No fluid flow occurs in this direction (Z-axis in Figure II.7) but the volume of the exchanged fluid between two consecutives macroscopic element is based on the volume of each element ($V(e)$). These two parameters become variables that depend on the macroscopic decompaction (ε_{ma}) when dual-scale decompaction is introduced.

Microscopic geometry. The decompaction phenomenon induces also a microstructural reorganization of the fibrous reinforcement as tows swell while the stack thickness increases. The tows geometry (h_t and w_t) as well as inter-tow channels size (h_c and w_c) become variables that depend on the microscopic decompaction (ε_{mi}) when dual-scale decompaction is introduced. The length of 1D-microscopic elements is also modified.

Porosity content and permeability. As presented in section 9.3 and Figure I.53 of the first chapter, the porosity contents and permeabilities are impacted at both scales when dual-scale decompaction occurs. Thus, porosity content ϕ_c and permeability $\mathbf{K_c}$ depend both on the macroscopic element volume evolution and on the tows and inter-tow channels geometry. Porosity content ϕ_t and tow permeability $\mathbf{K_t}$ depend on the tows geometry evolution.
The parameters impacted by the dual-scale decompaction are summarized in Table II.2.

Macroscopic geometry	
Element thickness	$h(e)$
Element volume	$V(e)$
Microscopic geometry	
Tow width	w_t
Tow thickness	h_t
Inter-tow channel width	$w_c = w_{uc} - w_t$
Inter-tow channel thickness	$h_c = h_{uc} - h_t$
Porosity content and permeability	
Inter-tow channel/overall volume ratio	ϕ_c
Inter-tow channel permeability	$\mathbf{K_c}$
Intra-tow porosity	ϕ_t
Tow permeability	$\mathbf{K_t}$

Table II.2: Parameters impacted by the dual-scale decompaction phenomenon

3.2.2 A simplified dual-scale decompaction model

First, a simplified decompaction model is proposed to conduct the feasiblity of its implementation in the presented simulation tool. The four main assumptions, detailed hereafter, are partially justified with results from literature and confronted to the experimental work conducted during the transient state.

Assumptions:

(A) *Decompaction occurs only in the fully-saturated region.* The parameters impacted by the decompaction are only modified in the fully-saturated region. No over-compaction or decompaction are taken into account near the flow front (in the unsaturated region), just after the wetting phase. This assumption is mainly based on the experimental study conducted by Yenilmez et al. [72]. For four plies of random mat fibrous reinforcement, the stack thickness decreases significantly just after wetting (10%) whereas small stack thickness variations are measured for four plies of the glass woven fabric (1%) and the glass NCF (4%) they studied.

(B) *Decompaction is identical at macroscopic and microscopic scales.* Experimental measurements reported in the previous chapter at macroscopic (with confocal chromatic scanner) and mesoscopic (with XCT device) scales lead to the following conclusion: "The relative macroscopic decompaction (displacement of the vacuum bag, corresponding to the global stack deformation) is close to the relative mesoscopic decompaction (tows deformation)". This experimental observation, obtained for a fully-saturated state, is extended to the transient state. Thus, $\varepsilon_{ma} = \varepsilon_{mi} = \varepsilon$ in each macroscopic element: ε is driving the parameters modification at both scales.

(C) *Decompaction is linear with the flow front position.* At fully-saturated state, the decompaction measured experimentally is linear with X-position (see Figure I.28 in the first chapter). This experimental observation is extended to the transient state. For a given fully-saturated flow front position X_{front}, the decompaction is negligible at both macroscopic and microscopic scale ($\varepsilon(X_{front}) = 0$) whereas the maximum decompaction rate is located at the fluid inlet ($\varepsilon(0) = \varepsilon_{max}$).

(D) *Viscoelastic effects are not taken into account.* Kelly et al. [73] characterized the viscoelastic response of a mat fibrous material at saturated state under a uniaxial transverse compaction. The experiments conducted highlighted the complex time-dependent response of this fibrous reinforcement. Moreover, the relaxation at saturated state recorded with the confocal chromatic scanner (Figure I.24 in the first chapter) strengthen the existence of viscoelastic effects occurring during the decompaction phenomenon. As the initial goal of this study is to validate the ability of the proposed numerical methods to compute a dual-scale flow inside a deformable porous media, this viscoelastic response is not taken into account for a first approximation. Improvement of the dual-scale decompaction model will be proposed in section 4 and the mechanical behavior of tows will be studied deeper in the next chapter.

Under these assumptions, a simplified linear model is proposed for the decompaction level ε evolution:

$$\varepsilon(no) = \frac{-\varepsilon_{max}}{X_{front}} X(no) + \varepsilon_{max} \tag{II.18}$$

where no is the considered node of a macroscopic element and $X(no)$ its X-position.

Confrontation to transient experimental measurements:

Following the experimental setup and methods presented in section 9.3 of the previous chapter, the vacuum bag displacement is recorded during the transient impregnation of the quasi-UD NCF. The position of the flow front is estimated visually and measured with a graduated steel rule. Figure II.8b presents three Z-profiles recorded for three X-positions of the flow front (X_{front}). The comparison with the simplified model plotted for the same X_{front} positions (Figure II.8a) shows that the model overestimates the decompaction. This is mainly due to the assumption (D) which neglects the viscoelastic effects. This simplified model is an unfavourable case from a numerical standpoint, due to the problem stiffness. Thus, this first model will be used for the numerical validation of the upgraded simulation tool, and will be improved to present the numerical results (for instance, viscoelastic effects may be taken into account with a maximal decompaction depending on the flow front position: $\varepsilon_{max}(X_{front})$).

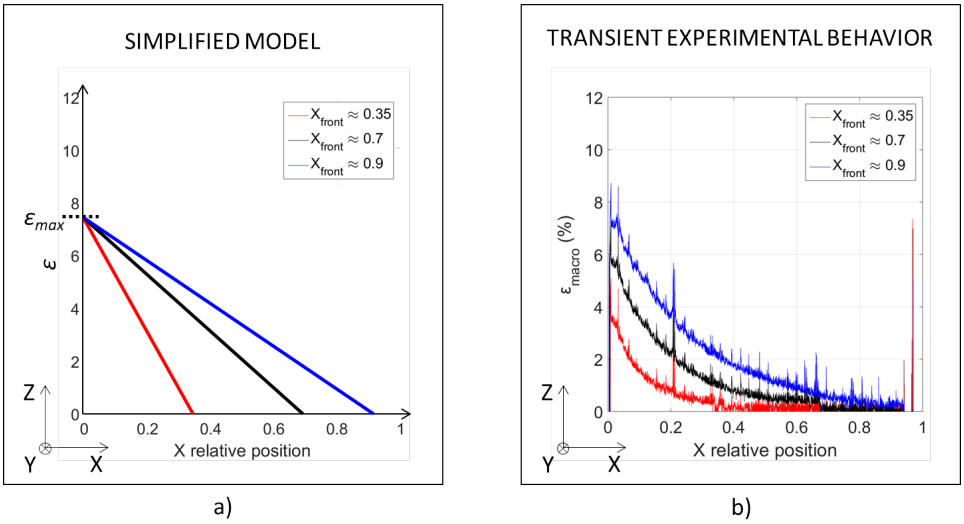

Figure II.8: Comparison between the simplified proposed model and the transient experimental behavior

3.2.3 Methodology to ensure the mass balance

The volume of the elements $V(e)$ in the fully-saturated region increases due to the decompaction phenomenon. Thus, the fluid contained in these elements is overestimated if the flow front is not updated: from a time step to another, the volume of fluid inside a saturated element numerically increases.

As presented in the literature review (section 2.3 and section 2.4), the overestimation of fluid is taken into account in the mass balance at the macroscopic scale only: Acheson et al. [12] wrote the mass balance in a non-rigid macroscopic control volume and Bayldon et al. [14] use a mass balance formulation equivalent to the one proposed by Correia et al. [62] for a single-scale flow. In the case of a dual-scale decompaction, the fluid inside the channels at macroscopic scale and the fluid inside the tows at microscopic scale are

both overestimated. Then, the right-hand side of Eq. II.7, which could be seen as a sink term, may be added in mass balance equations at both macroscopic and microscopic scales. Looking at the complexity of the microscopic filling algorithm proposed by Imbert (see details in [36]), adding sink terms at both scales becomes computationally intensive. Another methodology is then proposed and detailed hereafter.

In his numerical algorithm, Dang-Huu [65] uses a classical mass balance equation (Eq. II.2 for a single-scale flow, without sink term) and computes the fluid volume surplus induced by the decompaction phenomenon at each time step. The last nodes to be filled are then tracked and emptied until the mass balance is ensured. Thus, the fluid volume surplus can be just considered as a volume of fluid to be relocated. The flow front position is then updated before computing the pressure field. This approach is incorporated in the dual-scale filling algorithm proposed by Imbert.
At each time step, the fluid volume to be relocated Q_{decomp} due to both macroscopic and microscopic decompaction is computed (Figure II.9b):

$$\begin{aligned} Q^n_{decomp} = &\sum_e I_c^{n-1}(e)\left(V_c^n(e) - V_c^{n-1}(e)\right) \\ &+ \sum_e I_{t,1}^{n-1}(e)\left(V_{t,1}^n(e) - V_{t,1}^{n-1}(e)\right) \\ &+ \sum_e I_{t,2}^{n-1}(e)\left(V_{t,2}^n(e) - V_{t,2}^{n-1}(e)\right) \end{aligned} \tag{II.19}$$

where e is a macroscopic element, the superscripts $n-1$ and n represent respectively the previous and the actual time step, I_c, $I_{t,1}$ and $I_{t,2}$ are respectively the fluid fraction in channels, in tows in direction 1 and in tows in direction 2. V_c, $V_{t,1}$ and $V_{t,2}$ are respectively the volume of channels, of tows in direction 1 and of tows in direction 2 in an element e. These volumes are impacted by the tow and channel sizes evolution.
Dang-Huu numerical algorithm tracks the last nodes to be filled and empties them until the mass balance is ensured. Because the microscopic filling strategy developed by Imbert is complex, emptying channels and tows is not obvious. To overcome this issue, a strategy of fluid evacuation is proposed. The amount of fluid inside the overall part VOF is registered at each time step. For an actual time step n where $Q_{decomp} > 0$, the flow front position that best ensures mass balance (Figure II.9c) is one of the previously computed at a time step t and verifying:

$$\begin{cases} VOF^t & \leq & VOF^n - Q^n_{decomp} \\ VOF^{t+1} & > & VOF^n - Q^n_{decomp} \\ VOF^t + q^n_{exc} & = & VOF^n - Q^n_{decomp} \end{cases}$$

where q^n_{exc} corresponds to the excess volume of fluid removed from the elements. This volume is redistributed into emptied elements during the time step n. This strategy could be easily adapted to a 2D flow simulations, as the new flow front position corresponds to a flow front position computed at a previous time step. The excess volume of fluid q_{exc} should stay smaller than the fluid volume relocated in macroscopic elements Q_{decomp} to avoid numerical artefacts.
To avoid the fluid emptying at inlet elements, the decompaction occurs after a fully-saturation of at least 2 cm in the fluid flow direction. This condition does not depend on the mesh size (see section 3.3.3).

A deeper analysis of this methodology employed to ensure mass balance is detailed in section 3.3.4.

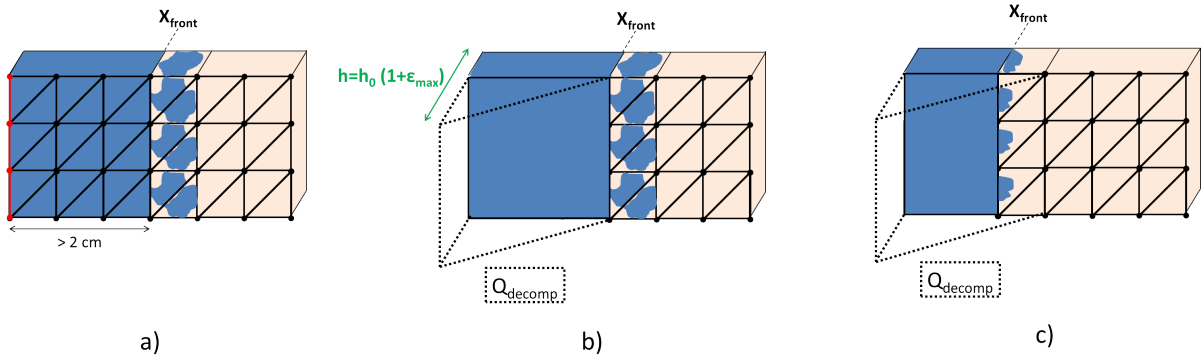

Figure II.9: Illustration of the methodology to ensure mass balance: a) time step n, before introducing the decompaction. b) time step n, after introducing decompaction, before the emptying phase. c) time step n, after the emptying phase. X_{front} is the fully saturated flow front position.

3.2.4 General algorithm and flow chart

The modification of the thickness and the microstructure induced by the dual-scale decompaction is introduced at the beginning of each time step of the flow chart depicted in Figure II.7. The steps of the upgraded algorithm are detailed hereafter and illustrated in Figure II.10.

❶ Computation of the decompaction: From the flow front position, the decompaction rate ε is computed in each macroscopic element, following the simplified linear model (Eq. II.18).
❷ Updating of the variables: The variables listed in Table II.2 are updated for each macroscopic element, depending on the value of ε. For instance, the new volume of each macroscopic element is defined as:

$$V^n(e) = V^{n-1}(e) \cdot (\varepsilon(e) + 1) \tag{II.20}$$

The permeability model developed in the previous chapter (see *Case 1* in section 9.3) is used to compute permeability evolutions ($\mathbf{K_c}$ and $\mathbf{K_t}$) with the decompaction level.
❸ Computation of the fluid to be relocated: The fluid volume Q_{decomp} has to be relocated from the flow front to the additional volume of fluid due the dual-scale decompaction in all the saturated region. This value is computed following Eq. II.19.
❹ Computation of the new flow front position: Following the methodology described in section 3.2.3, the new flow front position is computed to ensure mass balance. As for the computation of the sink term in the algorithm proposed by Imbert, no convergence loop is resorted to since the scheme is explicit. The error due to this explicit scheme is limited because the time step duration is kept small.

From the new flow front position, the algorithm proposed by Imbert (Figure II.7) is followed step by step, with the updated parameters for each macroscopic element that have been impacted by the dual-scale decompaction phenomenon.

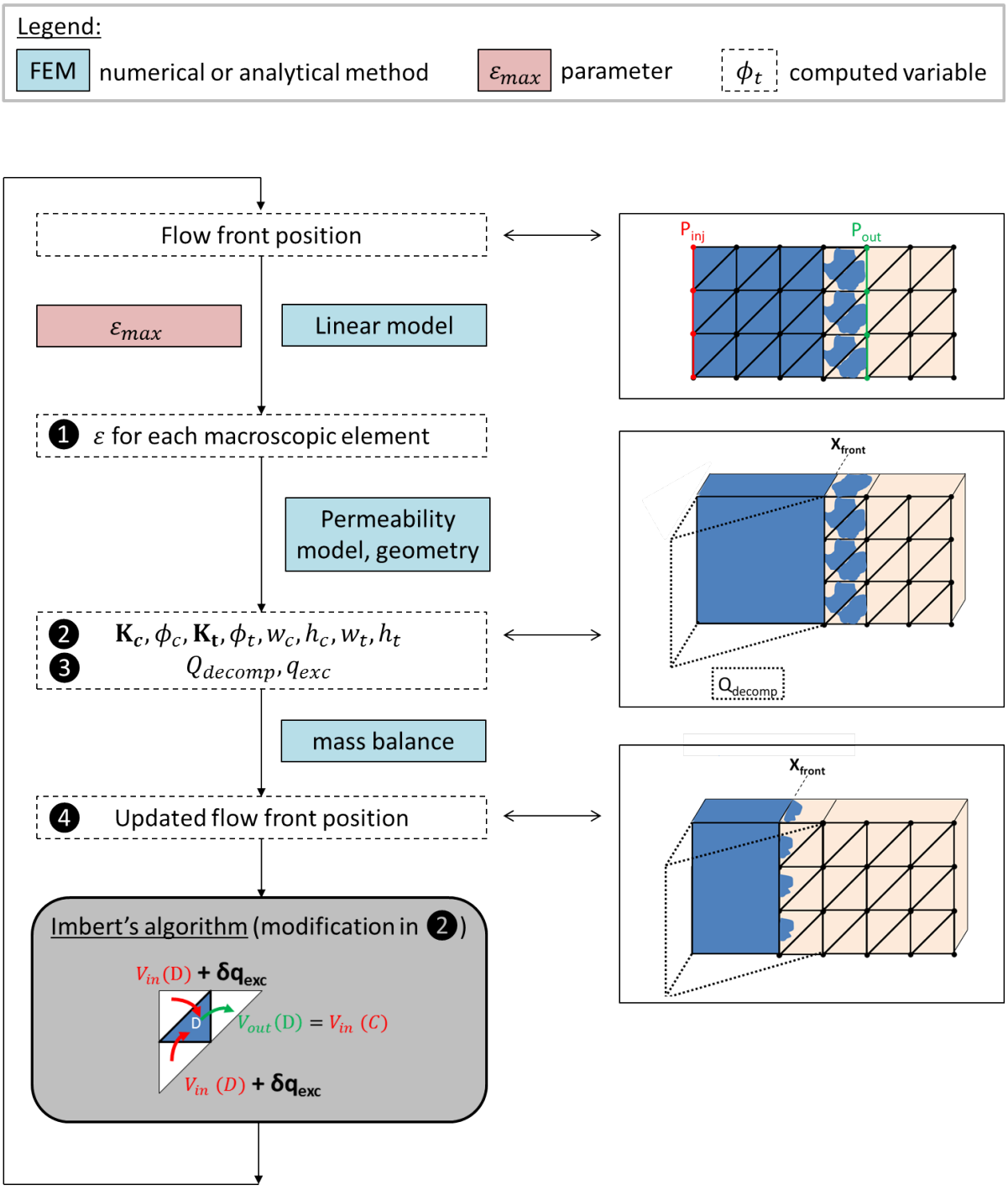

Figure II.10: Flow chart of the upgraded algorithm: integration of dual-scale decompaction in the algorithm proposed by Imbert

3.3 Numerical validation of the upgraded simulation tool

A numerical algorithm allowing the computation of a dual-scale flow inside a deformable porous material has been described in the previous sections. Several numerical validations are conducted on 1D filling simulations to ensure that mesh convergence and mass balance are robust. First, the length of the unsaturated region is computed using the complex microscopic filling strategy proposed by Imbert in order to validate the proposed simplified microscopic filling. Then, the influence of the mesh size on representative outputs is studied when the dual-scale decompaction is taken into account or not. Finally, the mass balance methodology presented in section 3.2.3 is analyzed for several mesh sizes.

3.3.1 Material parameters and constitutive laws

For the following numerical validations, the material parameters chosen correspond to the quasi-UD NCF studied experimentally in the first chapter. As the maximal decompaction level near the fluid inlet is around 7% for this fibrous reinforcement, $\varepsilon_{max} = 0.07$. Again, the microstructural evolution retained is the one measured experimentally on the quasi-UD NCF: when the thickness increases by 7%, tows swell only in the vertical direction, with a mesoscopic decompaction level of 7%. The microstructural reorganization follows then the *Case 1* presented in section 9.3 of the first chapter. Table II.3 summarizes the material parameters selected for the numerical validations and Figure II.11 underlines the influence of the microstructural evolution on both inter-tow channels $\mathbf{K_c}$ and tows $\mathbf{K_t}$ permeabilities.

Material parameters	
Dimensions of the cavity	18 cm × 18 cm × 10 mm
Initial tow width	3.27 mm
Initial tow thickness	0.9 mm
Initial inter-tow channel width	0.23 mm
Initial inter-tow channel thickness	0.1 mm
Behavior law	
Maximal decompaction level	0.07
Length of the saturated region before decompaction	2 cm
Microstructural evolution	*Case 1*
Processing parameters	
Fluid viscosity	0.3 Pa.s
Injection pressure	1 bar (abs.)

Table II.3: Material parameters used for the numerical validations

3.3.2 Length of the unsaturated region

Two simulations are launched with the parameters listed hereinbefore with two mesh sizes (the size of a macroscopic element equals to 5 or 10 mm) following the microscopic filling strategy detailed by Imbert in [36] (refer to "First filling solution" in section 3.1.3, superscript ^{insat} herefater). For these tests, the length of the unsaturated region is computed as the ratio between the length where the tows are fully saturated ($I_t > 0.95$) and the length where the inter-tow channels are fully saturated ($I_c > 0.95$). The simulation

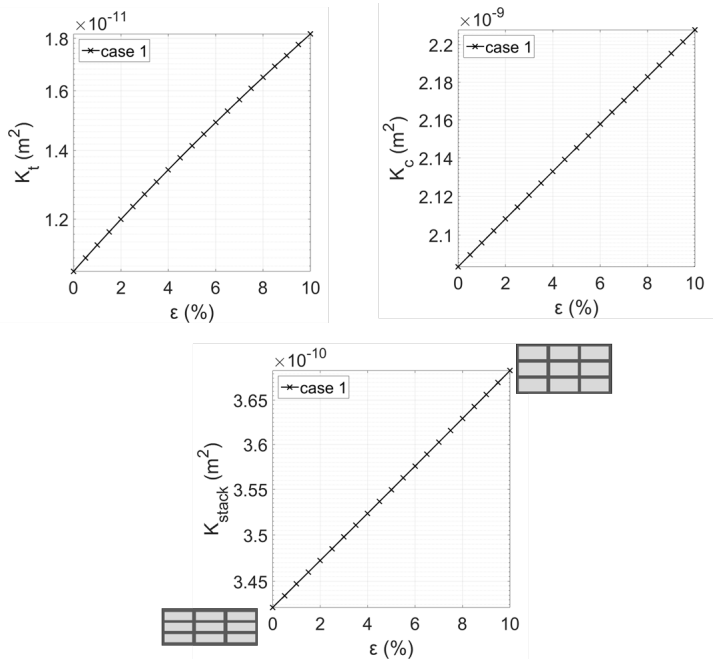

Figure II.11: Tows, inter-tow channels and stack permeability evolutions with the macroscopic decompaction ε, when the microstructural evolution follows the *Case 1*

tests are stopped when 16 cm of the inter-tow channels are fully saturated. Moreover, the same simulations tests are launched following a simplified microscopic filling strategy which neglects the sink effects (refer to "Second filling solution" in section 3.1.3, superscript ^{sat} hereafter). The time to fill 16 cm of the part t_{16} is computed in all simulations, and the ratio $R = \frac{t_{16}^{insat}}{t_{16}^{sat}}$ is calculated to evaluate the impact of the microscopic filling strategy on the computed filling time.
The Table II.4 summarizes the relevant outputs coming from these simulations. The unsaturated lengths are illustrated for both mesh size in Figure II.12.

Mesh size	**Unsaturated length**	**Total flow length**	t_{16}^{insat}	t_{16}^{sat}	R
5 mm	1.5 cm	16 cm	57.51 s	56.60 s	1.02
10 mm	1.5 cm	16 cm	57.64 s	58.61 s	0.98

Table II.4: Output values of unsaturated length and filling time for 2 microscopic filling strategies and two mesh sizes

The length of the unsaturated region is smaller than 1/5 of the length of the part, and the ratio R is really close to 1. Thus, the microscopic filling strategy can be simplified.

Refining the description of the unsaturated length during the dual-scale filling and the dual-scale decompaction of the quasi-UD NCF has no major impact on the filling times. Thus, a simplified microscopic filling algorithm is adopted for the following validations of the upgraded simulation tool.

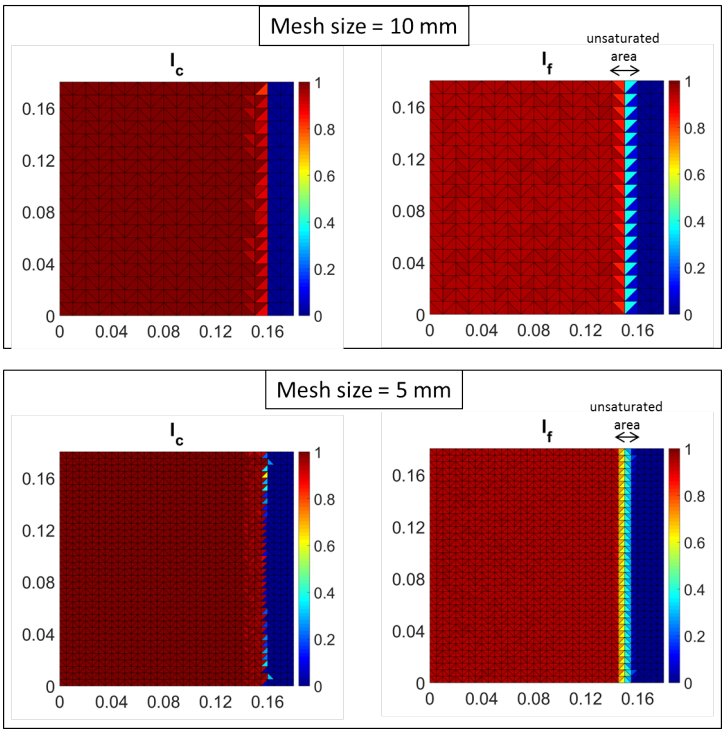

Figure II.12: Inter-tow channels and tows filling factor (I_c and I_t) for the two studied mesh sizes in Table II.4.

Table II.5: Influence of the mesh size on the time to fill 16 cm of the part

	No decompaction		*Decompaction*	
Mesh size	**Time to fill 16 cm**	**Error to the 3 mm mesh**	**Time to fill 16 cm**	**Error to the 3 mm mesh**
3 mm	60.83 s	-	61.89 s	-
5 mm	62.36 s	2.5%	63.46 s	2.5%
10 mm	64.33 s	5.7%	65.62 s	6.0%
15 mm	64.52 s	6.1%	65.92 s	6.5%

3.3.3 Mesh convergence

One of the claims of the developed technique is to be able to determine the influence of the dual-scale decompaction on the filling time. Thus, the influence of the mesh size on the filling time is analyzed. Four mesh sizes are selected (15, 10, 5 and 3 mm) and simulation tests are run: on one side, dual-scale decompaction is taken into account, and on the other side, no decompaction occurs during the filling. Table II.5 summarizes the time to fill 16 cm of the part for every mesh sizes in *decompaction* and *no decompaction* cases. For a *no decompaction* case, the analytical time to fill a single-scale porous material (the in-plane permeability K_{stack} corresponds to the one computed in Figure II.11) is 62.23 s, which is really close to the time computed for 3 and 5 mm mesh sizes. Figure II.13 illustrates the time to inject a same amount of fluid inside the part for all the mesh sizes (the reference time for normalization is the one computed for a 15 *mm* mesh size).
The integration of a dual-scale decompaction inside the existing simulation tool does

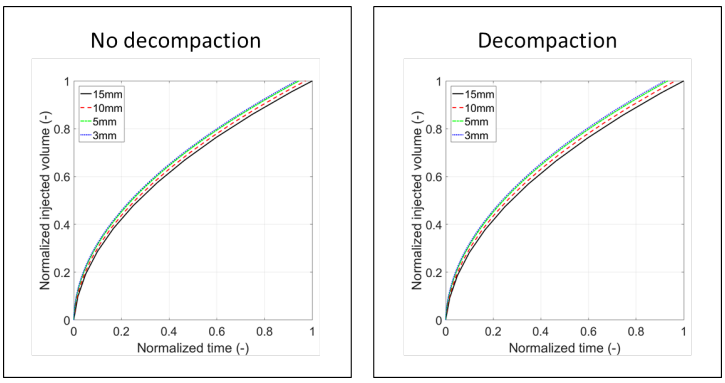

Figure II.13: Influence of the mesh size on the filling time estimation

not affect the mesh convergence: in both *no decompaction* or *decompaction* cases, the error to the 3 mm mesh are comparable. Moreover, the time to fill 16 cm of the part are comparable for mesh sizes of 3 and 5 mm; when the size of a macroscopic element exceed 10 mm, an error of at least 6% is recorded compared to the 3 mm mesh. For the following numerical studies, a mesh size of 5 mm is then selected.

Convergence of the result with respect to the mesh size is ensured for the simulation of a dual-scale flow with dual-scale decompaction. For the following numerical studies, a mesh size of 5 mm is selected to compute an accurate filling time of part.

3.3.4 Mass balance

The methology to ensure mass balance described in section 3.2.3 is submitted to several validations:

- the volume of injected fluid V_{inj}, depending on the inlet pressure field boundary condition, is equal to the volume of fluid inside the part V_{tot} at each time step ($V_{inj} = V_{tot}$),
- the volume of fluid to be relocated due to the decompaction phenomenon Q_{decomp} remains small compared to the volume of fluid inside the part at each time step ($Q_{decomp} \ll V_{tot}$),
- the excess volume of fluid removed from the macroscopic elements q_{exc} remains smaller than the volume of fluid to be relocated Q_{decomp} at each time step ($q_{exc} < Q_{decomp}$),

The evolution of the quantities of interest is plotted for each mesh size versus normalized injection time in Figure II.14. Figure II.14a confirms that for all mesh sizes, the mass balance is ensured, as $\frac{V_{tot}-V_{inj}}{V_{tot}} \approx 0$. Moreover, the volume of fluid to be relocated due to the decompaction stays really small compared to the overall volume of fluid present in the part (Figure II.14b), even for large mesh size (Q_{decomp} is directly linked to the macroscopic element size evolution, see Eq. II.19). Finally, the numerical excess volume of fluid that is redistributed into emptied elements remains 3 times smaller than the volume of fluid removed from macroscopic element to ensure mass balance (Figure II.14c).

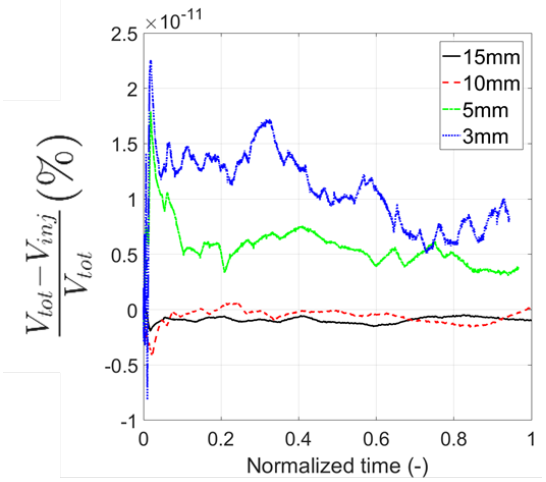

a)

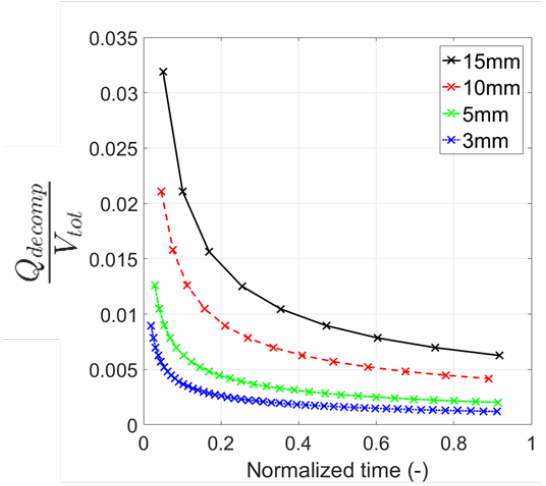

b)

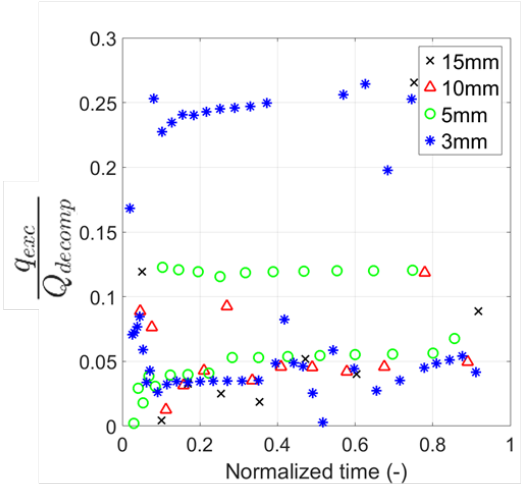

c)

Figure II.14: Validation of the methodology employed to ensure mass balance: a) Injected volume (V_{inj}) versus impregnated volume (V_{tot}) difference, b) Relocated volume (Q_{decomp}) versus impregnated volume (V_{tot}) ratio, c) Excess fluid volume (q_{exc}) versus relocated volume (Q_{decomp}) ratio

The strategy to ensure mass balance adopted is efficient: the volume of fluid in the part is corresponding to the volume of fluid injected. The fluid to be artificially relocated induced by the decompaction, and removed from the macroscopic element remains smaller than the volume of fluid inside the part: no major flow front mislocation is expected.

3.4 Conclusion about the developed numerical methods

In this section, an existing simulation tool proposed by Imbert et al. [71] dealing with the dual-scale flow inside a non-deformable porous material has been described in details. This algorithm has been upgraded in order to introduce the flow-induced dual-scale decompaction of the porous material during filling. A simplified decompaction model, based on the experimental results obtained in the first chapter, has been implemented. The numerical tests conducted validate the robustness of the proposed upgraded simulation tool: the fluid mass balance is ensured and the mesh size impact on the computed filling time is limited. It thus validates the ability of the proposed numerical methods to compute a dual-scale flow inside a porous material undergoing a deformation at both stack and tow scales.
The upgraded simulation tool can now be used to investigate the influence of the flow-induced dual-scale decompaction on the saturation and the filling time of a composite part.

4 Numerical results

The upgraded simulation tool allows the implementation of the decompaction phenomenon at both macroscopic and mesoscopic scales. Two main approaches can thus be considered. First, a study is proposed to investigate the impact of the microstructural reorganization on saturation and filling time of a composite part. For a same macroscopic decompaction, and thus a same fiber volume fraction inside the final part, several cases of microstructural modification may occur and impact the spatial organization of the reinforcement during its filling. Then, a second approach is considered: for a same microstructural reorganization, the macroscopic decompaction level can be negligible or reach 15% depending on the initial reinforcement stiffness. Thus, the influence of the initial textile design on the composite processing is studied.
Finally, the viscoelastic effects occuring during the transient filling are implemented in a novel simplified decompaction model. The impact of this viscoelastic effects on the filling time is investigated.

For all the following numerical investigations, a unidirectional flow is imposed in a long cavity (300*50 mm^2) where 10 plies of a quasi-UD NCF are laid down. The initial microstructural organization as well as the initial stack thickness are identical at dry state under vacuum (*Reference*) for all the studied cases.

4.1 Influence of the microstructural reorganization occurring during the filling

Three cases are explored in order to quantify the influence of microstructural reorganization on the filling process. For all the cases, the final fiber volume fraction is identical:

only the spatial distribution of intra-tow and inter-tow pores is modified. In this section, the studied cases are first detailed. Then, the unsaturated length and the filling time are computed using the simulation tool developed. Comparing these quantities of interest to those obtained in the *Reference* case allow the quantification of the microstructural reorganization influence on the filling process.

4.1.1 Studied cases and parameters

The studied cases correspond to those presented in the first chapter (section 9.3) for a maximal decompaction level of 7%, as measured experimentally. The variables impacted by this dual-scale decompaction are summarized in Table II.6 and the description of the studied cases is underlined hereafter:

- *Reference*. No decompaction is taken into account.
- *Case 1*. Decompaction is occurring at both macroscopic and mesoscopic scales: while the stack thickness increases by X%, the tows swell vertically by X%. This case corresponds best to the experimental behavior of the quasi-UD NCF studied in the first chapter.
- *Case 2*. Decompaction is occurring only at macroscopic scale, and no tow swelling is taken into account. This case may represent a quasi-UD NCF where the tows are tightly constrained by the stitch yarn.
- *Case 3*. Decompaction is occurring at both macroscopic and mesoscopic scales: while the stack thickness increases by X%, the tows swell vertically by X% and shrink horizontally by X/2%. This case may correspond to a quasi-UD NCF where a loose stitch would allow a vertical and an horizontal deformation of the tows.

	Ref.	**Case 1**	**Case 2**	**Case 3**
		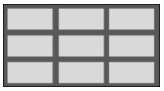	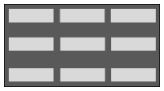	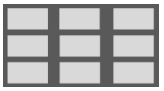
$h_{uc}(mm)$	1	1×1.07	1×1.07	1×1.07
$w_{uc}(mm)$	3.5	3.5	3.5	3.5
$h_t(mm)$	0.9	0.9×1.07	0.9	0.9×1.07
$w_t(mm)$	3.27	3.27	3.27	3.27×(-1.035)

Table II.6: Geometrical parameters impacted by the dual-scale decompaction: for the reference case, values are taken from [32]. For the other cases, values are chosen for a maximal thickness rise ($\bar{\varepsilon} = 7\%$, then $h_{uc} = 1.07mm$)

Figure II.15 illustrates the impact of the these microstructural reorganizations on the porosity content at each scale (ϕ_c and ϕ_t) and on the in-plane permeability values (K_t and K_c). The methodology employed to compute these evolutions is detailed in section 9.3 of the first chapter. As expected, the final macroscopic volume fraction (ϕ_{stack}) is identical for all cases (Figure II.15): only the microstructural reorganization due to the dual-scale decompaction differs.

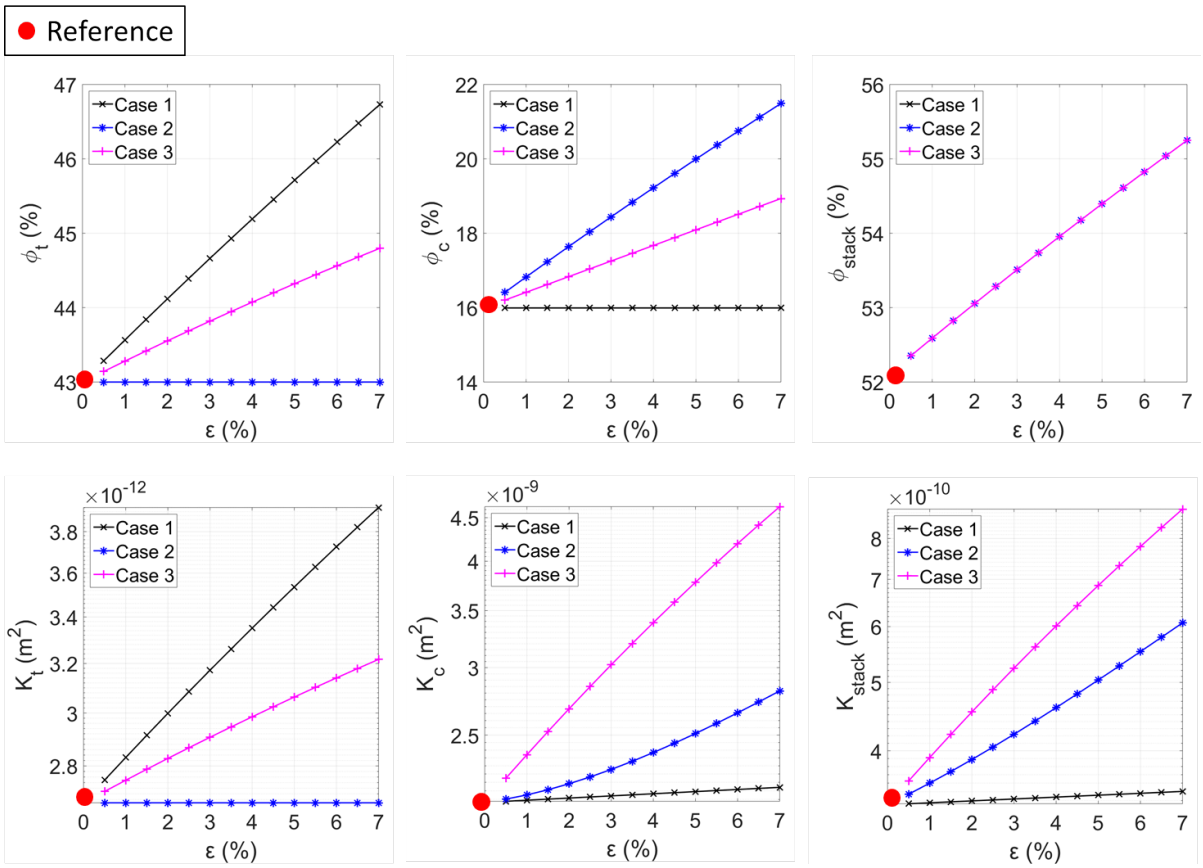

Figure II.15: Impact of the three microstructural reorganizations on porosity content and permeability at each scale. Resulting stack permeability and porosity content.

4.1.2 Impact on the unsaturated length

The unsaturated region correspond to the macroscopic elements where inter-tow channels are fully saturated ($I_c > 0.95$) while intra-tow pores are still being filled ($I_c < 0.95$). According to Imbert et al. [71], in the case where no decompaction occurs, the unsaturated length is impacted by both the ratio of in-plane permeabilities $\frac{K_c}{K_t}$ and the inter-tow channel ratio ϕ_c. Those parameters evolve from a simulation to another due to the microstructural parameters of the considered reinforcement (woven fabric or quasi-UD NCF). The results they obtained for a viscous pressure driven flow is summarized in Figure II.16. For a same ϕ_c and K_c, the decrease of tow permeability induces a longer unsaturated length: the fluid flow velocity is reduced in tows, which extend their filling time. When a same tow permeability (K_t) is considered, the increase of ϕ_c reduces the unsaturated length: the volume of tows being lower, the tow saturation is faster. A competition between permeability ratio and inter-tow channel content has been shown by Imbert.

In the case of a dual-scale decompaction, the evolution of the inter-tow and intra-tow permeabilities and the evolution of the inter-tow channel ratio is really low near the flow front: the maximal decompaction level 1 *cm* behind the flow front is less than 1%. Moreover, the evolution of those parameters is coupled for all the studied cases: when the ratio $\frac{K_c}{K_t}$ increases, the ratio ϕ_c decreases, as highlighted in Figure II.17. Thus, the impact of the decompaction phenomenon with different microstructural reorganizations on the length of the unsaturated length is negligible (Figure II.17) .

The dual-scale decompaction level occurring near the flow front is less than 1%. The impact of the microstructural reorganization due to the decompaction on the unsaturated length is thus negligible.

4.1.3 Impact on the filling time

The impact of the microstructural reorganization on the filling can be analyzed in two ways:

- The filling time and the length filled when a defined volume of fluid is injected can be computed,
- The filling time and the volume of fluid required to fill the entire part can also be analyzed.

Fixed injected volume of fluid. Figure II.18 illustrates the impact of the microstructural reorganization on the time required to inject a defined volume of fluid for all the studied cases. In comparison to the *Reference* case, injecting a same amount of fluid takes respectively 16%, 40% and 42% longer time in cases $1, 2$ and 3; moreover, the length filled is also impacted of at least 5% (*Case 1*). It should be noticed that the knowledge of the global porosity content (ϕ_{stack}) and inter-tow channel content (ϕ_c) evolutions (Figure II.15) are no sufficient to determine the time required to inject a defined volume of fluid. For instance, the inter-tow channels content is lower in *Case 3* than in *Case 2*, but the filling time required to inject a same volume of fluid is higher in *Case 3*.

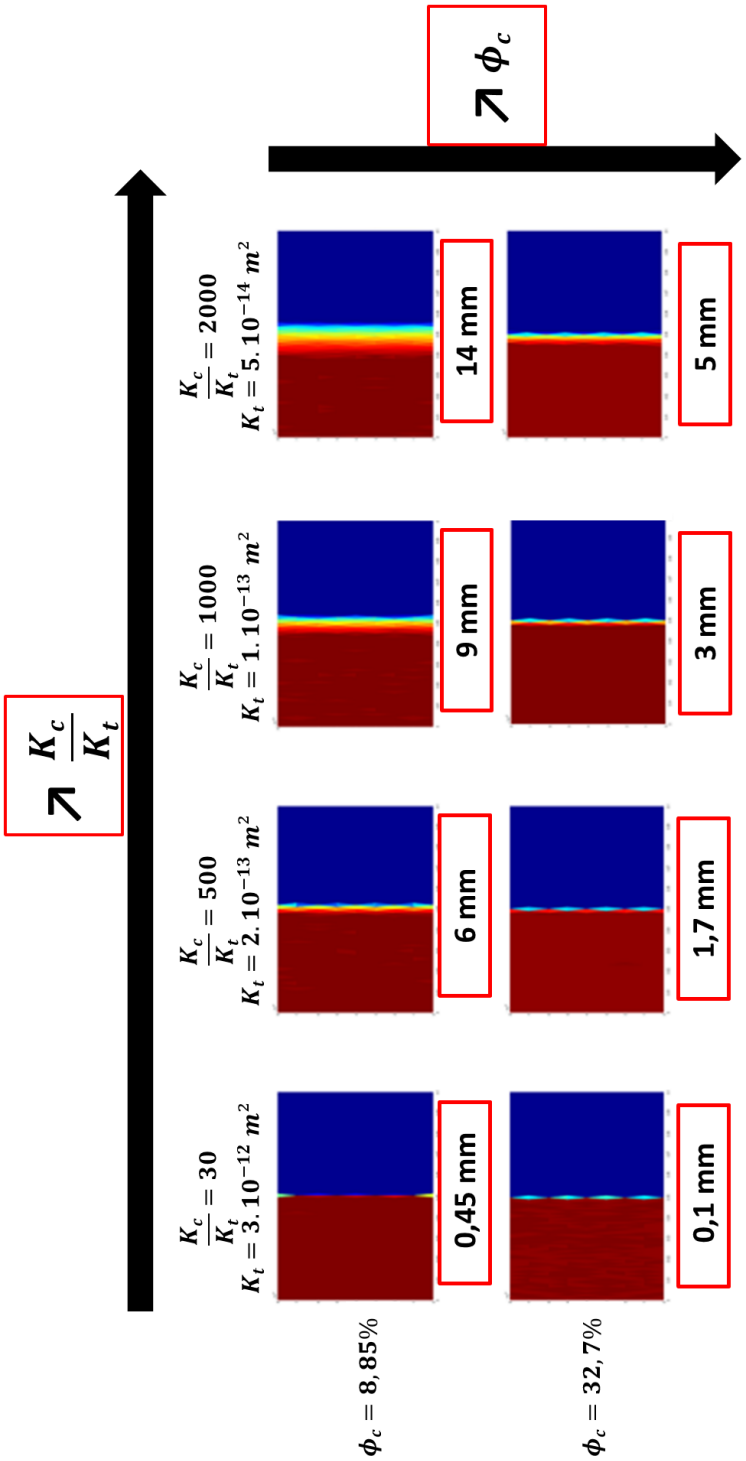

Figure II.16: For a defined K_c, impact of the ratio $\frac{K_c}{K_t}$ and the channel content on the unsaturated length [71]

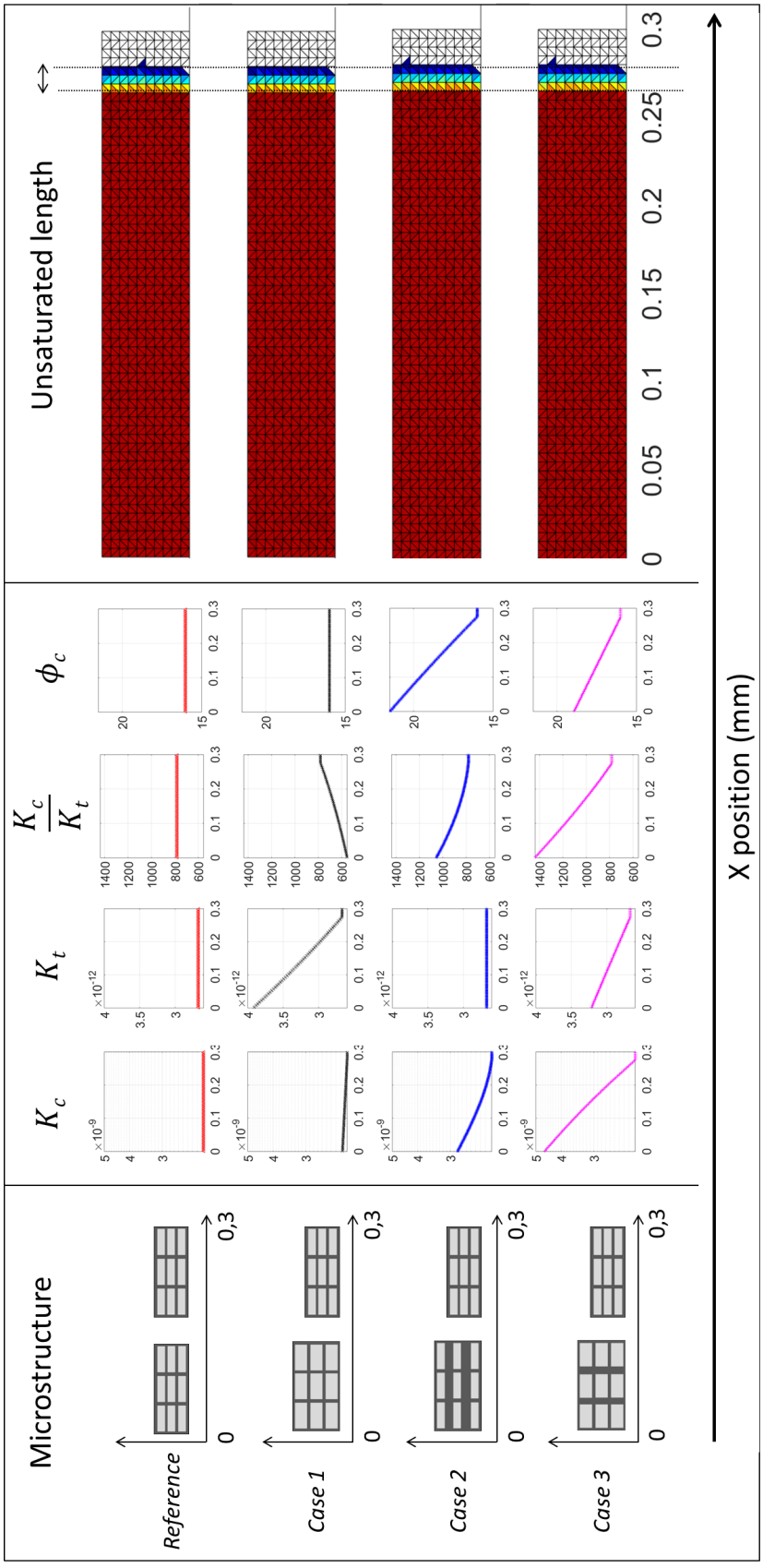

Figure II.17: Resulting unsaturated lengths and parameters evolutions versus X-position for the *Reference* and the three other cases

In these cases, the tow permeability evolution due to the decompaction has a significant impact on the filling time.
Finally, the measured experimental dual-scale decompaction (*Case 1*) has a significant impact on both the length filled and the filling time. The manufacturing of large parts using the infusion process (wind turbine blade for instance) requires the dual-scale decompaction to be taken into account to ensure the good quality of the final part.

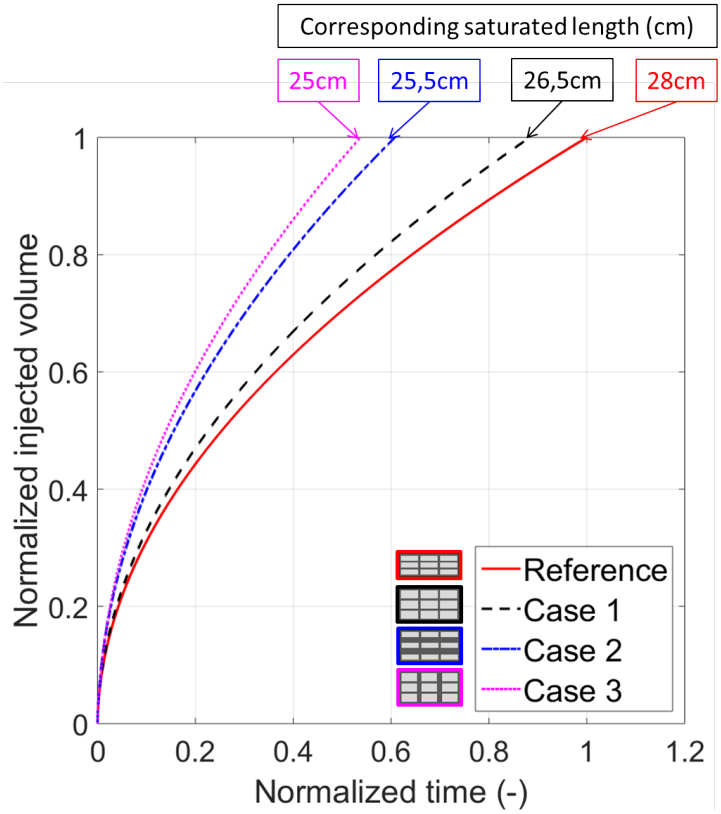

Figure II.18: Impact of the microstructural reorganization on the time required to inject a defined volume of fluid

Fixed filled length of the composite part. Table II.7 summarizes the time and the volume of fluid required to fill 28 *cm* of the composite part. The volume of fluid needed is identical in cases 1, 2 and 3 because the macroscopic decompaction behavior is the same. For a maximal linear decompaction of 7% (measured experimentally in the first chapter), the volume required to fill 28 *cm* is 7% higher than in a case where no decompaction occurs (*Reference*). However, the time required to fill this volume is very different for the considered microstructural reorganizations. In *Case 1*, the time to fill 28 *cm* is higher than in the *Reference* case: the increase of the overall stack permeability K_{stack} is not high enough to compensate the increase of the volume of fluid needed to fill 28 *cm* of the decompacted composite part. In cases 2 and 3, the time to fill 28 *cm* is really lower than in the no decompacted case: this is mainly due to the presence of large inter-tow channels, that increase significantly the in-plane stack permeability. It should be noticed that the measured experimental dual-scale decompaction (*Case 1*) has a significant impact on both the volume of fluid and the time required to fill a defined length of a composite part. Again, while considering large manufactured using

Table II.7: Time and volume of fluid required to fill 90% of the composite part: cases 1,2 and 3

	Reference	*Case 1*	*Case 2*	*Case 3*
Filling time (s)	188.5	191.8	130.8	115.1
Percentage to the Reference	-	+1.7 %	-30.6 %	-38.9 %
Volume of fluid ($10^{-5}m^3$)	7.09	7.61	7.57	7.56
Percentage to the Reference	-	+7.3 %	+6.8 %	+6.6 %

the infusion process, the dual-scale decompaction has to be taken into account to ensure the good quality of the final part.

For a given macroscopic decompaction level, and thus the same final fiber volume fraction, the induced microstructural reorganization has a significant impact on the time required to saturate a composite part.

4.1.4 Conclusion about the microstructural reorganization influence

In the literature review, it has been highlighted that authors simulating the infusion process (single or dual-scale flow) consider that the mechanical fibrous reinforcement evolution and thus the macroscopic in-plane permeability evolution are only due to the macroscopic fiber volume fraction evolution. The study presented hereinbefore reveals the significant impact of the microstructural reorganization on the filling time. For a given macroscopic decompaction level, and thus a same fiber volume fraction, the time required to fill a part can be lower or higher: the spatial distribution of intra-tow and inter-tow pores affects the filling process.
It should be reminded that the methodology used to determine the in-plane permeability of the stack for the different microstructural configurations (section 9.3 in the first chapter) is based on simplified geometrical considerations. Thus, new image-based numerical tools to compute the permeability tensor [11] may be of interest to improve the accuracy of the presented results.

4.2 Influence of the textile design

As highlighted in Martin's PhD thesis [32], a given tow can lead to really different macroscopic mechanical behaviors. Textile manufacturer can adjust the stiffness of a preform stack and the tow tightness behavior when integrated within different fabric architectures. Therefore, they would benefit from a tool that predicts the effects of various textile architectures on composite processability. In this section, the developed numerical tool is used within this context: the impact of different fabric designs on the unsaturated length and the filling time is analyzed.

4.2.1 Studied cases and parameters

The studied cases explored are three quasi-UD NCF made of a given tow constituent. The stitch yarn constrains these tows identically and thus, for all cases, the tow deformation is of the same amount. The vertical decompaction of each tow is considered linear with the flow front position, and the maximal decompaction level is fixed at 2%. However,

the maximal macroscopic decompaction is tailored and increases by 0.01%, 8% and 16% (respectively *Case 4*, *Case 5* and *Case 6*). This difference of decompaction behavior could be due to a weft-back ply (as for the quasi-UD NCF studied experimentally in the first chapter) that separates a ply from another one.
The parameters impacted by this dual-scale decompaction are summarized in Table II.8 and Figure II.19 highlights the impact of the these microstructural reorganizations on the porosity content at each scale (ϕ_c and ϕ_t) and on the in-plane permeability values (K_t and K_c). The methodology employed to compute these evolutions is detailed in section 9.3 of the first chapter.

	Ref.	**Case 4**	**Case 5**	**Case 6**
			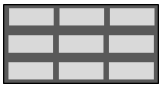	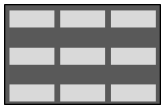
$h_{uc}(mm)$	1	1×1.0001	1×1.08	1×1.16
$w_{uc}(mm)$	3.5	3.5	3.5	3.5
$h_t(mm)$	0.9	0.9×1.02	0.9×1.02	0.9×1.02
$w_t(mm)$	3.27	3.27	3.27	3.27

Table II.8: Geometrical parameters impacted by the dual-scale decompaction: for the reference case, values are taken from [32]. For the other cases, the maximal tow thickness rise is identical for all the cases (2%).

4.2.2 Impact on the unsaturated length

For the same reasons than the ones previously developed in section 4.1.2, the unsaturated length is not impacted by the macroscopic decompaction occurring during the filling process (Figure II.20). Other physical phenomena, not taken into account in these simulations, could be added in order to refine the quantification of the decompaction impact on the unsaturated length:

- As reported by Imbert et al. [74], the storage of the fluid inside tows is not permanent in the saturated region. The fluid is released in the inter-tow channels with a rate depending on the reinforcement architecture and on fiber volume fraction. Thus, adding the model they developed could refine the quantification of the decompaction influence on the unsaturated length when chemo/thermal coupling is considered.

- Several experimental and numerical works [75], [76] studied the capillary effects during the infusion process. A capillary pressure could easily be added in the developed simulation tool.

The dual-scale decompaction level occurring near the flow front is less than 1%. The impact of the microstructural reorganization due to the decompaction on the unsaturated length is thus negligible.

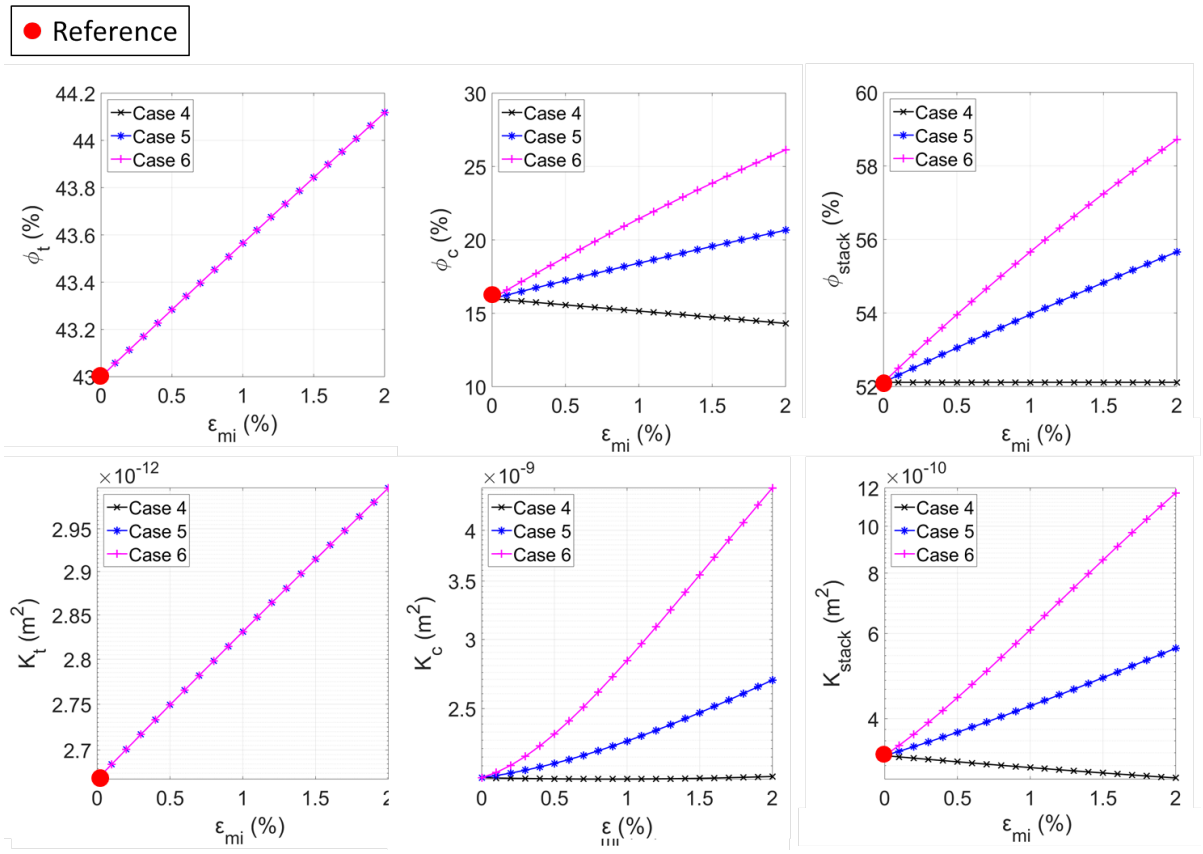

Figure II.19: Impact of the three textile designs on porosity content and permeability at each scale. Resulting stack permeability and porosity content.

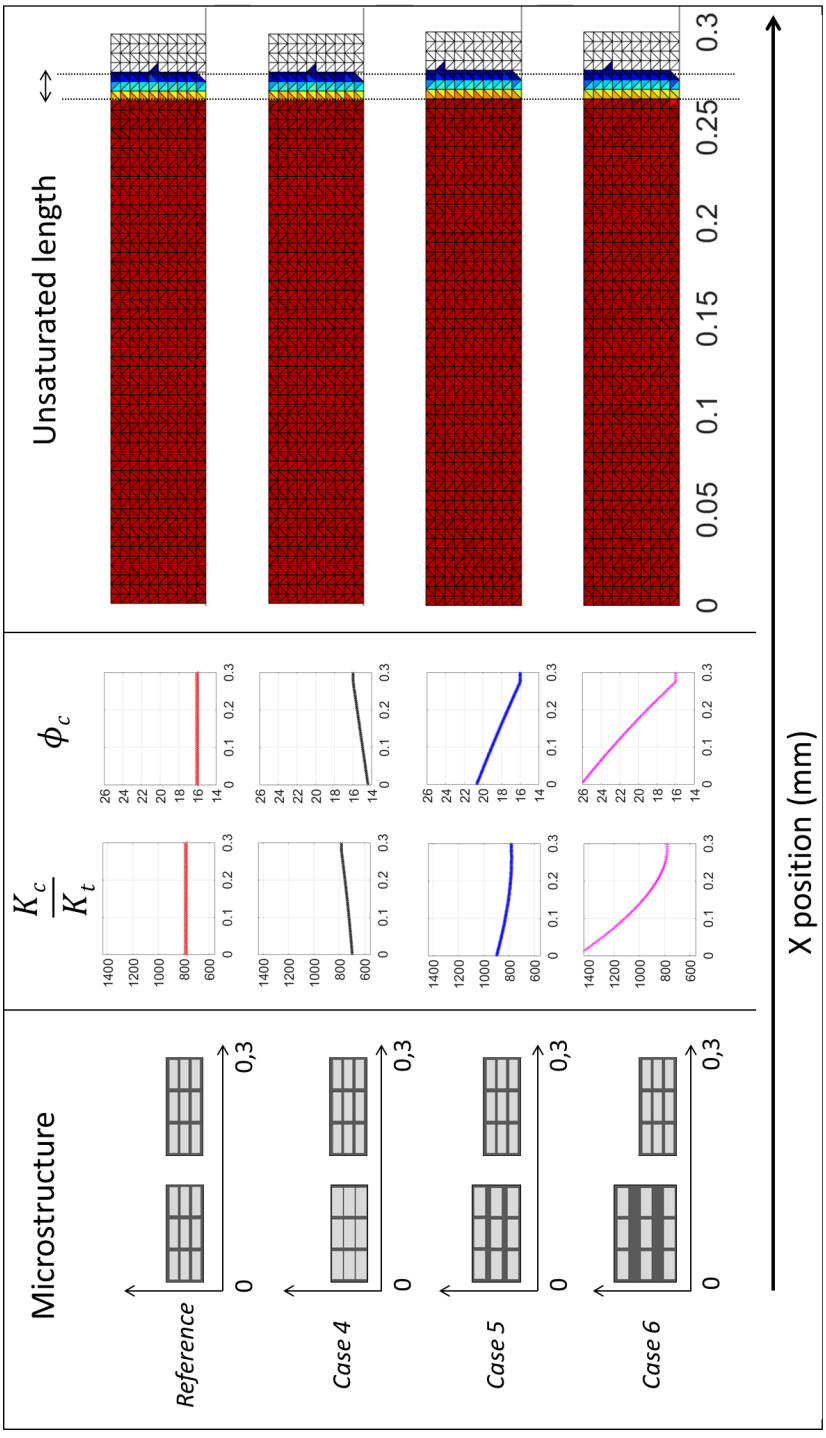

Figure II.20: Resulting unsaturated lengths and parameters evolutions versus X-position for the *Reference* and the three other cases

4.2.3 Impact on the filling time

As presented in the section 4.1.3, two types of analysis can be conducted to evaluate the impact of the textile design on the filling.

Fixed injected volume of fluid. The time required to inject a given volume of fluid is longer in *Case 4* than in the *Reference* case (10% in Figure II.21): the negligible rise of the inter-tow channel permeability, coupled with the significant decrease of ϕ_c and the significant tow permeability rise (Figure II.19) results in reducing the global fluid velocity. For the two other cases (*5* and *6*), the filling time is respectively 56% and 61% faster than the *Reference* case, due to the significant increase of both inter-tow channels permeability and content.

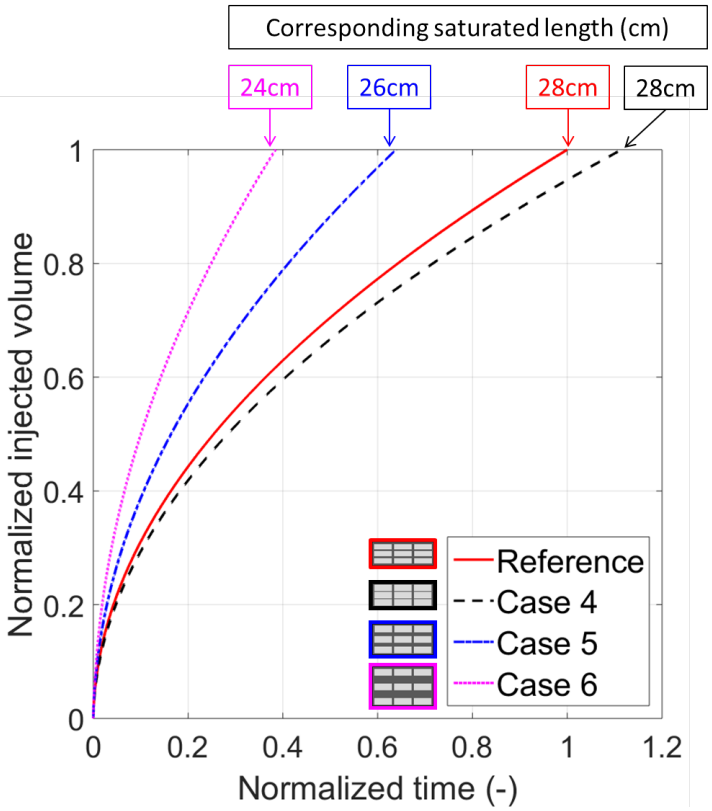

Figure II.21: Impact of the textile design on the time required to inject a defined volume of fluid

Fixed filled length of the composite part. As expected, the volume of fluid required to fill 28 *cm* of a quasi-UD NCF is directly linked to the maximal macroscopic decompaction rate (Figure II.22 and Table II.9). However, even if the volume of fluid required to fill the quasi-UD NCF *4* is really close to the one required for the *Reference* case (the maximal decompaction has been settled to 0.01%), the filling time is significantly higher (11% in Table II.9). Only a small tow deformation (settled to 2%) modifies significantly the filling time of a composite part.
The evolution of the volume of fluid required to fill 28 *cm* is linear with the maximal level of decompaction (due to the simplified linear decompaction model) whereas the filling time is not (Figure II.22). This non-linearity is due to the non-linear evolution of

Table II.9: Time and volume of fluid required to fill 90% of the composite part: cases 4,5 and 6

	Reference	*Case 4*	*Case 5*	*Case 6*
Filling time (s)	188.5	209.2	138.4	95.1
Percentage to the Reference	-	+11.0 %	-26.6 %	-49.5 %
Volume of fluid ($10^{-5}m^3$)	7.09	7.11	7.64	8.18
Percentage to the Reference	-	+0.3 %	+7.8 %	+15.4 %

the microstructural parameters (K_t, K_c...) during the decompaction phenomenon (for instance, the inter-tow channel permeability K_c in *Case 6*, see Figure II.19).

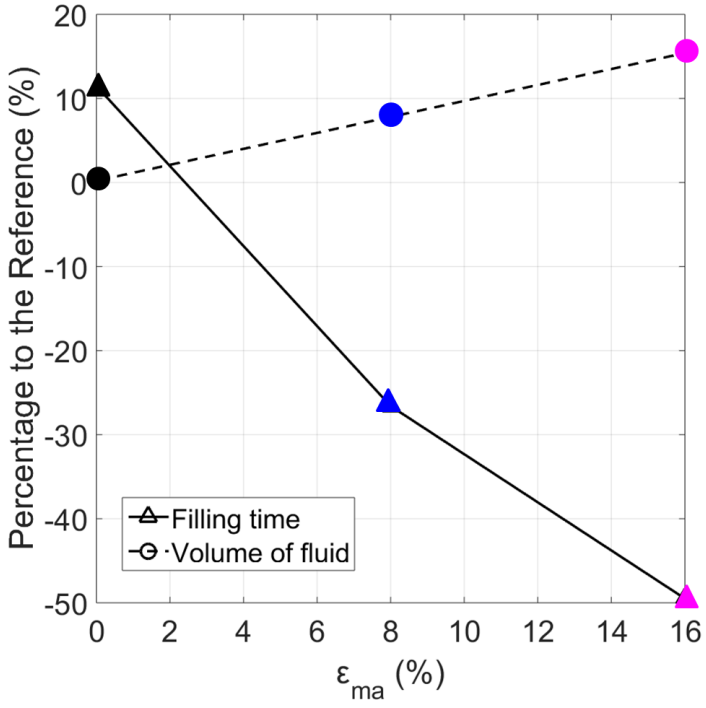

Figure II.22: Illustration of the time and volume required to fill 28 *cm* of a quasi-UD NCF depending on its maximal macroscopic decompaction level

The numerical tool combined to the former experimental findings allows to generate a decision making tool for fabric designers.

4.2.4 Conclusion about the textile design influence

Three new decompaction scenarios have been envisaged, corresponding to three quasi-NCF made of the same tow constituent: each tow behaves identically (decompaction of 2%) whereas the global macroscopic decompaction differs. Again, with the simulation tool used, the detected influence of these decompaction scenarios on the unsaturated length is negligible. Nonetheless, even if the volume of fluid required to fill a composite part is linked linearly to the maximal macroscopic decompaction level, the filling

time estimation is more complex and depends on the evolution of the microstructural parameters (K_c, Kt, ϕ_c, ϕ_t), directly linked to the fabric architecture and its behavior. The simplified analytical computation of the in-plane permeabilities (as highlighted in section 4.1.4) combined with the simplification of the quasi-UD NCF weft-back plies to inter-to channels should be improved to refine the results obtained. Nonetheless, these first approximations show the significant influence of the initial textile design on the composite processing and the capability of such numerical tool for textile designers.

4.3 Influence of the decompaction delay

The decompaction model implemented in the simulation tool is based on simplified assumptions that have been discussed in section 3.2.2. It appears that the viscoelastic effects, well known in the literature and characterized experimentally during the transient filling, seem of interest as they reduce the maximal decompaction level during the filling stage. In this section, the viscoelastic deformation is taken into account and implemented in the simulation tool. The considered model, where the decompaction is delayed, and its assumptions are first detailed and the impact of this delayed decompaction model on the filling time is investigated.

4.3.1 Studied cases and parameters

For this study, the three microstructural reorganizations investigated are the one proposed in section 4.1.1. For these cases, two decompaction models are studied. Both are linear with the flow front position but the second one takes into account a decompaction delay due to viscoelastic effects.

Non-delayed linear decompaction model. As detailed in section 3.2.2, a linear decompaction model has been considered to compute the filling time. The main hypothesis, discussed in section 3.2.2, is that viscoelastic effects are neglected: the saturated state behavior measured experimentally in the first chapter is considered equivalent to the transient state behavior. Thus, as illustrated in Figure II.8, this model overestimates the decompaction.

Delayed linear decompaction model. As proposed in section 3.2.2, viscoelastic effects are taken into account by introducing a delay in the decompaction phenomenon: near the fluid inlet, the maximal decompaction is not reached instantaneously, but step by step. This model can be defined as:

$$\begin{cases} \varepsilon(no) = \frac{-\varepsilon_{delay}}{X_{front}} X(no) + \varepsilon_{delay} \\ \varepsilon_{delay} = \frac{X_{front}}{L} \varepsilon_{max} \end{cases}$$

where no is the considered node of a macroscopic element, $X(no)$ its X-position and L the length of the considered part (in X direction).

The resulting macroscopic decompaction behaviors for both models with the X-position are plotted in Figure II.23. The impact of the delayed decompaction on the unsaturated length is out-of-interest here: no impact has been detected with the non-delayed linear model, and the decompaction in the unsaturated region is even smaller when a delayed decompaction is taken into account.

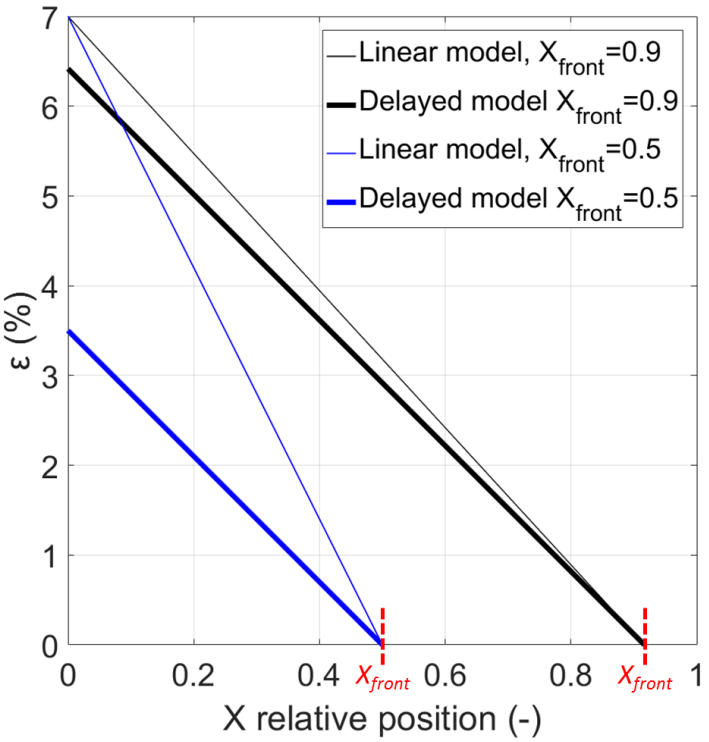

Figure II.23: Resulting macroscopic decompaction VS X-position (fluid flow direction) depending on the decompaction model implemented

4.3.2 Impact on the filling time

As illustrated in Figure II.24, taking into account a decompaction delay tends to slightly shift the filling time closer to the one computed for the *Reference* case: when integrated over the X-position, the decompaction impact is lower than in the non-delayed linear decompaction case (see the decompaction profile in Figure II.23). Nonetheless, the impact of the viscoelastic effects to fill 28 cm of the part is not identical for all the microstructural reorganizations (Table II.10): when compared to the non-delayed linear case, the *Case 3* is more impacted (24.3%) than the *Case 1* (3.2%).
The final macroscopic decompaction is quasi-identical when 28 cm of the part is filled: thus, the volume of fluid required are closer in both cases for both decompaction models.

Table II.10: Time and volume of fluid required to fill 90% of the composite part: non-delayed and delayed models

	Reference	*Case 1*	*Case 2*	*Case 3*
"Delayed" filling time (s)	188.5	198.02	157.63	143.11
Percentage to the Reference	-	+5.0 %	-16.4 %	-24.1 %
Comparison to the non-delayed model	-	+3.2 %	+20.5 %	+24.3 %
"Delayed" volume of fluid ($10^{-5}m^3$)	7.09	7.56	7.56	7.54 %
Percentage to the Reference	-	+6.6 %	+6.6 %	+6.3 %
Comparison to the non-delayed model	-	-0.6 %	-0.1 %	-0.3 %

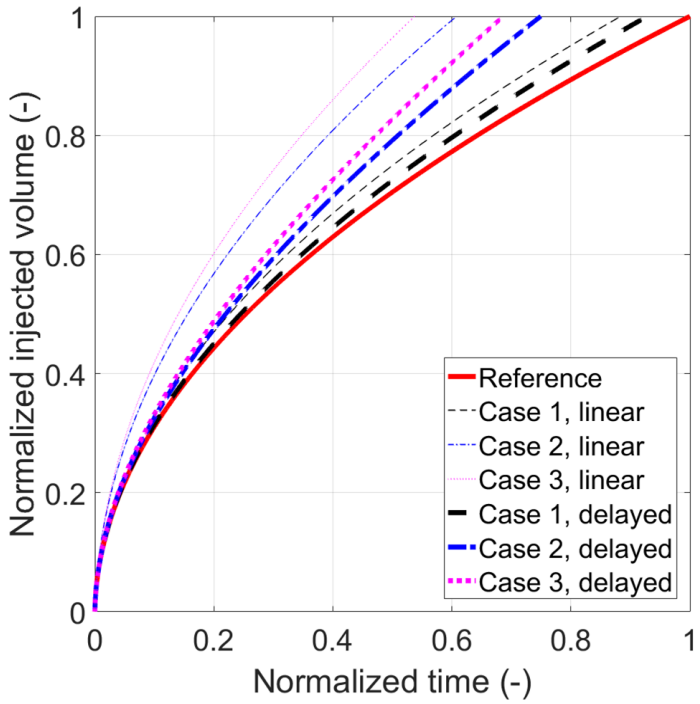

Figure II.24: Impact of the viscoelastic effects on the time required to inject a defined volume of fluid

4.3.3 Conclusion about the viscoelastic effects influence

Taking into account a delayed decompaction does not change the trends obtained with a non-delayed decompaction: the impact of the microstructural reorganization on the filling time remains significant. Nonetheless, this study highlights the necessity of an accurate decompaction model to quantify the filling times.

5 Conclusion

As discussed in the first chapter, the infusion process induces a dual-scale decompaction of the fibrous reinforcement during its filling: while the stack thickness increases, the tows swell. This dual-scale decompaction impacts the overall stack permeability because the induced microstructural reorganization modifies the spatial distribution of intra-tow and inter-tow pores. To evaluate the impact of these modifications on macroscopic process outputs such as filling time and saturation, simulations would provide a valuable help.

Therefore, a numerical tool has been developed to take into account a dual-scale decompaction during a dual-scale filling. This tool, based on the numerical developments proposed by Imbert et al., associates a refined microstructure (tow geometry and size) to each macroscopic element of the fibrous reinforcement. New features have been implemented to update the tows size and stack thickness evolutions that are due to the dual-scale decompaction occurring during the filling. The mesh convergence and the mass balance tests conducted ensure the robustness of the simulation tool.

This numerical tool has been thus employed to investigate the influence of the dual-scale decompaction on macroscopic composite processing output parameters. A unidirectional flow is imposed in a deformable quasi-UD NCF and several decompaction scenario are envisaged. The results show that for a given macroscopic fiber volume fraction, the filling time is significantly impacted by the spatial distribution of intra-tow and inter-tow pores. The simple knowledge of the macroscopic fiber volume fraction is thus not sufficient when the infusion of a dual-scale fibrous reinforcement is envisaged. Finer descriptors of both scales are necessary and influence the processing results. Therefore, this simulation tool, coupled with accurate experimental data, would help in decisions making for composite manufacturers and textile designers.

The results concerning the viscoelastic effects influence on the filling time estimation highlight the necessity of a more accurate dual-scale decompaction model. It might be improved by studying the dual-scale mechanical behavior of a fibrous reinforcement during the unloading stage, at saturated state. Moreover, providing a mechanical model would allow 2D flow simulations, as the tow and stack geometries would only depend on the fluid pressure, and not on the flow front position.

CHAPTER III

Mechanical behavior of tows through the infusion process

1 Introduction

During the infusion process, the stress applied to the fibrous reinforcements is modified due to the vacuum bag flexibility. The deformations induced by the filling stage have been measured in the first chapter at both tow and fabric scales: while the stack thickness increases, the tows swell vertically. The spatial distributions of the intra-tow and inter-tow pores and their geometrical evolution have been investigated without any mechanical consideration. However, an insight of the mechanical tow behavior during the infusion process would improve the understanding of the quasi-UD NCF behavior. Additionally, a model able to predict the mechanical behavior of tows would be useful to enhance the accuracy of the computed filling time of composite parts, as highlighted in the second chapter. Therefore, the objectives of the present chapter are the following:

- investigate experimentally the mechanical behavior of single tows through two stages of the infusion process: the loading stage at dry state and the unloading stage at saturated state,
- propose a 3D model able to predict both the transverse and the lateral tow deformation occurring during the loading stage,
- estimate the ability of the proposed 3D tow model to give first predictions of the quasi-UD NCF mechanical behavior.

To achieve the proposed aims, compressive tests at dry and saturated states are conducted on single tows under two types of boundary conditions. The two approaches adopted to apply a defined stress to fibrous samples and to monitor both lateral and transverse deformations are detailed in the first section. Then, according to literature, the Ogden-Hill model is selected and updated to take into account the large compressibility of the tows and the anisotropy of the tows in the fiber direction. Ogden-Hill model will be finally used with two distinct lateral boundary conditions: by fitting the model with the experimental data measured on laterally-free tows, it will be possible to capture the mechanical behavior of a laterally-constrained tow.

2 Experimental characterization of tows: compressive loading and unloading tests

The deformations induced on a quasi-UD NCF stack by the decompaction phenomenon occur only in the transverse direction: as highlighted in the first chapter (Figure I.51), no width evolution of tows has been measured during this unloading stage at saturated state. Nonetheless, no information have been measured concerning the width evolution of the overall stack. Therefore, in this section, the single ply fabric mechanical behavior is first investigated through the three main steps occurring during the infusion process:

- *Dry compaction:* the considered sample is loaded at dry state from 0 *bar* (abs.) to 1 *bar* (abs.) (i.e. 0.1 MPa),
- *Wetting phase:* the considered sample is impregnated with a model fluid,
- *Saturated decompaction:* the considered sample is unloaded at saturated state from 1 *bar* (abs.) to 0 *bar* (abs.).

Many authors characterized finely the wetting phase [5],[6],[75], where boundary conditions concerning the filling are defined with accuracy. The wetting phase will thus remain out of the scope of the present study.

In this first approach (*infusion approach*), the sample is laid down in a cavity closed with a flexible vacuum bag: the stress is applied onto the sample using a vacuum pump and the sample thickness and width are monitored. After analyzing the single ply fabric behavior, the same approach is used to monitor the thickness and width evolutions of single tow samples.
A second approach is then proposed to impose a unidirectional transverse compressive load on the single tow samples (*unidirectional approach*), following again the three main steps of the infusion process. The tow is laid down in a rigid cavity whose thickness is variable and imposed by the user; the unidirectional force imposed to the sample due to the cavity thickness evolution and the sample width are measured.

In this section, a literature overview of the existing experimental characterizations at tow scale is first presented. Then, the setup and methodology developed are detailed for the *infusion approach*, and the single ply fabric as well as single tow width and thickness evolutions are analyzed for the three infusion process steps. Finally, to impose a unidirectional load to the single tow, a new setup is presented and the single tow width and thickness evolutions are again analyzed for the three infusion process steps.

2.1 Literature overview [1]

The microstructural evolution of tows for different loading conditions, in dry or saturated states, has been investigated by many authors. In these studies, the geometrical characterization of tows within a fabric is mainly studied, whereas few authors investigate the geometrical characetrization of single tows. Table III.1 summarizes some of the studies of the available literature and details are given hereafter.

2.1.1 Tows in a fabric

Experimental studies have quantified the in-plane displacement and deformations of tows inside fabrics of several architectures such as woven glass fabric [77], [78], [92], bidirectional glass fabrics [20], biaxial stitched glass fabrics [79], 3D warp-interlaced glass fabrics [80] and 3D interlocks [86]-[89]. Although providing useful information regarding the evolving geometry of the architecture, these measurements cannot be directly related to intrinsic properties of the tow, since boundary conditions of a single tow inside textiles are not fully prescribed. Also most of the analyses are realized at a single given level of macroscopic compaction and very few studies present results over a wide range of compaction. An interesting study by [86] follows the tow's elongation within a 3D interlock during forming using resistive lineal sensors.

2.1.2 Single tows

Microstructural evolutions of an isolated compacted or elongated tow have rarely been observed. In these studies, after the measurement of the initial geometry, the geometrical dimensions are directly calculated from through thickness and in-plane transverse displacements measured during a free-edge-transverse compression applied to an isolated single tow, [93]-[96].

2.1.3 Conclusion

The conducted literature overview highlights that few work exists when the single tow mechanical behavior is considered. Additionally, to the author knowledge, no experimental measurements have been conducted during the unloading phase at saturated state, expected recently by Kabachi et al. [97] at the macroscopic scale (fabric stack). Therefore, the experimental methodologies and setups presented in this chapter have been designed to allow the measurement of single tow width and thickness evolutions during the infusion process stages: dry loading phase and saturated unloading phase. Two approaches, differing by their boundary conditions, are detailed and studied hereafter.

Table III.1: Features of the tow scale experimental measurements: tows within fabric and single tows

Architecture	Fibre & fluid	Loading	Measurement techniques	Measurements	Ref.
Plain weave	Glass and Unsat. polyester	Transverse compression	Optical & scanning	Tow cross-section, waviness	[77]
NCF & plain weave	Glass and vinylester	Transverse compression	Optical microscope	Tow aspect ratio, waviness	[78]
NCF & woven	Glass & water/silicon	Transverse compression	Optical microscope	Tow spreading	[20]
NCF	Glass	Transverse compression	X-ray CT	Tow cross-section	[79]
3D textiles	Glass & epoxy	Transverse compression	Optical and X-ray CT	Tow cross-section, spacing	[80]
Twill weave	Glass	In-plane shear	X-ray CT	Tow cross-section, local fiber volume fraction	[81]
Plain weave	Glass/carbon & water/glycerine & vinylester	Transverse compression static/dynamic	Stereo microscope	Tow aspect ratio, waviness	[82]
Unbalanced textile	Glass	Transverse compression	Optical camera	Tow's Poisson's ratio	[83]
Twill weave	Carbon	In-plane shear	X-ray CT	Tow-cross section, spacing	[84]
Woven & NCF	Glass, Glass/PP and Carbon	In-plane shear and tensile	Digital Image Correlation	Tow displacements, rotations	[85]
3D warp interlocks	Commingled glass/PP	3D forming	Resistive sensor, 3 optical cameras	Tow longitudinal elongations	[86]
3D woven interlock	Carbon	Transverse compression	X-ray CT	Tow crimp angle	[87]
3D orthogonal non-crimp woven	Glass	Transverse compression	X-ray CT	Tow cross-section and elongation	[88]
3D interlocks	Carbon	-	X-ray CT	Fiber orientation in tows	[89]
Ultra-thin chopped tapes	Carbon	-	X-ray CT	Fiber orientation in tapes	[90]
3D woven	Carbon	Transverse compression	Optical microscope	Tow cross sections	[91]
Woven	Glass	No loading	Office scanner	Yow width, orientation and spacing	[92]
Prototype roving	PVDF & olive oil	Transverse compression	X-ray CT	Contacts	[93]
Prototype roving	PA66	Transverse compression	Optical camerao	Width, thickness	[94]
Tow	12k carbon	Transverse compression	Digital Image Correlation	Width, thickness	[95]
Yarns	Acrylic	Transverse compression	CCD cameras	Width, thickness	[96]

2.2 Under infusion process boundary conditions

In this *infusion approach*, the mechanical load is applied on the fibrous reinforcement (dry and then saturated) by imposing a vacuum level inside the flexible cavity. After detailing the materials and equipments required, the setup and the experimental methodology implemented to measure the sample width and thickness for a defined stress level are presented. Post-treatment methods are detailed for both single ply fabric and single tow samples and allow the analysis of the experimental mechanical behavior for each kind of sample.

2.2.1 Materials and equipments

The materials (fibrous reinforcement, model fluid and vacuum bag) and equipments (chromatic confocal scanner and vacuum pump) used for this experimental approach are described hereafter.

Textile. The fibrous reinforcement selected for this study is the one described in the first chapter (section 2.2.1). This quasi-UD NCF is made of two layers: one layer of UD glass tows (4800 tex) and one weft backing glass layer oriented at $\pm$ 80° (68 tex). Both layers are stitched (warp-knitting) with a very thin polyester thread, symmetrical and spaced of 5 mm, that may constrain locally the tows in the width direction.
When a single tow sample is considered, the UD glass tow is extracted from the fabric with tweezers.
Model fluid. Technical Glycerol from VWR is used in dilution with 5% of distilled water to obtain a viscosity of 0.3 $Pa.s$ at 25° C.
Vacuum bag. Cellophane, more flexible than the vacuum bag selected for the infusions conducted in the first chapter (section 2.2.1), is used to close the cavity in order to enhance the width detection of tows and fabrics at saturated state.

Chromatic confocal scanner (CCS). The chromatic confocal scanner (CCS) described in the section 3.3 of the first chapter is used to monitor the width and the thickness of the considered sample during the mechanical test. The pen (sensor) selected for this study (*CL4 CCS-Prima*), with 7 μm lateral resolution, presents a suitable compromise between a wide range of thickness acquisition (4000 μm) and a sufficient thickness accuracy (0.2 μm).
Vacuum pump. To apply several stress levels on the sample, vacuum is used as driving force. The vacuum pump (the one described in the section 3.2.4 of the first chapter) is a *PC 3001 Vario Pro* from Vacuubrand GmbH allowing an automatic control of the vacuum level thanks to the diaphragm pump motor speed adjustment.

2.2.2 Setup and experimental protocol

Setup. The sample, which is composed of several single tows with free edges (Figure III.1a) or of tows within a fabric (Figure III.1b), is laid down on a PVC plate. To avoid edge effects, a breather felt (presented in the first chapter, section 2.3) is laid down near the fluid inlet and near the vacuum vent. The cavity is closed with a cellophane film and tackytape; the sealing is reinforced with a double vacuum circuit, as illustrated in Figure III.1.

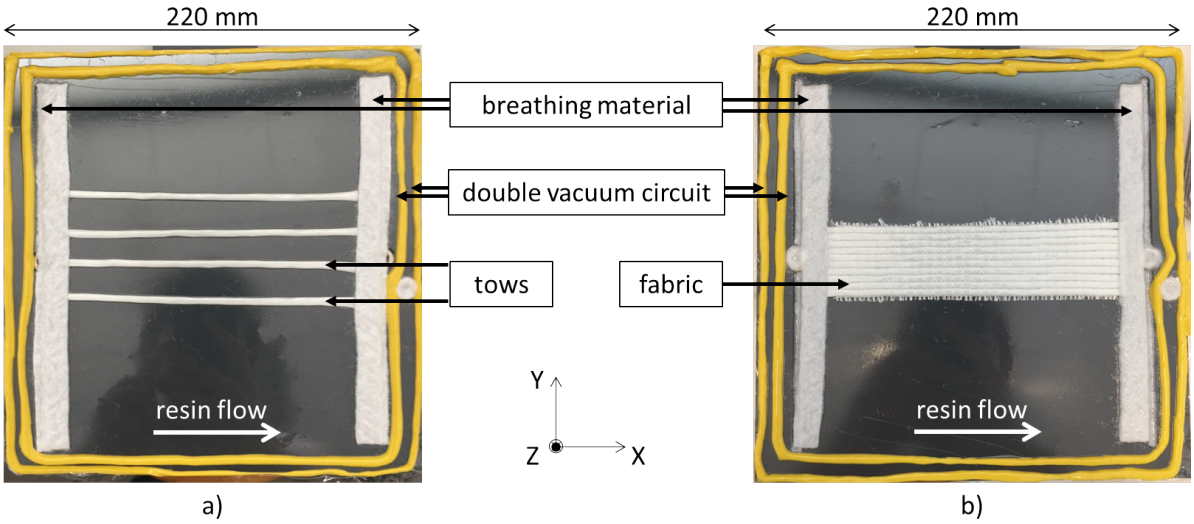

Figure III.1: Top view of the infusion setup: a) for single tows sample. b) for a single ply fabric sample.

This setup is settled on the moving support of the chromatic confocal scanner (CCS), as illustrated in Figure III.2, and a sample profile (YZ) is recorded every 10 mm (in the X-direction), for each stress level. The sample is 140 mm long (in the X-direction). 14 profiles are acquired for every stress level. For each YZ profile, a Z-position is recorded every 5 μm in the Y-direction.

Experimental protocol. The experimental protocol is summarized in Figure III.3. During the dry compaction phase, the stress applied to the fibrous sample σ is considered homogeneous along the X-position (Figure III.4a), as 10 min are waited for the stabilization of the vacuum level. During the saturated decompaction phase, σ follows the Terzaghi's law. Thus, each X-position corresponds to a specific stress σ (Figure III.4b), as the fluid pressure P evolves from 0.1 MPa near the fluid inlet (X=0) to the vacuum pressure at the vacuum vent location (X=1). Appendix A presents a detailed method to compute the fluid pressure P with X-position when a deformable media with a varying permeability is considered.

This experimental protocol is first followed for single ply fabric sample, and then for single tow samples. The next subsections present the post-treatment and the results for both kind of samples.

2.2.3 Single ply fabric: post-treatment

In this section, the post-treatment method applied to extract the thickness and the width of the single ply fabric sample for each stress level is detailed.

Width and thickness computation. For each stress level, the final CCS file obtained is a matrix $CCS(i,j,k)$ where $i \in [1,N]$, $j \in [1,m]$, and $k \in [1,n]$, as illustrated in Figure III.2. For each X-position and for each stress level, the fabric raw profile is extracted to compute its width and thickness.
As shown in Figure III.5, the thickness of the sample h is defined as $h = Z_{fabric} - Z_{PVC}$

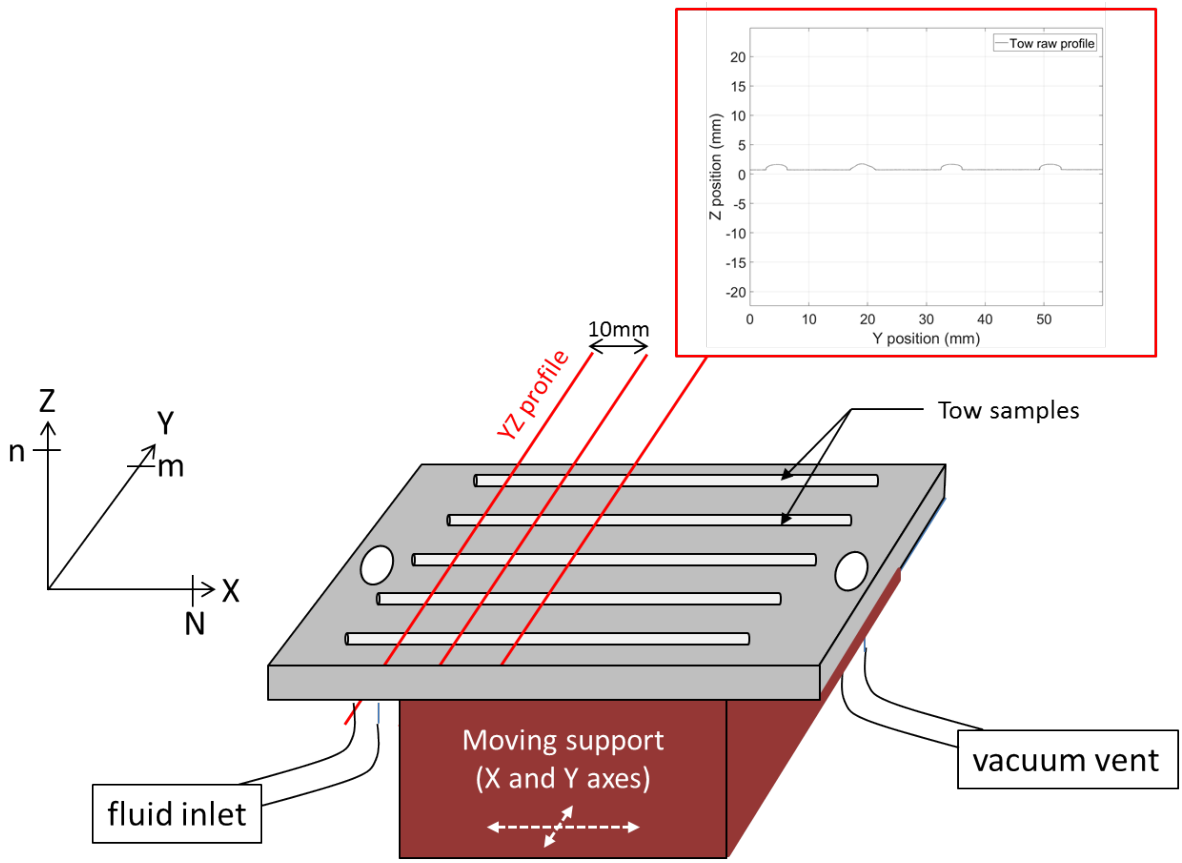

Figure III.2: Schematic view of the overall setup placed on the CCS moving support. Precisions about the recorded data are given (N, m, n).

Step	Description	Duration
Setup preparation	The fibrous sample and the breather felt are placed on the PVC plate. The mold is tightly sealed with tackytape and cellophane film.	around 20 min
Setup positioning	The infusion setup is taped on the moving support of the chromatic confocal scanner.	around 1 min
DRY COMPACTION		
Set of the vacuum level	The vacuum level is set inside the cavity step by step from 900mbar (abs.) to 60mbar (abs.). The vacuum levels selected for this study are [900, 800, 700, 600, 500, 400, 300, 200, 100, 60] mbar (abs.).	around 1 min for 1 vacuum level
Stabilization	For each vacuum level, 10 min of stabilization are necessary to allow fibrous relaxation before the recording of the YZ profiles.	10 min
Thickness and width record	For each vacuum level, 14 YZ profiles are recorded along the X-direction. 10 mm in X-direction separate each YZ profile. For each YZ profile, a Z-position is recorded every 5 µm in the Y-direction.	around 11 min
WETTING PHASE		
Infusion state under vacuum (transient)	At the end of the last vacuum level (60 mbar (abs.)) at dry state, the fluid inlet is opened. The fluid is then infusing the fibrous reinforcement, and the vacuum level at the vacuum vent location equals 60 mbar (abs.).	around 20 min
Saturated state under vacuum (quasi-static)	When the flow front appears in a defined position of the outlet pipe, the fibrous reinforcement is considered saturated. The inlet valve is kept open.	
SATURATED DECOMPACTION		
Thickness and width record	14 YZ profiles are recorded along the X-direction (identical X-positions as the one selected during the dry compaction phase). 10 mm in X-direction separate each YZ profile. For each YZ profile, a Z-position is recorded every 5 µm in the Y-direction.	around 11 min
Cleaning	The infusion setup is removed from the moving support of the chromatic confocal scanner. The mold is opened and the cavity so as the pipes are cleaned and dried.	around 10 min

Figure III.3: Step by step experimental protocol, following the three main stages of the infusion process

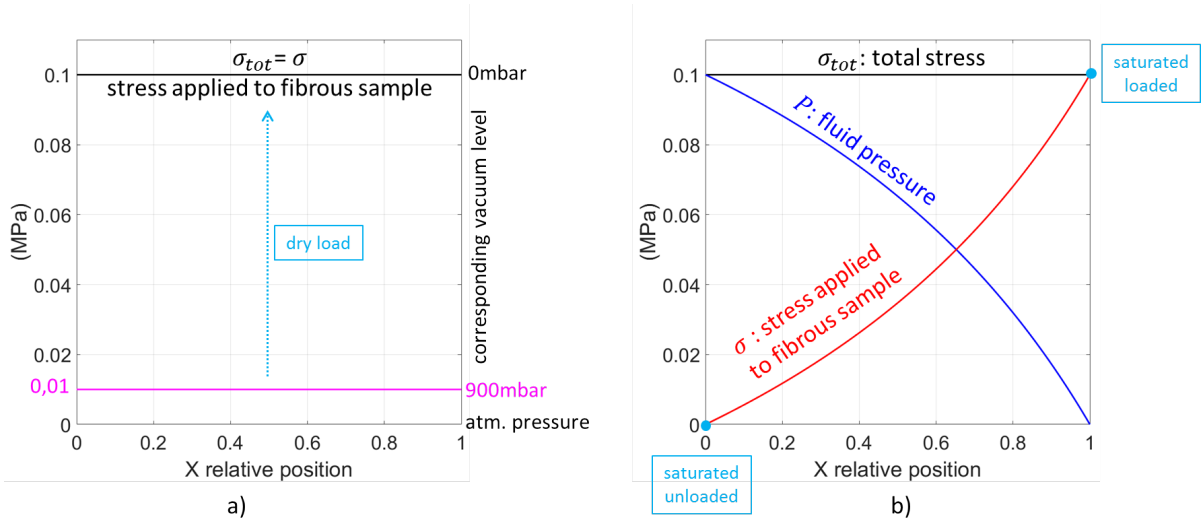

Figure III.4: Definition of the stress and corresponding vacuum level applied on the fibrous reinforcement along the X-position: a) during the dry loading phase. b) during the saturated unloading phase.

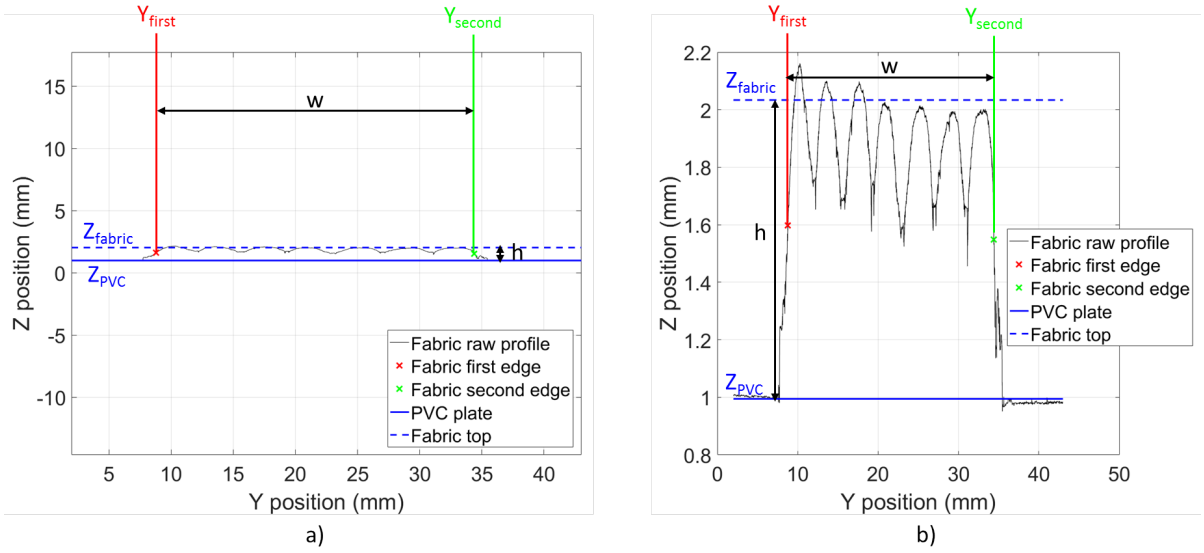

Figure III.5: Raw profile of the single ply fabric at a defined stress level and a defined X-position and its corresponding width and thickness definitions: a) full scale. b) close-up view.

where Z_{PVC} is the PVC plate location and Z_{fabric} is the fabric top location. The PVC plate location is defined as:

$$Z_{PVC} = \underset{j=1\rightarrow 100; m-100\rightarrow m}{mean}(Z(j)) \tag{III.1}$$

To define the fabric top location Z_{fabric}, several steps are required. First, the approximative position of each tow belonging to the single ply fabric are extracted and then, the maximal Z-position of each tow ($Z_{max} = \underset{j}{max}(Z(j))$) and its corresponding Y-position Y_{max} are computed. The tow top location Z_{tow} is thus defined as:

$$Z_{tow} = \underset{j=Y_{max}-10\rightarrow Y_{max}+10}{mean}(Z(j)) \tag{III.2}$$

Finally, the fabric top position Z_{fabric} is defined as (Figure III.5):

$$Z_{fabric} = \underset{N_{tow}}{mean}(Z_{tow}) \tag{III.3}$$

where N_{tow} corresponds to the number of tow composing the sample (here, N_{tow}=7). The fabric width w is defined as the difference between the fabric first Y_{first} and second edges Y_{second},. The fabric edges are given by the two Y-positions where $Z = \frac{h}{2}$.

Available data. For the fabric test, a single fabric has been laid down on the PVC plate. During the dry compaction, for each stress level, the width and the thickness are averaged among all the X-positions. Nonetheless, during the saturated decompaction, as the stress level applied on the fibrous fabric σ depends on the X-position (Figure III.4), the fabric width and thickness are not averaged.

Mechanical variables definition. Large strain extensions are defined to present all the results:

$$\lambda_y = \frac{w}{w_0} \tag{III.4}$$

$$\lambda_z = \frac{h}{h_0} \tag{III.5}$$

where w and h are respectively the width and the thickness of the fabric at specific stress level, w_0 and h_0 being respectively the initial width and thickness of the fabric (i.e. at dry state, under $\sigma = 0.01MPa$).
As in the first chapter (section 3.5 Eq. I.1), the decompaction level during the saturated decompaction phase is defined at each X-position, both laterally (ε_y) and transversely (ε_z):

$$\varepsilon_y(X) = \frac{w_{sat}(X) - w_{dry}(X)}{w_{dry}(X)} \tag{III.6}$$

$$\varepsilon_z(X) = \frac{h_{sat}(X) - h_{dry}(X)}{h_{dry}(X)} \tag{III.7}$$

where $w_{sat}(X)$ and $h_{sat}(X)$ are respectively the width and thickness of the single ply at a given X-position during the saturated decompaction phase and $w_{dry}(X)$ and $h_{dry}(X)$ are respectively the width and thickness of the single ply at a given X-position under the highest stress applied to the tows during the dry compaction phase ($\sigma \approx 0.0940MPa$,

for the 60 *mbar* abs. vacuum level, just before the wetting phase (details are given in the experimental protocol hereinbefore).

2.2.4 Single ply fabric: results

Figure III.6 illustrates the evolution of the fabric thickness and width during the dry compaction phase. During this loading phase up to 0.094 MPa, the fabric thickness significantly decreases by 12.5% ($\lambda_z = 0.875 \pm 0.009$, Figure III.6a) whereas the fabric width slightly decreases by 1.4%($\lambda_y = 0.986 \pm 0.048$, Figure III.6b). The limited width evolution could be explained by the stitch. The fabric densifies as the load increases.

During the saturated decompaction phase, each X-position is subjected to a specific stress σ. A fabric thickness decompaction gradient is thus expected along the X-position, as reported in the first chapter (section 4.1). As illustrated in Figure III.7a, the maximal decompaction occurs near the fluid inlet ($\varepsilon_z(X = 0.07) = 11.4\%$) whereas the minimal decompaction occurs near the vacuum vent ($\varepsilon_z(X = 0.93) = 1.1\%$). Even if no repeatability study has been conducted for this experiments, the trends are really close to the one measured in the first chapter for a stack of 10 quasi-NCF plies ($\varepsilon_{macro}(X = 0) = 9.1\%$; $\overline{\varepsilon}_{CT}(X = 0) = 8.4 \pm 0.8\%$, as illustrated in Figure I.28). The fabric width evolution remains negligible (less than 1%, excepted at X=0.07). This result agrees with the one obtained with the XCT device in the first chapter, as no width evolution of the tows within the stack has been observed (see section 9.2.2).

Finally, Figure III.8 summarizes the fabric width and thickness evolutions during the three main stages of the infusion process. To ease the interpretation of the unloading phase, a linear approximation of the width evolution presented in Figure III.7b has been employed, as its evolution is negligible. During the wetting phase, the fabric thickness increases significantly ($\lambda_z = 0.875 \pm 0.009$ at the beginning of the wetting phase and $\lambda_z = 0.8808$ at the end of the wetting phase) whereas the fabric width slightly reduces ($\lambda_y = 0.986 \pm 0.004$ at the beginning of the wetting phase and $\lambda_y = 0.984$ at the end of the wetting phase).
A permanent transverse deformation of the fabric is observed at the end of this cycle (loading, wetting, unloading). The final fabric thickness (measured at saturated state, near the fluid inlet where $\sigma \approx 0MPa$) is 2.8% smaller than the initial one (measured at dry state under $\sigma = 0.001MPa$). Nonetheless, the final fabric width is equivalent to the initial one (less than 0.4% of difference between the initial and final widths).

The fabric deformation occurs mainly in the transverse direction (thickness evolution) during all the three steps of the infusion process. The results obtained during the decompaction phase are in good agreement with the one observed with the XCT device in the first chapter.

The same experimental procotol is realized on single tows samples to analyze their width and thickness evolutions during the main steps of the infusion process. These results are presented hereafter.

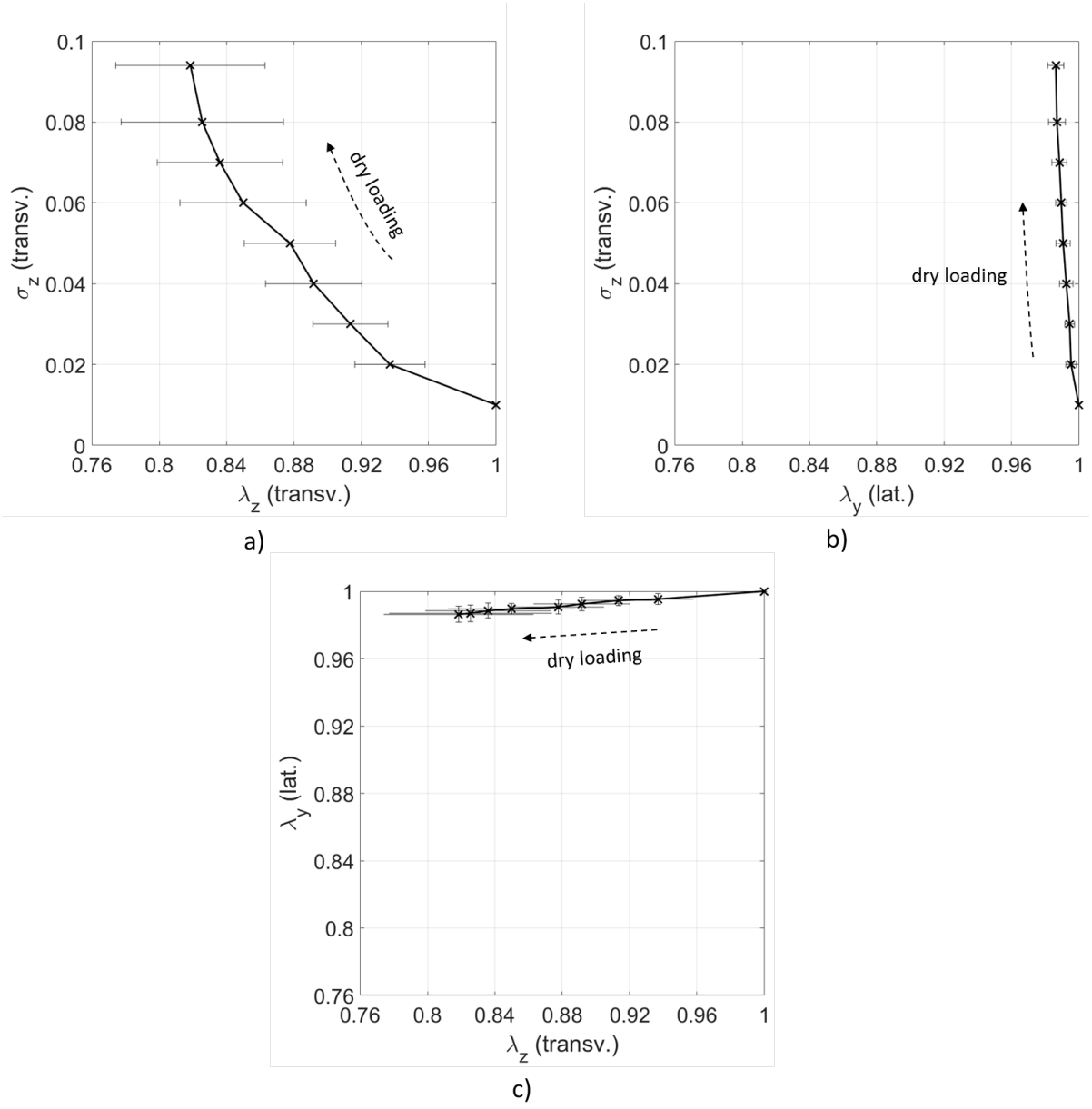

Figure III.6: Single ply fabric evolution during the dry loading stage: a) transverse strain extension with stress. b) lateral strain extension with stress. c) transverse strain extension with lateral strain extension.

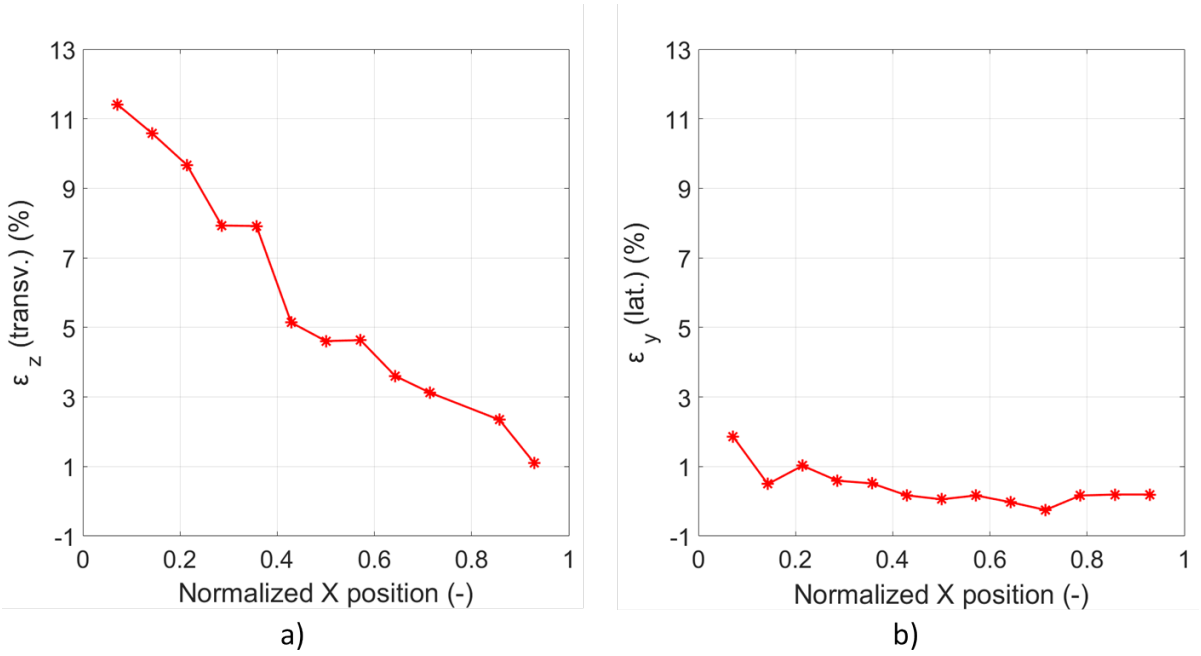

Figure III.7: Thickness (a) and width (b) deformations of the single ply fabric during the saturated unloading stage.

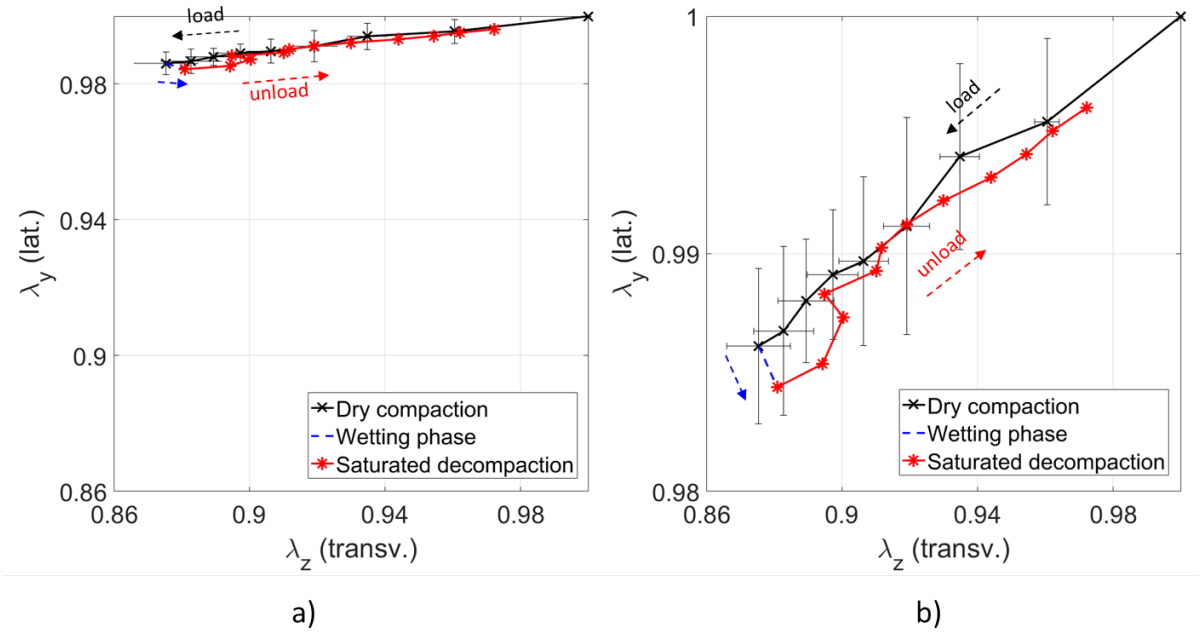

Figure III.8: Thickness and width extensions of the single ply fabric through the three infusion stages: a) scaled view. b) zoomed view.

2.2.5 Single tows: post-treatment

In this section, the post-treatment method applied to extract the thickness and the width of the single tows for each stress level is detailed.

Width and thickness computation. For each stress level, the final CCS file obtained is a matrix $CCS(i,j,k)$ where $i \in [1,N]$, $j \in [1,m]$, and $k \in [1,n]$, as illustrated in Figure III.2. For each X-position and for each stress level, single tows profiles are extracted at given Y-position ranges to compute their width and thickness.
As illustrated in Figure III.9, the thickness h is defined as the difference between the PVC plate location Z_{PVC} and the tow top location Z_{tow}. Z_{PVC} is defined in Eq. III.1. Z_{max} being the maximal Z-position of the tow ($Z_{max} = \underset{j}{max}(Z(j))$) and Y_{max} its corresponding Y-position, Z_{tow} is defined as:

$$Z_{tow} = \underset{j=Y_{max}-10 \rightarrow Y_{max}+10}{mean}(Z(j)) \tag{III.8}$$

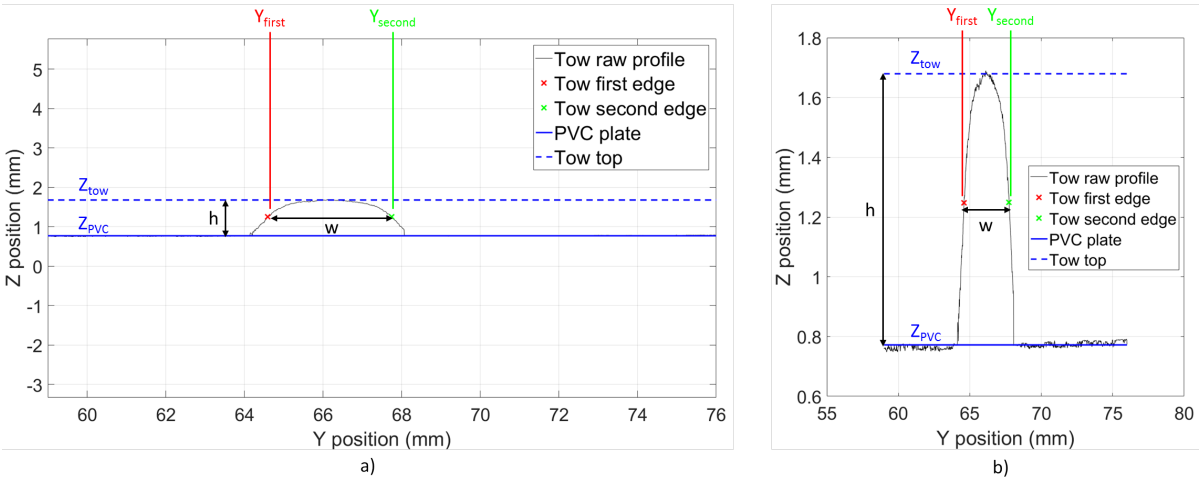

Figure III.9: Raw profile of a single tow at a defined stress level and a defined X-position and its corresponding width and thickness definitions: a) full scale. b) close-up view.

The width w is defined as the difference between the tow first Y_{first} and second edges Y_{second}. The tow width is thus defined between the two edges given by the two Y-positions where $Z = \frac{h}{2}$.

Available data. For the single tow test, 10 tows have been laid down on the PVC plate. During the dry compaction, for each stress level, the width and the thickness of the tows are averaged among all the X-positions and among all the tows. Nonetheless, during the saturated decompaction, as the stress level applied on the fibrous tows σ depends on the X-position, the width and the thickness of the tows are only averaged among all the single tows.

Mechanical variables definition. As for the single ply fabric post-treatment, large strain extensions are defined (Eq. III.4 and Eq. III.5). The decompaction level during the

saturated decompaction is also defined at each X-position, both laterally (ε_y in Eq. III.6) and transversely (ε_z in Eq. III.7).

2.2.6 Single tows: results

Figure III.10 illustrates the evolution of the tow thickness and width during the dry compaction phase. The reference state is chosen for $\sigma = 0.01MPa$ ($\lambda_y(0.01) = 1$) in dry conditions. During the loading, both tow thickness and width decrease when σ increases (Figure III.10a and b). The tow thickness decreases by $5.3 \pm 0.4\%$ ($\lambda_z(0.094) = 0.946 \pm 0.004$) whereas the tow width decreases by $7.3 \pm 1.8\%$ ($\lambda_y(0.094) = 0.926 \pm 0.018$). Therefore, imposing a vacuum level inside a deformable cavity made of a cellophane film induces quasi-hydrostatic deformations of tows.
This behavior may be not representative of the one occurring for a tow within a fabric. In a fabric, no tow width evolution is expected: first, as reported in the section 2.2.4, the fabric width evolution is limited. Additionally, the cellophane film is not able to apply a lateral load to the tows located in a fabric. Therefore, transverse unidirectional loading and unloading phases should be more appropriate to capture the mechanical behavior of tows.

During the saturated decompaction phase, each X-position is directly linked to a specific stress σ (Figure III.4b): a thickness gradient is thus expected along the X-position. A slight gradient is observed concerning the tow thickness evolution: as illustrated in Figure III.11a, the maximal decompaction occurs near the fluid inlet ($7.8 \pm 1.0\%$) whereas the minimal decompaction occurs near the vacuum vent ($5.0 \pm 0.9\%$). A significant decompaction gradient is yet observed concerning the tow width evolution: as illustrated in Figure III.11b, the maximal width rise occurs near the fluid inlet ($4.8 \pm 2.3\%$) whereas the width reduces slightly near the vacuum vent ($-0.8 \pm 1.1\%$).
These results do not seem in good agreement with the tow's behavior measured with the XCT experiment in the first chapter: no tow width evolution has been measured (section 9.2.2) and the tow thickness evolution showed a higher gradient along the X-position (Figure I.49: tow deformation at X=0.76 has been measured around 1%). This could be explained by the boundary conditions applied to the tows in both cases. A single tow under a vacuum bag undergoes quasi-hydrostatic deformations (both width and thickness decreases during the loading) whereas a tow inside a fabric experiences a more unidirectional load. Therefore, the resulting saturated unloading behavior differs: the single tow undergoes both lateral and transversal deformations whereas the tows inside the fabric undergo only a transversal deformation, as measured in the first chapter with XCT experiments.

Figure III.12 summarizes the tow width and thickness evolutions during the three main steps of the infusion process. During the wetting phase, the tow thickness increases significantly ($\lambda_z = 0.95 \pm 0.004$ down to 0.99 ± 0.009) whereas the tow width slightly reduces ($\lambda_y = 0.93 \pm 0.018$ down to 0.92 ± 0.01). Nonetheless both tow width and thickness increase significantly during the saturated unloading phase.
A permanent deformation is observed at the end of this 3-stage cycle: the final tow thickness (measured near the fluid inlet at saturated state $\sigma \approx 0MPa$) is 2% higher than the initial thickness (measured at dry state under $\sigma \approx 0.01MPa$) whereas the final tow width remains 3% smaller than the initial width.

Under the specific boundary conditions provided by the infusion setup, the single tow deformation is quasi-equivalent in width and thickness directions during the dry loading phase. The same behavior is observed during the unloading saturated phase: both tow width and thickness increase. This tow behavior differs from the one measured with XCT experiments in the first chapter, where no tow width evolution has been observed.

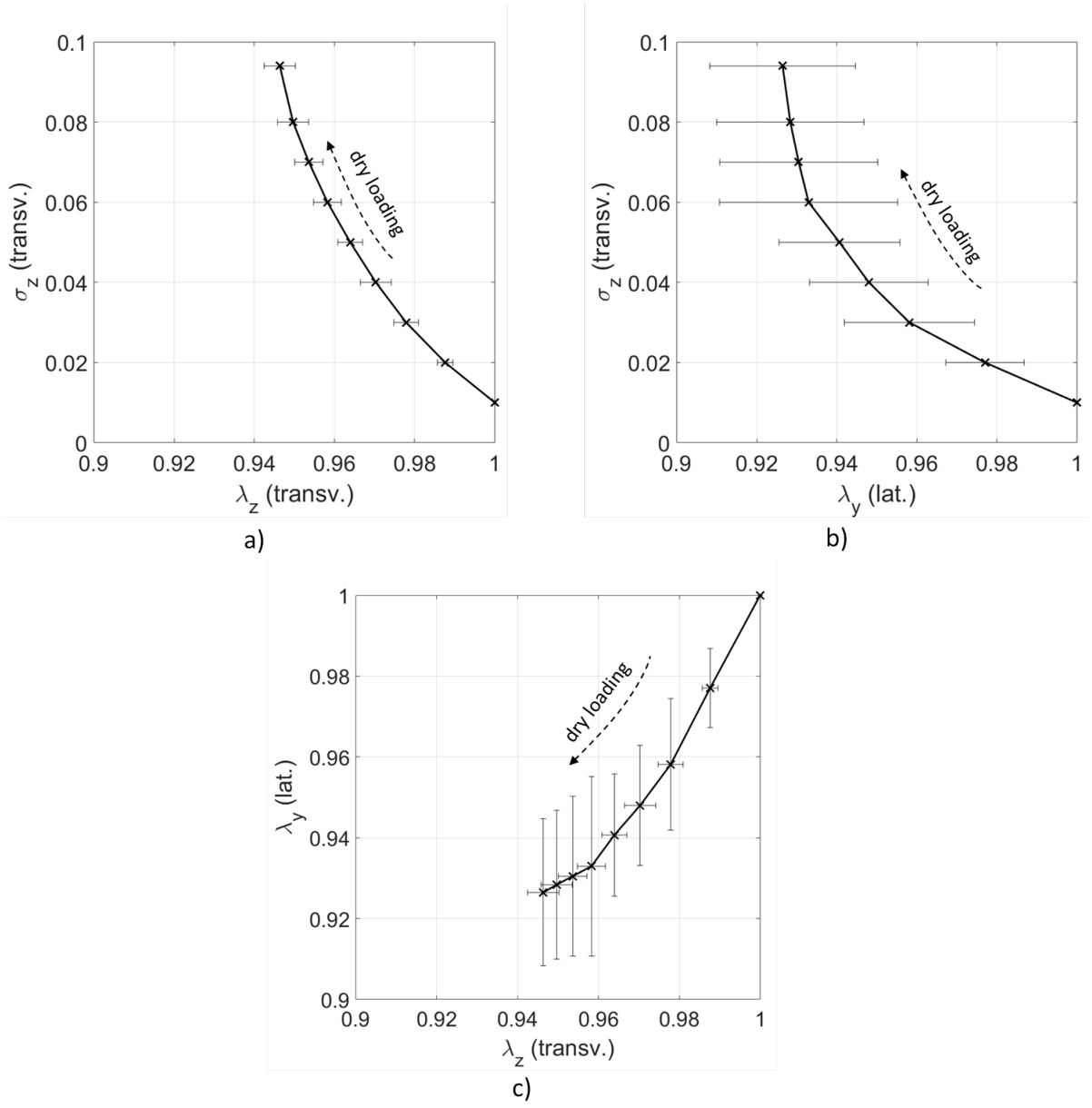

Figure III.10: Single tow evolution during the dry loading stage: a) transverse strain extension with stress. b) lateral strain extension with stress. c) transverse strain extension with lateral strain extension.

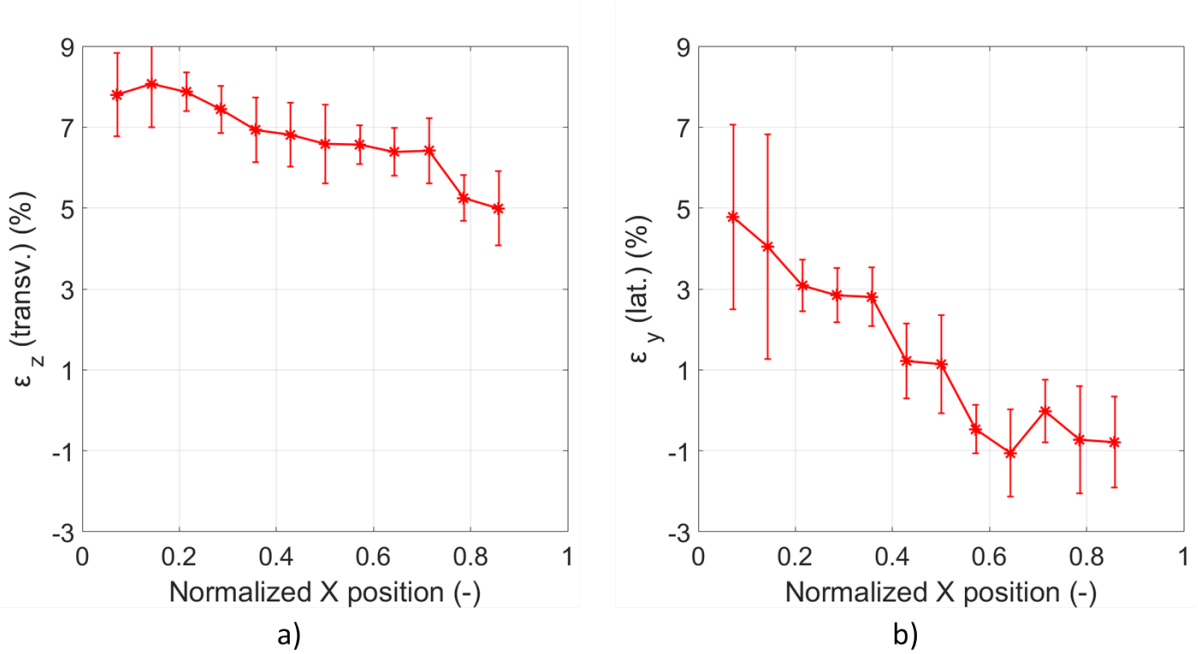

Figure III.11: Thickness (a) and width (b) evolutions of the single tow during the saturated unloading stage

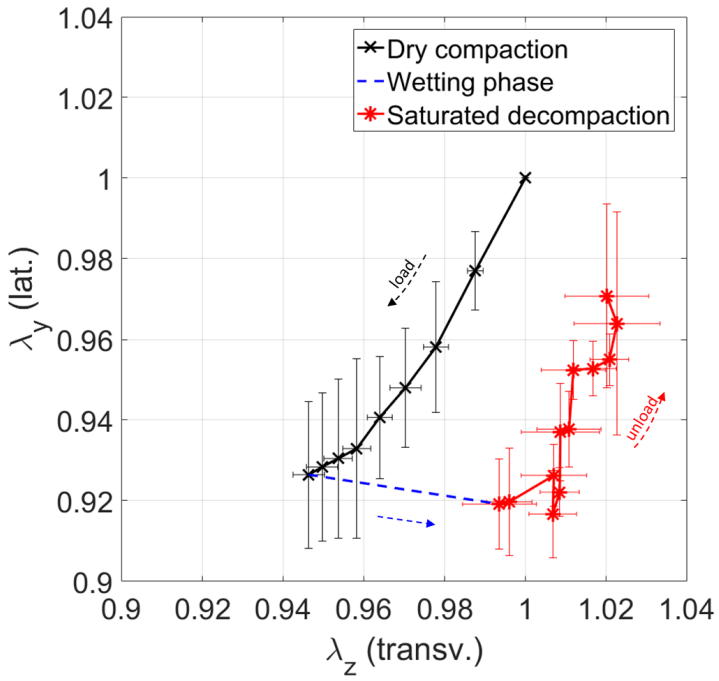

Figure III.12: Thickness and width extensions of the single tows through the three infusion stages

2.2.7 Conclusion

Infusions have been conducted on a single ply of quasi-UD NCF and single tows extracted from this fabric. During the three main stages of the infusion process (dry loading phase, wetting phase and saturated unloading phase), both transverse and lateral deformations of the fibrous samples have been experimentally measured. The resulting evolutions are schematically represented in Figure III.13 for both types of sample. With the boundary conditions imposed by the vacuum bag, the single tow deforms in both lateral and transverse directions whereas the fabric mainly deforms in the transverse direction. Then, during the infusion process, tows inside a fabric may mainly undergo unidirectional transverse compressive load and unload. It is thus of interest to conduct unidirectional compressive tests on single tows. The following section presents the experimental setup and methodology developed to conduct unidirectional compressive tests on tows, and an analysis of the tow behavior is then provided.

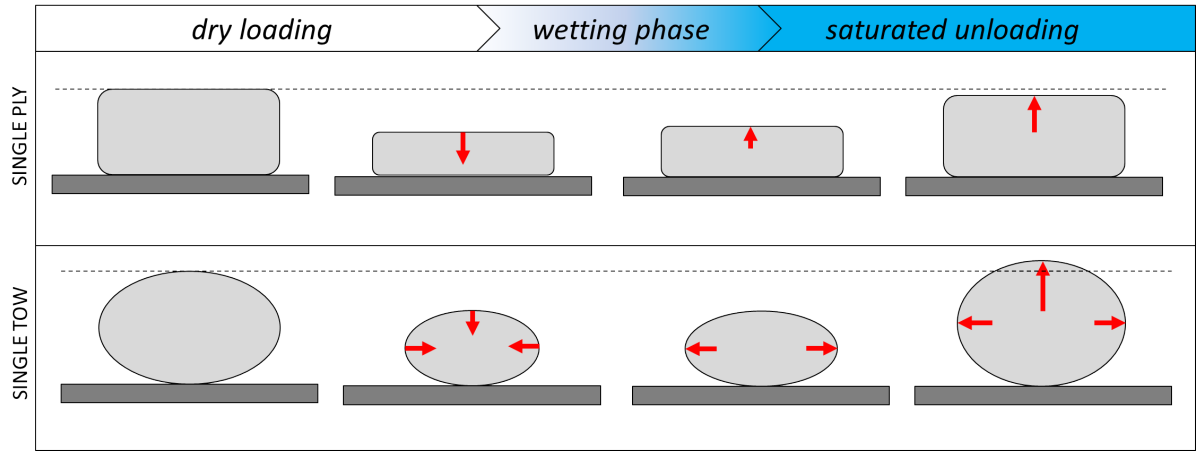

Figure III.13: Schematic view of the width and thickness evolutions of the two considered samples during the three main stages of the infusion process: a single ply of quasi-UD NCF and a tow extracted from this quasi-UD NCF

2.3 Unidirectional compressive loading and unloading

The experimental work presented in this section is mainly based on the concept and setup presented by Dharmalingam at al. in [1]. In this *unidirectional approach*, single tows are laid down on a rigid cavity. A specific setup has been designed to allow the modification of the cavity thickess and thus to apply a unidirectional load on the tows. In this section, the setup and the methodology used to apply unidirectional load and monitor sample thickness and width is first detailed. Then, the post-treatment method is presented and the analysis of the tow mechanical behavior under unidirectional compressive loading and unloading is provided.

2.3.1 Materials and equipments

The materials (tow sample and fluid) and equipment (chromatic confocal scanner) used for this study are identical to the ones presented in the section 2.2.1.

2.3.2 Setup and experimental protocol

Setup. A compression device has been specially designed to apply uniaxial (Z-direction) transverse compression on tows under the chromatic confocal scanner (CCS). This device is presented in Figure III.14b. It is composed of a micrometric compact lab jack (LJ 750, *Thorlabs*), through which vertical displacements are applied, a 2 kN cell force (Type U3, *HBM*), a bottom mobile steel platen, and a top PMMA plate, bonded to a steel frame (two columns). A pool made of stainless platen and plasticine (Figure III.14a) is placed on the bottom mobile steel platen and contains the fibrous sample (2 single tows).

This setup is settled on the moving support of the CCS and a sample profile (YZ) is recorded every 10 mm (in the X-direction). The tow sample is 75 mm long and 6 profiles are acquired for each stress level. For each YZ profile, a Z-position is recorded every 5 μm in the Y-direction, allowing the determination of both sample width and thickness.

Experimental protocol. The experimental procotol followed to conduct unidirectional compressive tests on tows is summarized in Figure III.15. As in the previous section, three phases are considered: after a loading phase at dry state, the tows are filled with a fluid and the unidirectional stress (σ_z) is then released step by step at saturated state.

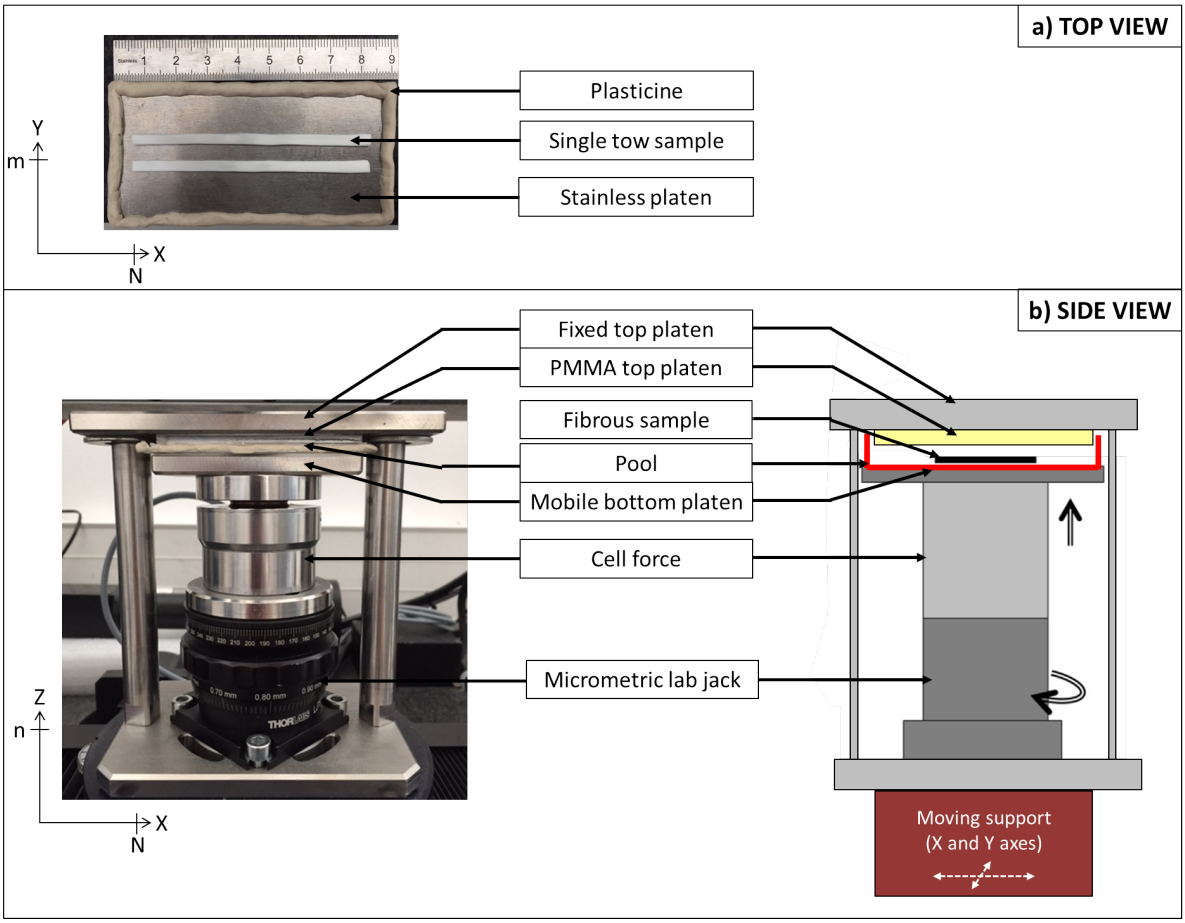

Figure III.14: Schematic view and pictures of the setup developed to impose a unidirectional force to single tows: a) Top view of the pool. b) Side view of the overall setup. Size of the recorded data is also detailed (m, n, N).

Step	Description	Duration
Setup preparation	The fibrous sample is cut and placed on the stainless platen of the pool.	around 10 min
Setup positioning	The pool is positioned on the cell force support, above the upper PMMA platen.	around 1 min
DRY COMPACTION		
Set of the cavity thickness	The thickness of the cavity is gradually reduced to apply a stress on the fibrous sample going from 0 to 0.1 MPa. Each cavity thickness corresponds to a force that is recorded with the cell force. 10 to 12 cavity thicknesses are selected.	around 2 min from one force level to another one
Stabilization	For each cavity thickness, and therefore for each force level, 5 min of stabilization are necessary to allow fibrous relaxation before the recording of the YZ profiles.	5 min
Thickness, force and width record	For each cavity thickness, 6 YZ profiles are recorded along the X-direction. 10 mm in X-direction separate each YZ profile. For each YZ profile, a Z-position is recorded every 5 µm in the Y-direction. The force and the displacement of the jack are also recorded.	around 1 min
WETTING PHASE		
Infusion state under vacuum (transient)	When the maximum force corresponding to a stress applied around 0.1 MPa is reached, the cavity is filled from one side with a 'syringe+needle' (around 3ml of fluid). The impregnation is driven by capillary forces.	around 1 hour
Saturated state under vacuum (quasi-static)	When the flow front reaches the other side of the sample (around 20 min after the beginning of the impregnation), more fluid is added (2ml) and 40 min more are waited on to ensure good saturation.	
SATURATED DECOMPACTION		
Set of the cavity thickness	The thickness of the cavity is gradually decreased to apply a stress on the fibrous sample going from 0.1 to 0 MPa. Each cavity thickness corresponds to a force that is recorded with the cell force. 10 to 12 cavity thicknesses are selected.	around 2 min from one force level to another one
Stabilization	For each cavity thickness, and therefore for each force level, 5 min of stabilization are necessary to allow fibrous relaxation before the recording of the YZ profiles.	5 min

Figure III.15: Step by step experimental protocol, following the three main stages of the infusion process

2.3.3 Calibration

Several calibrations are conducted to ensure the accuracy of the methodology and the measurement:

- the thickness and the width of calibrated stainless shim plates are monitored at dry state with the developed setup to validate the accuracy of the measurement,
- the impact of the fluid presence on the thickness and the width measured at saturated state is estimated,
- the compliance of the system is estimated to ensure an accurate measurement of the thickness at saturated state.

The maximal contact surface being around $75 \times 5\ mm^2 \times 2$ (2 single tows), the maximal force applied to reach $\sigma_{\mathbf{z}} = 0.1MPa$ remains below $80N$ ($\sigma_{\mathbf{z}}$ being defined as the transverse stress applied to the fibrous reinforcement). Calibrations tests are thus conducted in the range of [0-100]N.

Width and thickness measurements at dry state. With the chromatic confocal scanner, usually the pen scans the sample surface without any obstacle between the pen (sensor) and the sample to be scanned. However, in this study, a top platen (10 mm thick) has been inserted between the pen and the tow sample. Therefore, a verification and calibration of the bench has been performed by measuring calibrated stainless steel shim plates below the top platen under a 100 N force. The dimensions of the calibrated shim plates are given in Table III.2. For each calibrated shim plate, 5 YZ profiles have been acquired: the width and thickness presented in Table III.2 are the average values. The measured widths and thicknesses values show that performing measurement through the top platen of the compression bench does not alter the accuracy and is within 3% of tolerance. It also highlights that even if the bench deflects, it has no influence on the accuracy of the thickness and width measurements.

Table III.2: Measurements performed for the calibration of the bench

Calibrated nominal width×thickness (mm)	Measured average width (mm)	Measured average thickness (mm)
50×0.1	49.992	0.101
50×0.2	50.014	0.206
50×0.5	50.069	0.514
50×1.0	50.001	1.024

Width and thickness measurements at saturated state. During the wetting phase, the fluid is introduced in the pool to saturate the sample. The presence of fluid does not impact the width measurement (Figure III.16a). Nonetheless, the fluid presence modifies the intensity of the reflected light measured by the CCS: for a given jack Z-position and thus an identical bottom platen Z-position, the Z-position detected by the CSS is 200 μm higher when the fluid is in the cavity (Figure III.16a). Moreover, when the bottom platen is descended, the Z-position of the bottom platen measured by the CCS is not evolving. Thus, the Z-position of the bottom platen, essential to estimate the sample

thickness, cannot be measured with accuracy by the CCS when the fluid is in the cavity. During the saturated unloading phase, the only way to monitor the bottom platen displacement is thus to measure the micrometric lab jack displacement. To ensure an accurate measurement of the thickness evolution during the saturated unloading, both the lab jack displacement and the bottom plate displacement detected by the CCS have been monitored during the dry loading phase. The results are presented hereafter.

Lab jack displacement and system compliance. Both the lab jack displacement and the bottom plate displacement detected by the CCS have been monitored during the dry loading phase (Figure III.16b). Due to the overall setup compliance, the micrometric lab jack displacement is overestimated compared to the one measured by the CCS. In the following tests, during the unloading saturated phase, the bottom platen displacement will be acquired by the micrometric lab jack and corrected by the linear curve fitted in Figure III.16b.

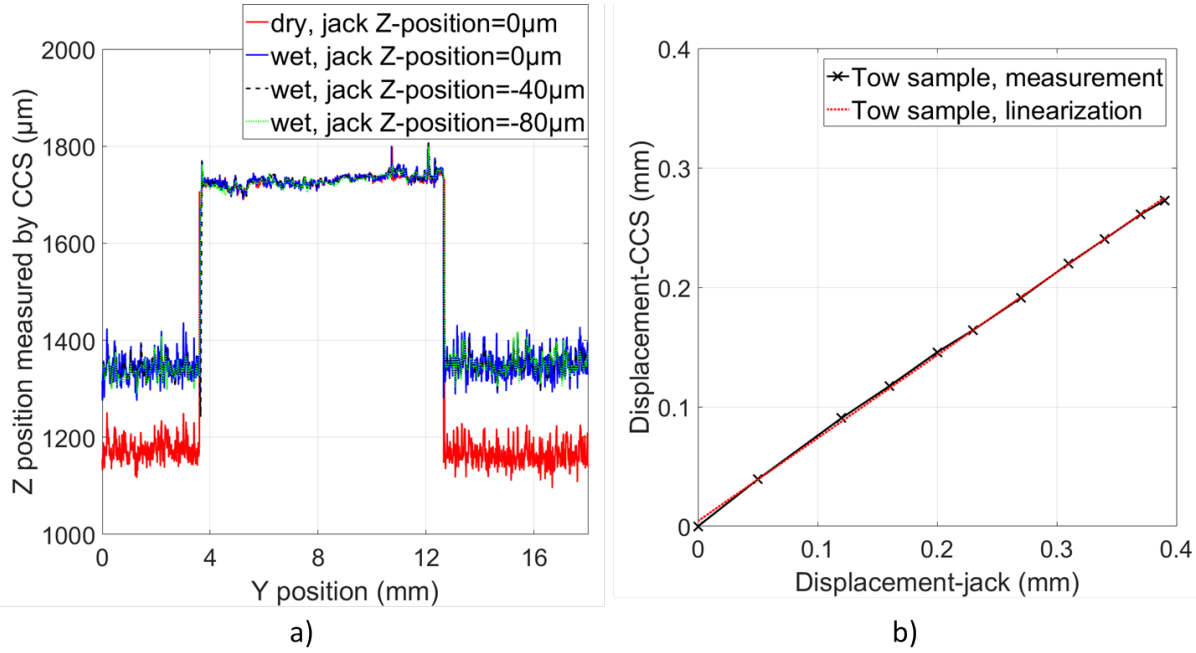

Figure III.16: Calibration at saturated state: a) detections of the bottom platen displacement when the fluid is in the pool. b) Correction curve of the overall system between the imposed displacement by the jack and the one measured by the CCS.

2.3.4 Single tows: post-treatment

In this section, the post-treatment method applied to extract the thickness and the width of the single tows for each stress level is detailed.

Width and thickness computation. As described in section 2.2.5, the CCS file obtained is a matrix $CCS(i, j, k)$. For each X-position, and for each stress level, single tows are extracted from the CCS file to compute their width and thickness (Figure III.17). The thickness h is again defined as the difference between the bottom platen Z-position (Z_{platen}, equivalent to Z_{PVC} defined in Eq. III.1) and the Z-position of the tow Z_{tow}

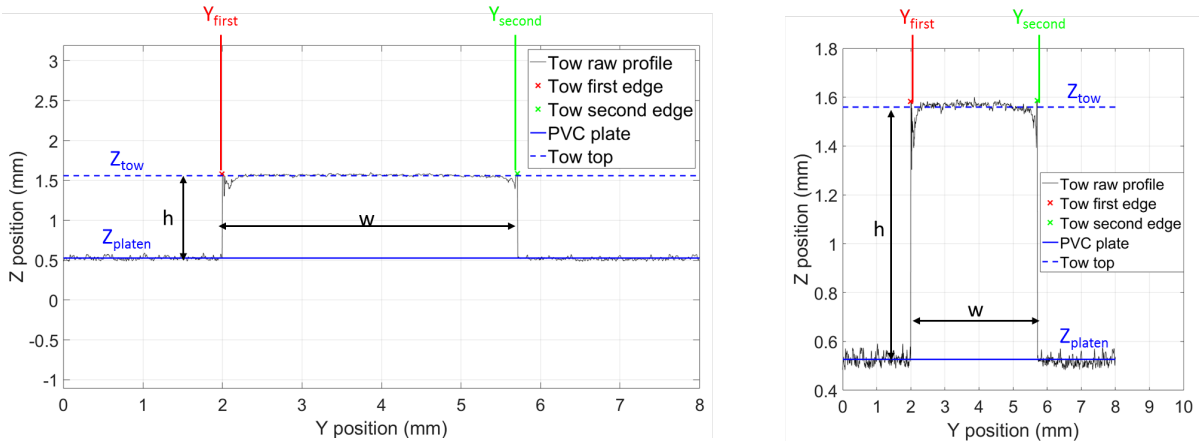

Figure III.17: Raw profile of a single tow at a defined stress level and a defined X-position and its corresponding width and thickness definitions: a) full scale. b) close-up view.

(Eq. III.8). The width w is again defined as the difference between the tow first Y_{first} and second edges Y_{second}.

Available data. For the single tow tests, 2 single tows have been laid down on the pool. The tow width and thickness is thus averaged among the 2 considered tows and among the 6 X-positions.

Mechanical variables definition. The lateral and transverse large strain extensions (λ_y and λ_z) are identical to the one defined respectively in Eq. III.4 and III.5, where the initial tow width w_0 and thickness h_0 are the one measured at the beginning of the dry loading phase, under the minimal stress level.

2.3.5 Single tows: results

Figure III.18 presents the tow width and thickness evolutions during the dry loading phase. The reference state being $\sigma_{\mathbf{z}} = 0.007MPa$ ($\lambda_z(0.007) = 1$ and $\lambda_y(0.007) = 1$), the tow thickness reduces by $22.5 \pm 0.6\%$ ($\lambda_z(0.13) = 0.775 \pm 0.006$ in Figure III.18a) whereas the tow width increases by $9.6 \pm 0.7\%$ ($\lambda_y(0.13) = 1.096 \pm 0.007$ in Figure III.18b). No stress being applied to the lateral edges of the tow, it widens. The same behavior has been measured by Dharmalingham et al. [1] for the tows referred as "4800 tex". This widening behavior is significantly different from the one observed in Figure III.10: when a quasi-hydrostatic load is applied to a single tow, both thickness and width decreases, inducing a limited thickness decrease during the loading phase and a densification of the tow.

Figure III.19 presents the tow width and thickness evolutions during the wetting and the saturated unloading phases. During the wetting phase, the tow thickness slightly reduces (2.9% in Figure III.19a) whereas the tow width evolution is negligible (rise of 0.04% in Figure III.19b). The thickness diminution could be explained by the lubrication of the fiber/fiber contacts. During the saturated unloading phase, the thickness significantly increases (11.9%) whereas the tow width increases slightly (3.5%).

It should be noticed that the tow thickness evolution between the end of the dry state loading phase and the end of the saturated state is about 9%. This result is in good agreement with the tow behavior measured with the XCT experiments in the first chapter: the tow thickness evolution near the fluid inlet location between the compacted dry state and the decompacted saturated state is about 7% (Figures I.49 and I.51).

Under the unidirectional compression boundary conditions provided by the setup, the single tow widens during the loading phase. However, a significant tow thickness rise is observed during the unloading saturated phase, whereas a negligible width evolution is detected. This tow behavior at saturated state is in good agreement with the one measured with XCT experiments in the first chapter.

Figure III.20 illustrates the single tow behavior under unidirectional stress load and unload as well as the single ply fabric behavior under infusion process boundary conditions.

2.4 Experimental conclusions and prospects

A loading/unloading cycle has been applied to a single ply fabric and single tows to monitor both the lateral and transverse deformations of the fibrous sample during the main steps of the infusion process: loading phase at dry state, wetting phase, unloading phase at saturated state. Two types of boundary conditions have been investigated: a quasi-static compressive load has been applied with a vacuum bag and the vacuum force to samples and a unidirectional transverse compressive load has been applied to single tows with a specific setup.

The unloading behaviors observed at the saturated state for the fabric under vacuum bag and for the single tow under unidirectional boundary conditions are consistent with the behavior of the fabric and the tows belonging to the fabric measured with the XCT experiments presented in the first chapter. During the saturated unloading phase, a stack of the quasi-UD NCF, a tow belonging to this quasi-UD NCF stack, a single ply of the quasi-UD NCF, and a single tow extracted from the quasi-UD NCF undergo a maximal transverse deformation near the fluid inlet, where the transverse stress applied to the fibrous material is released ($\sigma_{\mathbf{z}} \approx 0MPa$). Between the dry state under a maximal transverse stress ($\sigma_{\mathbf{z}} \approx 0.0940MPa$) and the saturated state under the minimal transverse stress ($\sigma_{\mathbf{z}} \approx 0MPa$, near the fluid inlet), this maximal transverse deformation reaches 7 to 9%.

During the loading phase, the single tow behavior under unidirectional boundary conditions and the fabric behavior under vacuum bag boundary conditions differ. The single tow significantly widens (the width increases by 9.6%) during the loading phase, inducing then a significant thickness decrease (22.5%). Nonetheless, the fabric width slightly decreases (1.4%), inducing a limited thickness decrease (12.5%). This could be explained by the stitch in the fabric, that constrains laterally the tows during the loading phase. A possibility to verify this hypothesis would be to monitor a new stack microstructure with the XCT device described in the first chapter, under several stress level at dry state. Therefore, both tows and stack widths and thicknesses evolutions could be analyzed along the dry loading phase.

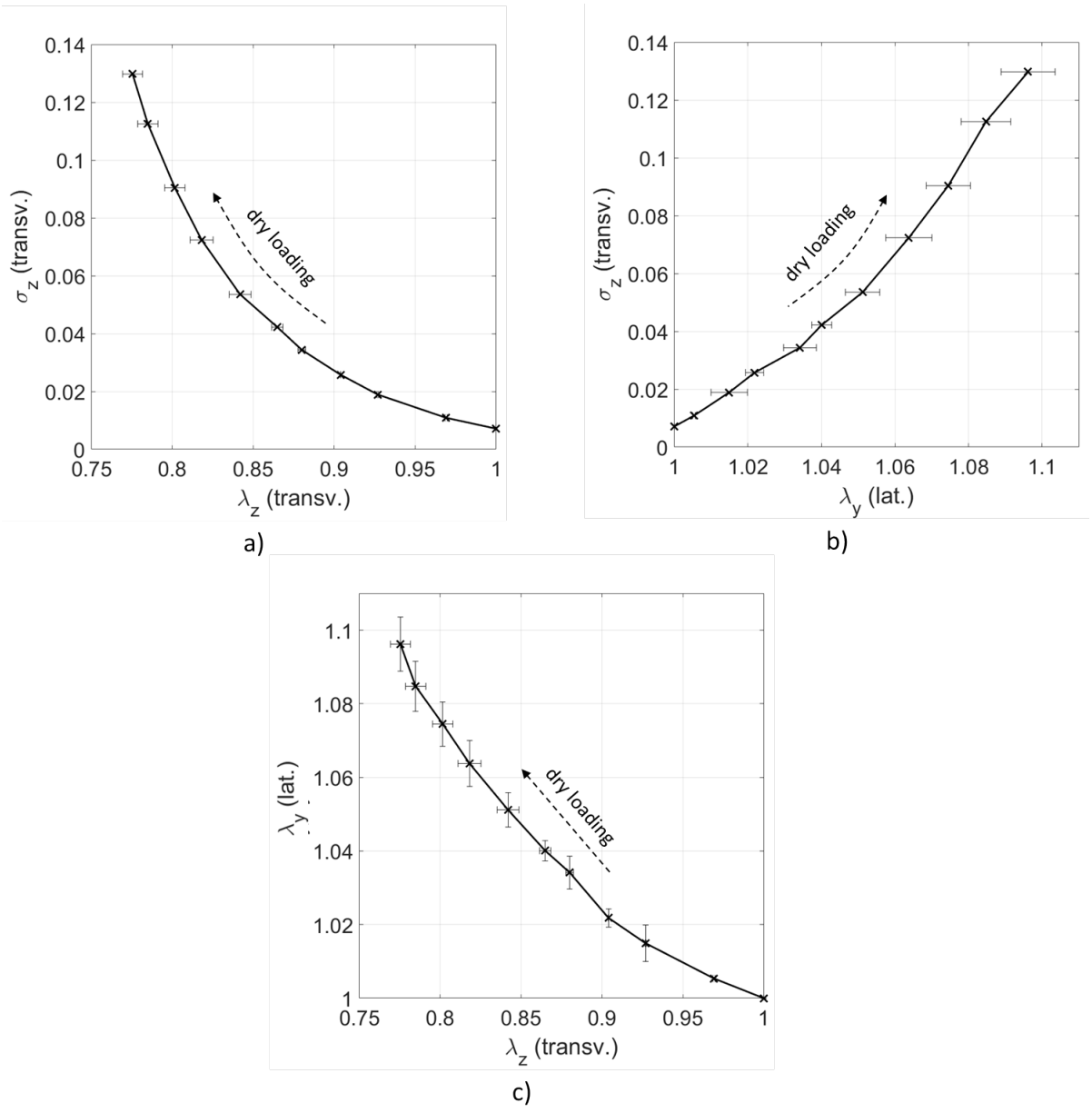

Figure III.18: Single tow evolution during the dry unidirectional loading stage: a) transverse strain extension with stress. b) lateral strain extension with stress. c) transverse strain extension with lateral strain extension.

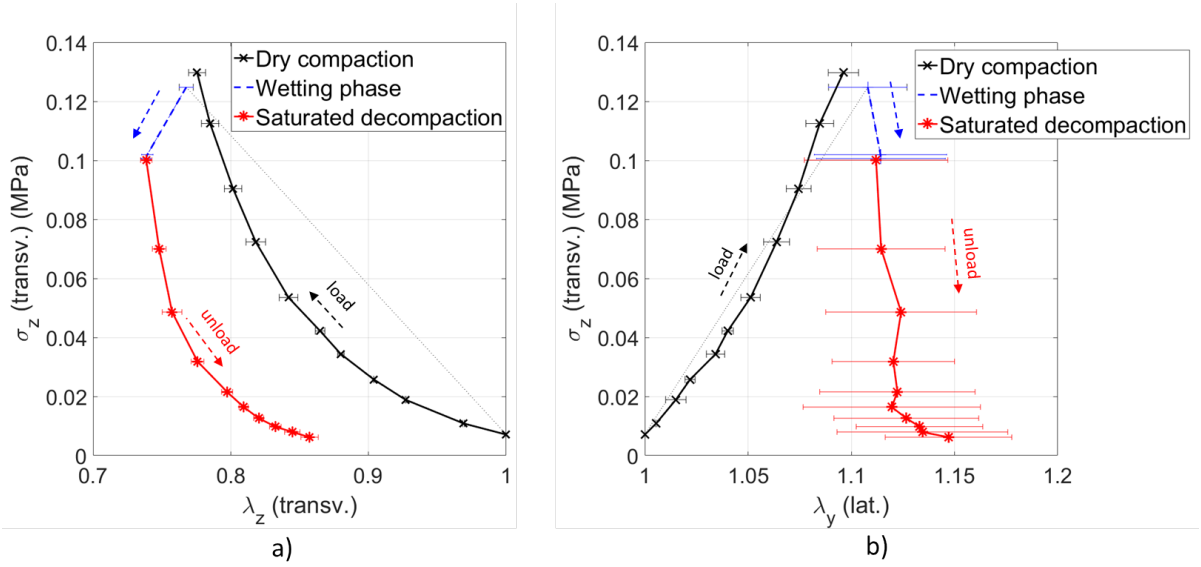

Figure III.19: Thickness and width extensions of the single tow through the three infusion stages, for unidirectional compression: a)transverse strain extension with transverse stress. b) lateral strain extension with transverse stress.

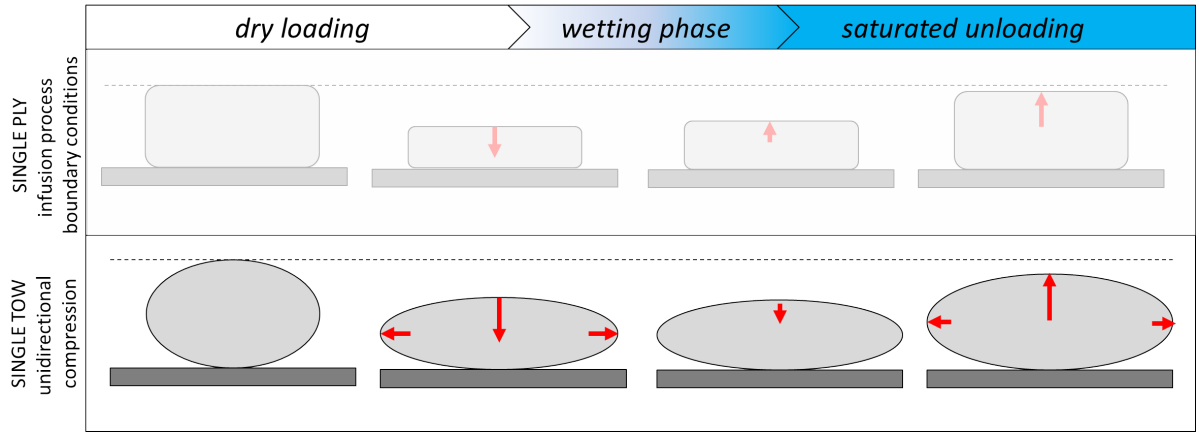

Figure III.20: Schematic view of the width and thickness evolutions of the quasi-UD fabric under the vacuum bag and of the single tow under unidirectional boundary conditions.

The dry loading phase might have a significant impact on the initial microstructural organization of a stack prior to the infusion process, as the tows inside a fabric might widen or not. For instance, Figure III.21 presents the potential microstructural evolutions during the loading phase for two quasi-UD NCFs, made of the same glass tows but with different stitches. For the quasi-UD NCF with a loose stitch, its tows are free to widen laterally during the dry compaction loading. It implies that the vertical inter-tow channels size reduces. Nonetheless, the quasi-UD NCF presented on the right of Figure III.21, made of the same tows of the one presented on the left, has a tight stitch. The tows are lateraly constrained and do not widen during the dry compaction loading. Then, an evolution of the inter-tow channels size is not expected. These microstructural reorganizations occur prior to the infusion process and condition the initial microstructure of the fibrous reinforcement. Depending on the spatial distributions of inter-tow and intra-tow pores, the quasi-UD NCF will have a different in-plane permeability, as it has been highlighted at the end of the first chapter.

The mechanical behavior of such quasi-UD NCF has been already investigated at macroscopic scale by Vallons et al. [98]. Nonetheless, at mesoscopic scale, most models concerning the transverse compression of a single tow are unidirectional or neglect the lateral deformations of the modeled tow. Therefore, a new tow model is proposed in the following section, and the influence of the lateral boundary conditions on the mechanical tow behavior is analyzed.

3 3D modeling of the tow mechanical behavior: unidirectional compressive loading

During the dry loading phase, the previously studied glass single tows undergo significant lateral and transverse evolutions: while the tow thickness reduces by 22.5%, its width increases by 9.6%. Depending on the lateral boundary conditions applied to a tow within a fabric (for instance with a loose or a tight stitch), its mechanical behavior is expected to differ. It is thus of great interest to model the mechanical behavior of a single tow under compressive loading to improve the understanding of the fabric behavior.

This section will first focus on the selection of an hyperelastic model able to predict both the nonlinear evolution of the tow thickness and the slight evolution of the tow width. Then, the influence of the lateral boundary conditions applied to the tow on its 3D mechanical response will be studied. Finally, the parameters of the selected model will be fitted to the experimental data measured in the previous section for a laterally-free glass tow. An analysis will be additionally provided to predict the mechanical behavior of a laterally-constrained tow.

3.1 Selection of the model

The literature context and the preliminary studies presented in this section have been mainly extracted from the work realized by Anne-Sophie Lectez [99], [100]. Her main objective was to develop a 3D model able to predict both lateral and transverse evolution of a tow under cyclic compressive loading.

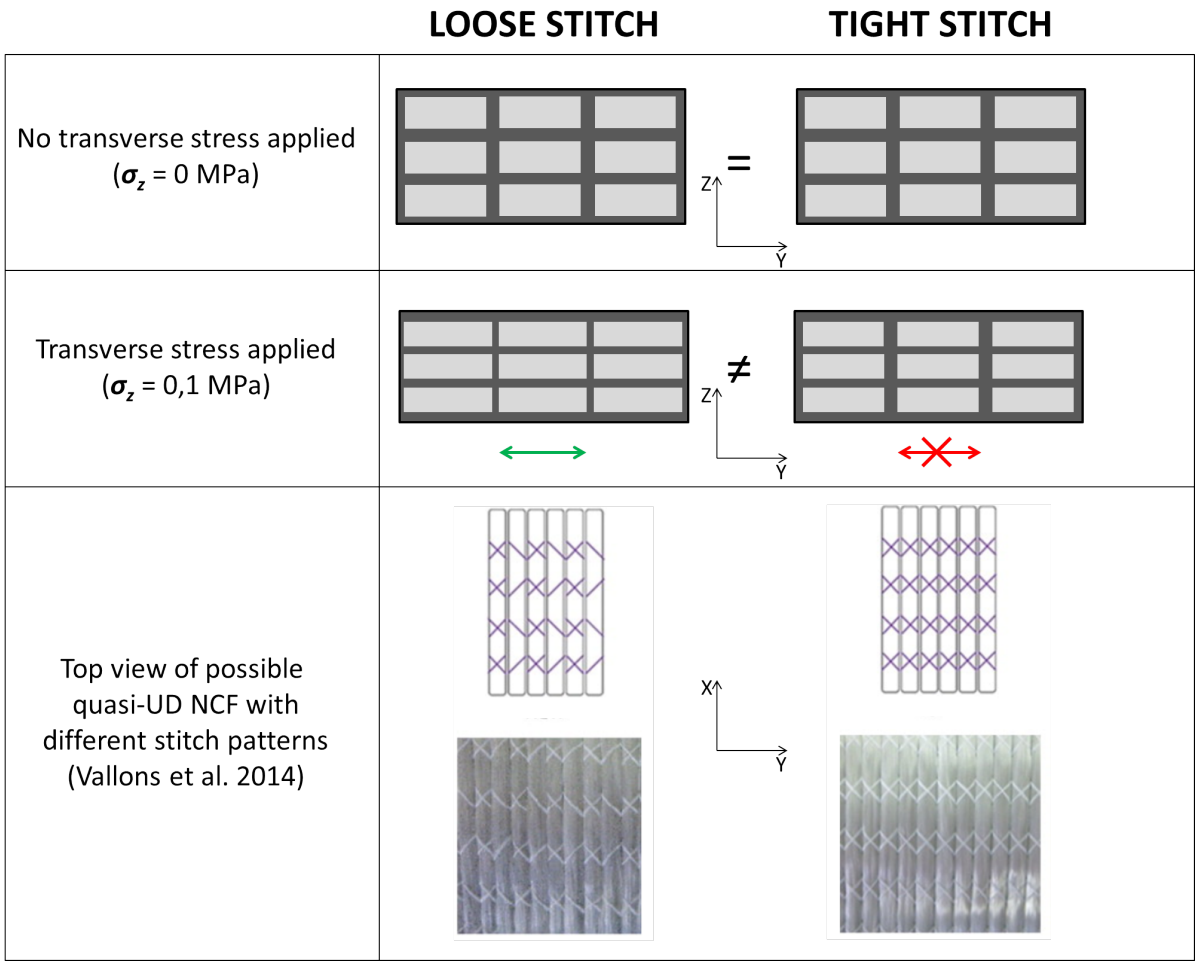

Figure III.21: Schematic view of the possible microstructural evolution during the loading phase of stacks of quasi-UD NCFs with a loose or a tight stitch

3.1.1 Literature context: hyperelasticity, compressibility and inextensibility

When sujected to a transverse compressive loading, a single tow undergoes a highly nonlinear elastic behavior, as highlighted in Figure III.18a and b.
Lectez et al. presented a comprehensive analysis concerning the modeling of a single tow subjected to cyclic compressive loading [100]. Concerning the first loading phase, the authors recommand the use of hyperelastic models, originally developed for elastomers, to model highly nonlinear elastic behavior in finite strain (Mooney-Rivling, Ogden, Yeoh: most of them are well detailed in [101]). In the general theory of hyperelasticity, it is assumed that the stress tensors (in this chapter σ, the true or Cauchy stress tensor) derive from a strain energy function W. However, these models written in terms of with strain energy function have to be adapted to take into account the large change in volume of tows during the compressive load (as highlighted experimentally in [1]) and to take into account the inextensibility of the tow in the fiber direction:

- *Large change in volume.* Lectez et al. recommand to extend the classical incompressible hyperelastic models to the compressible case by adding a strain energy depending on the Jacobian of the transformation (J, representing the volume variation during a transformation). The addition of this strain energy and its formulation are detailed in [102].

- *Inextensibility in fiber direction.* Two approaches are possible to take into account the inextensibility of the tow in the fiber direction. First, the modeling of an isotropic material can be considered and an internal stress can be imposed in the fiber direction. Alternatively, an isotropic transverse strain energy can be added to the considered model. A large stiffness parameter has to be selected in the fiber direction, as done for instance for biological soft tissues [103]. This second adaptation will be used in the hyperelastic models studied hereafter in the form of a standard reinforcement model, detailed for instance by Merodio et al. [104].

The total elastic strain energy W of a possible 3D hyperelastic tow model can be written as:

$$W = W_{model} + W_{compress} + W_{aniso} \tag{III.9}$$

where W_{model} is the strain energy corresponding to the considered incompressible isotropic hyperelastic model (for instance Mooney-Rivling, Ogden), $W_{compress}$ is the additional term to take into account large compressibility and W_{aniso} is the additional term for the anisotropy in the fiber direction.
Table III.3 summarizes the common notations used to describe such hyperelastic models. X is the longitudinal axis of the tow (fiber direction), Y is the lateral axis of the tow (width) and Z is the transverse direction of the tow (thickness). From the total elastic strain energy W, the Cauchy stress tensor σ can be expressed in the eigen basis of the transformation gradient (so that $J = \lambda_x \lambda_y \lambda_z$) [105]:

$$\sigma_{\mathbf{i}} = \frac{1}{J} \lambda_i \frac{\partial W}{\partial \lambda_i} \tag{III.10}$$

where $i = x, y, z$, J is the jacobian transformation and W is the total elastic strain energy.

Lectez et al. [99] has analyzed several hyperelastic models and compared the obtained behavior (lateral and transverse extensions) with the one experimentally measured on a

Table III.3: Notations and corresponding definitions of the main parameters of hyperelastic models

Notation	Definition	Mathematical definition
W	total strain energy	-
$\lambda_{x,y,z}$	principal extensions in X, Y and Z directions	-
J	jacobian of the deformation gradient	$J = \lambda_x \lambda_y \lambda_z$
I_1	first invariant of the transformation	$I_1 = \lambda_x^2 + \lambda_y^2 + \lambda_z^2$
I_2	second invariant of the transformation	$I_2 = \lambda_x^2\lambda_y^2 + \lambda_y^2\lambda_z^2 + \lambda_x^2\lambda_z^2$
I_3	third invariant of the transformation	$I_3 = \lambda_x^2\lambda_y^2\lambda_z^2 = J^2$
I_4	pseudo-invariant: square of the principal extension in fiber direction	$I_4 = \lambda_x^2$

single dry tow of continuous carbon fibers. These results, not published yet, are presented in the two following sections to justify the selection of the Ogden-Hill hyperelastic model to best represent the tow behavior under transverse compressive loading. First, the four selected hyperelastic models are presented and then, their material parameters are fitted with the experimental data in order to underline their ability to account for both lateral and transverse extensions evolutions.

3.1.2 Preliminary study: presentation of four hyperelastic models

Four different hyperelastic models have been analyzed by Lectez et al. [99]. For the sake of clarity, in the following mathematical expressions of the considered hyperelastic models, the material parameters are written in blue.

Neo-hooken model. The neo-Hookean model is one of the simpliest hyperelastic model, as only one material parameter is required to fit with experimental data. This parameter C represents the shear modulus of the material for infinitesimal deformations; it comes out of the molecular theory on vulcanized rubber. As explained hereinbefore, this model is adapted to account for both compressibility and inextensibility:

$$W_{NH} = \underbrace{C_1(I_1 - 3)}_{\text{isotropic stiffness}} + \underbrace{C(J-1)^2 - 2C_1 ln(J)}_{\text{compressibility}} + \underbrace{C_f(I_4 - 1)^2}_{\text{inextensibility}} \tag{III.11}$$

where C, C_1, C_f are the material parameters of the model.

Mooney-Rivlin model. Mooney [106] first developed a simple hyperelastic model by observing that rubber response is linear under shear loading conditions. Rivlin [107], [108] extended this model by developing W as a polynomial series of $(I_1 - 3)$ and $(I_2 - 3)$. This form of strain energy is classical and used for very large strain problems. As explained hereinbefore, two terms have been added to the initial model to account for both large compressibility and anisotropy:

$$\begin{aligned} W_{MR} = &\underbrace{C_1(I_1 - 3) + C_{11}(I_1 - 3)^2 + C_{13}C_{13}(I_1 - 3)^4}_{\text{isotropic stiffness}} \\ &+ \underbrace{C(J-1)^2 - 2C_1 ln(J)}_{\text{compressibility}} + \underbrace{C_f(I_4 - 1)^2}_{\text{inextensibility}} \end{aligned} \tag{III.12}$$

where $C, C_1, C_{11}, C_{13}, C_f$ are the material parameters of the model.

Blatz-Ko model. In 1962, Blatz and Ko [109] modeled the deformation of a highly compressible polyurethane foam rubber. It becomes one of the most used models describing the behavior of rubber in the compressible case. As detailed hereinbefore, a strain energy term is added to account for the inextensibility in fiber direction:

$$\begin{aligned} W_{BK} = f\left[C_1(I_1-3) + C_{13}(I_1-3)^4 + \frac{C_1}{\beta}(I_3^{-\beta}-1)\right] \\ +(1-f)C_1\left[\left(\frac{I_2}{I_3}-3\right) + \frac{1}{\beta}(I_3^{-\beta}-1)\right] \\ + \underbrace{C_f(I_4-1)^2}_{\text{inextensibility}} \end{aligned} \tag{III.13}$$

Ogden-Hill model. In 1972, Ogden [110] proposed to derive the strain energy in terms of generalized strain: he expanded W through a series of real power of $(\lambda_i)_{i=x,y,z}$. Hill [111], and Storåkers [112] modified this model to take into account a large compressibility of the material. Finally, this model is adapted to account for the inextensibility in the fiber direction:

$$W_{OH} = \sum_i \frac{\mu_i}{{\alpha_i}^2}\left(\underbrace{\lambda_x^{\alpha_i} + \lambda_y^{\alpha_i} + \lambda_z^{\alpha_i} - 3}_{\text{isotropic stiffness}} + \underbrace{\frac{1}{\beta_i}(J^{-\alpha_i\beta_i}-1)}_{\text{compressibility}}\right) + \underbrace{C_f(I_4-1)^2}_{\text{inextensibility}} \tag{III.14}$$

where $\mu_i, \alpha_i, \beta_i, C_f$ are the material parameters of the model. According to Marckmann [101], the material parameters should fulfill the stability condition ($\mu_i\alpha_i > 0$). According to Lectez [99], a unique set of parameters (i.e. $i = 1$) is sufficient to reproduce both the experimental shape of the transverse stress/strain curve and the lateral extension. This model with a unique set of parameters will be compared to experimental data hereafter.

In the following section, the material parameters (in blue) of these models have been fitted to the experimental data measured by Lectez et al. [99] on a dry carbon tow.

3.1.3 Preliminary study: fitting with experimental data

Lectez et al. [99] used the setup presented in section 2.3.2 to characterize the lateral and transverse extensions of single dry tows made of continuous carbon fibers. Figure III.22 presents the results obtained: while the tow thickness decreases by 30% (Figure III.22b), the tow width rises by 2.2% (Figure III.22a).
For all models, Lectez uses a Newton-Raphson method where increments of transverse extension λ_z are imposed and longitudinal as well as lateral extensions (λ_x, λ_y) are computed by minimizing the residue $R = [\sigma_x, \sigma_y]$). The Table III.4 summarizes the material parameters manually choosen by Lectez to best fit the considered hyperelastic model with the experimental data. The analysis of these fittings is detailed hereafter for the four considered models.

Neo-Hookean model. During the transverse loading phase, the lateral extension evolution (λ_y in Figure III.23a) is close to the one measured experimentally. Additionally, the

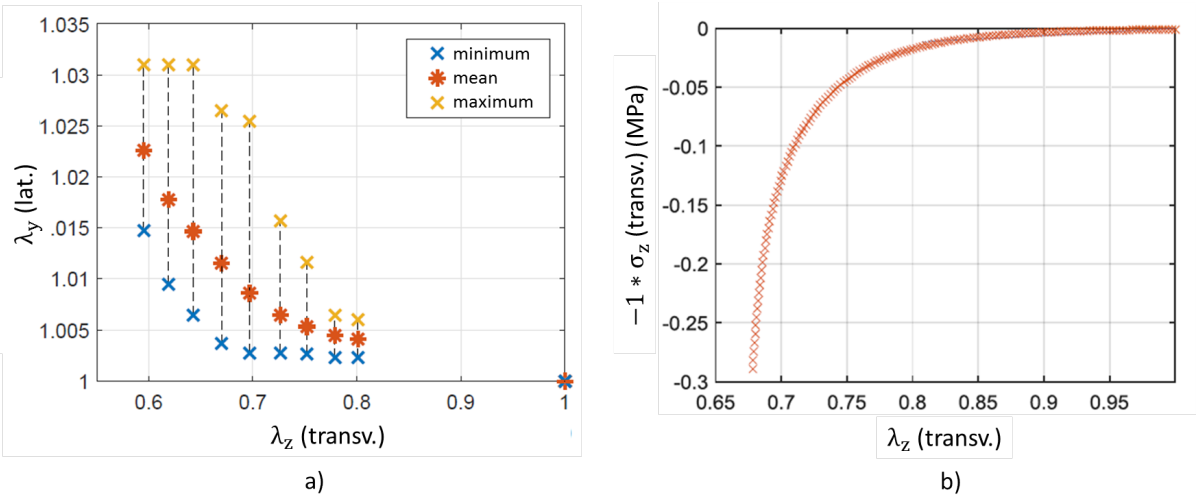

Figure III.22: Single carbon tow evolution during a dry loading compressive test: a) transverse strain extension with lateral strain extension. b) transverse strain extension with stress. [99].

Table III.4: Value of the material parameters choosen to fit experimental data for carbon tows. The four hyperelastic models are detailed.

Hyperelastic model	Material parameter and values
Neo-Hookean	$C = 0.003MPa, C_1 = 0.015MPa, C_f = 1MPa$
Mooney-Rivlin	$C_1 = 0.015MPa, C_{11} = 0.01MPa, C_{13} = 10MPa, C_f = 30MPa$
Blatz-Ko	$f = 0.1, \beta = 18.3, C_1 = 0.003MPa, C_{13} = 35MPa, C_f = 50MPa$
Ogden-Hill	$\mu_{OH} = 0.05MPa, \alpha = 360, \beta = 0.05, C_f = 1550MPa$

inextensibility in the fiber direction is verified ($\lambda_x = 1$). The transverse stress evolution predicted ($\sigma_\mathbf{z}$ in Figure III.23b) is correct for limited transverse extensions ($\lambda_z > 0.9$); nonetheless, the significant stiffening of the tow for transverse extension smaller than 0.9 is not well modeled with this neo-Hookean approach.

Mooney-Rivlin model. During the transverse loading phase, the lateral extension evolution is too large compared to the one measured experimentally: for a transverse extension of 0.7, the tow width rises by 30% (Figure III.24a). The nonlinearity predicted for the transverse stress evolution occurs for too small transverse extension (from $\lambda_z < 0.95$, in (Figure III.24b). This model seems not able to predict the significant compressibility of the dry carbon tows.

Blatz-Ko model. During the transverse loading phase, the lateral extension evolution is too large compared to the one measured experimentally: for a transverse extension of 0.7, the tow width rises by 22% (Figure III.25a). Nonetheless, in comparison to the Mooney-Rivlin model, the Blatz-Ko model predicts well the transverse stress evolution with the transverse extension evolution (Figure III.25b). This model, better than the two previous one, is still predicting a too large lateral extension evolution.

Ogden-Hill model. The Ogden-Hill model reproduces well the experimental behavior of carbon dry tows: the lateral extension evolution reaches 2% during the loading phase (Figure III.26a) and the transverse stress/strain behavior is well predicted. Additionally, the inextensibility of the tow in the fiber direction is respected.

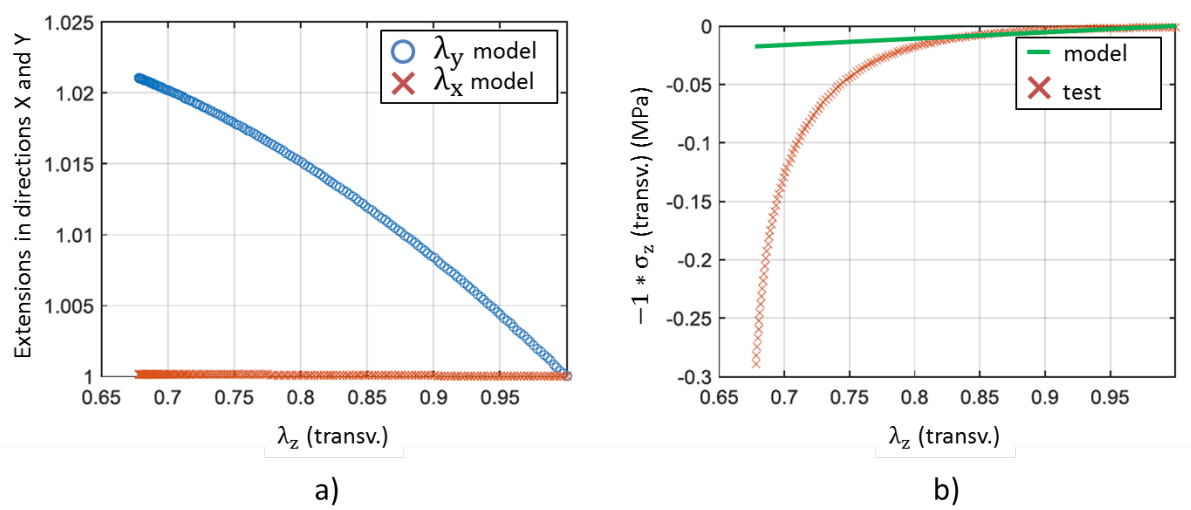

Figure III.23: Carbon tow behavior and neo-Hookean model: a) transverse strain extension with lateral and longitudinal strain extension. b) transverse strain extension with stress. [99].

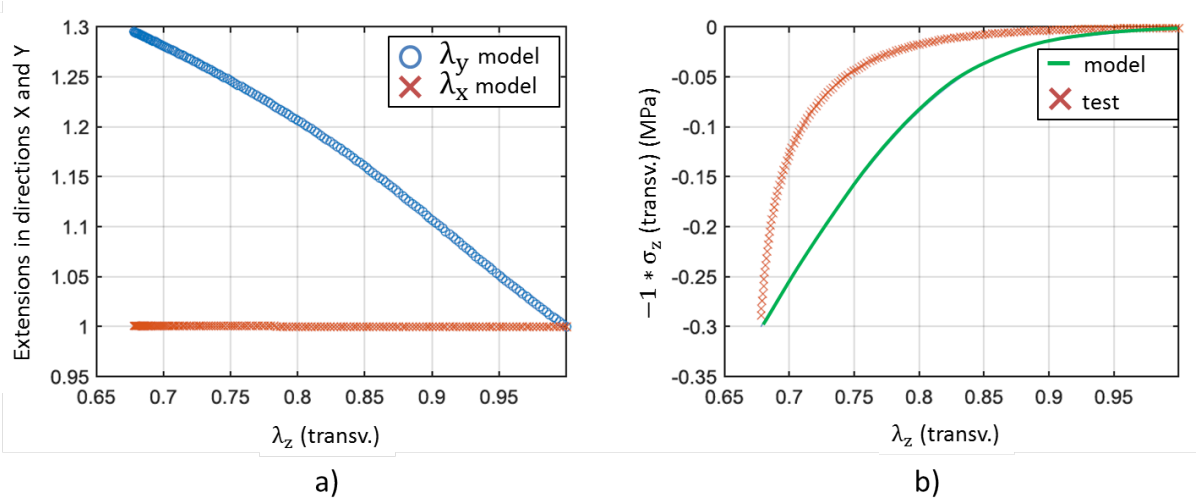

Figure III.24: Carbon tow behavior and Mooney-Rivlin model: a) transverse strain extension with lateral and longitudinal strain extension. b) transverse strain extension with stress. [99].

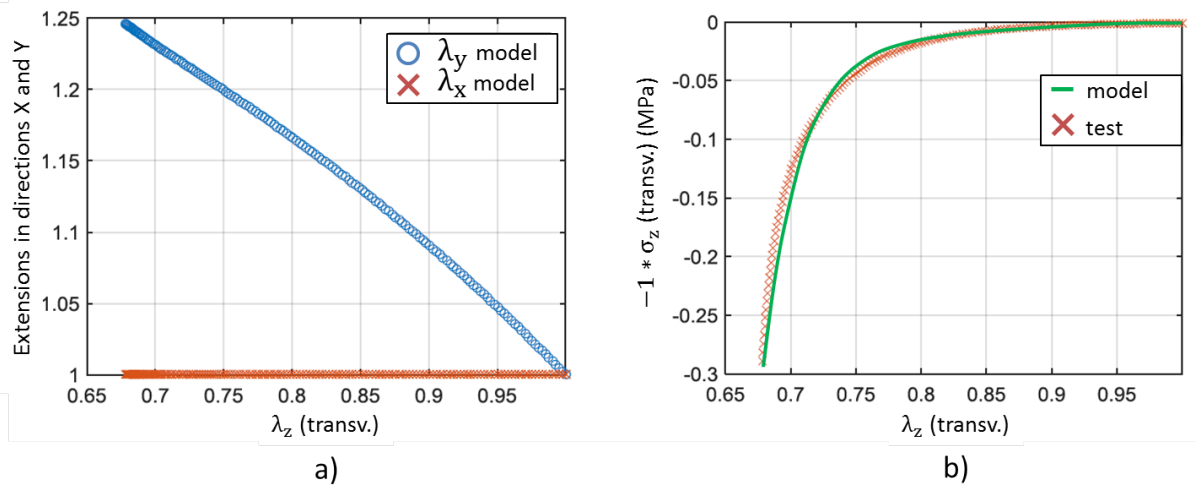

Figure III.25: Carbon tow behavior and Blatz-Ko model: a) transverse strain extension with lateral and longitudinal strain extension. b) transverse strain extension with stress. [99].

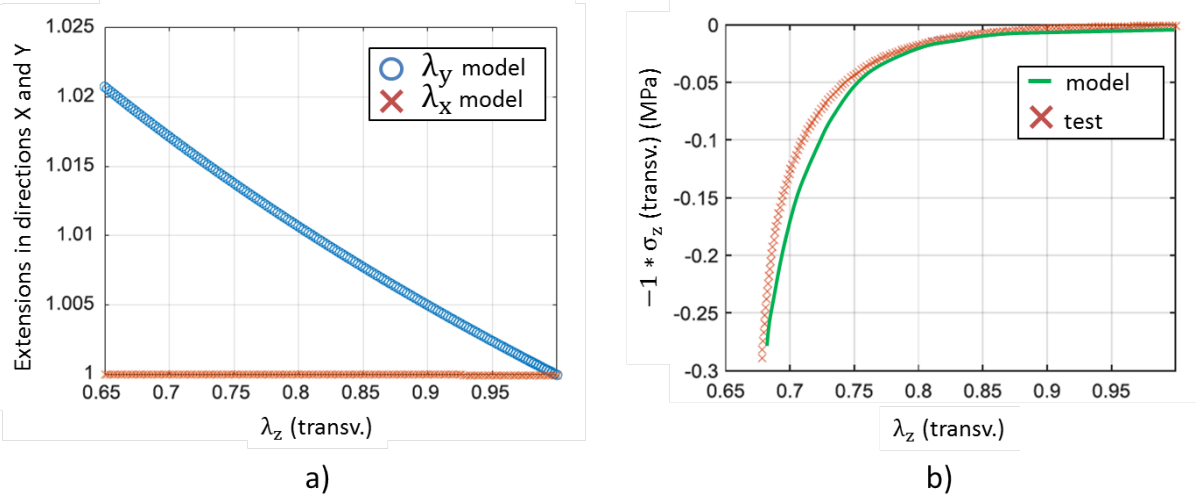

Figure III.26: Carbon tow behavior and Ogden-Hill model: a) transverse strain extension with lateral and longitudinal strain extension. b) transverse strain extension with stress. [99].

The Ogden-Hill model has been adapted to take into account both the large compressibility of tows subjected to compressive load and the inextensibility in the fiber direction. Lectez et al. [99] highlighted the ability of this hyperelastic model to reproduce, during a compressive loading, both the highly nonlinear thickness evolution and the slight width evolution of a single tow.

3.2 Influence of the lateral boundary conditions

The Ogden-Hill model has been selected to model the 3D behavior of a tow under a transverse compressive loading. To compute the 3D mechanical behavior, two kind of boundary conditions can be imposed on the lateral edges of the tows:

- *Laterally-free boundary condition.* The considered tow is free to deform in the lateral direction (Figure III.27a). This boundary condition is expressed as $\sigma_{\mathbf{y}} = 0$ and could represent the case of a single tow under a transverse compressive loading.
- *Laterally-constrained boundary condition.* The considered tow is constrained in the lateral direction, inducing that no lateral deformation is possible (Figure III.27b). This boundary condition is expressed as $\lambda_{\mathbf{y}} = 1$ and could represent the case of a tow within a tight stitched quasi-UD NCF.

Two analyses are proposed hereafter to evaluate the influence of the boundary conditions on the transverse mechanical behavior of the tow. First, two Newton-Raphson algorithms are implemented to take into account the two possible lateral boundary conditions. Then, a 2D analytical solution is proposed, where the inextensibility of the tow is imposed ($\lambda_x = 1$).

3.2.1 Numerical 3D solution

Two Newton-Raphson algorithms are implemented to take into account the two possible lateral boundary conditions:

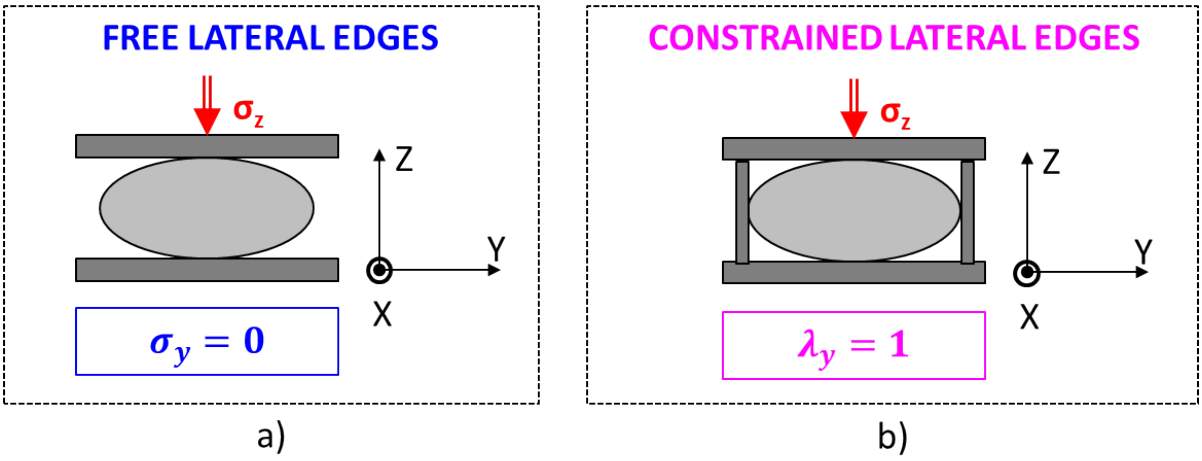

Figure III.27: Cross-section of a single tow subjected to a transverse compressive loading (σ_z): a) free lateral edge boundary condition. b) constrained lateral edge boundary condition.

- *Laterally-free boundary conditions.* In this numerical problem, increments of transverse extension λ_z are imposed. The aim is to compute the longitudinal and lateral extensions (λ_x, λ_y) for each increment and to minimize the residue $R = [\sigma_x, \sigma_y]$.
- *Laterally-constrained boundary conditions.* In this numerical problem, increments of transverse extension λ_z are imposed. The aim is to compute the longitudinal extension and the lateral stress (λ_x, σ_y) for each increment and to minimize the residue $R = [\sigma_x, \lambda_y - 1]$.

Using the material parameters summarized in Table III.4, the evolution of the longitudinal and the lateral extensions as well as the transverse stress evolution are computed for the two kinds of lateral boundary conditions. Figure III.28 illustrates the behavior obtained in both considered boundary conditions. The longitudinal extension evolution is negligible (Figure III.28a): the strain energy ($C_f(I_4 - 1)^2$) added to take into account the inextensibility in fiber direction is thus efficient. For a laterally-free dry carbon tow, the lateral extension slightly evolves (Figure III.28b): when the tow thickness reduces by 35%, the tow width increases by 2%, as measured experimentally by Lectez et al. [99]. As expected, when the tow is laterally-constrained, the tow width does not evolve. The lateral extension evolution affects the transverse behavior of the tow (Figure III.28c): the tow laterally-constrained is slightly stiffer in the tranverse direction than the tow laterally-free.
The transverse stiffening observed when the tow is laterally constrained might be enhanced for the glass tow of the study, whose lateral extension during a transverse loading can reach 9% (Figure III.18 in section 2.3.5).

The Ogden-Hill material parameters have been choosen to fit the experimental behavior of a dry carbon tow. A stiffening of the transverse behavior is highlighted when this tow is numerically laterally-constrained. This model is used further for the glass tows experimentally characterized at the beginning of the chapter.

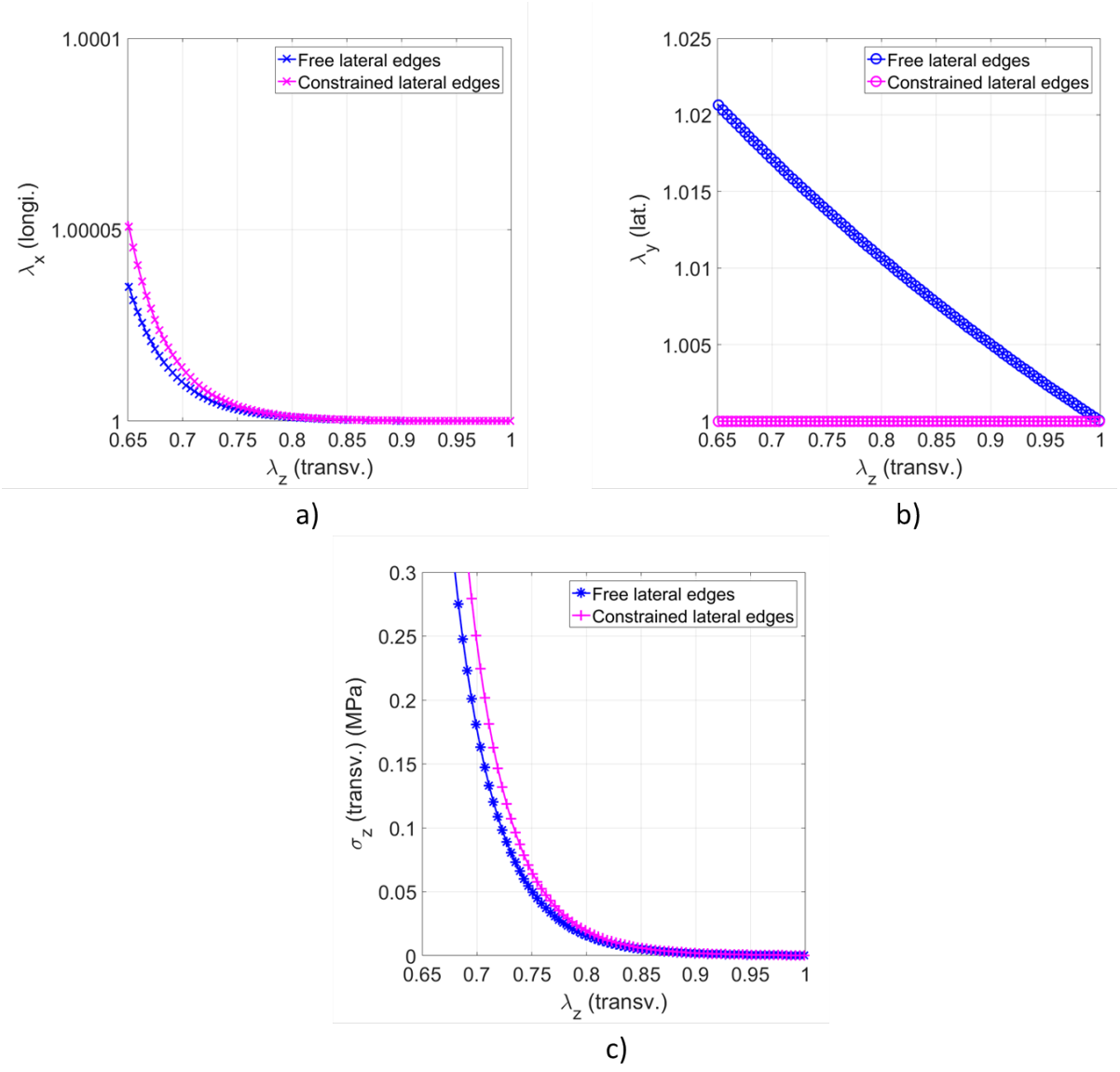

Figure III.28: 3D mechanical behavior of laterally free and constrained carbon tow: a) longitudinal extension. b) lateral extension. c) transverse stress.

3.2.2 Analytical 2D solution

An analytical solution is developed here to highlight again the impact of the lateral boundary conditions on the expression of the transverse mechanical behavior of the tows. In order to obtain an analytical solution, the Ogden-Hill model has been reduced to a 2D model: the fiber inextensibility has been taken into account by imposing $\lambda_x = 1$. The Cauchy stress tensor can be expressed in the eigen basis of the transformation gradient (so that $J = \lambda_x\lambda_y\lambda_z$) as detailed in Eq.III.10. Additionally, the Ogden-Hill model presented in the previous section can be written as:

$$W_{OH} = \frac{\mu_{OH}}{\alpha^2}\left(\underbrace{\lambda_x^\alpha + \lambda_y^\alpha + \lambda_z^\alpha - 3}_{\text{isotropic stiffness}} + \underbrace{\frac{1}{\beta}(J^{-\alpha\beta} - 1)}_{\text{compressibility}}\right) + \underbrace{C_f(I_4 - 1)^2}_{\text{inextensibility}} \tag{III.15}$$

Then, by combining Eq. III.10 and III.15, the lateral and transverse stress (respectively $\sigma_\mathbf{y}$ and $\sigma_\mathbf{z}$) can be expressed as:

$$\sigma_\mathbf{y} = \frac{\mu_{OH}}{\alpha}\frac{1}{\lambda_z}\left[\lambda_y^{\alpha-1} - \lambda_z^{-\alpha\beta}\lambda_y^{-\alpha\beta-1}\right] \tag{III.16}$$

$$\sigma_\mathbf{z} = \frac{\mu_{OH}}{\alpha}\frac{1}{\lambda_y}\left[\lambda_z^{\alpha-1} - \lambda_y^{-\alpha\beta}\lambda_z^{-\alpha\beta-1}\right] \tag{III.17}$$

Using these two expressions, the transverse mechanical behavior of the tow can be expressed in two different ways, depending on the lateral boundary conditions:

Laterally-free boundary conditions. The laterally-free boundary conditions induces $\sigma_\mathbf{y} = 0$. From Eq. III.16, a relationship between the lateral and the transverse extension can be expressed:

$$\lambda_y = \lambda_z^{\frac{-\beta}{1+\beta}} \tag{III.18}$$

Finally, by replacing Eq. III.18 in Eq. III.17:

$$\sigma_z^{free} = \frac{\mu_{OH}}{\alpha}\left(\lambda_z^{\frac{\alpha+\alpha\beta-1}{1+\beta}} - \lambda_z^{\frac{-\alpha\beta-1}{1+\beta}}\right)$$

Laterally-constrained boundary conditions. The laterally-constrained boundary conditions induces $\lambda_y = 1$. From Eq. III.17, the transverse stress can be expressed:

$$\sigma_z^{cstr} = \frac{\mu_{OH}}{\alpha}\left(\lambda_z^{\alpha-1} - \lambda_z^{-\alpha\beta-1}\right)$$

Figure III.29 presents the laterally-free and constrained behavior of carbon tows (material parameters detailed in Table III.4) computed numerically with the 3D model, and computed analytically with the corresponding 2D model. Even if the longitudinal extension slightly differs depending on the used method (Figure III.29a), both numerical and analytical methods give identical trends concerning the lateral extension evolution (Figure III.29b) and the transverse tow behavior (Figure III.29c). The conclusions drawn

previously with the 3D numerical solution concerning the transverse tow stiffening when laterally-constrained are thus still valid when the 2D analytical solution is considered.

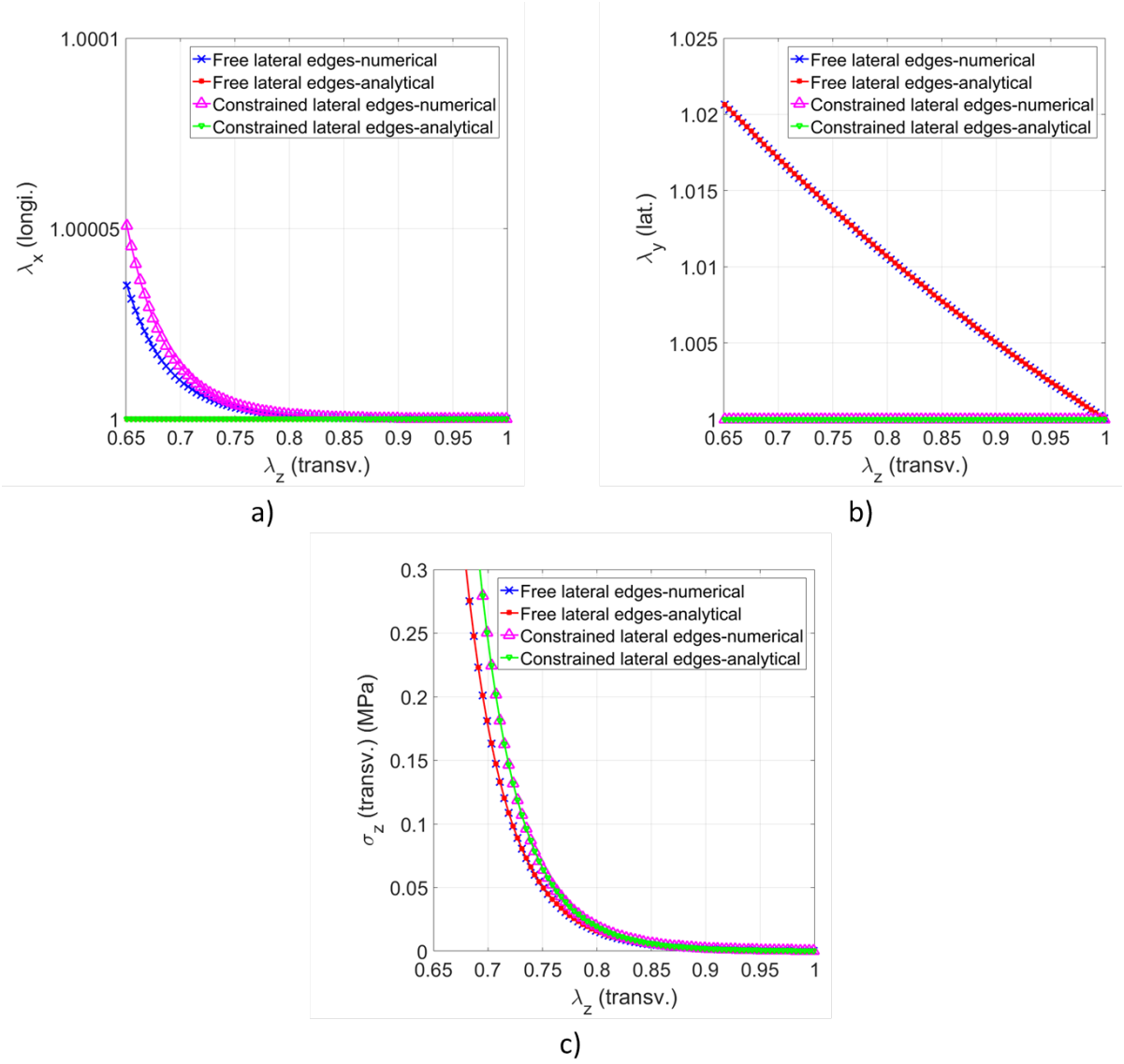

Figure III.29: 3D mechanical behavior of laterally free and constrained carbon tow computed with analytical and numerical methods: a) longitudinal extension. b) lateral extension. c) transverse stress.

Both numerical and analytical methods can be used to compute the mechanical behavior of tows using the Ogden-Hill model.

The material parameters of the Ogden-Hill model will be fitted with the experimental behavior of glass tows in the next section, and the resulting transverse stiffening observed when tows are laterally constrained will be discussed.

Table III.5: Identification of the material parameters to fit experimental data obtained on single glass tows

Hyperelastic model	Material parameter and values
Ogden-Hill	$\mu_{OH} = 0.15MPa, \alpha = 25, \beta = 0.55, C_f = 1550MPa$

3.3 Application to the glass tows characterized experimentally

In this section, the material parameters $\mu_{OH}, \alpha, \beta, C_f$ of the Ogden-Hill model are identified to best fit with the experimental data measured in section 2.3.5 on glass single tow. With this new set of material parameters, the influence of the lateral boundary conditions on the 3D mechanical behavior of the tow is investigated. Finally, the predicted behavior of a laterally-constrained glass tow will be compared with the experimental behavior of the quasi-UD NCF fabric measured in section 2.2.4.

3.3.1 Material parameters identification

Figure III.30 presents the experimental data monitored on single glass tows under unidirectional compressive loading and the corresponding Ogden-Hill model. The material parameters of the Ogden-Hill model, detailed in Table III.5, have been manually identified to best fit the experimental data. These parameters are kept identical for the studies presented hereafter.
It should be noticed that the initial tow width and thickness have been measured experimentally under an initial transverse stress $\sigma_{\mathbf{z}} = 0.01MPa$. New experimental data would be measured starting with a null initial transverse stress ($\sigma_{\mathbf{z}} = 0MPa$) to improve the fitting with the Ogden-Hill model.

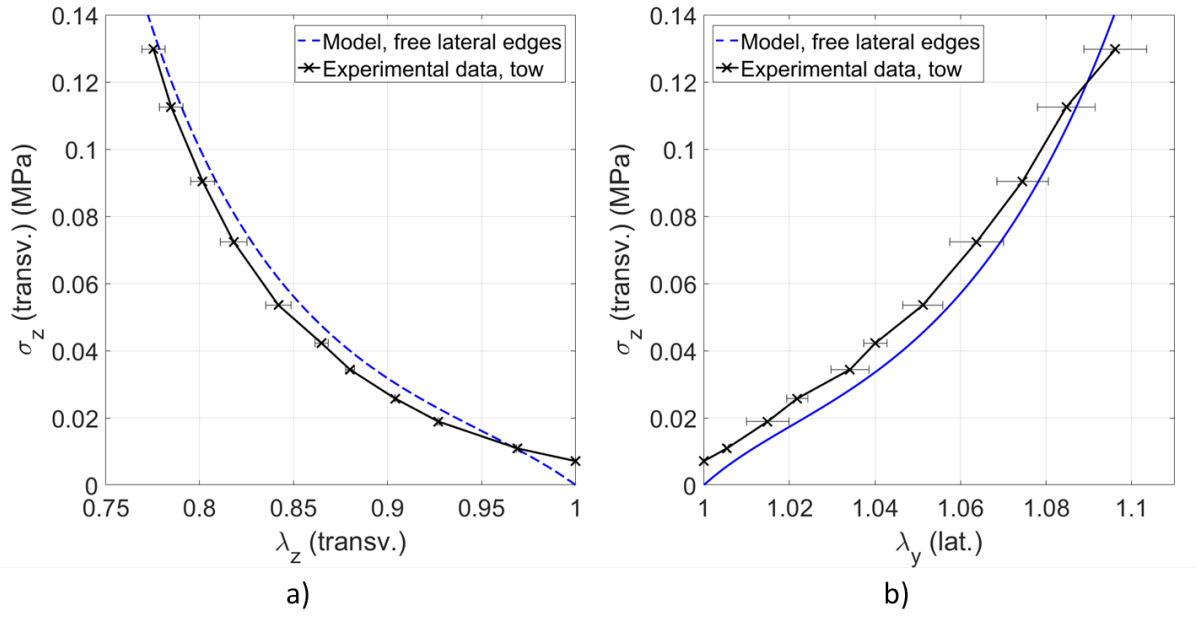

Figure III.30: Visualisation of the laterally-free Ogden-Hill model fitted with the glass tow experimental data: a) transverse stress/strain curve. b) lateral extension evolution.

3.3.2 Influence of the lateral boundary conditions: application to glass tows

Using the material parameters detailed in Table III.5, the influence of the lateral boundary conditions on the resulting 3D mechanical behavior is studied. In Figure III.31, the blue curves are the ones obtained with the laterally-free Ogden-Hill model, fitted previously with the experimental data; the pink curves correspond to the predicted behavior of the same tow (i.e. identical set of material parameters) that has been laterally-constrained.
As highlighted in Figure III.31a, the new set of parameters allows to reproduce the inextensibility of the tow in the fiber direction for both lateral boundary conditions. As expected, the lateral extension evolution of the laterally-free tow reproduces the rise of the tow width experimentally observed. Additionally, the width evolution of the corresponding laterally-constrained tow remains null during the transverse loading (Figure III.31b). The transverse behavior predicted for the laterally-constrained tow is significantly stiffer than the one of the laterally-free tow (Figure III.31c). Indeed, during the loading, the laterally-free tow significantly widens: the densification of the tow is thus limited. The same tow being laterally-constrained (pink curves in Figure III.31), the densification of the tow induces a stiffer transverse behavior.

3.3.3 Comparison between the predicted behavior of laterally-constrained tow and the experimental behavior of the quasi-UD NCF

With identical material parameters, the 3D mechanical behavior of a laterally-constrained tow has been also predicted. This laterally-constrained behavior may represent the one of tows within the quasi-UD NCF, that are potentially laterally-constrained by the stitch. Therefore, the predicted behavior of a laterally-constrained tow will be compared to the experimental behavior observed for the quasi-UD NCF.

Figure III.32 presents the experimental data measured on laterally-free single tow and the corresponding fitted Ogden-Hill model (blue) as well as the predicted laterally-constrained behavior of tows (pink) and the experimental data obtained for the quasi-UD NCF from where tows were extracted (section 2.2.4).
Figure III.32a highlights that the predicted transverse behavior of a laterally-constrained glass tow is in good agreement with the transverse behavior measured experimentally for a quasi-UD NCF ply. Concerning the lateral extension evolution, the fabric width decreases slightly (due to the vacuum bag boundary condition) whereas the predicted width of the laterally-constrained tow does not evolve. This comparison validates thus the ability of the proposed Ogden-Hill model to give a first prediction of the mechanical behavior of a quasi-UD NCF.
This comparison gives promising results concerning the usefulness of such a 3D model at tow scale. When a transverse compressive mechanical behavior is considered, it is possible to measure experimentally the lateral and transverse extensions evolution of a single tow, which is the main constituent of fabrics. With these experimental data and the presented model, textile manufacturers would have a reasonable prediction of the mechanical behavior of a quasi-UD NCF manufactured with a tight stitch. This model could therefore bring a first range of the transverse behavior of quasi-UD NCFs, from a loose to a tight stitch.

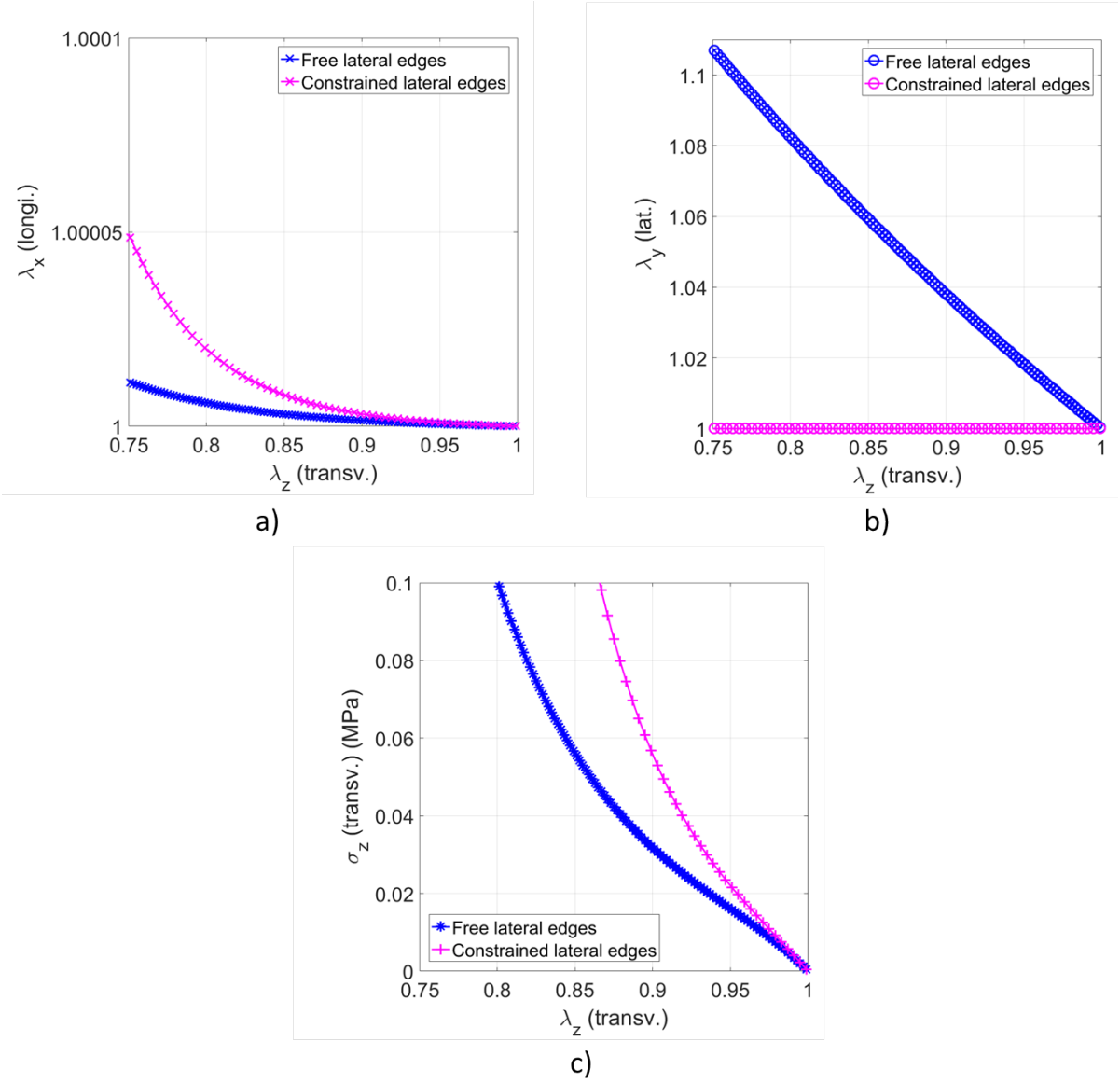

Figure III.31: 3D mechanical behavior of laterally free and constrained glass tow: a) longitudinal extension. b) lateral extension. c) transverse stress.

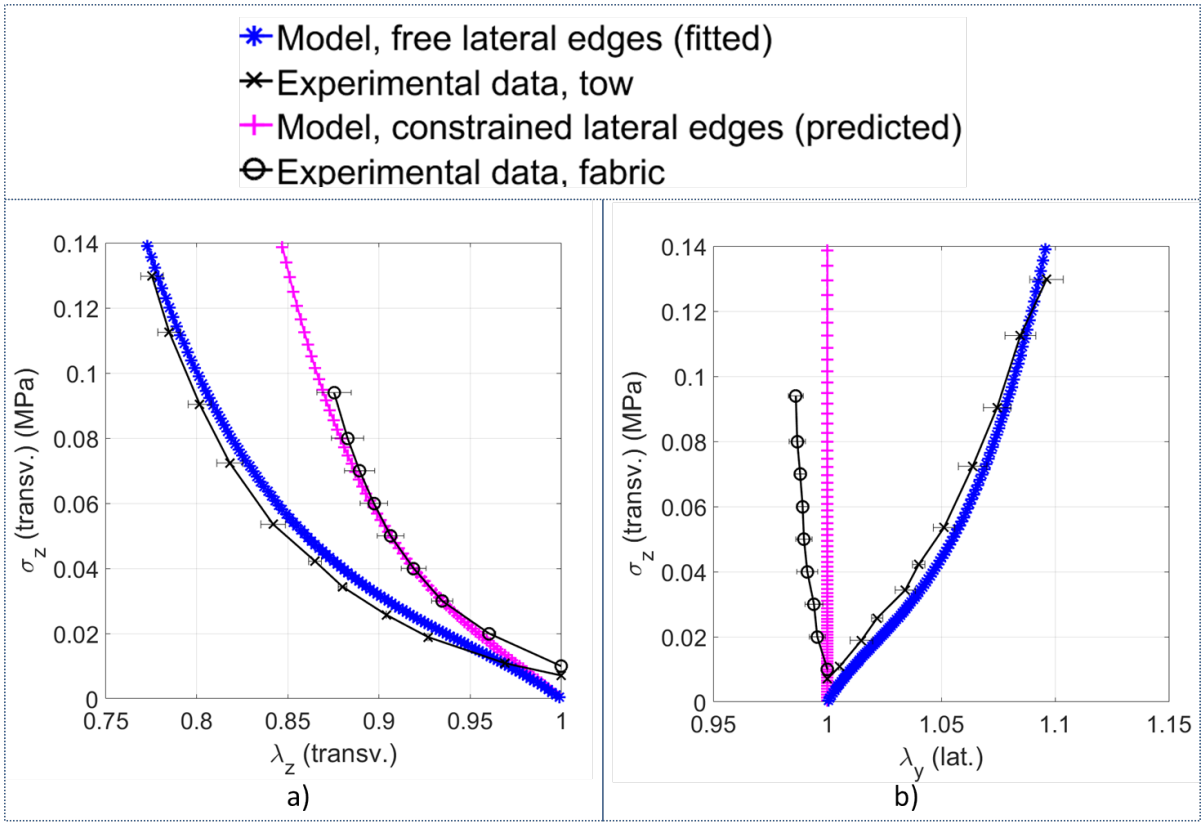

Figure III.32: Comparison of the predicted laterally-constrained glass tow behavior with the fabric experimental data: a) transverse stress/strain curve. b) lateral extension evolution.

The Ogden-Hill model is in good agreement with the 3D mechanical behavior of a glass tow extracted from a quasi-UD NCF. Modifying the lateral boundary conditions applied to this tow allows the behavior prediction of a laterally-constrained tow, which appears comparable to the quasi-UD NCF mechanical behavior.

3.4 Modeling conclusions and prospects

Several hyperelastic models have been compared to evaluate their ability to reproduce the 3D tow behavior under a dry unidirectional transverse compression. To take into account the high compressibility of the tows (highlighted in [1]) and their inextensibility in the fiber direction, these models (Neo-Hookean, Mooney-Rivlin, Blatz-Ko and Ogden) have been updated by adding adapted energy strain terms in their initial formulation. The Ogden-Hill model, detailed in Eq. III.14, is a promising model as it can both reproduce the highly non-linear transverse behavior of the tow and its widening.

Two types of lateral boundary conditions can be studied with this model: the tow can be considered laterally-free (the tow width evolution is free) or laterally-constrained (the tow width remains constant during the transverse loading). For identical materials parameters, and thus an identical tow material, the predicted transverse behavior of a laterally-constrained tow is stiffer than the one of a laterally-free tow. It could be explained by the fact that a laterally-free tow densifies less than a laterally-constrained one.

The Ogden-Hill model material parameters have been finally selected to fit the experimental behavior previously measured on single glass tows, that are laterally-free. Modifying the lateral boundary conditions leads again to a stiffer transverse behavior of the considered tow. This laterally-constrained glass tow behavior is in good agreement with the one measured on a quasi-UD NCF, made of these glass tows. This model could be thus useful for textile designers, in order to have a first understanding of the quasi-UD NCF behaviors.

There are still possibilities to improve this model. For instance, to mimic the modification of the lateral boundary conditions, an energy strain can be added in the considered hyperelastic model, as it has been done to reproduce the inextensibility in the fiber direction. This energy could be defined as $W_{lateral} = C_l(\lambda_y^2 - 1)^2$, where C_l could be choosen high to represent the behavior of a tow inside a tight stitch NCF, or low to represent the behavior of a tow inside a loose stitch NCF. Nonetheless, adding this energy will completely modify the meaning of the "lateral boundary conditions": instead of being "boundary conditions", they will become part of the "material parameters".
Moreover, the Ogden-Hill model could be fitted with the experimental data measured during the saturated unloading. Even if the tow width evolution is limited during this phase, this model could be used as an input for the simulation tool developed in the second chapter.

4 Conclusion and prospects

As highlighted in the second chapter, the filling time of a bidisperse and deformable dual-scale fibrous reinforcement depends on the tow width and thickness evolutions during

the infusion process. These geometrical evolutions, induced by a specific mechanical behavior, impact the spatial distribution of inter-tow and intra-tow pores inside the fibrous reinforcement during its filling stage. It appears thus of great interest to quantify the mechanical behavior of tows during the stages of the infusion process: the dry loading phase (occurring prior to the infusion itself) as well as the saturated unloading phase (occurring during the infusion). Additionally, modelling this tow mechanical behavior seems useful: the obtained model could be used as an input for the simulation tool developed in the second chapter.

Therefore, experimental investigations have been first conducted both on a single ply of quasi-UD NCF and on single tows extracted from this fabric. Infusion has been conducted on a single ply, and the fabric width and thickness evolutions have been measured with a chromatic confocal scanner. The stress applied on the fabric has been linked to the vacuum level set inside the cavity. Moreover, a specific setup has been designed to apply transverse unidirectional deformation to single tows, and to monitor the lateral extension of the tow (i.e. the evolution of its width) and the corresponding transverse stress level. The fabric behavior and single tow behavior measured during the saturated unloading phase are in good agreement with the geometrical evolutions of the tows and the stack monitored with the XCT experiments.
The dry loading phase, not measured in the first chapter with the XCT device, highlights an interesting behavior at both fabric and tow scale. While the fabric width remains almost constant, the width of the single tow (laterally free to deform) increases significantly (9.6%). The resulting transverse behavior is thus impacted: the fabric thickness reduces by 12.5% whereas the tow thickness reduces by 22.5%. It means that the fabric densifies whereas the lateraly-free single tow widens. The modeling of the 3D behavior of a tow subjected to a unidirectional transverse load appears thus of great interest. Indeed, by modifying the lateral boundary conditions applied on a single tow, the model could predict the resulting transverse behavior.

Based on the study presented by Lectez et al. [99], the Ogden-Hill hyperelastic model has been selected and adapted to take into account the compressibility of a single tow and its inextensibility in the fiber direction. The four material parameters of this model has been determined manually to best fit the lateral and transverse behaviors measured on single tows. Then, the transverse behavior of the tow, modeled initially with lateral boundary conditions allowing the evolution of the tow width, has been analyzed when a condition of no displacement is imposed at the lateral edges of the tow. It appears that this modeled laterally-constrained behavior is in good agreement with the experimental transverse behavior measured for the quasi-UD NCF. This first model seems thus promising for textile designers: for instance, they could estimate the transverse behavior of a tight stitched quasi-UD NCF by knowing the 3D mechanical behavior of the constitutive tow.

Several prospects have been identified about this mechanical study. Concerning the experimental aspect, several tracks have been identified:

- The transverse and lateral behavior of the quasi-UD NCF ply should be analyzed during an unidirectional transverse compressive tests. It would ensure the homogeneity of the results, presented for instance in the modeling section of this chapter.

- For both fibrous samples (tow and fabric), the dry loading behavior should be measured starting from a null stress ($\sigma_{\mathbf{z}} = 0MPa$), in order to improve the fitting with the Ogden-Hill model.
- The overall experimental work should be reproduced with two kinds of quasi-UD NCF, made of the same constitutive tows: one quasi-UD NCF with a tight stitch, the other one with a looser stitch.
- The XCT device presented in the first chapter could be used to visualize the geometrical evolution of tows within the aforesaid quasi-UD NCFs.

Concerning the modeling aspect, several tracks have been also identified:

- The Ogden-Hill model could be fitted with the experimental data measured during the saturated unloading. Even if the tow width evolution is limited during this phase, this model could be used as an input for the simulation tool developed in the second chapter.
- The Ogden-Hill model could be modified by adding a strain energy representing the "lateral boundary conditions" or in other words the tow confinement.
- Lectez et al. also worked on the behavior of tows subjected to load/unload cycles. The experimental work has been published in [100]. The modeling part, not published yet, could be used to predict the cyclic behavior undergone by a tow during the complete infusion process.

These items are part of the ungoing work.

Conclusion

In the current context of producing composite structural large parts at reduced costs, a deep study of the infusion process conducted with deformable dual-scale fibrous reinforcements has been addressed at mesoscopic and macroscopic scales. The goal of this thesis has been to characterize experimentally the flow-induced microstructural evolution of a quasi-unidirectional non-crimp fabric (quasi-UD NCF) during the infusion process, and to quantify the impact of this microstructural reorganization on relevant macroscopic parameters, such as the modelled in-plane permeability as well as the computed filling time of parts.

This investigation has been first addressed experimentally by conducting in situ infusions inside an X-ray Computed Tomography (XCT) device. The results obtained highlight a microstructural reorganization of the studied quasi-UD NCF. Additionally, a simplified model has been proposed from the image-based results to predict the in-plane permeability. The influence of the microstructural reorganization on the in-plane permeability has been established.
Then, an existing simulation tool dealing with dual-scale flow in non-deformable porous material has been upgraded to take into account both the macroscopic and mesoscopic deformations occurring for a quasi-UD NCF during the infusion process. This numerical tool allows to estimate the impact of the dual-scale decompaction phenomenon on the macroscopic filling time of parts.
As only geometrical evolutions of tows and fabrics had been captured and analyzed previously, a mechanical investigation of the tow behavior during the infusion process has been additionally carried out. Therefore, the 3D mechanical behaviors of a single tow and single ply of quasi-UD fabric have been experimentally analyzed through the infusion process stages. From these results, an hyperelastic model has been proposed to predict the 3D mechanical behavior of tows during the dry loading phase, prior to the infusion process.
The major conclusions obtained along this thesis are detailed hereafter.

The infusion process conducted on the quasi-UD NCF inside the XCT device leads to the following major conclusions:

- While the stack thickness increases by 9%, the constitutive tows of the fabric swell by 8%, only in the thickness direction. No width evolution of the tows has been detected between the dry and the saturated states.

Depending on the tensile force applied during the stitching, the resulting quasi-UD fabric allows more or less tows deformation during the decompaction phenomenon. Therefore, several flow-induced microstructural reorganizations have been envisaged and a simplified model has been used to predict the in-plane permeability corresponding to each decompaction scenario. It leads to the following conclusion:

- For a given macroscopic fiber volume fraction (V_f) evolution during the infusion process, the macroscopic permeability evolution of the stack can be impacted by a factor 3, depending on the considered microstructural reorganization scenario. V_f does not seem the appropriate descriptor to estimate the in-plane permeability when the infusion of dual-scale fabrics is considered.

A simulation tool dealing with the dual-scale flow in bidisperse deformable fibrous material has been developed. The influence of the dual-scale decompaction on the filling time has been thus estimated and it is found that:

- The developed numerical tool, coupled with relevant experimental data, could help in decisions making for composite manufacturers and textile designers.

The mechanical behavior of single tows and single ply recorded through the main steps of the infusion process as well as the 3D model proposed to predict the mechanical tow behavior lead to the following conclusions:

- The unidirectional dry loading occurring during the vacuuming process, prior to the infusion, appears to have a significant impact on the initial spatial distribution of meso and micro pores. Depending on the lateral boundary conditions applied to a single tow, it widens or densifies.

- The Ogden-Hill model is able to fit both the lateral and transverse evolution of tow during a transverse compressive test. By modifying the lateral boundary conditions applied to the tows, the model is able to predict the 3D mechanical behavior of a laterally-constrained tow. This behavior appears close to the experimental behavior of a quasi-UD fabric, from which the tows were extracted.

Prospects

The following prospects are organized in mid-term and long-term prospects. For both of them, experimental, numerical and modelling standpoints are discussed.

Mid-term prospects

From an experimental standpoint, it would be interesting to study deeper two quasi-UD NCFs made of given glass tows, but with two different stitches. The first step would be to use the XCT device developed in the first chapter to record identical microstructure during the dry loading phase. With image post-processing tools, it would be possible to identify the impact of the stitch on the tow widening, occurring inside the fabric. Secondly, these results could be compared with unidirectional tests conducted on both single tows and fabrics using the setup developed in the third chapter.
Linked to the previous discussed prospects, the Ogden-Hill model could be modified to vary the lateral boundary conditions applied to single tows. It would be thus possible,

from the laterally-free fitted behavior, to predict the mechanical behaviors of quasi-UD NCFs manufactured with different stitches.
Finally, the upgraded Ogden-Hill model, once fitted with transverse unloading experimental data, could be used as an input for the simulation tool developed in the second chapter, allowing thus the computation of 2D dual-scale flow inside deformable fibrous reinforcement.

Long-term propects

This study was focused on the dry and the saturated states of the infusion process. Transient mechanisms occurring during the filling have been simplified through chapters. Long-term prospects could be then focused on investigating the transient filling occurring during the infusion process.

From an experimental standpoint, the setup developed in the first chapter might be used in a synchrotron to capture the transient deformation occurring at the flow front during the impregnation. Fluids with high viscosity should be considered to allow acquisitions of longer duration.
From a modelling standpoint, viscous effects should be introduced in order to fuel appropriately the simulation tool previously developed. A significant experimental campaign could be considered to obtain relevant data.
Finally, it appears of interest to add the thermo-chemo-rheological mechanisms linked to the resin reactivity to build a tool able to take into account a reactive dual-scale flow in a bidisperse deformable fibrous material. Imbert et al. [36] have already implemented the equations to account for and follow the resin cure and temperature kinetics.

Appendix A

In the third chapter, the transverse and lateral evolutions of the tow during the saturated unloading phase of the infusion process have been presented along the X-position. This Appendix highlights the possibility of computing these results in a more standard form, as a strain-stress curve. To do so, a relationship is required between the X-position (fluid flow direction) and the fluid pressure in the deformable tow.

Analytical developement

A unidirectional flow is imposed in the X-direction inside a simple scale fibrous reinforcement (a single tow), which deforms during its filling. Assuming that the *saturation is perfect* and that the *fluid is incompressible*, mass conservation equation for unidirectional fluid flow is [42]:

$$\frac{\partial \phi}{\partial t} + \frac{\partial v_x}{\partial x} = 0 \tag{19}$$

where v_x is the fluid Darcy's velocity in X-direction and ϕ is the porosity content inside the tow. In the present study, the saturated state is studied instead of the transient state. Therefore, ϕ, even if varying with the X-position, is constant over time. Eq. 19 becomes thus $\frac{\partial v_x}{\partial x} = 0$.
Following the *hypothesis of a Darcy's flow*, the fluid velocity can be expressed as [41]:

$$v_x = \frac{-K(x)}{\mu} \frac{\partial P}{\partial x} \tag{20}$$

where μ is the fluid viscosity (constant here), K is the longitudinal permeability of the tow and P is the fluid pressure. K depends on the position x as the tow deforms during the filling stage.
The longitudinal permeability of the tow can be expressed with the model proposed by Gebart et al. [17]:

$$K(x) = \frac{8 r_f^2}{c} \frac{\phi(x)^3}{(1-\phi(x))^2} \tag{21}$$

where $K(x)$ is the in-plane permeability of the tow, r_f is the radius of the constitutive fiber, c is a parameter of the Gebart's law depending on the fiber arrangement inside the tow and $\phi(x)$ is the tow porosity content.
Additionally, by assuming that *the amount of fiber is kept equal in the considered tow* and that the *tow cross-section is rectangular*, the porosity content evolution can be expressed as:

$$\phi(x) = 1 - \frac{(1-\phi_{ini})h_{ini}w_{ini}}{h(x)w(x)} \tag{22}$$

where $\phi_{ini}, h_{ini}, w_{ini}$ are respectively the initial tow porosity content, the initial tow thickness and the initial tow width whereas h, w stands for the tow thickness and width evaluated at the position x.

Combining Eqs. 19-21, it is possible to obtain a differential equation for the pressure P:

$$f(x)\frac{\partial^2 P}{\partial x^2} + \frac{\partial f(x)}{\partial x}\frac{\partial P}{\partial x} = 0 \tag{23}$$

where f is function of the porosity content ϕ: $f(x) = \frac{\phi(x)^3}{(1-\phi(x))^2}$.
When a unidirectional tow of length L is infused, the boundary conditions of the problem are:

$$\begin{cases} P(x=0) &= P_{inj} \\ P(x=L) &= P_{vac} \end{cases}$$

where P_{inj} is the atmospheric pressure and P_{vac} is the vacuum level at the vacuum vent.

Application

Table 6 summarizes the values choosen for the analytical problem presented hereinbefore. As measured experimentally in the first chapter, the tow thickness evolution is considered linear with the x position.
Figure 33a shows the resulting evolution of the function f (defined in Eq. 22). The resulting pressure P (Figure 33b) depends on the tow deformation: if the tow thickness evolves significantly ($e = 0.5$, meaning that the tow thickness rises of 50%), the fluid pressure cannot be considered linear with the X-position. This behavior is in good agreement with the one computed by Acheson et al. [12].

This relationship between the fluid pressure and the X-position has been obtained by knowing the tow deformation along the X-position. This methodology could be thus used to plot the tow transverse and lateral deformations versus the total stress applied on the tow (Terzaghi's law can be used to compute the stress applied on the tow when knowing the fluid pressure).

Table 6: Parameters used to compute the pressure evolution. e is a parameter between 0 and 1 defining the amplitude of the decompaction phenomenon.

Injection parameters	
P_{inj}	1 bar
P_{vac}	0 bar
Tow geometry	
ϕ_{ini}	0.57
h_{ini}	0.9 mm
w_{ini}	3.27 mm
Tow geometry evolution	
h(x) (linear law)	$e \times h_{ini}(1-x)$
w(x)	w_{ini}

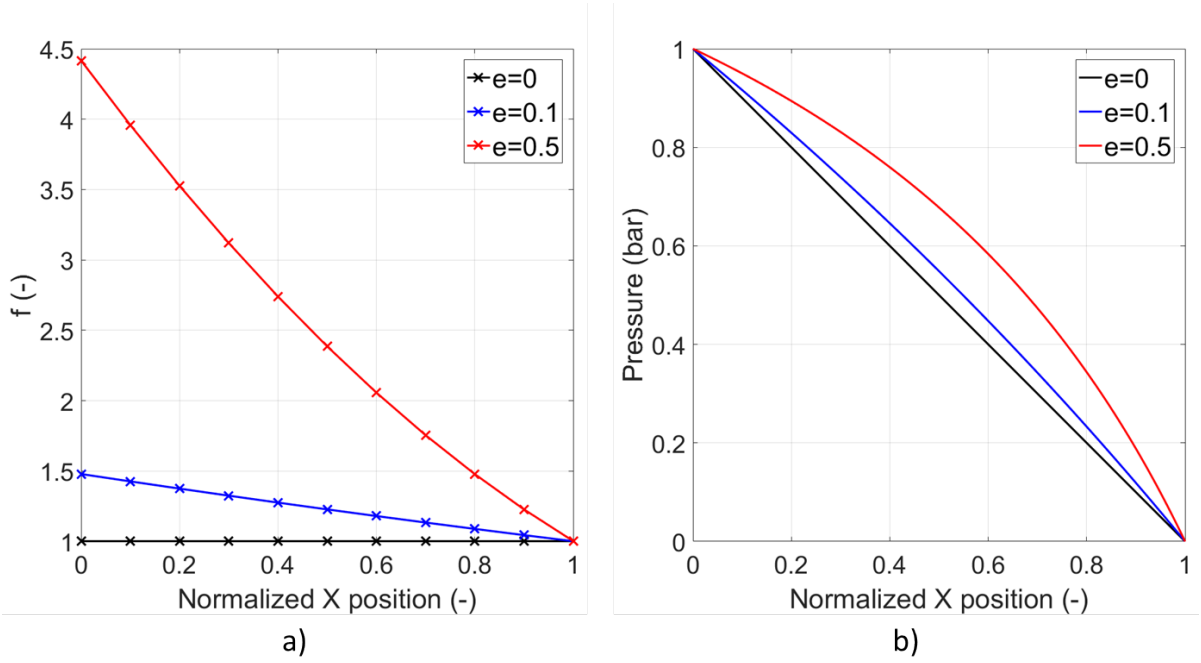

Figure 33: Evolution of the function f (a) and evolution of the resulting computed fluid pressure with X-position (b).

Nomenclature

A	area of a single tow
α_{CT}	relative mesoscopic decompaction of a tow measured with XCT
$\varepsilon, \varepsilon_z$	relative macroscopic theoretical transverse decompaction
ε_y	relative macroscopic theoretical lateral decompaction
ε_{macro}	relative macroscopic decompaction recorded with CCS
ε_{CT}	relative macroscopic decompaction recorded with XCT
fvf	macroscopic fiber volume fraction
GL	gray level
h_i	thickness of the component i (unit cell, tow, stack)
I	fluid filling factor
J	jacobian of the deformation gradient
$\mathbf{K}$	permeability tensor
K_c, $K_{channels}$	channels longitudinal permeability
K_t, K_{tow}	tow longitudinal permeability
K_{stack}	stack longitudinal permeability
λ_y	lateral large strain extension
λ_z	transverse large strain extension
μ	fluid viscosity
$\mu_{OH}, \alpha, \beta, C_f$	parameters of Ogden-Hill model
N_{tow}	number of tows
P	fluid pressure
ϕ_i	porosity of the phase i (tow, channels or stack)
q	sink term
Q_{decomp}	quantity of fluid to be relocated
q_{exc}	excess volume of fluid removed from elements
R	residual of the Newton-Raphson method
r_f	fiber radius
ρ	density of the fluid
σ	stress tensor applied to the solid phase (fabric or tow)
σ_z	transverse stress applied to the solid phase (fabric or tow)
t	time
$\mathbf{v}$	fluid velocity
$V(e)$	volume of the element e (fluid + fiber + porosity)
V_{in}	volume of fluid entering an element
VOF	volume of fluid
V_{tot}	total volume of fluid inside an element

W	total strain energy
w_i	width of the component i (unit cell, tow, stack)
x	direction of the fluid flow
X	normalization of x
X_{front}	normalized fluid front position
y	direction of the fabric width
Y	normalization of y
z	direction of the fabric thickness
Z	normalization of z
Z_i	altitude in a state i (dry or saturated)
Z_j	altitude of a component j (tow, fabric or PVC)

Bibliography

[1] A. S. Dharmalingam, J. Hemmer, A. S. Lectez, C. Binetruy, and S. Comas-Cardona, "Evolution of single carbon and glass fibrous tow cross-sections in dry and lubricated states during compaction perpendicular to the fibers," *Composites Part B: Engineering*, vol. 148, pp. 235–242, 2018.

[2] K. D. Tackitt and S. M. Walsh, "Experimental study of thickness gradient formation in the vartm process," *Materials and Manufacturing Processes*, vol. 20, no. 4, pp. 607–627, 2005.

[3] B. Yenilmez, M. Senan, and E. M. Sozer, "Variation of part thickness and compaction pressure in vacuum infusion process," *Composites Science and Technology*, vol. 69, p. 1710–1719, 2009.

[4] J. Yang, J. Xiao, J. Zeng, D. Jiang, and C. Peng, "Compaction behavior and part thickness variation in vacuum infusion molding process," *Applied Composite Materials*, vol. 19, no. 3-4, pp. 443–458, 2012.

[5] J. Vilà, F. Sket, F. Wilde, G. Requena, C. González, and J. LLorca, "An in situ investigation of microscopic infusion and void transport during vacuum-assisted infiltration by means of X-ray computed tomography," *Composites Science and Technology*, vol. 119, pp. 12–19, 2015.

[6] N. M. Larson and F. W. Zok, "Insights from in-situ X-ray computed tomography during axial impregnation of unidirectional fiber beds," *Composites Part A: Applied Science and Manufacturing*, vol. 107, pp. 124–134, 2018.

[7] G. Francucci, E. S. Rodríguez, and A. Vázquez, "Study of saturated and unsaturated permeability in natural fiber fabrics," *Composites Part A: Applied Science and Manufacturing*, vol. 41, no. 1, pp. 16–21, 2010.

[8] V. H. Nguyen, M. Lagardère, C. H. Park, S. Panier, *et al.*, "Permeability of natural fiber reinforcement for liquid composite molding processes," *Journal of materials science*, vol. 49, no. 18, pp. 6449–6458, 2014.

[9] D. Salvatori, B. Caglar, H. Teixidó, and V. Michaud, "Permeability and capillary effects in a channel-wise non-crimp fabric," *Composites Part A: Applied Science and Manufacturing*, vol. 108, pp. 41 – 52, 2018.

[10] B. Caglar, L. Orgéas, S. R. du Roscoat, E. M. Sozer, and V. Michaud, "Permeability of textile fabrics with spherical inclusions," *Composites Part A: Applied Science and Manufacturing*, vol. 99, pp. 1 – 14, 2017.

[11] E. Syerko, C. Binetruy, S. Comas-Cardona, and A. Leygue, "A numerical approach to design dual-scale porosity composite reinforcements with enhanced permeability," *Materials and Design*, vol. 131, pp. 307–322, 2017.

[12] J. Acheson, P. Simacek, and S. Advani, "The implications of fiber compaction and saturation on fully coupled vartm simulation," *Composites Part A: Applied Science and Manufacturing*, vol. 35, p. 159–169, 2004.

[13] J. Wolfrath, V. Michaud, A. Modaressi, and J. A. Månson, "Unsaturated flow in compressible fibre preforms," *Composites Part A: Applied Science and Manufacturing*, vol. 37, no. 6 SPEC. ISS., pp. 881–889, 2006.

[14] J. M. Bayldon and I. M. Daniel, "Flow modeling of the VARTM process including progressive saturation effects," *Composites Part A: Applied Science and Manufacturing*, vol. 40, no. 8, pp. 1044–1052, 2009.

[15] M. S. Rouhi, M. Wysocki, and R. Larsson, "Modeling of coupled dual-scale flow–deformation processes in composites manufacturing," *Composites Part A: Applied Science and Manufacturing*, vol. 46, p. 108–116, 2013.

[16] P. Carman, "Fluid flow through granular beds," *Transaction-Institution of Chemical Engineers*, vol. 15, pp. 150–166, 1937.

[17] B. R. Gebart, "Permeability of unidirectional reinforcements for RTM," *Journal of Composite Materials*, vol. 26, no. 8, pp. 1100–1133, 1992.

[18] S. Comas-Cardona, P. L. Grognec, C. Binetruy, and P. Krawczak, "Unidirectional compression of fibre reinforcements. part 1: A non-linear elastic-plastic behaviour," *Composites Science and Technology*, vol. 67, no. 3, pp. 507 – 514, 2007.

[19] T. G. Gutowski, T. Morigaki, and Z. Cai, "The consolidation of laminate composites," *Journal of Composite Materials*, vol. 21, no. 2, pp. 172–188, 1987.

[20] F. Robitaille and R. Gauvin, "Compaction of textile reinforcements for composites manufacturing," *Polymer Composites*, vol. 20, no. 1, pp. 48–61, 1999.

[21] N. Correia, F. Robitaille, A. Long, C. Rudd, P. Simacek, and S. Advani, "Analysis of the vacuum infusion moulding process: I. analytical formulation," *Composites Part A: Applied Science and Manufacturing*, vol. 36, p. 1645–1656, 2005.

[22] B. Martin, S. Comas-Cardona, C. Binetruy, N. Billon, J. L. Bouvard, and P. Lucas, "Influence of fabrics' design parameters on the morphology and 3D permeability tensor of quasi-unidirectional non-crimp fabrics," *Composites Part A: Applied Science and Manufacturing*, vol. 90, pp. 470–479, 2016.

[23] M. Deléglise, C. Binétruy, and P. Krawczak, "Solution to filling time prediction issues for constant pressure driven injection in RTM," *Composites Part A: Applied Science and Manufacturing*, vol. 36, no. 3, pp. 339–344, 2005.

[24] J. Courtney-Pratt and R. Gregory, "Microscope with enhanced depth of field and 3-D capability," *Applied Optics*, vol. 12, no. 10, pp. 2509–2519, 1973.

[25] S. Van Oosterom, T. Allen, M. Battley, and S. Bickerton, "Evaluation of a variety of vacuum assisted resin infusion processes," *21th International Conference on Composites Materials*, 20-25th August 2017.

[26] B. De Man, J. Nuyts, P. Dupont, G. Marcham, and P. Suetens, "Reduction of metal streak artifacts in,x-ray computed tomography using a transmission maximum a posteriori algorithm," *IEEE transactions on nuclear science*, vol. 47, no. 3, pp. 977–981, 2000.

[27] EasyCompositesLtd, "How to do perfect vacuum resin infusion of a carbon fibre (fiber) part - basic tutorial," 2010. Youtube Video: step 10, at 5 min. 9 sec.

[28] J.-Y. Buffiere, E. Maire, J. Adrien, J.-P. Masse, and E. Boller, "In situ experiments with x ray tomography: An attractive tool for experimental mechanics," *Experimental Mechanics*, no. 50, pp. 289–305, 2010.

[29] D. Sage, D. Prodanov, J.-Y. Tinevez, and J. Schindelin, "Mij: Making interoperability between imagej and matlab possible," *ImageJ User and Developer Conference*, 24-26 October 2012.

[30] E. Meijering, *FeatureJ: an ImageJ plugin suite for image feature extraction.* https://imagescience.org/meijering/software/featurej/, 1996-2017.

[31] J.-P. Thirion, "Image matching as a diffusion process : an analogy with maxwell's demons," *Medical Image Analysis*, vol. 2, no. 3, pp. 243–260, 1998.

[32] B. Martin, *Experimental investigation of the influence of the design parameters of unidirectional NCF fabrics on their processing and mechanical properties.* PhD thesis, Mines ParisTech, France, 2015.

[33] *Mécanique expérimentale des fluides, T.II: Dynamique des fluides réels et turbomachines.* Masson, 1994.

[34] M. Nordlund, T. Lundstrom, V. Frishfelds, and A. Jakovics, "Permeability network model for non-crimp fabrics," *Composites Part A: Applied Science and Manufacturing*, vol. 37, no. 6, p. 826–835, 2006.

[35] A. Endruweit, X. Zeng, M. Matveev, and A. C. Long, "Effect of yarn cross-sectional shape on resin flow through inter-yarn gaps in textile reinforcements," *Composites Part A: Applied Science and Manufacturing*, vol. 104, pp. 139–150, 2018.

[36] M. Imbert, E. Abisset-Chavanne, S. Comas-Cardona, and D. Prono, "Efficient dual-scale flow and thermo-chemo-rheological coupling simulation during on-line mixing resin transfer molding process," *Journal of Composite Materials*, vol. 52, no. 3, pp. 313–330, 2018.

[37] J. Slade, K. M. Pillai, and S. G. Advani, "Investigation of unsaturated flow in woven, braided and stitched fiber mats during mold-filling in resin transfer molding," *Polymer Composites*, vol. 22, no. 4, pp. 491–505, 2001.

[38] N. Patel, V. Rohatgi, and L. J. Lee, "Micro scale flow behavior and void formation mechanism during impregnation through a unidirectional stitched fiberglass mat," *Polymer Engineering & Science*, vol. 35, no. 10, pp. 837–851, 1995.

[39] M. Nordlund and V. Michaud, "Dynamic saturation curve measurement for resin flow in glass fibre reinforcement," *Composites Part A: Applied Science and Manufacturing*, vol. 43, p. 333–343, 2012.

[40] E. Ruiz, V. Achim, S. Soukane, F. Trochu, and J. Bréard, "Optimization of injection flow rate to minimize micro/macro-voids formation in resin transfer molded composites," *Composites Science and Technology*, vol. 66, no. 3, pp. 475 – 486, 2006.

[41] H. Darcy, "Les fontaines publiques de la ville de dijon : exposition et application," *Victor Dalmont*, 1856.

[42] C. Tucker and R. Dessenberger, "Governing equations for flow and heat transfer in stationary fiber beds," *Composite Materials Series*, p. 257, 1994.

[43] M. V. Bruschke and S. G. Advani, "A finite element/control volume approach to mold filling in anisotropic porous media," *Polymer Composites*, vol. 11, no. 6, pp. 398–405, 1990.

[44] U. Moon-Kwang and L. W. Il, "A study on the mold filling process in resin transfer molding," *Polymer Engineering & Science*, vol. 31, no. 11, pp. 765–771, 1991.

[45] Y. Yeong-Eun and L. W. Il, "Numerical simulation of the resin transfer mold filling process using the boundary element method," *Polymer Composites*, vol. 17, no. 3, pp. 368–374, 1996.

[46] S. Soukane and F. Trochu, "Application of the level set method to the simulation of resin transfer molding," *Composites Science and Technology - COMPOSITES SCI TECHNOL*, vol. 66, pp. 1067–1080, 2006.

[47] H. Tan and K. M. Pillai, "Numerical simulation of reactive flow in liquid composite molding using flux-corrected transport (fct) based finite element/control volume (fe/cv) method," *International Journal of Heat and Mass Transfer*, vol. 53, no. 9, pp. 2256 – 2271, 2010.

[48] P. Simacek and S. G. Advani, "Desirable features in mold filling simulations for liquid composite molding processes," *Polymer Composites*, vol. 25, no. 4, pp. 355–367, 2004.

[49] F. Trochu, R. Gauvin, and D.-M. Gao, "Numerical analysis of the resin transfer molding process by the finite element method," *Advances in Polymer Technology*, vol. 12, no. 4, pp. 329–342, 1993.

[50] V. Michaud, "A Review of Non-saturated Resin Flow in Liquid Composite Moulding processes," *Transport in Porous Media*, vol. 115, no. 3, pp. 581–601, 2016.

[51] J. Bréard, Y. Henzel, F. Trochu, and R. Gauvin, "Analysis of dynamic flows through porous media. part i: Comparison between saturated and unsaturated flows in fibrous reinforcements," *Polymer Composites*, vol. 24, no. 3, pp. 391–408, 2003.

[52] M. Van Genuchten, "A closed-form equation for predicting the hydraulic conductivity of unsaturated soils," *Soil Science Society of America Journal*, vol. 44, 1980.

[53] I. D. Patiño-Arcila and J. D. Vanegas-Jaramillo, "Modeling and simulation of filling in dual-scale fibrous reinforcements: state of the art and new methodology to quantify the sink effect," *Journal of Composite Materials*, vol. 52, no. 14, pp. 1915–1946, 2017.

[54] P. Simacek and S. G. Advani, "A numerical model to predict fiber tow saturation during liquid composite molding," *Composites Science and Technology*, vol. 63, no. 12, pp. 1725–1736, 2003.

[55] M. Biot, "General theory of three dimensional consolidation," *Journal of Applied Physics*, vol. 12, no. 2, pp. 155 – 164, 1941.

[56] L. Preziosi, D. Joseph, and G. Beavers, "Infiltration of initially dry, deformable porous media," *International Journal of Multiphase Flow*, vol. 22, no. 6, pp. 1205 – 1222, 1996.

[57] T. G. Gutowski, Z. Cai, J. Kingery, and S. J. Wineman, "Resin flow fiber deformation experiments," *Sampe Q; (United States)*, vol. 17, no. 4, pp. 54–58, 1986.

[58] T. Ouahbi, A. Saouab, B. Joel, O. Pierre, and C. Sylvain, "Modelling of hydro-mechanical coupling in infusion processes," *Composites Part A: Applied Science and Manufacturing*, vol. 38, no. 7, pp. 1646 – 1654, 2007.

[59] T. Tran, S. Comas-Cardona, N. E. Abriak, and C. Binetruy, "Unified micro-poromechanical approach for mechanical behavior and permeability of misaligned unidirectional fiber reinforcement," *Composites Science and Technology*, vol. 70, no. 9, pp. 1410–1418, 2010.

[60] Q. Govignon, S. Bickerton, and P. A. Kelly, "Simulation of the reinforcement compaction and resin flow during the complete resin infusion process," *Composites Part A: Applied Science and Manufacturing*, vol. 41, no. 1, pp. 45–57, 2010.

[61] G. Goncharova, B. Cosson, and M. Deléglise Lagardère, "Analytical modeling of composite manufacturing by vacuum assisted infusion with minimal experimental characterization of random fabrics," *Journal of Materials Processing Technology*, vol. 219, pp. 173–180, 2015.

[62] N. C. Correia, F. Robitaille, A. C. Long, C. D. Rudd, P. Simacek, and S. G. Advani, "Use of Resin Transfer Molding Simulation to Predict Flow, Saturation, and Compaction in the VARTM Process," *Journal of Fluids Engineering*, vol. 126, no. 2, p. 210, 2004.

[63] F. Robitaille and R. Gauvin, "Compaction of textile reinforcements for composites manufacturing: I, ii, iii," *Polymer Composites*, vol. 19, no. 5, pp. 543 –557, 1998.

[64] J. Kozeny, "Ueber kapillare leitung des wassers im boden," *Sitzungsber Akad. Wiss. Wien*, vol. 136, no. 2a, pp. 271–306, 1927.

[65] T. Dang-Huu, *Etude de l'infusion et de l'injection de composites dans une cavité déformable*. PhD thesis, Mines ParisTech, France, 2009.

[66] A. Dereims, *Simulation industrielle des procédes d 'élaboration de pièces composites par infusion de résine : couplage fluide / solide poreux très faiblement perméable en grandes déformations.* PhD thesis, Ecole Nationale Supérieure des Mines de Saint-Etienne, France, 2013.

[67] P. Celle, S. Drapier, and J. M. Bergheau, "Numerical modelling of liquid infusion into fibrous media undergoing compaction," *European Journal of Mechanics, A/Solids*, vol. 27, no. 4, pp. 647–661, 2008.

[68] M. S. Rouhi, M. Wysocki, and R. Larsson, "Holistic modeling of composites manufacturing using poromechanics," *Advanced Manufacturing: Polymer & Composites Science*, vol. 2, no. 1, pp. 14–26, 2016.

[69] O. Coussy, *Mécanique des Milieux Poreux.* Editions Technip, 1991.

[70] J. Cheng, P. Kelly, and S. Bickerton, "A rate-independent thermomechanical constitutive model for fiber reinforcements," *Journal of Composite Materials*, vol. 46, pp. 247–256, 2012.

[71] M. Imbert, *High speed reactive RTM with on-line mixing in dual-scale fibrous reinforcements: Experimental and numerical developments and investigations.* PhD thesis, Ecole Centrale de Nantes, France, 2017.

[72] B. Yenilmez and E. M. Sozer, "Compaction of e-glass fabric preforms in the vacuum infusion process, a: Characterization experiments," *Composites Part A: Applied Science and Manufacturing*, vol. 40, no. 4, pp. 499 – 510, 2009.

[73] P. A. Kelly, R. Umer, and S. Bickerton, "Viscoelastic response of dry and wet fibrous materials during infusion processes," *Composites Part A: Applied Science and Manufacturing*, vol. 37, pp. 868–873, 2006.

[74] M. Imbert, S. Comas-Cardona, E. Abisset-Chavanne, and D. Prono, "Introduction of intra-tow release/storage mechanisms in reactive dual-scale flow numerical simulations," *Journal of Composite Materials*, p. 002199831878049, 2018.

[75] C. Balbinot, F. Martoïa, L. Orgéas, P. Carion, F. Flin, S. Rolland du Roscoat, J.-F. Bloch, M. Terrien, and P. J. Dumont, "In situ 3D observations of the impregnation of model fibrous networks," in *The 14th international conference on Flow Processing in Composite Materials, Luleå, Sweden*, 2018.

[76] K. Andriamananjara, N. Moulin, J. Bruchon, and S. Drapier, "Prise en compte des effets capillaires locaux dans la simulation des procédés d'infusion pour les composites structuraux," in *Journées Nationales sur les Composites, Champs-sur-Marne, France*, 2017.

[77] R. Saunders, C. Lekakou, and M. Bader, "Compression and microstructure of fiber plain woven cloths in the processing of polymer composites," *Composites Part A: Applied Science and Manufacturing*, vol. 4, no. 29, pp. 443–54, 1998.

[78] P. Simacek and V. Karbhari, "Notes on the modeling of preform compaction: I-micromechanics at the fiber bundle level," *Journal of Reinforced Plastics and Composites*, vol. 15, no. 1, pp. 86–122, 1996.

[79] A. Somashekar, S. Bickerton, and D. Bhattacharyya, "Compression deformation of a biaxial stitched glass fibre reinforcement: Visualisation and image analysis using x-ray micro-ct.," *Composites Part A: Applied Science and Manufacturing*, vol. 42, no. 2, pp. 140–150, 2011.

[80] F. Desplentere, S. Lomov, D. Woerdeman, I. Verpoest, M. Wevers, and A. Bogdanovich, "Micro-ct characterization of variability in 3d textile architecture.," *Composites Science and Technology*, vol. 65, no. 13, pp. 1920–1930, 2005.

[81] P. Badel, E. Vidal-Salle, E. Maire, and P. Boisse, "Simulation and tomography analysis of textile composite reinforcement deformation at the mesoscopic scale," *Composites Science and Technology*, vol. 68, no. 12, pp. 2433–2440, 2008.

[82] T. Kruckenberg, L. Ye, and R. Paton, "Static and vibration compaction and microstructure analysis on plain-woven textile fabrics," *Composites Part A: Applied Science and Manufacturing*, vol. 39, no. 3, pp. 488–502, 2008.

[83] D. Wang, E. Vidal-Salle, and P. Boisse, "Longitudinal compression and poisson ratio of fiber yarns in meso-scale finite element modeling of composite reinforcements," *Composites Part B: Engineering*, vol. 141, pp. 9–19, 2018.

[84] M. Barburski, I. Straumit, X. Zhang, M. Wevers, and S. Lomov, "Micro-ct analysis of internal structure of sheared textile composite reinforcement," *Composites Part A: Applied Science and Manufacturing*, vol. 73, pp. 45–54, 2015.

[85] S. Lomov, P. Boisse, E. Deluycker, F. Morestin, K. Vanclooster, D. Vandepitte, and A. Willems, "Full-field strain measurements in textile deformability studies," *Composites Part A: Applied Science and Manufacturing*, vol. 39, no. 8, pp. 1232–1244, 2008.

[86] C. Dufour, F. Boussu, P. Wang, and D. Soulat, "Local strain measurements of yarns inside of 3d warp interlock fabric during forming process," *International Journal of Material Forming*, pp. 1–14, 2017.

[87] Y. Mahadik, K. Brown, and S. Hallett, "Characterisation of 3d woven composite internal architecture and effect of compaction," *Composites Part A: Applied Science and Manufacturing*, vol. 41, no. 7, pp. 872–880, 2010.

[88] N. Naouar, E. Vidal-Salle, J. Schneider, E. Maire, and P. Boisse, "3d composite reinforcement meso fe analyses based on x-ray computed tomography," *Composite Structures*, vol. 132, pp. 1094–1104, 2015.

[89] I. Straumit, S. Lomov, and M. Wevers, "Quantification of the internal structure and automatic generation of voxel models of textile composites from x-ray computed tomography data," *Composites Part A: Applied Science and Manufacturing,*, vol. 69, pp. 150–158, 2015.

[90] Y. Wan, I. Straumit, J. Takahashi, and S. Lomov, "Micro-ct analysis of internal geometry of chopped carbon fiber tapes reinforced thermoplastics," *Composites Part A: Applied Science and Manufacturing*, vol. 91, pp. 211–221, 2016.

[91] A. Endruweit and L. AC, "Analysis of compressibility and permeability of selected 3d woven reinforcements," *Journal of composite materials*, vol. 44, no. 24, pp. 2833–2862, 2010.

[92] E. Swery, T. Allen, and P. Kelly, "Automated tool to determine geometric measurements of woven textiles using digital image analysis techniques," *Textile Research Journal*, vol. 86, no. 6, pp. 618–635, 2016.

[93] P. Latil, L. Orgeas, C. Geindreau, P. Dumont, and S. Du Roscoat, "Towards the 3d in-situ characterisation of deformation micro-mechanisms within a compressed bundle of fibres," *Composites Science and Technology*, vol. 71, no. 4, pp. 480–488, 2011.

[94] S. Jeguirim, S. Fontaine, C. Wagner-Kocher, N. Moustaghfir, and D. Durville, "Transverse compression behavior of polyamide 6.6 rovings: Experimental study," *Textile research journal*, vol. 82, no. 1, pp. 77–87, 2012.

[95] D. Ivanov and S. Lomov, "Compaction behaviour of dense sheared woven preforms: Experimental observations and analytical predictions," *Composites Part A: Applied Science and Manufacturing*, vol. 64, pp. 167–176, 2014.

[96] R. Harwood, S. Grishanov, S. Lomov, and T. Cassidy, "Modelling of two-component yarns part i: the compressibility of yarns," *The Journal of The Textile Institute*, vol. 88, no. 4, pp. 373–384, 1997.

[97] A. Kabachi, M. Danzi, and P. Ermanni, "Experimental study on the influence of cyclic compaction on the fiber-bed static and dynamic responses," in *The 14th international conference on Flow Processing in Composite Materials, Luleå, Sweden*, 2018.

[98] K. Vallons, G. Adolphs, P. Lucas, S. V. Lomov, and I. Verpoest, "The influence of the stitching pattern on the internal geometry, quasi-static and fatigue mechanical properties of glass fibre non-crimp fabric composites," *Composites Part A: Applied Science and Manufacturing*, vol. 56, pp. 272–279, 2014.

[99] A.-S. Lectez, "Caractérisation et modélisation isotherme et anisotherme du comportement mécanique de meches de fibres seches sous compression transverse," tech. rep., IRT Jules Verne - GeM Institute, 2016.

[100] A. S. Lectez, K. El Azzouzi, C. Binetruy, S. Comas-Cardona, E. Verron, and J. M. Lebrun, "Three-dimensional mechanical properties of dry carbon fiber tows subjected to cyclic compressive loading," *Journal of Composite Materials*, vol. 52, pp. 2661–2677, 2018.

[101] G. Marckmann and E. Verron, "Comparison of hyperelastic models for rubberlike materials," *Rubber Chem Technol*, vol. 79, pp. 835–858, 2006.

[102] P. G. Ciarlet and G. Geymonat, "Sur les lois de comportement en élasticité non linéaire compressible," *CR Acad. Sci. Paris Sér. II*, vol. 295, pp. 423–426, 1982.

[103] F. Velardi, F. Fraternali, and M. Angelillo, "Anisotropic constitutive equations and experimental tensile behavior of brain tissue," *Biomechanics and Modeling in Mechanobiology*, vol. 5, no. 1, pp. 53–61, 2006.

[104] J. Merodio and R. Ogden, "Instabilities and loss of ellipticity in fiber-reinforced compressible non-linearly elastic solids under plane deformation," *International Journal of Solids and Structures*, vol. 40, pp. 4707–4727, 2003.

[105] *Mécaniquedes matériaux solides.* Dunod, 2009.

[106] M. Mooney, "A theory of large elastic deformation," *Journal of Applied Physics*, vol. 11, no. 9, pp. 582–592, 1940.

[107] "Large elastic deformations of isotropic materials. i. fundamental concepts," *Philosophical Transactions of the Royal Society of London A: Mathematical, Physical and Engineering Sciences*, vol. 240, no. 822, pp. 459–490, 1948.

[108] "Large elastic deformations of isotropic materials iv. further developments of the general theory," *Philosophical Transactions of the Royal Society of London A: Mathematical, Physical and Engineering Sciences*, vol. 241, no. 835, pp. 379–397, 1948.

[109] P. J. Blatz and W. L. Ko, "Application of finite elastic theory to the deformation of rubbery materials," *Transactions of the Society of Rheology*, vol. 6, no. 1, pp. 223–252, 1962.

[110] R. W. Ogden, "Large deformation isotropic elasticity–on the correlation of theory and experiment for incompressible rubberlike solids," *Proceedings of the Royal Society of London. Series A*, vol. 326, no. 1567, pp. 565–584, 1972.

[111] R. Hill, "Aspects of invariance in solid mechanics," *Advances in Applied Mechanics*, vol. 18, pp. 1–75, 1978.

[112] B. Storåkers, "On material representation and constitutive branching in finite compressible elasticity," *Journal of the Mechanics and Physics of Solids*, vol. 34, no. 2, pp. 125–145, 1986.

Titre : Couplage hydro-mécanique dans un renfort fibreux à double échelle de porosité : des caractérisation et modélisation mésoscopiques à la simulation du procédé d'infusion de résine liquide

Mots clés : Procédé d'infusion, Microstructure, Double-échelle de porosité, Expérimental, Modélisation

Résumé : L'un des objectifs de l'industrie éolienne est de produire de grandes pièces de structure à moindre coût. Dans ce contexte, la fabrication de pièces composites à partir de renforts quasi-unidirectionnels (quasi-UD NCF) avec le procédé d'infusion est compétitive tant sur le plan mécanique que financier.

Le procédé d'infusion engendre un phénomène de décompaction dû à la flexibilité de la bâche à vide. De plus les NCF présentent un écoulement à double échelle pendant leur imprégnation. La modélisation des deux phénomènes est souvent réalisée en supposant que la préforme fibreuse est un milieu continu à perméabilité variable. Néanmoins, la perméabilité est influencée par la répartition et la taille des mésopores, qui dépendent de l'état de compaction. Le but de cette thèse est de caractériser expérimentalement l'évolution d'un quasi-UD lors de l'infusion et d'évaluer l'impact de la réorganisation microstructurale sur des quantités macroscopiques d'intérêt, tels que la perméabilité et le temps de remplissage des pièces.

Des infusions ont été réalisées à l'intérieur d'un tomographe pour capter l'évolution d'une même microstructure avant et après infusion. Un modèle simplifié a été proposé pour prédire la perméabilité dans le plan et ainsi évaluer l'influence de la réorganisation microstructurelle sur celle-ci. De plus, un outil numérique a été développé pour prendre en compte un écoulement double échelle dans un milieu fibreux déformable bidisperse. L'impact de la décompaction sur le temps de remplissage des pièces a été établi. Une étude mécanique expérimentale du comportement de la mèche tout au long de l'infusion a également été réalisée afin de mieux comprendre le comportement du quasi-UD. Un modèle hyperélastique a finalement été proposé pour prédire le comportement mécanique 3D des mèches pendant la phase de chargement à sec, avant l'infusion.

Title: Hydro-mechanical coupling in a deformable dual-scale fibrous reinforcement: from mesoscale characterization and modeling to liquid resin infusion process simulation

Keywords: Infusion process, Microstructure, Dual-scale porosity, Experimental, Modelling

Abstract: A current aim of wind turbine industries is to produce large structural parts at reduced costs. In this context, manufacture composite blades made of quasi-unidirectional non-crimp fabrics (quasi-UD NCF) using the infusion process is competitive on both mechanical and cost aspects.

The infusion process involves an unloading phenomenon due to the vacuum bag flexibility. Additionally, during the impregnation, NCFs exhibit a dual-scale flow. Usual modeling of both phenomena assumes that the fibrous preform is a continuous medium with a varying permeability. Nonetheless, the permeability is affected by the meso-pores size and spatial distribution, which depend on the compaction state.

The goal of this thesis is thus to characterize experimentally the flow-induced microstructural evolution of a quasi-UD NCF during the infusion process, and to quantify the impact of this microstructural reorganization on relevant macroscopic parameters, such as modelled in-plane permeability as well as computed filling time of parts.

In situ infusion process has been conducted inside X-ray Computed Tomography device to capture a dual-scale fibrous microstructure prior and after the infusion process. Additionally, a simplified model has been proposed to predict the in-plane permeability and thus to evaluate the influence of the microstructural reorganization on it. Then, a numerical tool has been developed to account for dual-scale flow in a bidisperse deformable fibrous media. The impact of the dual-scale unloading on the macroscopic filling time of parts has been established. A mechanical investigation of the tow behavior during the infusion process has been additionally carried out experimentally to better understand the quasi-UD NCF behavior. From these results, a hyperelastic model has been proposed to predict the 3D mechanical behavior of tows during the dry loading phase, prior to the infusion process.